

School of Chemical and Petroleum Engineering

Department of Chemical Engineering

**Catalytic Oxidative Degradation of Hydrocarbons Using Novel
Metal-Free Nanocarbon Catalysts**

Xiaoguang Duan

**This thesis is presented for the Degree of
Doctor of Philosophy
of
Curtin University**

December 2015

Declaration

To the best of my knowledge and belief this thesis contains no material previously published by any other person except where due acknowledgement has been made. This thesis contains no material which has been accepted for the award of any other degree or diploma in any university.

Signature: _____ (Xiaoguang Duan)

Date: _____

Acknowledgement

I would like to express my most enthusiastic gratitude to my principal supervisor, Prof Shaobin Wang. Prof Wang is the most rigorous and learned scholar I have ever met. He is so modest and humble and is always ready to stop his work in hand for discussion with me on my results and confusions. The discussions with Prof Wang always motivate me to spark many new ideas. He led me to and has guided me adventuring in the fantastic world full of academic and scientific unknowns. Prof Wang's great guidance and passion for research have been and will be profoundly influencing my whole life.

Equally, I owe my sincere gratitude to my co-supervisor Dr Hongqi Sun for the inspiration and warm encouragement. It is Dr Sun who supervised me how to design the experiment, structure and format the manuscript, and address the reviews' critical comments during my PhD study without reservation. I would not have these great publications if there were no his continuous inputs to my manuscripts. I am lucky and proud to be his student.

I am grateful to my postgraduate supervisor, Prof Honghong Shan at China University of Petroleum, for her encouragement and support to pursue my PhD degree overseas and chase my dream. My sincere gratitude also goes to Prof Shaomin Liu for all the kind suggestions for the benefits of my research and career.

I am thankful to Prof Guoxiu Wang, Dr Zhimin Ao and Dr Kane O'Donnell for providing the excellent theoretical calculations to support my ideas for the insightful mechanistic studies. I am thankful to Prof Degang Li who taught me a lot about electrochemistry which has opened up a new gate for my future research. I also thank Prof Zongping Shao and Dr Chao Su for helping me analyze my materials via electrochemical evaluations. I also appreciate the characterization from Prof John Zhu's group at the University of Queensland.

I want to appreciate Yuxian Wang for the fruitful discussions and for his company in numerous nights and weekends when we did experiments together. I also want to thank

Jian Kang, my trusted friend, who is always there to help me go through my hard time overseas.

I am also thankful to my friends and colleagues, Chi, Chao, Xiaochen, Huayang, Ping, Wenjie, Stacey, Li, Chen, Zana, Jijiang, Yilin, Qiaoran, Leon, Wei, Xin, Min, Mingming, Jun, Qi, Lu, and Gang. Thank you, pals, I cannot imagine the life without you!

I want to give my gratitude to the technician team, Roshanak, Yu, Jimmy, Andrew, Guanliang, Ann, Anja, Jason, Araya, and Karen. Thanks you all for helping prepare the chemicals and training me how to use the equipment and software.

And last, but not the least, I would like to express my deepest love to my family, Mei, Xiaohui and Xiao. I truly thank you for your unconditional love and tremendous supports. I cannot go so far without your constant and eternal encouragement. The faith to make you be proud has guided me to go through such changeling and depressing time. I love you all dearly.

Abstract

Advanced oxidation processes (AOPs) have attracted considerable interests in environmental remediation due to the excellent capability in completely destroying toxic organics into harmless mineralized acids, carbon dioxide and water. Metal-free nanocarbons have demonstrated to be promising alternatives to conventional metal-based catalysts for green AOPs. This study presents several novel nanocarbon materials such as reduced graphene oxide, annealed nanodiamond, nitrogen-doped graphene or single-walled carbon nanotubes, and sulfur-, nitrogen- co-doped graphene for heterogeneous activation of persulfate (PS) and peroxymonosulfate (PMS). Proper surface modification of nanocarbons was achieved via facile physical and chemical strategies and the surface chemistry was revealed by advanced characterization techniques and density functional theory (DFT) calculations. The prepared carbocatalysts were employed for heterogeneously activating PS and PMS for catalytic oxidation of various contaminants such as dyes, phenolics, and antibiotics. The activation of peroxides and evolution of the reactive radicals (sulfate and hydroxyl radicals) on nanocarbon catalysts were investigated by means of deliberate materials and experimental design, *in situ* electron paramagnetic resonance (EPR), and theoretical calculations. Mechanistic studies were performed to identify the intrinsic active sites on pristine carbocatalysts and illustrate the heteroatom-doping effect on heterogeneous activation of PS or PMS. This study not only presents novel and superb nanocarbons for metal-free AOPs, but also facilitates the first insight into superoxide O-O bond activation with state-of-the-art carbocatalysis. The findings in this study would significantly contribute to materials science, environmental catalysis, carbocatalysis and other related fields.

Publications by the Author

Published and Accepted Papers:

1. **Duan XG**, Sun HQ, Kang J, Wang YX, Indrawirawan S, Wang SB. Insights into heterogeneous catalysis of persulfate activation on dimensional-structured nanocarbons. *ACS Catal.* 2015;5(8):4629-36.
2. **Duan XG**, O'Donnell K, Sun HQ, Wang YX, Wang SB. Sulfur and nitrogen co-doped graphene for metal-free catalytic oxidation reactions. *Small.* 2015;11(25):3036-44.
3. **Duan XG**, Ao ZM, Sun HQ, Zhou L, Wang GX, Wang SB. Insights into N-doping in single-walled carbon nanotubes for enhanced activation of superoxides: a mechanistic study. *Chem. Commun.* 2015;51(83):15249-52.
4. **Duan XG**, Sun HQ, Wang YX, Kang J, Wang SB. N-doping-induced nonradical reaction on single-walled carbon nanotubes for catalytic phenol oxidation. *ACS Catal.* 2015;5(2):553-9.
5. **Duan XG**, Ao ZM, Sun HQ, Indrawirawan S, Wang YX, Kang J, et al. Nitrogen-doped graphene for generation and evolution of reactive radicals by metal-free catalysis. *ACS Appl. Mater. Interfaces.* 2015;7(7):4169-78.
6. **Duan XG**, Indrawirawan S, Sun HQ, Wang SB. Effects of nitrogen-, boron-, and phosphorus-doping or codoping on metal-free graphene catalysis. *Catal. Today.* 2015;249:184-91.
7. **Duan XG**, Ao ZM, Zhou L, Sun HQ, Wang GX, Wang SB, Occurrence of radical and nonradical pathways from carbocatalysts for aqueous and nonaqueous catalytic oxidation. *Appl. Catal., B* 2016, **in press** (doi:10.1016/j.apcatb.2016.01.059).
8. Wang YX, Indrawirawan S, **Duan XG**, Sun HQ, Ang HM, Tade MO, et al. New insights into heterogeneous generation and evolution processes of sulfate radicals for phenol degradation over one-dimensional alpha-MnO₂ nanostructures. *Chem. Eng. J.* 2015;266:12-20.
9. Wang YX, Sun HQ, **Duan XG**, Ang HM, Tade MO, Wang SB. A new magnetic nano zero-valent iron encapsulated in carbon spheres for oxidative degradation of phenol. *Appl. Catal., B* 2015;172:73-81.
10. Indrawirawan S, Sun HQ, **Duan XG**, Wang SB. Low temperature combustion synthesis of nitrogen-doped graphene for metal-free catalytic oxidation. *J. Mater. Chem. A* 2015;3(7):3432-40.
11. Indrawirawan S, Sun HQ, **Duan XG**, Wang SB. Nanocarbons in different structural dimensions (0-3D) for phenol adsorption and metal-free catalytic oxidation. *Appl. Catal., B* 2015;179:352-62.

12. Ai B, **Duan X**, Sun H, Qiu X, Wang S. Metal-free graphene-carbon nitride hybrids for photodegradation of organic pollutants in water. *Catal. Today*. 2015;258, Part 2:668-75.
13. He JJ, Sun HQ, Indrawirawan S, **Duan XG**, Tade MO, Wang SB. Novel polyoxometalate@g-C₃N₄ hybrid photocatalysts for degradation of dyes and phenolics. *J. Colloid Interface Sci.* 2015;456:15-21.
14. Wang YX, Zhou L, **Duan XG**, Sun HQ, Tin EL, Jin WQ, et al. Photochemical degradation of phenol solutions on Co₃O₄ nanorods with sulfate radicals. *Catal. Today*. 2015;258, Part 2:576-84.
15. Kang J, **Duan XG**, Zhou L, Sun HQ, Tade MO, Wang SB. Carbocatalytic activation of persulfate for removal of antibiotics in water solutions. *Chem. Eng. J.* 2015; 288: 399-405.

Manuscripts Submitted or in Preparation:

16. **Duan XG**, Chao S, Zhou L, Sun HQ, Suvorova A, Odedairo T, Zhu ZH, Shao ZP, Wang SB. Controlled Generation of Reactive Radicals by Carbocatalysis on Nanodiamonds. (**Submitted**)
17. **Duan XG**, Ao ZM, Li DG, Sun HQ, Zhou L, Suvorova A, Saunders M, Wang GX, Wang SB. Surface-Tailored Nanodiamonds as Excellent Metal-Free Catalysts for Organic Oxidation. (**Submitted**)
18. **Duan XG**, Ao ZM, Zhou L, Sun HQ, Wang GX, Wang SB. Origins from pristine-graphene-based carbocatalysis for cleaving the O-O bond of peroxy monosulfate toward catalytic oxidation. (**To be Submit**)

Referred Conference

Duan XG, Sun HQ, Wang SB. Chemically Modified Graphene as Superior Carbocatalysts for Metal-Free Oxidation. IWA Nano & Water Regional Conference. May 20-22, 2015, Dalian, China. (**Oral presentation**)

Content

Declaration	i
Acknowledgement	ii
Abstract	iv
Publications by the Author	v
Content	vii
Chapter 1. Introduction	1
1.1 Background of demanding environmental remediation.....	1
1.2 Research objectives.....	3
1.3 Thesis organization	4
References.....	5
Chapter 2. Literature review	8
2.1 Introduction.....	8
2.2 Fenton and Fenton-like reactions.....	12
2.2.1 Conventional Fenton reactions	12
2.2.2 Improved Fenton processes	13
2.3 Physical and catalytic activation of persulfate.....	17
2.3.1 Physical techniques for persulfate activation	17
2.3.2 Metal and metal oxide catalyzed persulfate activation.....	18
2.3.3 Persulfate activation with carbocatalysis.....	20
2.4 Catalytic activation of peroxymonosulfate	22
2.4.1 Homogeneous activation of peroxymonosulfate	22
2.4.2 Peroxymonosulfate activation with metal oxides.....	23
2.4.3 Peroxymonosulfate activation with carbocatalysts	26
2.5 Conclusion	27
References.....	28
Chapter 3. Insights into Heterogeneous Catalysis of Persulfate Activation on Dimensional-Structured Nanocarbons	41
Abstract.....	41
3.1 Introduction.....	42
3.2 Experimental Section.....	44
3.3 Results and Discussions.....	46
3.4 Conclusions.....	59
References.....	60

Chapter 4. Controlled Generation of Reactive Radicals by Carbocatalysis on Nanodiamonds	64
Abstract.....	64
4.1 Introduction.....	65
4.2 Experimental Sections	67
4.3 Results and Discussions.....	68
4.4 Conclusions.....	84
References.....	84
Chapter 5. Nitrogen-Doped Graphene for Generation and Evolution of Reactive Radicals by Metal-Free Catalysis	89
Abstract.....	89
5.1 Introduction.....	90
5.2 Experimental Section.....	92
5.3 Results and Discussions.....	94
5.3.1 Characterization of Carbon Materials.	94
5.3.2 Catalytic Performance of Carbon Materials in Phenol Degradation.	99
5.3.3. Mechanism of Generation and Evolution of Active Radicals and Reaction Pathways.....	104
5.4 Conclusions.....	110
References.....	110
Chapter 6. Sulfur and Nitrogen Co-Doped Graphene for Metal-Free Catalytic Oxidation Reactions	115
Abstract.....	115
6.1 Introduction.....	116
6.2 Experimental Section.....	117
6.3 Results and Discussion	119
6.3.1 Characterization of Materials.	119
6.3.2 Phenol Oxidative Degradation on Nanocarbons.	124
6.3.3 Catalytic Mechanism of PMS Activation on Graphene.	127
6.4 Conclusions.....	135
References.....	136
Chapter 7. Effect of Nitrogen-Doped Single-Walled Carbon Nanotubes on Activation of Superoxide O-O Bond for Enhanced Metal-Free Oxidation	141
Abstract.....	141
Part 1. N-Doping-Induced Nonradical Reaction on Single-Walled Carbon Nanotubes for Catalytic Phenol Oxidation	142
7.1 Introduction.....	142
7.2 Experimental Section.....	144
7.3 Results and Discussion	145

7.4 Conclusions.....	156
Part 2. Insights into N-Doping in Single-Walled Carbon Nanotubes for Enhanced Activation of Superoxides: A Mechanistic Study.....	157
7.5 Introduction.....	157
7.6 Theoretical Calculation Section.....	158
7.7 Results and discussion	159
7.8 Conclusions.....	168
References.....	168
Chapter 8. Conclusions and Perspectives	174
8.1 Conclusions.....	174
8.2 Perspectives and suggestions for future research	177

Chapter 1. Introduction

1.1 Background of demanding environmental remediation

In recent centuries, the expansion of human society along with the rapid industrialization has severely burdened the ecosystem, and has severely interrupted the harmony between human beings and the nature that has lasted for thousands of years. The deteriorating environmental issues, especially air pollution and water contamination, have triggered worldwide concerns.

Freshwater is one of the most critical natural resources for human beings on the Earth. Our beautiful home, the *blue planet*, is mostly covered by water (71%) that enables the population of immense creatures, however, only about 2.5% water on the Earth is freshwater.(1) Most of the freshwater (68%) is either stored deeply underground or permanently frozen in the Arctic and Antarctic Continents. No more than 0.77% of all water (~10,665,000 km³) on the surface (e.g. lakes, rivers, plant life) and in the atmosphere is accessible and available for human living, agricultural irrigation, and industrial application, and being shared with other living species.(2) However, the industrial and domestic usage of water has increased dramatically due to the modern urbanization and population explosion. Many rivers are now drying up before running into the sea and the underground water has also been exploited far beyond the rate of replenishment in many areas.

In spite of the basic needs such as drinking and sanitation, people nowadays more concern about the quality, security and the availability of water supplies.(3) Recent researches have detected trace amount of pharmaceutical compounds and pesticides in soil, lakes, and underground waters which are stubbornly resistant to natural degradation with microorganisms. What even worse are that they are only emerging contaminatants in addition to the large quantity of harmful organic pollutants discharged from industries and households that far beyond the eco self-purification capacity. The scarce resources, deteriorating quality, and severe contaminations of available freshwater have impaired the ecological environment and restrained the economic prosperity in human society.(4, 5)

On the other hand, researchers never stop the race to develop state-of-the-art technologies to provide clean drinking water for households and to deal with the polluted waterbodies. In regard to wastewater treatment, various effective approaches such as physical adsorption, flocculation/coagulation, photocatalysis, bio-degradation, and chemical oxidation were developed to remove the harmful pollutants in contaminated waterbodies.(6-8) Among the techniques mentioned above, chemical oxidation is one the most efficient approaches that can rapidly decompose organics into less toxic mineralized acids or even completely oxidize the contaminants into non-hazardous carbon dioxide (CO₂) and water.

Advanced oxidation processes (AOPs) have attracted intensive attention in recent decades due to the superb capability toward oxidizing recalcitrant organics.(9) In an typical AOPs system, superoxides such as hydrogen peroxide (H₂O₂), ozone (O₃), peroxymonosulfate (PMS), persulfate (PS, also known as peroxydisulfate or PDS) to evolve highly reactive oxygen species such as hydroxyl radical ([•]OH), superoxide radical (O₂^{•-}) or sulfate radical (SO₄^{•-}), to attack the target organics. A series of complicated reactions, *e. g.* addition reaction, one-electron transfer, and H-abstraction, are always involved in the AOPs.(10, 11) Commercial Fenton reaction using H₂O₂/Fe^{II} can effectively generate a myriad of [•]OH for decomposing a variety of organics. However, the H₂O₂/Fe^{II} system suffers from some intrinsic drawbacks, including use of the chemically unstable Fenton agents (ferrous salts and H₂O₂), requirement of extreme reaction condition (pH ~ 3), and generation of vast amount of sludge for separation, giving rise to intensive energy inputs for storage, transportation, reaction, and post-treatment.(12, 13)

Sulfate radical based AOPs (SR-AOPs) were expected to be a promising alternative strategy to overcome the defects of hydroxyl radical-based systems by employing more stable oxidants (PMS and PS), and providing a higher oxidative potential and a better selectivity to target compounds in a wider basic/acidic range.(9) Effective homogeneous and heterogeneous catalytic systems with transition metals and metal oxides have been proposed for activating PMS and PS to generate sulfate radicals for organic decomposition.(14-16) However, the poor stability of metal-based catalysts and inevitable leaching of toxic metal ions to the waterbody have seriously restrained the practical applications.

Very recently, Sun and co-workers first uncovered that reduced graphene oxide (rGO) can activate PMS for catalytic oxidation of aqueous organic pollutants.(17) The green and efficient carbocatalysts possessed unique physical, chemical, and electronic properties, and have been widely investigated in electrochemistry, photocatalysis and oxidative dehydrogenation reactions.(18-20) The discovery of nanocarbons for superoxide activation may open up a bright avenue for metal-free carbocatalysis and sustainably environmental remediation.

1.2 Research objectives

This study aims to develop novel and robust nanocarbon catalysts for heterogeneous activation of peroxymonosulfate and persulfate to decompose hydrocarbons, dyes, and antibiotics in aqueous solution. Meanwhile, this research also dedicates to providing the first insight into the intrinsic mechanisms of PMS and PS activation and radical evolution in carbocatalysis. To this end, comprehensive studies integrating deliberate materials design, delicate catalysis, advanced instrumentation of *in situ* electron paramagnetic resonance (EPR), and density functional theory (DFT) calculation, were implemented. The specific objectives of this study are listed as follows.

1. Synthesizing surface-tuned nanocarbons such as reduced graphene oxide (rGO), nanodiamond, heteroatom-doped graphene and single-walled carbon nanotubes (SWCNTs) with facile physical and chemical modifications.
2. Employing the carbocatalysts for activation of superoxides (PS and PMS) for catalytic degradation of organic contaminants such as dyes, phenolics, and antibiotics.
3. Probing the mechanism unveiling the intrinsic active sites of the carbocatalysis for heterogeneous PMS and PS activation.
4. Investigating the heteroatom doping effects on graphene- and SWCNT-based catalysts for PMS activation with deliberate materials design and theoretical calculations.
5. Identifying emerging carbocatalysis and novel oxidation pathways on modified nanocarbons with mechanistic studies.

1.3 Thesis organization

This thesis consists of eight chapters, including introduction, literature review, results and discussions (five chapters), conclusions and perspectives for future studies.

Chapter 1 — Introduction — gives a brief introduction to the background, encountered issues, and solutions in regard to environmental remediation especially for wastewater treatment. This chapter also includes the objectives of the research and structural organization of the thesis.

Chapter 2 — Literature review — comprehensively summarizes the various AOPs and different physical and chemical strategies to activate the superoxides with an emphasis on heterogeneous activation of hydrogen peroxide, persulfate, and peroxymonosulfate using metal/metal-oxide and emerging nanocarbon catalysts.

Chapter 3 — Insights into Heterogeneous Catalysis of Persulfate Activation on Dimensional-Structured Nanocarbons. (*ACS Catal.* 2015; 5(8): 4629-36). — investigates the persulfate activation mechanism on nanocarbons with different dimensional structures, and reveals the active sites for PS activation in carbocatalysis.

Chapter 4 — Controlled Generation of Reactive Radicals by Carbocatalysis on Nanodiamonds. — unravels the persulfate activation processes on thermal annealed nanodiamonds for catalytic oxidation and electrochemical analysis. The versatile environmental implications are evaluated for the novel oxidative systems.

Chapter 5 — Nitrogen-Doped Graphene for Generation and Evolution of Reactive Radicals by Metal-Free Catalysis. *ACS Appl. Mater. Interfaces.* 2015; 7(7): 4169-78— reports the preparation of nitrogen-doped graphene with a high doping level and controlled N-dopants for catalytic oxidation. The dominant reactive doping species are identified by materials design and density functional theory (DFT) calculations.

Chapter 6 — Sulfur and Nitrogen Co-Doped Graphene for Metal-Free Catalytic Oxidation Reactions. *Small.* 2015; 11(25): 3036-44. — synthesizes sulfur and nitrogen co-doped graphene for enhanced metal-free catalysis toward PMS activation. The

electronic state and surface chemistry of graphene are probed with sulfur and nitrogen co-doping effect and co-doping level by both experimental and theoretical investigations.

Chapter 7 — *Effect of Nitrogen-doping on Single-Walled Carbon Nanotubes on Activation of Superoxide O-O Bond for Enhanced Metal-Free Oxidation* —

Part 1: *N-Doping-Induced Nonradical Reaction on Single-Walled Carbon Nanotubes for Catalytic Phenol Oxidation. ACS Catal. 2015; 5(2): 553-9.* This part investigates the emerging non-radical oxidation upon N-doping on single-walled carbon nanotubes (N-SWCNTs) for PMS activation.

Part 2: *Insights into N-doping in single-walled carbon nanotubes for enhanced activation of superoxides: a mechanistic study. Chem. Commun. 2015; 51(83): 15249-52.* This section reports the exclusively N-doping effect on SWCNTs toward activation of various superoxides with *in situ* EPR and advanced DFT calculations.

Chapter 8 — *Conclusions and perspectives* — highlights the meaningful findings in this study and proposes suggestions for further research in the field.

References

1. Oki T, Kanae S. Global hydrological cycles and world water resources. *Science*. 2006;313(5790):1068-72.
2. Postel SL, Daily GC, Ehrlich PR. Human appropriation of renewable fresh water. *Science*. 1996;271(5250):785-8.
3. Schewe J, Heinke J, Gerten D, Haddeland I, Arnell NW, Clark DB, et al. Multimodel assessment of water scarcity under climate change. *P. Natl. Acad. Sci.* 2014;111(9):3245-50.
4. Hoekstra AY, Mekonnen MM, Chapagain AK, Mathews RE, Richter BD. Global monthly water scarcity: blue water footprints versus blue water availability. *Plos One*. 2012;7(2).
5. Postel SL. Entering an era of water scarcity: The challenges ahead. *Ecol. Appl.* 2000;10(4):941-8.
6. Wang XB, Qin YL, Zhu LH, Tang HQ. Nitrogen-doped reduced graphene oxide as a bifunctional material for removing bisphenols: synergistic effect between adsorption and catalysis. *Environ. Sci. Technol.* 2015;49(11):6855-64.

7. Vilar VJP, Moreira FC, Ferreira ACC, Sousa MA, Goncalves C, Alpendurada MF, et al. Biodegradability enhancement of a pesticide-containing bio-treated wastewater using a solar photo-Fenton treatment step followed by a biological oxidation process. *Water Res.* 2012;46(15):4599-613.
8. Verma AK, Dash RR, Bhunia P. A review on chemical coagulation/flocculation technologies for removal of colour from textile wastewaters. *J. Environ. Manage.* 2012;93(1):154-68.
9. Hu P, Long M. Cobalt-catalyzed sulfate radical-based advanced oxidation: A review on heterogeneous catalysts and applications. *Appl. Catal., B* 2016;181:103-17.
10. Anipsitakis GP, Dionysiou DD, Gonzalez MA. Cobalt-mediated activation of peroxymonosulfate and sulfate radical attack on phenolic compounds. Implications of chloride ions. *Environ. Sci. Technol.* 2006;40(3):1000-7.
11. Grebel JE, Pignatello JJ, Mitch WA. Effect of halide ions and carbonates on organic contaminant degradation by hydroxyl radical-based advanced oxidation processes in saline waters. *Environ. Sci. Technol.* 2010;44(17):6822-8.
12. Neyens E, Baeyens J. A review of classic Fenton's peroxidation as an advanced oxidation technique. *J. Hazard. Mater.* 2003;98(1-3):33-50.
13. Duan XG, Sun HQ, Kang J, Wang YX, Indrawirawan S, Wang SB. Insights into heterogeneous catalysis of persulfate activation on dimensional-structured nanocarbons. *ACS Catal.* 2015;5(8):4629-36.
14. Ahn S, Peterson TD, Righter J, Miles DM, Tratnyek PG. Disinfection of ballast water with iron activated persulfate. *Environ. Sci. Technol.* 2013;47(20):11717-25.
15. Avetta P, Pensato A, Minella M, Malandrino M, Maurino V, Minero C, et al. Activation of persulfate by irradiated magnetite: Implications for the degradation of phenol under heterogeneous photo-fenton-like conditions. *Environ. Sci. Technol.* 2015;49(2):1043-50.
16. Saputra E, Muhammad S, Sun HQ, Ang HM, Tade MO, Wang SB. Different crystallographic one-dimensional MnO₂ nanomaterials and their superior performance in catalytic phenol degradation. *Environ. Sci. Technol.* 2013;47(11):5882-7.
17. Sun HQ, Liu SZ, Zhou GL, Ang HM, Tade MO, Wang SB. Reduced graphene oxide for catalytic oxidation of aqueous organic pollutants. *ACS Appl. Mater. Interfaces.* 2012;4(10):5466-71.
18. Navalon S, Dhakshinamoorthy A, Alvaro M, Garcia H. Carbocatalysis by graphene-based materials. *Chem. Rev.* 2014;114(12):6179-212.
19. Wang XC, Maeda K, Thomas A, Takanabe K, Xin G, Carlsson JM, et al. A metal-free polymeric photocatalyst for hydrogen production from water under visible light. *Nat. Mater.* 2009;8(1):76-80.

20. Zhang J, Liu X, Blume R, Zhang AH, Schlogl R, Su DS. Surface-modified carbon nanotubes catalyze oxidative dehydrogenation of n-butane. *Science*. 2008;322(5898):73-7.

Every reasonable effort has been made to acknowledge the owners of copyright material. I would be pleased to hear from any copyright owner who has been omitted or incorrectly acknowledged.

Chapter 2. Literature review

2.1 Introduction

In recent decades, the environment has encountered severe contaminations due to regardless discharges of the vast amounts of chemicals and pollutants produced from industrial processes, agricultural application, and households, which rapidly grow up with the fast industrialization and population explosion.(1) The serious pollution of air, soil, and water has become far beyond the self-purification capacity of the natural eco-system, and then breaks the harmonious balance of human and the nature that has already existed for thousands of years. In terms of water resources, the lack of freshwater and its uneven distribution on the Earth have affected the living standard and restricted the regional economic prosperity. The water pollution problems have made the situation even worse. The contaminants include poisonous gases (SO_x , NO_x , CO), heavy metal ions (Cr, As, Cu etc) and toxic organics. The diverse organic compounds, such as aromatic hydrocarbons, dyes, antibiotics, pesticides, and surfactants, discharged from versatile human activities are the main contaminants in wastewater. A variety of physical, biological, and chemical strategies have been developed to efficiently remove the pollutants from water.(2-4)

Physical adsorption is a mild and effective approach for pollution control. Carbon materials such as activated carbon(5), graphene(6), and carbon nanotubes(7), and other porous materials such as clays(8), fly ash(9), siliceous materials(10), zeolites(11), and biomass(12) have been demonstrated to be excellent adsorbents to remove dyes, phenolics, pesticides, and natural organic matters (NOMs) in aqueous phase. The adsorption mechanism between the organic compounds and the adsorbents lies in the strong molecular interactions such as electrostatic interaction, hydrophobic effect, π - π interaction, hydrogen bonding, and covalent bonding.(2, 13) The adsorption capability of the adsorbents is closely related with the origin of the material, porous structure (pore size and pore volume), and surface chemistry (surface electronic negativity, acid/basic degree, functional groups etc.). Besides, the environmental conditions also affect the adsorption processes, e. g. pH, ionic strength, temperature, adsorption time, inorganic ligand, and competing organics and other background matters.(12)

Biodegradation is the major degradation pathway of the organic compounds in nature. The bioremediation processes can effectively decompose pollutants into harmless/nonhazardous compounds in relative mild conditions without intensive inputs of chemicals and energy.(3) It was also reported that the biodegradation is the principal pathway for removal of polycyclic aromatic hydrocarbons (PAHs) in spite of the fact that PAHs may also undergo adsorption, volatilization, photolysis and chemical degradation in the natural system.(14, 15) The catabolic activity of the microbes plays the dominant role in biodegradation, though the transformation and degradation processes of microbial communities are still under investigation, currently being treated as a 'black box' model.(16) The microorganism for bioremediation can be classified as algae, bacteria and fungi, which can consume the organic complexes via biotransformation into smaller metabolites molecules, which will then be subsequently mineralized into inorganic minerals, carbon dioxide and water (aerobic), or methane (anaerobic). The degradation efficiency is determined by many factors such as the environment (pH, temperature, oxygen content), microbial population, acclimation degree, nutrients supply, organic structure, and cellular transport properties.(3, 16)

Photocatalytic degradation presents great potential for a low-cost, environmentally friendly, and sustainable remediation strategy for wastewater treatment.(17) Semiconductors such as metal oxides (e.g. TiO_2 , ZnO , WO_3 , B_2WO_4 , and BiOCl) and metal sulphides (e.g. ZnS , MoS , and CdS) can be employed as photocatalysts owing to their unique electronic structures with a filled valence band (VB) and a half-empty conduction band (CB).(18) Chemical and energy transformation was induced under irradiation in which a photon with energy of $h\nu$ matches or exceeds the band gap energy (E_g) of a semiconductor, giving rise to an electron exciting from VB to CB and leaving a positive hole in VB. This process can *in situ* generate highly reactive hydroxyl radicals ($\cdot\text{OH}$) and superoxide radicals ($\text{O}_2^{\cdot-}$) to attack persistent organic compounds, microorganisms, and disinfection by-products in a waterbody.(4, 19) More recently, nanocarbons such as graphene, carbon nanotubes, and graphitic carbon nitride also demonstrate great abilities for photo-oxidation of dyes and phenols.(20-22) Photodegradation has several merits for its feasible application in wastewater remediation such as facile operation condition (ambient pressure and temperature),

low cost, and effective mineralization of target compounds without inducing secondary contamination.(17)

Flocculation-coagulation is an effective, chemically enhanced wastewater treatment technology for organic removal, especially for decolorization of various dyes in textile industry.(23) The dyes discharged from the effluent of textile factories contain high molecular weights and complex structures and are resistant to bio- or photo-degradation. The surfactants and dyes with macromolecular structures were first pre-treated by the coagulation/flocculation processes, then followed by a post-treatment such as sedimentation, flotation and filtration.(24) The coagulation always involves complicated adsorption and flocculation processes. The adsorption and charge neutralization between the coagulants and organics and inter-particle bridging play crucial roles in a typical coagulation process.(25) In the applications, aluminium (III), magnesium (II), iron (II or III) salts and polyaluminium chloride (PACl) are the most widely used coagulants.(23) Besides, the non-toxic natural coagulants derived from plant, animal and micro-organism are demonstrated either as coagulants or chemical assistants for effective treatment of textile wastewater.(23, 26)

However, the adsorption and coagulation processes do not really decompose the hazardous and toxic pollutants but transform them into other phases, meanwhile generating vast amounts of sludge and harmful wastes which require further post-treatment for separation and purification. Heterogeneous photodegradation presents a relatively low oxidation efficiency with poor recovery of the photocatalysts. Bioremediation has strict requirements for the environment and feedstock. Advanced oxidative processes (AOPs) utilizing various superoxides such as wet air (O_2), ozone (O_3), hydrogen peroxide (H_2O_2), peroxymonosulfate (PMS, or oxone), and persulfate (PS, also known as peroxydisulfate) to produce highly reactive species to completely decompose pollutants into mineralized smaller molecular acids, carbon dioxide and water. AOPs were then proposed to be very effective and powerful tools for wastewater remediation and have been widely applied for practical applications.(27, 28)

Conventional Fenton reactions utilizing H_2O_2 as an oxidant and ferrous salts as a heterogeneous catalyst to generate $\cdot OH$ can be adapted to decompose a wide range of

contaminants. However, Fenton reactions suffer from strict environmental requirements (pH ~ 3), low-recovery efficiency of the catalyst (from Fe^{3+} to Fe^{2+}), generating massive sludge for post-treatment, and inevitably introducing toxic metal ions to the water cycle. External stimulations such as electrolytic assistance and UV radiation have been applied to enhance the activation of H_2O_2 .(29, 30) Several heterogeneous catalytic systems with immobilized metal catalysts on carbon or zeolites were also developed to minimize the metal leaching.(31-33)

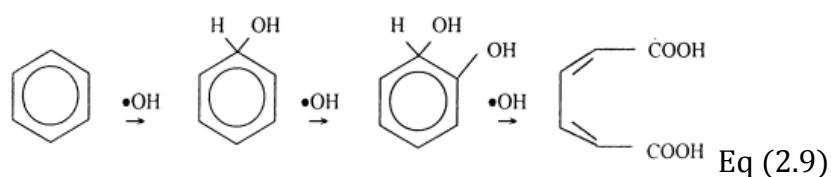
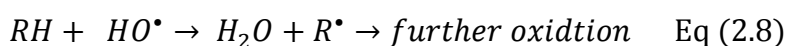
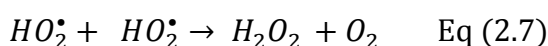
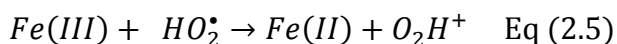
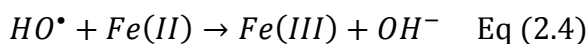
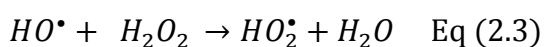
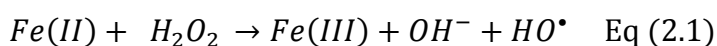
In recent years, sulfate radical ($\text{SO}_4^{\bullet-}$) based advanced oxidative processes (SR-AOPs) have attracted considerable attentions due to several unique merits. Firstly, $\text{SO}_4^{\bullet-}$ possesses a higher oxidation potential (2.5 - 3.1 V vs. NHE) compared with $\cdot\text{OH}$ (1.8 - 2.7 V) thus can demonstrate a greater ability to attack the refractory and non-biodegradable products. Besides, different from the unselective hydroxyl radicals, $\text{SO}_4^{\bullet-}$ has been proven to present a better selectivity to attack organics with unsaturated bond and aromatic structure especially at neutral conditions, enabling mineralizing trace target compounds in a complicated water matrix.(34-36) Moreover, sulfate radicals can be generated from cheap and chemically stable peroxy sulfate salts such as PMS and PS, which can be effectively activated in heterogeneous catalytic systems with transition metals and metal oxides as the catalysts.(37-39) Moreover, the SR-AOPs can be applied in a much wider pH range than Fenton reactions without producing large amounts of sediments demanding post-processing.

More recently, Sun and co-workers firstly uncovered that nanocarbons such as surface modified reduced graphene oxide (rGO) and multi-walled carbon nanotubes (MWCNTs) can be utilized as green and metal-free heterogeneous catalysts to effectively activate PMS and PS for catalytic degradation of contaminants in aqueous solution.(40-42) The state-of-the-art carbocatalysts, with unique physical, chemical, and electronic properties and the metal-free nature, have demonstrated great potential for green remediation in environmental catalysis. This chapter ends up with a summary of H_2O_2 -, PS-, and PMS- based catalytic oxidation reactions, with an emphasis on heterogeneously activating the superoxides with metal- and carbon- based heterogeneous catalysts.

2.2 Fenton and Fenton-like reactions

2.2.1 Conventional Fenton reactions

Hydrogen peroxide (H_2O_2) is a powerful oxidant for selective oxidation in organic synthesis, cleaning or etching of metals, leaching of pulp and paper in industrial production.(43) However, in environmental remediation, the oxidative potential of H_2O_2 alone is very low (1.80 and 0.87 V at pH 0 and 14, respectively) and not strong enough to degrade high concentration of some refractory pollutants.(43) Various techniques such as ozone and UV-radiation were developed to activate H_2O_2 to generate hydroxyl radicals ($\cdot OH$, 2.7 V), a stronger oxidant that is able to attack a wide range of organics at very high reaction rates. Iron salts (Fe^{II} and Fe^{III}) have been demonstrated as the most efficient catalysts to drive the oxidation processes, known as classic Fenton reactions.



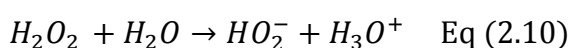
Ferrous ions are able to induce H_2O_2 to generate $\cdot OH$ via a series of complicated reactions (Eqs 2.1–2.7) in aqueous solutions. The $\cdot OH$ subsequently attacks the organic molecules via one-electron transfer, H abstraction (Eq 2.8), and addition reactions (Eq 2.9), eventually completely oxidizes the hydrocarbon pollutants into mineralized products, CO_2 and H_2O .

The Fenton reactions usually require an optimized environment (pH ~ 3) to maximize the generation of hydroxyl radicals and avoid the coagulation of iron salts.(44) In spite of the low-cost and environmentally benign Fenton reagents, the strict acid condition to prevent ion precipitation and the production of vast amounts of sludge have impeded the green and sustainable remediation in future application. Researches also discovered many other effective homogeneous iron-free Fenton-like systems with active catalysts such as $\text{Cu}^+/\text{Cu}^{2+}$, Co^{2+} , $\text{Cr}^{3+}/\text{Cr}^{6+}$, $\text{Ce}^{3+}/\text{Ce}^{4+}$, $\text{Ru}^{x+}/\text{Ru}^{x+1}$, $\text{Mn}^{x+}/\text{Mn}^{x+1}$, which can be adapted to a wider pH range without the soluble problems of iron species.(45)

2.2.2 Improved Fenton processes

2.2.2.1 Ozone-assisted Fenton reactions

Ozonation is an effective oxidation process using ozone as the strong oxidant for wastewater treatment. However, ozonation or Fenton reaction alone is not satisfactory for the complicated wastewater matrix with large amounts of versatile refractory contaminants. A combination of Fenton oxidation and ozonation ($\text{O}_3/\text{H}_2\text{O}_2/\text{Fe}^{2+}$) provides a more effective solution for AOPs. Brunet et al. discovered that coupling $\text{O}_3/\text{H}_2\text{O}_2$ is more efficient than the isolated system for degradation of organic compounds with carbonyl groups.(46) More importantly, ozone can activate hydrogen peroxide via Eqs 2.10–2.11, which synergistically minimize the dose of ferrous salts and promote the oxidative performance of the new system.(47)



Aliz and co-workers designed an ozone/Fenton system as indicated in Figure 2.1, and applied a new AOP for treatment of stabilized leachate.(48) In the study, they explored the optimum operation conditions such as molar ratio and concentration of Fenton reagent, pH variance, and contact time. In a natural solution, the combined Fenton/ozone demonstrated a higher oxidation potential for degradation of stabilized leachate than the Fenton system without ozone, with a greater organic carbon removal efficiency, shorter reaction time, and a wider pH range.

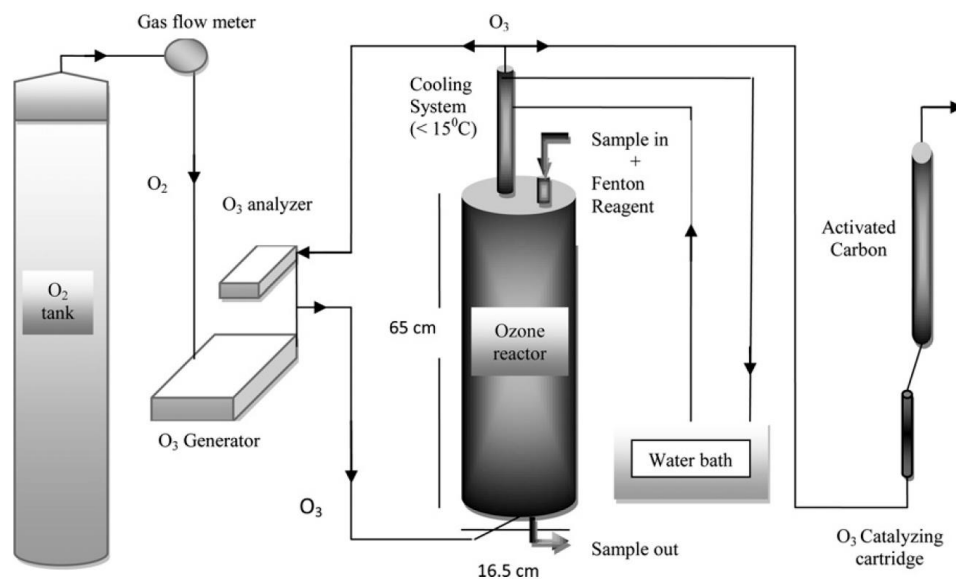


Figure 2.1. Flowchart of ozone/Fenton equipment procedures.(48)

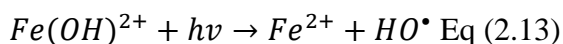
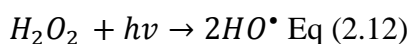
2.2.2.2 Electro-Fenton Reactions

Electrochemistry has been demonstrated as an effective approach to decompose industrial non-biodegradable pollutants and pesticides via anodic oxidation and indirect electro-oxidation.(49) Organics can be destroyed by direct electron transfer reactions and then be mineralized with the hydroxyl radicals on the electrode surface.(47) In the electro-Fenton process, H_2O_2 can be activated on the cathode to receive electrons or undergo catalysis by the ferrous ions generated from a sacrificial anode to produce hydroxyl radicals.(50) Besides, ferrous ions can be externally added with *in situ* production of H_2O_2 from an oxygen sparging cathodes.(51) The reactive species can also be generated from Fenton reagent in an electrolytic cell with the ferric ions regenerated on the cathode to ferrous ions.(52, 53) Thus, the heterogeneous catalysts, Fe^{2+} , can be used in a neutral solution to overcome the drawback of acidic environment of conventional Fenton reactions. Some factors were reported to affect the efficiency of electron-Fenton process, such as the electrode nature, catalyst concentration, solution pH, dissolved oxygen level, and current density.(47)

2.2.2.3 Photo-Fenton process

UV radiations can also induce H_2O_2 to generate hydroxyl radicals via Eq 2.12. The assistance of photolysis would be weakened in the $\text{H}_2\text{O}_2/\text{Fe}^{2+}$ system as iron complexes can strongly absorb radiation, leading to a smaller portion of photo-induced degradation. However, photocatalysis is able to chemically regenerate the Fe^{3+} to Fe^{2+}

via photo-reduction (Eq 2.13), thereby significantly fulfilling the catalytic cycle of Fenton process and improving the degradation effectiveness.(54) The photolysis and decarboxylation of ferric-peroxyl complex ($\text{Fe(III)-O}_2\text{H}^{2+}$) may contribute to the oxidation of pollutants and the ring-opening of intermediates via carboxyl and hydroxyl groups.(54)



2.2.2.4 Heterogeneous Fenton-like reaction

Development of heterogeneous catalysts for H_2O_2 activation gives no disposal problems and enables mild operational conditions. Extensive studies have worked on immobilizing iron on zeolite and carbon, exhibiting a higher total organic carbon (TOC) removal, a higher reactivity, and a reduced dependence on the solution pH in comparison to the homogeneous Fe^{3+} catalysts (31, 55-57) The metal leaching has been controlled for multiple runs with a much better stability.

Navalon et al. reported that nanodiamond supported gold nanoparticles can be employed as a highly efficient Fenton catalyst.(58) Phenol was chosen as the target compound for selective oxidation into catechol and hydroquinone as model reactions. The gold/nanodiamond hybrids demonstrated excellent performance for H_2O_2 activation to generate $\cdot\text{OH}$, with 79% phenol removal efficiency. The stunning turnover number (TON) of 321000 was nearly orders of magnitude higher than other heterogeneous Fenton catalysts. The preliminary experiment indicated that the gold grafted on Fenton processed nanoparticle diamond (HO-npD) is more efficient than Au/CeO_2 , Au/TiO_2 , $\text{Au/Fe}_2\text{O}_3$, and Au/C , whereas the HO-npD itself presents no catalytic activity. The Au/HO-npD can be used for three consecutive uses without significantly passivation, and the deactivated catalysts can be almost fully recovered by thoroughly acid washing and used for a large phenol dosage for several cycles. The mechanism of catalytic evolution of hydroxyl radical was proposed in Figure 2.2. The H_2O_2 activation process involved swing in Au/Au^{3+} . When phenol co-exists in the catalytic system, it can be oxidized by Au^{3+} , and no oxygen evolution was observed. The stoichiometry of oxidized phenol and consumed H_2O_2 approaches 1:1.

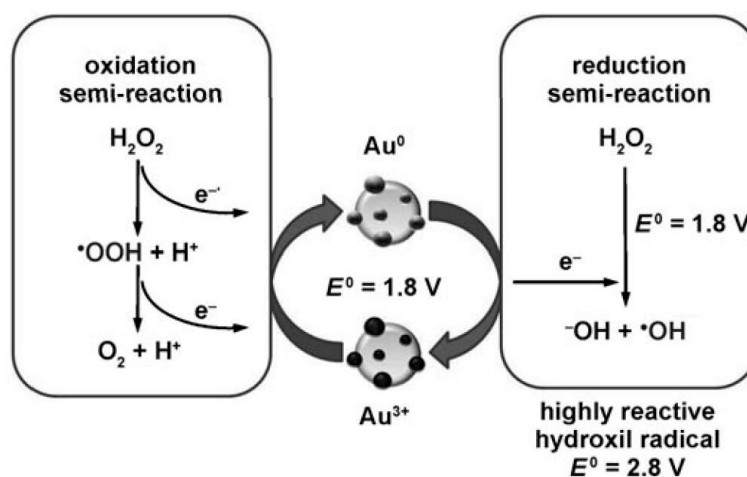
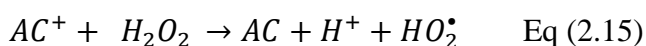
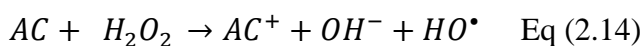


Figure 2.2. Proposed mechanism of hydroxyl radical generation on Au/HO-npD.(58)

2.2.2.5 Hydrogen peroxide activation with carbocatalysts

In water remediation, activated carbon (AC) with a porous structure, large surface area, and rich functional groups has been widely used as an environmentally-benign adsorbent for contaminant removal.(58, 59) It was reported that AC can also be utilized for catalytic wet peroxide oxidation (CWPO) to generate reactive species such as hydroxyl radicals ($\cdot\text{OH}$) and superoxide radical anions ($\cdot\text{OOH}/\text{O}_2^{\cdot-}$) for degradation of a wide range of pollutants.(60, 61) The catalytic activity of AC for H_2O_2 degradation is well related to the carbon structure and surface oxygen groups.(62, 63) Activated carbon with a basic surface, well disordered structure, and high content of electron-rich centers are favored for decomposition of H_2O_2 .(63) However, the mechanism of H_2O_2 on activated carbon for $\cdot\text{OH}$ generation still remains controversially. A generally accepted mechanism is that AC can be regarded as an electron-transfer catalyst with an oxidized (AC^+) and reduced states (AC) cycle (Eqs 2.14–2.15) similar to $\text{Fe}^{2+}/\text{Fe}^{3+}$ in Fenton reaction.(64, 65)



More recently, Fang et al. combined surface modification and electron paramagnetic resonance (EPR) to reveal that the free radicals in AC might play the crucial role for $\cdot\text{OH}$ generation, while the C-OH groups primarily contributed to H_2O_2 decomposition.(66) Zhou and co-workers also discovered that biochar can effectively

activate H_2O_2 for organic degradation and the activation mechanism was probed by EPR and radical trapping strategy.(67) The study elucidated that the persistent free radicals (PFRs) in biochar are the active sites for H_2O_2 activation which facilitates the one-electron transfer to H_2O_2 to form $\cdot\text{OH}$ as shown in Figure 2.3.

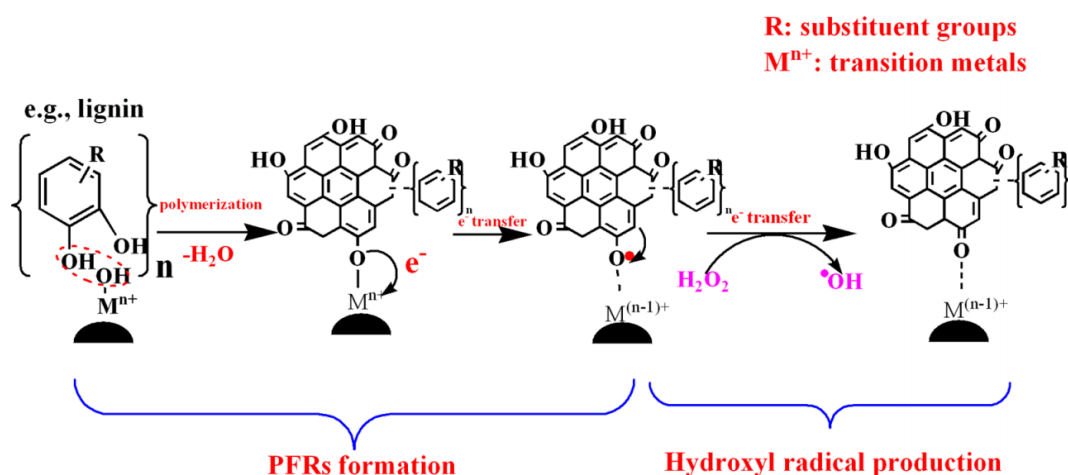


Figure 2.3. Proposed mechanism of H_2O_2 activation on biochar.(67)

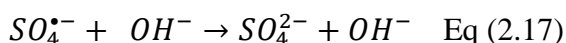
2.3 Physical and catalytic activation of persulfate

2.3.1 Physical techniques for persulfate activation

Owing to the great merits of sulfate radicals as mentioned in the introduction, persulfate (PS, also known as peroxydisulfate or PDS), a kind of white solid powder, has been utilized to provide $\text{SO}_4^{\cdot-}$ for oxidation of organic pollutants. Persulfate possesses a high solubility in water, a great stability in subsurface applications, and a lower cost so it has been applied as a more environmentally-benign product compared with permanganate (MnO_4^-) and ozone (O_3). (68)

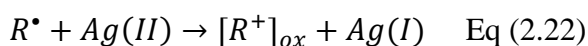
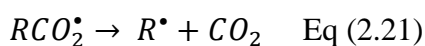
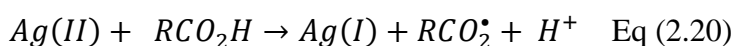
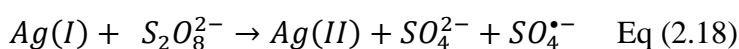
Several physical techniques have been applied to activate PS for pollutant removal with in situ chemical oxidation (ISCO).(69) UV irradiations are well reported to be able to activate persulfate to generate sulfate radicals in neutral conditions.(70) Studies indicated that the $\text{UV}/\text{S}_2\text{O}_8^{2-}$ is more active for decontamination in aqueous solution than $\text{UV}/\text{H}_2\text{O}_2$ and UV/HSO_5^- systems, since $\text{S}_2\text{O}_8^{2-}$ presents a higher quantum efficiency for photolysis to generate free radicals.(71, 72) Besides, heat activation is another facile strategy and persulfate decomposition can be enhanced under a higher temperature, resulting in greater effectiveness.(73, 74) The contaminants

concentration, solution pH, and pressure may also affect the organic oxidation efficiency during the heat treatment.(75-77) Persulfate-based ISCO can also be achieved by alkaline activation to form $SO_4^{\bullet-}$ and $\cdot OH$ to remediate refractory contaminants in groundwater and soils. The mechanism was proposed by several studies wherein the PS activation process in basic condition can be summarized as Eq 2.16 and Eq 2.17.(78-80) It should be pointed out that in the practical application, excess base is always consumed to overcome the base neutralizing capacity of water matrix and soil, giving rise to environmental and economic implications.(81) The fast PS decomposition rate under basic condition and radical self-quenching effect can lead to the low efficiency for pollutant oxidation.



2.3.2 Metal and metal oxide catalyzed persulfate activation

The electrophilic transition metal ions, e.g. Ag^+ and Fe^{2+} , are able to donate an electron to PS to form sulfate radicals and sulfate groups for SR-AOPs.(34, 36) Silver(I) was observed to be able to catalyze PS via a series of one-equivalent oxidation-reduction cycles for decarboxylation of acids (Eqs 2.18 – 2.22).(82, 83) Interestingly, Ag(II) was discovered as the predominant reactive intermediates, generated from the rate-limiting oxidation of Ag(I) by PS, rather than the sulfate or hydroxyl radicals in the oxidation process.(82)



Different from ferrous ions (Fe^{2+}) which is only soluble in acid conditions, zero-valent iron (ZVI) has been widely studied as a promising heterogeneous catalyst to activate

PS to produce $\text{SO}_4^{\bullet-}$.(84, 85) Besides, the ZVI/PS systems were reported to be applied for disinfection of ballast water and oxidation of acyclic aliphatic acids from oil sands process-affected water.(86, 87) The ZVI can directly donate electrons to PS via Eq 2.23 meanwhile release Fe^{2+} to aqueous solution, which continuously activate PS to generate $\text{SO}_4^{\bullet-}$ via Eq 2.24. The oxidized state of Fe^{3+} can also interact with ZVI to produce Fe^{2+} (Eq 2.25). The deactivation of ZVI was possibly due to the coverage of ferrous sulfate or ferric hydroxide as elucidated in Figure 2.4.(88)

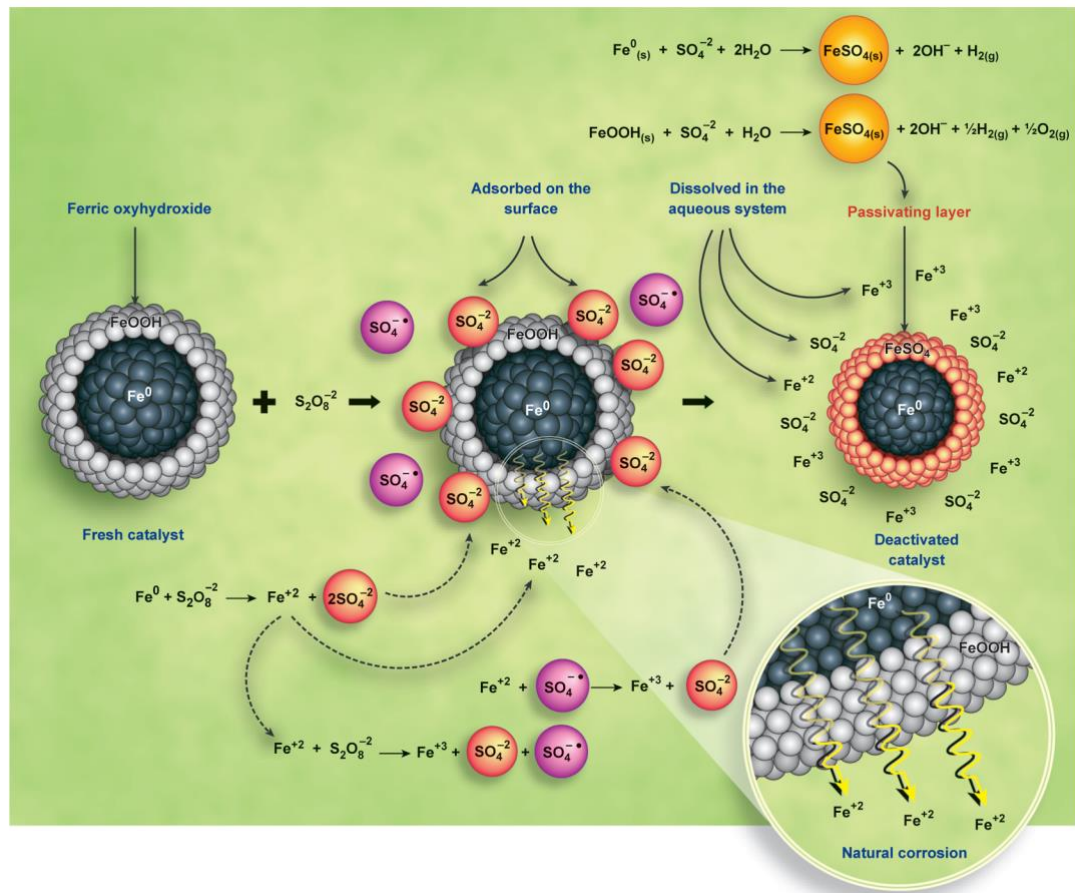
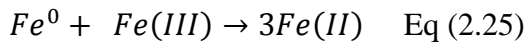
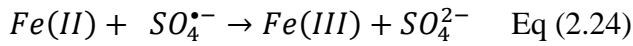
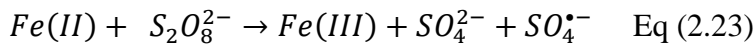


Figure 2.4. Conceptual model of persulfate activation and ZVI deactivation processes.(88)

Effective heterogeneous catalytic systems were also developed for activating PS to mineralize organic pollutants in aqueous solution. Fang et al. reported that increasing pH and the dissolved oxygen level could promote the formation of superoxide radicals ($O_2^{\cdot-}$) on the surface of magnetite nanoparticles (MNPs) for the enhanced PS activation to form sulfate radicals.(89) Avetta et al. found that irradiated magnetite could efficiently activate persulfate for phenol oxidation under heterogeneous photo-Fenton conditions.(90) The surface-bounded Fe(II) on MNPs could increase the electron density of the MNPs and reduce the redox potential of Fe(II), promoting the charge-transfer process between catalysts and target organics.(89, 91-93) More recently, it was reported that PS could be activated by CuO through the out-sphere interaction without generation of sulfate radicals and followed by a rapid oxidation with the model compound of 2,4-dichlorophenol (2,4-DCP) as shown in Figure 2.5.(94) The CuO/PS system demonstrated a superb selectivity toward the target organics even in the presence of high dose of radical quenching agents (ethanol and chlorides). In a subsequent study, Zhang et al. synthesized a CuO/Fe₃O₄ composites that combined the high catalytic activity of CuO and the magnetic property of Fe₃O₄ for PS activation.(95) The new catalytic system presented a great stability for reuse and very low Cu²⁺ leaching was detected.

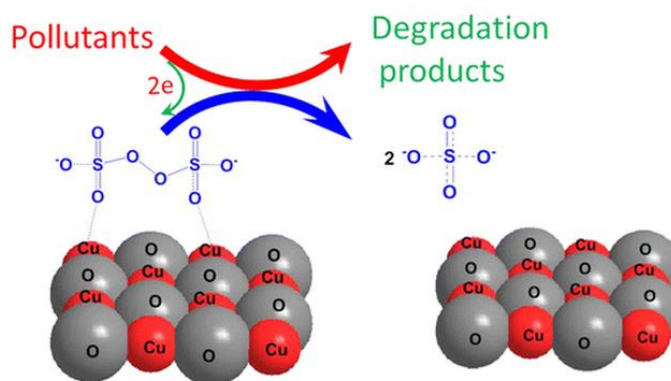


Figure 2.5. Mechanistic scheme of PS activation on CuO.(94)

2.3.3 Persulfate activation with carbocatalysis

The emerging carbocatalysis has attracted considerable attention due to the metal-free nature and the unique catalytic processes.(96-98) Su and co-workers first applied small molecular hydrocarbons as mimics of catalytic sites to probe the intrinsic active sites in carbon-based homogeneous catalysis.(99, 100) In environmental science, phenol

was discovered to be able to activate persulfate in basic conditions (pH ~ 12) via reduction reaction in the form of phenoxide.(101) Humic acid (HA) was found to have redox functional moieties, such as quinone groups, for conducting a redox process.(102, 103) Zhou and co-workers revealed that quinones can activate PS to generate sulfate radicals for degradation of 2,2,4'-trichlorobiphenyl (PCB28).(104) The study indicated that PS was activated via a semiquinone radical-dependent cycle as indicated in Figure 2.6.

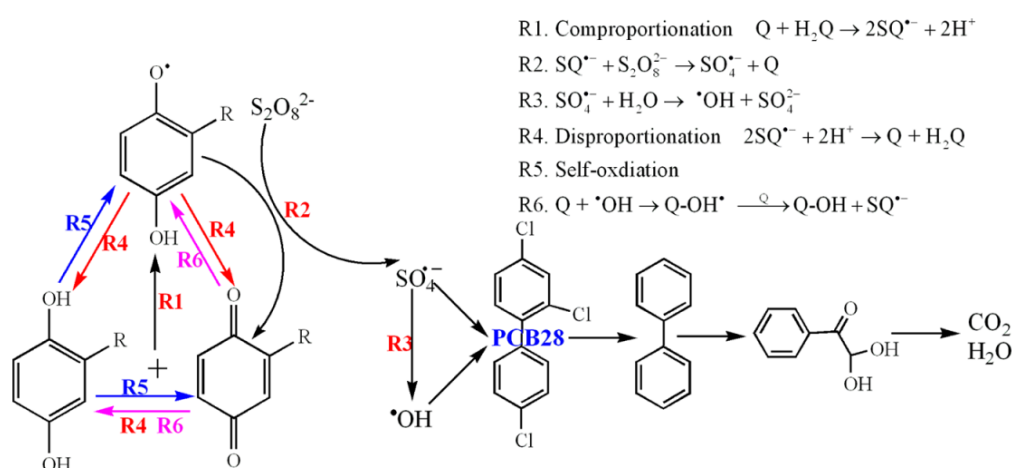


Figure 2.6. Proposed pathway for PS generation of sulfate radicals with quinone. (104)

Sun et al. first uncovered that pristine multi-walled carbon nanotubes (MWCNTs) can heterogeneously activate persulfate to generate reactive species for phenol oxidation, whereas the nitrogen-doping modification (pyridinic and pyrrolic nitrogen) did not show remarkable improvement of the catalytic performance.(42) The electron-rich ketonic groups (CNT-C=O) on MWCNTs were believed to be the active sites for PS activation, which can donate one electron to PS to form $SO_4^{\bullet-}$ and the highly graphitic structure of sp^3 hybridized carbon network might contribute to weakening the O-O bond in PS.(42) Lee et al. indicated that PS/CNT systems were not significantly affected by solution pH, introduction of HA and methanol, suggesting that a nonradical mechanism might be involved.(105) In a recent study, Wang et al. employed N-doped graphene as a bifunctional material for bisphenol removal.(106) A synergistic effect of adsorption and catalytic oxidation was found in the study, in which the pollutant was adsorbed and enriched on the surface of carbocatalyst, and would be rapidly degraded by the $SO_4^{\bullet-}$ which in turn facilitated the adsorption of residual pollutant.(106) Fang et al. indicated that the persistent free radicals in biochar and

superoxide radicals ($O_2^{\cdot-}$) may be responsible for the evolution of sulfate radicals in biochar/PS system.(107) Therefore, the intrinsic mechanism for PS activation with nanocarbons still remains to be explored with delicate experimental design and solid justifications.

2.4 Catalytic activation of peroxymonosulfate

2.4.1 Homogeneous activation of peroxymonosulfate

Peroxymonosulfate (PMS, also known as oxone) is a chemically stable, harmless, and soluble white-crystalline solid, and has been widely used in synthetic chemistry for C-H bond activation and selective oxidation.(108) Similar to other superoxide salts such as hydrogen peroxide and persulfate, physical strategies can effectively drive PMS to evolve reactive radicals for contaminant mineralization.(36, 109) Moreover, a PMS molecule possesses an asymmetry structure ($H-O-O-SO_3^-$) and presents a greater potential to accept electron to produce sulfate and hydroxyl radicals, making it an excellent candidate for catalytic activation.(110)

PMS can be homogeneously activated by various transition metal cations such as Mn^{2+} , Co^{2+} , Fe^{2+} , Ni^{2+} , V^{3+} , Ce^{3+} , Ru^{3+} , to name a few.(34, 111) Co^{2+} /PMS has been proven to be the most effective system to produce sulfate radicals and persulfate radicals as indicated in Figure 2.7.(36, 112) The recovery from Co^{3+} to Co^{2+} maintains the reaction, and the formation of $CoOH^+$ is a significant intermediate for PMS activation.(112, 113)

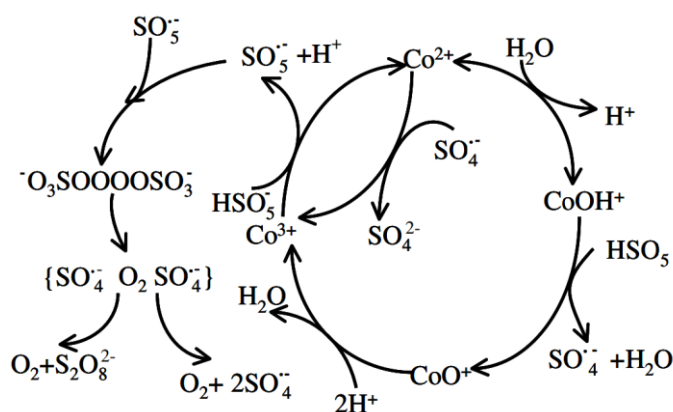


Figure 2.7. Homogeneous PMS activation in Co^{2+} -based aqueous system. (112)

2.4.2 Peroxymonosulfate activation with metal oxides

Anipsitakis et al. first employed cobalt oxides, such as CoO and Co₃O₄, for heterogeneous activation of PMS.(114) However, CoO/PMS can be regarded as a homogeneous system due to the severe leaching of Co²⁺. It was further found that the dissolution of CoO can be significantly depressed in the Co₃O₄ crystalline structure.(114, 115) The mechanism of PMS activation processes on Co₃O₄ can be described in Figure 2.8. The catalytic activity of Co₃O₄ significantly relies on the morphology and structure. Different Co₃O₄ facets may present entirely different geometric structure, electronic property, and activation energy for activating PMS.(111, 116, 117)

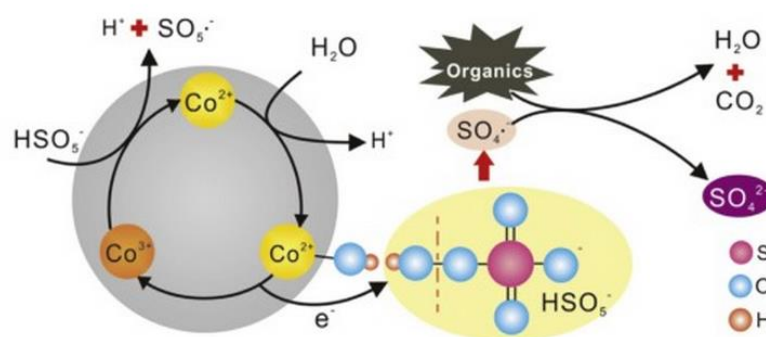


Figure 2.8. Mechanism of PMS activation on Co₃O₄ surface.(111)

Various supports such as metal oxides, molecular sieves, and carbon materials have been utilized to immobilize cobalt to minimize the cobalt leaching in the AOPs.(37, 118, 119) As cobalt ions can be referred to a Lewis acid, metal oxide with a basic surface is more favored for dispersion of the cobalt species.(111) TiO₂ and MgO with basic centres have demonstrated better capabilities to immobilize Co for PMS activation than Al₂O₃.(118, 120, 121) Besides, the basic sites with hydroxyl groups on support surface would contribute to form CoOH⁺ to further enhance PMS decomposition process.(121, 122) Moreover, interaction between metal oxide supports such as Co-Si (SiO₂) and Co-Ti (TiO₂) bonds can enhance the stability of the catalysts and effectively confine the metal leaching. Cobalt doped TiO₂ or ZnO photocatalysts can synergistically activate PMS to generate sulfate radicals under UV irradiation, in which Co²⁺ is the active site and TiO₂ (or ZnO) facilitates the regeneration of Co³⁺ via photo-reduction (Figure 2.9).(123-126) Molecular sieves supported cobalt catalysts, such as nature zeolite(127), SBA-15(128), and MCM-41(129), also demonstrated excellent activities for degradation of phenols and carffeine with PMS. The emerging

environmentally-friendly carbon materials, such as activated carbon, graphene, and carbon nanotubes, have high specific areas(SSAs), large pore volumes, and robust structures in strong acid or basic conditions, demonstrating great potentials as adsorbents and catalyst supports.(1, 2) Activated carbon (119) , carbon fibres (130), and carbon xerogel (131) have been applied as superb supports for cobalt oxides in catalytic oxidation. More recently, graphene oxide (GO), and reduced graphene oxide (rGO) supported cobalt catalysts have been utilized in AOPs with PMS activation.(132-134) The functional groups and covalent carbon layers with free-flowing π electrons of nanocarbons not only contribute the formation of strong Co-O-C bond for cobalt immobilization, but also promote the electron transfer from graphene to Co and Co to PMS owing to the synergistic coupling effect.

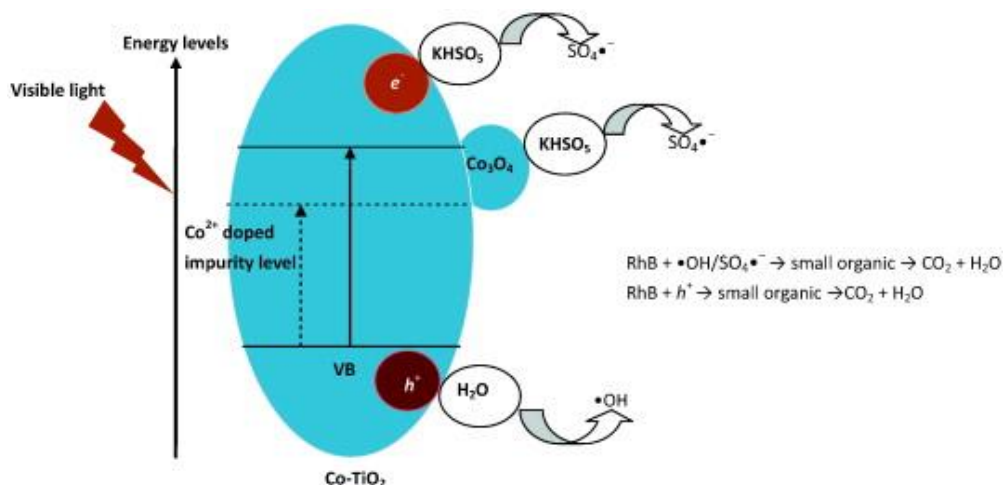


Figure 2.9. Model of Co–TiO₂ catalyst for PMS activation under UV irradiation.(123)

Morphology-controlled dimensional manganese oxides have been studied for SR-AOPs. Saputra et al. first synthesized three different one-dimensional MnO_2 nanocrystals for heterogeneous activation of PMS for catalytic phenol oxidation.(135) The α -, β -, and γ - MnO_2 presented different morphologies in nanowires, nanotubes, and nanofibers, respectively, giving different catalytic activities and activation energies for producing sulfate radicals with PMS. The α - MnO_2 /PMS demonstrated the best performance of phenol oxidation owing to the large specific areas, low oxygen loss, double tunnelled structure.(135) Wang et al. found that 2D γ - MnO_2 and 3D-hierarchically structured MnO_2 prepared via hydrothermal methods can activate PMS for oxidation reactions based on structure-dependant mechanisms.(135, 136) Shape-controlled α - Mn_2O_3 was performed for PMS activation and the activity followed the

order of $\text{Mn}_2\text{O}_3\text{-cubic} > \text{Mn}_2\text{O}_3\text{-octahedral} > \text{Mn}_2\text{O}_3\text{-truncated}$ which was associated with the large SSAs and surface atom arrangement.(137) Saputra et al. also compared the activity of manganese at different oxidation states for heterogeneous activation of PMS for organic degradation and the activity showed an order of $\text{Mn}_2\text{O}_3 > \text{MnO} > \text{Mn}_3\text{O}_4 > \text{MnO}_2$.(138) Yao and co-workers prepared $\text{Mn}_3\text{O}_4/\text{rGO}$ hybrids for decomposition of aqueous organics with PMS which exhibited a great stability for several successive runs.(139)

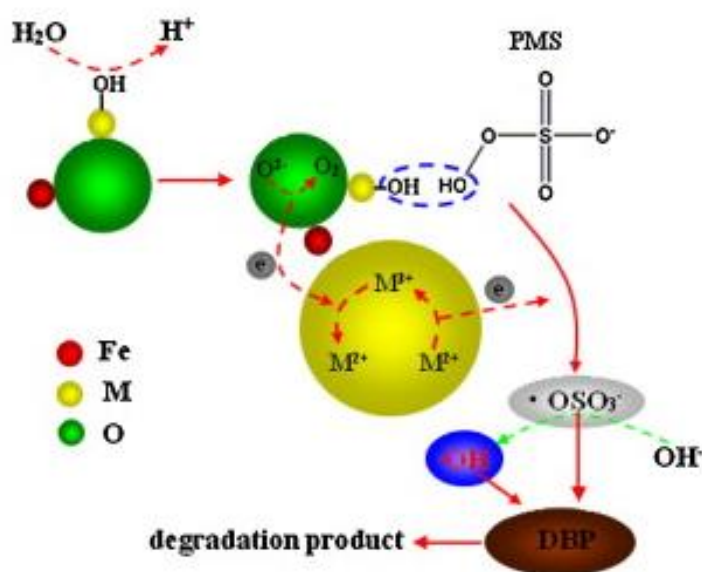


Figure 2.10. Mechanism of PMS activation on MFe_2O_4 ($\text{M} = \text{Co}, \text{Cu}, \text{Mn},$ and Zn). (145)

Magnetic materials have attracted increasing interest in environmental applications due to the remarkable magnetic nature for separation and morphology-dependent chemical properties. Tan et al. discovered that Fe_3O_4 magnetic nanoparticles (MNPs) can induce reactive radicals from activated PMS for catalytic oxidation of acetaminophen.(140) Wang et al. prepared magnetic $\text{Fe}_3\text{O}_4\text{-Co}$ /carbon sphere composites for phenol oxidation with PMS activation which could be uniformly dispersed in aqueous solution and be easily separated under a magnetic field.(141) Magnetic $\text{Fe}_3\text{O}_4\text{-MnO}_2$ core-shell nanocomposites were studied for 4-chlorophenol degradation with PMS activation, and the promoted catalytic performance was attributed to the synergistic interaction of Fe_3O_4 and MnO_2 .(142) Zhang et al. discovered that magnetically separable CuFe_2O_4 spinel can activate PMS with a

superior efficiency and stability.(143) The mechanistic study revealed that PMS participated in inner-sphere complexation with the surface Cu(II) centres and Cu(II)/Cu(III) redox cycle were responsible for evolution of sulfate radicals. Ma's groups have conducted several studies on magnetic ferrosphenel MFe_2O_4 ($M = Co, Cu, Mn, \text{ and } Zn$) for heterogeneously activating PMS to generate sulfate radicals as indicated in Figure 2.10.(144, 145) The catalytic performance followed an order of $CoFe_2O_4 > CuFe_2O_4 > MnFe_2O_4 > ZnFe_2O_4$ which was in good agreement of the reductive potential of H_2 -TPR and CV analysis, suggesting the PMS activation was favored on uncharged surface of the heterogeneous spinel catalysts.(145)

2.4.3 Peroxymonosulfate activation with carbocatalysts

In regard to heterogeneous PMS activation with state-of-the-art carbocatalysis, Wang's group first applied several activated carbons (ACs) as green and effective catalysts for generation of reactive radicals for phenol decomposition.(40) They found that the activity of ACs/PMS toward organic oxidation is much better than that of ACs/PS and ACs/ H_2O_2 , and the particle size dramatically affect the catalytic performance of ACs/PMS system.(146) Sun et al. first discovered that reduced graphene oxide, prepared via a hydrothermal method, can be employed as metal-free carbocatalysts for catalytic oxidation with PMS, however the graphene oxide with excess oxygen groups presented a very poor activity.(40) The curvature structure of graphene with defective sites, zigzag edges with delocalized π electrons, and the electron-rich ketonic groups were believed to possess a high chemical activity to conduct the redox processes as indicated in Figure 2.11.(40, 147-149) The dimensional effect of nanocarbons was also explored in a latest study indicating that the efficiency for phenol adsorption and catalytic degradation was closely related with carbon structure and surface oxygen functionalization.(150) The subsequent studies from Wang's group indicated that physical and chemical strategies can significantly increase the catalytic and adsorption capability of reduced graphene oxide due to the increased specific surface area, created defective decays, and optimized surface functional groups.(151, 152) Furthermore, nitrogen-doped graphene (N-rGO) was synthesized via a facile thermal annealing approach and exhibited a superb activity compared with pristine graphene.(41, 153) The nitrogen-doping with lonely-pair electrons and greater electronegativity considerably breaks up the inertness of graphene network and dramatically enhances the catalytic activity of sp^2 carbon.(154,

155) Besides, surface modified carbon nanotubes were also found to be effective to activate PMS to generate sulfate radicals.(42)

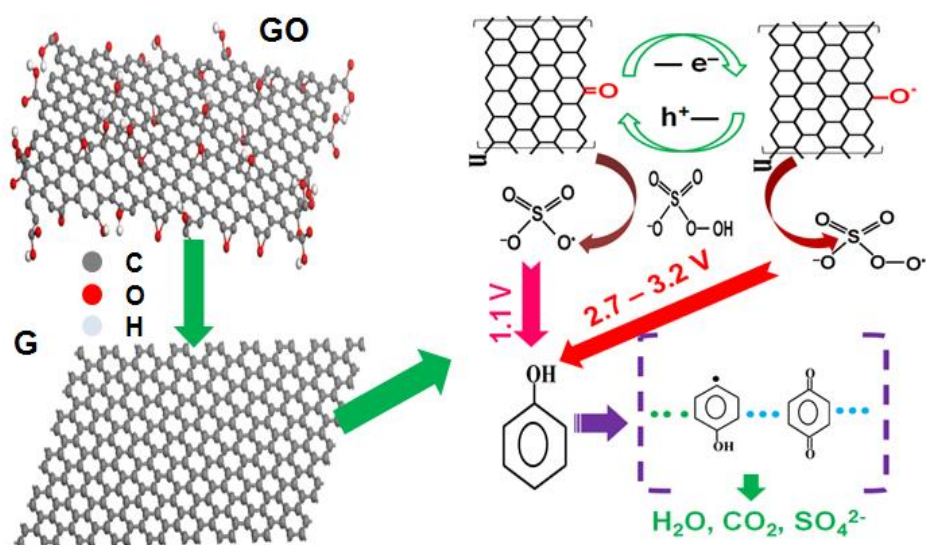


Figure 2.11. Illustration of graphene oxide reduction process and PMS catalytic activation for organic oxidation.(40)

2.5 Conclusion

Advanced oxidative processes are a promising technology for complete decomposition of toxic organic pollutants such as dyes, hydrocarbons, antibiotics in wastewater remediation. Versatile superoxides such as hydrogen peroxide, persulfate, and peroxymonosulfate are utilized to evolve reactive species for contaminant oxidation. Physical approaches such as heat, UV irradiation, and electrical energy can be used to activate the superoxides. Moreover, homogeneous or heterogeneous catalysts with transition metals and metal oxides can be employed to activate the superoxides for catalytic oxidation. State-of-the-art nanocarbons were also discovered to be superior metal-free catalysts for AOPs.

The physical technology not only requires intensive energy input but also presents a relative low efficiency for complete removal of contaminants. The catalytic oxidation system is more powerful for mineralization of organics into harmless compounds, carbon dioxide and water. Metal-based AOPs have exhibited a superb activity for contaminant destruction, however, inevitable metal-leaching and the introduction of

metal ions into water cycles are highly undesirable for the sustainable development. Therefore, green catalysis using metal-free and environmentally-benign nanocarbon catalysts become promising alternatives for environmental science. The carbocatalysts even present a better activity than the most popular metal catalysts.

Currently the carbocatalysts like graphene and carbon nanotubes are still expensive. The poor stability of nanocarbons in highly oxidative environment also impedes the practical applications. Developing facile techniques to synthesize robust carbocatalysts with low-cost and high effectiveness is still a great obstacle to be overcome for the future application. Different from metal-based catalysts with specific morphology, electronic and crystal structure, carbocatalysis always involves an intricate system with versatile carbon-covalent types, defective sites, functional groups, heteroatom-doping, making it more difficult to illustrate the real active sites and intrinsic mechanism of superoxide activation on carbocatalysts. Therefore, it is of great importance to unveil the mechanism of the activation process in carbocatalysis with a combination of well-designed materials and experiments, *in situ* characterization techniques, and theoretical calculations.

References

1. Wang SB, Sun HQ, Ang HM, Tade MO. Adsorptive remediation of environmental pollutants using novel graphene-based nanomaterials. *Chem. Eng. J.* 2013;226:336-47.
2. Perreault F, de Faria AF, Elimelech M. Environmental applications of graphene-based nanomaterials. *Chem. Soc. Rev.* 2015;44(16):5861-96.
3. Haritash AK, Kaushik CP. Biodegradation aspects of polycyclic aromatic hydrocarbons (PAHs): A review. *J. Hazard. Mater.* 2009;169(1-3):1-15.
4. Pera-Titus M, Garcia-Molina V, Banos MA, Gimenez J, Esplugas S. Degradation of chlorophenols by means of advanced oxidation processes: A general review. *Appl. Catal., B* 2004;47(4):219-56.
5. Tessmer CH, Vidic RD, Uranowski LJ. Impact of oxygen-containing surface functional groups on activated carbon adsorption of phenols. *Environ. Sci. Technol.* 1997;31(7):1872-8.
6. Xu J, Wang L, Zhu YF. Decontamination of bisphenol a from aqueous solution by graphene adsorption. *Langmuir.* 2012;28(22):8418-25.

7. Wu CH. Adsorption of reactive dye onto carbon nanotubes: Equilibrium, kinetics and thermodynamics. *J. Hazard. Mater.* 2007;144(1-2):93-100.
8. Tahir SS, Rauf N. Removal of a cationic dye from aqueous solutions by adsorption onto bentonite clay. *Chemosphere.* 2006;63(11):1842-8.
9. Wang SB, Boyjoo Y, Choueib A, Zhu ZH. Removal of dyes from aqueous solution using fly ash and red mud. *Water Res.* 2005;39(1):129-38.
10. Rosenholm JM, Czuryzkiewicz T, Kleitz F, Rosenholm JB, Linden M. On the nature of the bronsted acidic groups on native and functionalized mesoporous siliceous SBA-15 as studied by benzylamine adsorption from solution. *Langmuir.* 2007;23(8):4315-23.
11. Li ZH, Burt T, Bowman RS. Sorption of ionizable organic solutes by surfactant modified zeolite. *Environ. Sci. Technol.* 2000;34(17):3756-60.
12. Crini G. Non-conventional low-cost adsorbents for dye removal: A review. *Bioresource Technol.* 2006;97(9):1061-85.
13. Yang K, Xing BS. Adsorption of organic compounds by carbon nanomaterials in aqueous phase: Polanyi theory and its application. *Chem. Rev.* 2010;110(10):5989-6008.
14. Bumpus JA. Biodegradation of Polycyclic Aromatic-hydrocarbons by phanerochaete-chrysosporium. *Appl. Environ. Microb.* 1989;55(1):154-8.
15. Yuan SY, Chang JS, Yen JH, Chang BV. Biodegradation of phenanthrene in river sediment. *Chemosphere.* 2001;43(3):273-8.
16. Dua M, Singh A, Sethunathan N, Johri AK. Biotechnology and bioremediation: successes and limitations. *Appl. Microbiol. Biot.* 2002;59(2-3):143-52.
17. Chong MN, Jin B, Chow CWK, Saint C. Recent developments in photocatalytic water treatment technology: A review. *Water Res.* 2010;44(10):2997-3027.
18. Xiang QJ, Yu JG, Jaroniec M. Graphene-based semiconductor photocatalysts. *Chem. Soc. Rev.* 2012;41(2):782-96.
19. Esplugas S, Gimenez J, Contreras S, Pascual E, Rodriguez M. Comparison of different advanced oxidation processes for phenol degradation. *Water Res.* 2002;36(4):1034-42.
20. Zhang LL, Xiong ZG, Zhao XS. Pillaring Chemically exfoliated graphene oxide with carbon nanotubes for photocatalytic degradation of dyes under visible light irradiation. *ACS Nano.* 2010;4(11):7030-6.
21. Zhang H, Lv XJ, Li YM, Wang Y, Li JH. P25-graphene composite as a high performance photocatalyst. *ACS Nano.* 2010;4(1):380-6.

22. Wang Y, Wang XC, Antonietti M. Polymeric graphitic carbon nitride as a heterogeneous organocatalyst: From photochemistry to multipurpose catalysis to sustainable chemistry. *Angew. Chem. Int. Ed.* 2012;51(1):68-89.
23. Verma AK, Dash RR, Bhunia P. A review on chemical coagulation/flocculation technologies for removal of colour from textile wastewaters. *J. Environ. Manage.* 2012;93(1):154-68.
24. Golob V, Vinder A, Simonic M. Efficiency of the coagulation/flocculation method for the treatment of dyebath effluents. *Dyes Pigments.* 2005;67(2):93-7.
25. Rossini M, Garrido JG, Galluzzo M. Optimization of the coagulation-flocculation treatment: Influence of rapid mix parameters. *Water Res.* 1999;33(8):1817-26.
26. Ahmad AL, Yasin NHM, Derek CJC, Lim JK. Optimization of microalgae coagulation process using chitosan. *Chem. Eng. J.* 2011;173(3):879-82.
27. Deng Y, Ezyske CM. Sulfate radical-advanced oxidation process (SR-AOP) for simultaneous removal of refractory organic contaminants and ammonia in landfill leachate. *Water Res.* 2011;45(18):6189-94.
28. Lamsal R, Walsh ME, Gagnon GA. Comparison of advanced oxidation processes for the removal of natural organic matter. *Water Res.* 2011;45(10):3263-9.
29. Brillas E, Sires I, Oturan MA. Electro-fenton process and related electrochemical technologies based on Fenton's reaction chemistry. *Chem. Rev.* 2009;109(12):6570-631.
30. Brillas E, Mur E, Sauleda R, Sanchez L, Peral J, Domenech X, et al. Aniline mineralization by AOP's: anodic oxidation, photocatalysis, electro-Fenton and photoelectro-Fenton processes. *Appl. Catal., B* 1998;16(1):31-42.
31. Ramirez JH, Maldonado-Hodar FJ, Perez-Cadenas AF, Moreno-Castilla C, Costa CA, Madeira LM. Azo-dye Orange II degradation by heterogeneous Fenton-like reaction using carbon-Fe catalysts. *Appl. Catal., B* 2007;75(3-4):312-23.
32. Costa RCC, Lelis MFF, Oliveira LCA, Fabris JD, Ardisson JD, Rios RRVA, et al. Novel active heterogeneous Fenton system based on $\text{Fe}_3\text{-xMxO}_4$ (Fe, Co, Mn, Ni): The role of M^{2+} species on the reactivity towards H_2O_2 reactions. *J. Hazard. Mater.* 2006;129(1-3):171-8.
33. Navalon S, Alvaro M, Garcia H. Heterogeneous Fenton catalysts based on clays, silicas and zeolites. *Appl. Catal., B* 2010;99(1-2):1-26.
34. Anipsitakis GP, Dionysiou DD. Radical generation by the interaction of transition metals with common oxidants. *Environ. Sci. Technol.* 2004;38(13):3705-12.
35. Zou J, Ma J, Chen LW, Li XC, Guan YH, Xie PC, et al. Rapid Acceleration of ferrous iron/peroxymonosulfate oxidation of organic pollutants by promoting Fe(III)/Fe(II) cycle with hydroxylamine. *Environ. Sci. Technol.* 2013;47(20):11685-91.

36. Antoniou MG, de la Cruz AA, Dionysiou DD. Degradation of microcystin-LR using sulfate radicals generated through photolysis, thermolysis and e(-) transfer mechanisms. *Appl. Catal., B* 2010;96(3-4):290-8.
37. Shukla P, Wang S, Singh K, Ang HM, Tade MO. Cobalt exchanged zeolites for heterogeneous catalytic oxidation of phenol in the presence of peroxymonosulphate. *Appl. Catal., B* 2010;99(1-2):163-9.
38. Ding Y, Zhu L, Wang N, Tang H. Sulfate radicals induced degradation of tetrabromobisphenol A with nanoscaled magnetic CuFe₂O₄ as a heterogeneous catalyst of peroxymonosulfate. *Appl. Catal., B* 2013;129:153-62.
39. Yan JC, Lei M, Zhu LH, Anjum MN, Zou J, Tang HQ. Degradation of sulfamonomethoxine with Fe₃O₄ magnetic nanoparticles as heterogeneous activator of persulfate. *J. Hazard. Mater.* 2011;186(2-3):1398-404.
40. Sun HQ, Liu SZ, Zhou GL, Ang HM, Tade MO, Wang SB. Reduced graphene oxide for catalytic oxidation of aqueous organic pollutants. *ACS Appl. Mater. Interfaces* 2012;4(10):5466-71.
41. Sun HQ, Wang YX, Liu SZ, Ge L, Wang L, Zhu ZH, et al. Facile synthesis of nitrogen doped reduced graphene oxide as a superior metal-free catalyst for oxidation. *Chem. Commun.* 2013;49(85):9914-6.
42. Sun HQ, Kwan C, Suvorova A, Ang HM, Tade MO, Wang SB. Catalytic oxidation of organic pollutants on pristine and surface nitrogen-modified carbon nanotubes with sulfate radicals. *Appl. Catal., B* 2014;154:134-41.
43. Neyens E, Baeyens J. A review of classic Fenton's peroxidation as an advanced oxidation technique. *J. Hazard. Mater.* 2003;98(1-3):33-50.
44. Arnold SM, Hickey WJ, Harris RF. Degradation of atrazine by fentons reagent - condition optimization and product quantification. *Environ. Sci. Technol.* 1995;29(8):2083-9.
45. Bokare AD, Choi W. Review of iron-free Fenton-like systems for activating H₂O₂ in advanced oxidation processes. *J. Hazard. Mater.* 2014;275:121-35.
46. Brunet R, Bourbigot MM, Dore M. Oxidation of organic-compounds through the combination ozone-hydrogen peroxide. *Ozone-Sci. Eng.* 1984;6(3):163-83.
47. Babuponnusami A, Muthukumar K. A review on Fenton and improvements to the Fenton process for wastewater treatment. *Journal of Environmental Chemical Engineering.* 2014;2(1):557-72.
48. Abu Amr SS, Aziz HA. New treatment of stabilized leachate by ozone/Fenton in the advanced oxidation process. *Waste Manage.* 2012;32(9):1693-8.
49. Pulgarin C, Kiwi J. Overview on photocatalytic and electrocatalytic pretreatment of industrial non-biodegradable pollutants and pesticides. *Chimia.* 1996;50(3):50-5.

50. Kurt U, Apaydin O, Gonullu MT. Reduction of COD in wastewater from an organized tannery industrial region by Electro-Fenton process. *J. Hazard. Mater.* 2007;143(1-2):33-40.
51. Badellino C, Rodrigues CA, Bertazzoli R. Oxidation of pesticides by in situ electrogenerated hydrogen peroxide: Study for the degradation of 2,4-dichlorophenoxyacetic acid. *J. Hazard. Mater.* 2006;137(2):856-64.
52. Zhang H, Zhang DB, Zhou JY. Removal of COD from landfill leachate by electro-Fenton method. *J. Hazard. Mater.* 2006;135(1-3):106-11.
53. Zhang H, Fei CZ, Zhang DB, Tang F. Degradation of 4-nitrophenol in aqueous medium by electro-Fenton method. *J. Hazard. Mater.* 2007;145(1-2):227-32.
54. Sun YF, Pignatello JJ. Photochemical-Reactions Involved in the Total Mineralization of 2,4-D by Fe³⁺/H₂O₂/Uv (Vol 27, Pg 304, 1993). *Environ. Sci. Technol.* 1993;27(8):1696-.
55. Centi G, Perathoner S, Torre T, Verduna MG. Catalytic wet oxidation with H₂O₂ of carboxylic acids on homogeneous and heterogeneous Fenton-type catalysts. *Catal. Today.* 2000;55(1-2):61-9.
56. Fajerwerg K, Debellefontaine H. Wet oxidation of phenol by hydrogen peroxide using heterogeneous catalysis Fe-ZSM-5: A promising catalyst. *Appl. Catal., B* 1996;10(4):L229-L35.
57. Kuznetsova EV, Savinov EN, Vostrikova LA, Parmon VN. Heterogeneous catalysis in the Fenton-type system FeZSM-5/H₂O₂. *Appl. Catal., B* 2004;51(3):165-70.
58. Navalon S, Martin R, Alvaro M, Garcia H. Gold on diamond nanoparticles as a highly efficient fenton catalyst. *Angew. Chem. Int. Ed.* 2010;49(45):8403-7.
59. Vanvliet BM, Weber WJ, Hozumi H. Modeling and prediction of specific compound adsorption by activated carbon and synthetic adsorbents. *Water Res.* 1980;14(12):1719-28.
60. Rey A, Faraldos M, Bahamonde A, Casas JA, Zazo JA, Rodriguez JJ. Role of the activated carbon surface on catalytic wet peroxide oxidation. *Ind. Eng. Chem. Res.* 2008;47(21):8166-74.
61. Santos VP, Pereira MFR, Faria PCC, Orfao JJM. Decolourisation of dye solutions by oxidation with H₂O₂ in the presence of modified activated carbons. *J. Hazard. Mater.* 2009;162(2-3):736-42.
62. Ribeiro RS, Silva AMT, Figueiredo JL, Faria JL, Gomes HT. The influence of structure and surface chemistry of carbon materials on the decomposition of hydrogen peroxide. *Carbon.* 2013;62:97-108.
63. Rey A, Zazo JA, Casas JA, Bahamonde A, Rodriguez JJ. Influence of the structural and surface characteristics of activated carbon on the catalytic decomposition of hydrogen peroxide. *Appl. Catal., A* 2011;402(1-2):146-55.

64. Georgi A, Kopinke FD. Interaction of adsorption and catalytic reactions in water decontamination processes Part I. Oxidation of organic contaminants with hydrogen peroxide catalyzed by activated carbon. *Appl. Catal., B* 2005;58(1-2):9-18.
65. Huang HH, Lu MC, Chen JN, Lee CT. Catalytic decomposition of hydrogen peroxide and 4-chlorophenol in the presence of modified activated carbons. *Chemosphere*. 2003;51(9):935-43.
66. Fang GD, Liu C, Gao J, Zhou DM. New Insights into the Mechanism of the catalytic decomposition of hydrogen peroxide by activated carbon: implications for degradation of diethyl phthalate. *Ind. Eng. Chem. Res.* 2014;53(51):19925-33.
67. Fang GD, Gao J, Liu C, Dionysiou DD, Wang Y, Zhou DM. Key Role of persistent free radicals in hydrogen peroxide activation by biochar: implications to organic contaminant degradation. *Environ. Sci. Technol.* 2014;48(3):1902-10.
68. Sun HQ, Wang SB. Catalytic oxidation of organic pollutants in aqueous solution using sulfate radicals. *Catalysis*. 2015;27:209-47.
69. Tsitonaki A, Petri B, Crimi M, Mosbaek H, Siegrist RL, Bjerg PL. In situ chemical oxidation of contaminated soil and groundwater using persulfate: A review. *Crit. Rev. Environ. Sci. Technol.* 2010;40(1):55-91.
70. Xie PC, Ma J, Liu W, Zou J, Yue SYC, Li X, et al. Removal of 2-MIB and geosmin using UV/persulfate: Contributions of hydroxyl and sulfate radicals. *Water Res.* 2015;69:223-33.
71. Anipsitakis GP, Dionysiou DD. Transition metal/UV-based advanced oxidation technologies for water decontamination. *Appl. Catal., B* 2004;54(3):155-63.
72. Yang Y, Pignatello JJ, Ma J, Mitch WA. Comparison of halide impacts on the efficiency of contaminant degradation by sulfate and hydroxyl radical-based advanced oxidation processes (AOPs). *Environ. Sci. Technol.* 2014;48(4):2344-51.
73. Waldemer RH, Tratnyek PG, Johnson RL, Nurmi JT. Oxidation of chlorinated ethenes by heat-activated persulfate: Kinetics and products. *Environ. Sci. Technol.* 2007;41(3):1010-5.
74. Yang SY, Wang P, Yang X, Shan L, Zhang WY, Shao XT, et al. Degradation efficiencies of azo dye Acid Orange 7 by the interaction of heat, UV and anions with common oxidants: Persulfate, peroxymonosulfate and hydrogen peroxide. *J. Hazard. Mater.* 2010;179(1-3):552-8.
75. Liang CJ, Su HW. Identification of Sulfate and hydroxyl radicals in thermally activated persulfate. *Ind. Eng. Chem. Res.* 2009;48(11):5558-62.
76. Kronholm J, Metsala H, Hartonen K, Riekkola ML. Oxidation of 4-chloro-3-methylphenol in pressurized hot water/supercritical water with potassium persulfate as oxidant. *Environ. Sci. Technol.* 2001;35(15):3247-51.
77. Kronholm J, Riekkola ML. Potassium persulfate as oxidant in pressurized hot water. *Environ. Sci. Technol.* 1999;33(12):2095-9.

78. Furman OS, Teel AL, Watts RJ. Mechanism of base activation of persulfate. *Environ. Sci. Technol.* 2010;44(16):6423-8.
79. House DA. Kinetics and mechanism of oxidations by peroxydisulfate. *Chem. Rev.* 1962;62(3):185-203.
80. Kolthoff IM, Miller IK. The Chemistry of Persulfate. I. The kinetics and mechanism of the decomposition of the persulfate ion in aqueous medium. *J. Am. Chem. Soc.* 1951;73(7):3055-9.
81. Long AH, Lei Y, Zhang H. In Situ chemical oxidation of organic contaminated soil and groundwater using activated persulfate process. *Prog. Chem.* 2014;26(5):898-908.
82. Anderson JM, Kochi JK. Silver(I)-catalyzed oxidative decarboxylation of acids by peroxydisulfate. Role of silver(II). *J. Am. Chem. Soc.* 1970;92(6):1651-9.
83. Fristad WE, Fry MA, Klang JA. Persulfate/silver ion decarboxylation of carboxylic acids. Preparation of alkanes, alkenes, and alcohols. *The Journal of Organic Chemistry.* 1983;48(20):3575-7.
84. Liang CJ, Lai MC. Trichloroethylene degradation by zero valent iron activated persulfate oxidation. *Environ. Eng. Sci.* 2008;25(7):1071-7.
85. Liang CJ, Guo YY. Mass transfer and chemical oxidation of naphthalene particles with zerovalent iron activated persulfate. *Environ. Sci. Technol.* 2010;44(21):8203-8.
86. Ahn S, Peterson TD, Righter J, Miles DM, Tratnyek PG. Disinfection of ballast water with iron activated persulfate. *Environ. Sci. Technol.* 2013;47(20):11717-25.
87. Drzewicz P, Perez-Estrada L, Alpatova A, Martin JW, El-Din MG. Impact of peroxydisulfate in the presence of zero valent iron on the oxidation of cyclohexanoic acid and naphthenic acids from oil sands process-affected water. *Environ. Sci. Technol.* 2012;46(16):8984-91.
88. Al-Shamsi MA, Thomson NR. Treatment of organic compounds by activated persulfate using nanoscale zerovalent iron. *Ind. Eng. Chem. Res.* 2013;52(38):13564-71.
89. Fang GD, Dionysiou DD, Al-Abed SR, Zhou DM. Superoxide radical driving the activation of persulfate by magnetite nanoparticles: Implications for the degradation of PCBs. *Appl. Catal., B* 2013;129:325-32.
90. Avetta P, Pensato A, Minella M, Malandrino M, Maurino V, Minero C, et al. Activation of persulfate by irradiated magnetite: Implications for the degradation of phenol under heterogeneous photo-Fenton-Like conditions. *Environ. Sci. Technol.* 2015;49(2):1043-50.
91. Gregory KB, Larese-Casanova P, Parkin GF, Scherer MM. Abiotic Transformation of Hexahydro-1,3,5-trinitro-1,3,5-triazine by FeII Bound to Magnetite. *Environ. Sci. Technol.* 2004;38(5):1408-14.

92. Gorski CA, Scherer MM. Influence of magnetite stoichiometry on Fe(II) uptake and nitrobenzene reduction. *Environ. Sci. Technol.* 2009;43(10):3675-80.
93. Amonette JE, Workman DJ, Kennedy DW, Fruchter JS, Gorby YA. Dechlorination of carbon tetrachloride by Fe(II) associated with goethite. *Environ. Sci. Technol.* 2000;34(21):4606-13.
94. Zhang T, Chen Y, Wang Y, Le Roux J, Yang Y, Croué J-P. Efficient peroxydisulfate activation process not relying on sulfate radical generation for water pollutant degradation. *Environ. Sci. Technol.* 2014;48(10):5868-75.
95. Lei Y, Chen C-S, Tu Y-J, Huang Y-H, Zhang H. Heterogeneous degradation of organic pollutants by persulfate activated by CuO-Fe₃O₄: Mechanism, stability, and effects of pH and bicarbonate ions. *Environ. Sci. Technol.* 2015;49(11):6838-45.
96. Su CL, Loh KP. Carbocatalysts: Graphene oxide and its derivatives. *Accounts Chem. Res.* 2013;46(10):2275-85.
97. Su DS, Perathoner S, Centi G. Nanocarbons for the development of advanced catalysts. *Chem. Rev.* 2013;113(8):5782-816.
98. Fan XB, Zhang GL, Zhang FB. Multiple roles of graphene in heterogeneous catalysis. *Chem. Soc. Rev.* 2015;44(10):3023-35.
99. Wu SC, Wen GD, Liu XM, Zhong BW, Su DS. Model molecules with oxygenated groups catalyze the reduction of nitrobenzene: Insight into carbocatalysis. *Chemcatchem.* 2014;6(6):1558-61.
100. Wen GD, Wu SC, Li B, Dai CL, Su DS. Active Sites and Mechanisms for direct oxidation of benzene to phenol over carbon catalysts. *Angew. Chem. Int. Ed.* 2015;54(13):4105-9.
101. Ahmad M, Teel AL, Watts RJ. Mechanism of persulfate activation by phenols. *Environ. Sci. Technol.* 2013;47(11):5864-71.
102. Doong RA, Chiang HC. Transformation of carbon tetrachloride by thiol reductants in the presence of quinone compounds. *Environ. Sci. Technol.* 2005;39(19):7460-8.
103. Lovley DR, Coates JD, BluntHarris EL, Phillips EJP, Woodward JC. Humic substances as electron acceptors for microbial respiration. *Nature.* 1996;382(6590):445-8.
104. Fang GD, Gao J, Dionysiou DD, Liu C, Zhou DM. Activation of persulfate by quinones: Free radical reactions and implication for the degradation of PCBs. *Environ. Sci. Technol.* 2013;47(9):4605-11.
105. Lee H, Lee HJ, Jeong J, Lee J, Park NB, Lee C. Activation of persulfates by carbon nanotubes: Oxidation of organic compounds by nonradical mechanism. *Chem. Eng. J.* 2015;266:28-33.

106. Wang XB, Qin YL, Zhu LH, Tang HQ. Nitrogen-doped reduced graphene oxide as a bifunctional material for removing bisphenols: Synergistic effect between adsorption and catalysis. *Environ. Sci. Technol.* 2015;49(11):6855-64.
107. Fang GD, Liu C, Gao J, Dionysiou DD, Zhou DM. Manipulation of persistent free radicals in biochar to activate persulfate for contaminant degradation. *Environ. Sci. Technol.* 2015;49(9):5645-53.
108. Hussain H, Green IR, Ahmed I. Journey describing applications of oxone in synthetic chemistry. *Chem. Rev.* 2013;113(5):3329-71.
109. Guan YH, Ma J, Li XC, Fang JY, Chen LW. Influence of pH on the formation of sulfate and hydroxyl radicals in the UV/peroxymonosulfate system. *Environ. Sci. Technol.* 2011;45(21):9308-14.
110. Miroschnichenko AG, Lunenok-Burmakina VA. A quantum-mechanical study of the structure of inorganic derivatives of hydrogen peroxide. *Theor. Exp. Chem.* 1976;11(3):320-5.
111. Hu P, Long M. Cobalt-catalyzed sulfate radical-based advanced oxidation: A review on heterogeneous catalysts and applications. *Appl. Catal., B* 2016;181:103-17.
112. Chen X, Qiao X, Wang D, Lin J, Chen J. Kinetics of oxidative decolorization and mineralization of Acid Orange 7 by dark and photoassisted Co^{2+} -catalyzed peroxymonosulfate system. *Chemosphere.* 2007;67(4):802-8.
113. Kim J, Edwards JO. A study of cobalt catalysis and copper modification in the coupled decompositions of hydrogen-peroxide and peroxomonosulfate Ion. *Inorg. Chim. Acta.* 1995;235(1-2):9-13.
114. Anipsitakis GP, Stathatos E, Dionysiou DD. Heterogeneous activation of oxone using Co_3O_4 . *J. Phys. Chem. B.* 2005;109(27):13052-5.
115. Chan KH, Chu W. Degradation of atrazine by cobalt-mediated activation of peroxymonosulfate: Different cobalt counteranions in homogenous process and cobalt oxide catalysts in photolytic heterogeneous process. *Water Res.* 2009;43(9):2513-21.
116. Petitto SC, Marsh EM, Carson GA, Langell MA. Cobalt oxide surface chemistry: The interaction of $\text{CoO}(1\ 0\ 0)$, $\text{Co}_3\text{O}_4(1\ 1\ 0)$ and $\text{Co}_3\text{O}_4(1\ 1\ 1)$ with oxygen and water. *J. Mol. Catal. A* 2008;281(1-2):49-58.
117. Hu LH, Sun KQ, Peng Q, Xu BQ, Li YD. Surface Active sites on Co_3O_4 nanobelt and nanocube model catalysts for CO oxidation. *Nano Res.* 2010;3(5):363-8.
118. Liang HW, Ting YY, Sun HQ, Ang HM, Tade MO, Wang SB. Solution combustion synthesis of Co oxide-based catalysts for phenol degradation in aqueous solution. *J. Colloid Interf. Sci.* 2012;372:58-62.
119. Shukla PR, Wang SB, Sun HQ, Ang HM, Tade M. Activated carbon supported cobalt catalysts for advanced oxidation of organic contaminants in aqueous solution. *Appl. Catal., B* 2010;100(3-4):529-34.

120. Hu LX, Yang F, Lu WC, Hao Y, Yuan H. Heterogeneous activation of oxone with CoMg/SBA-15 for the degradation of dye Rhodamine B in aqueous solution. *Appl. Catal., B* 2013;134:7-18.
121. Stoyanova M, Slavova I, Christoskova S, Ivanova V. Catalytic performance of supported nanosized cobalt and iron-cobalt mixed oxides on MgO in oxidative degradation of Acid Orange 7 azo dye with peroxymonosulfate. *Appl. Catal., A* 2014;476:121-32.
122. Yang Q, Choi H, Chen Y, Dionysiou DD. Heterogeneous activation of peroxymonosulfate by supported cobalt catalysts for the degradation of 2,4-dichlorophenol in water: The effect of support, cobalt precursor, and UV radiation. *Appl. Catal., B* 2008;77(3-4):300-7.
123. Chen QK, Ji FY, Guo Q, Fan JP, Xu X. Combination of heterogeneous Fenton-like reaction and photocatalysis using Co-TiO₂ nanocatalyst for activation of KHSO₅ with visible light irradiation at ambient conditions. *J. Environ. Sci.-China*. 2014;26(12):2440-50.
124. Sathishkumar P, Pugazhentiran N, Mangalaraja RV, Asiri AM, Anandan S. ZnO supported CoFe₂O₄ nanophotocatalysts for the mineralization of Direct Blue 71 in aqueous environments. *J. Hazard. Mater.* 2013;252:171-9.
125. Chen QK, Ji FY, Liu TY, Yan P, Guan W, Xu X. Synergistic effect of bifunctional Co-TiO₂ catalyst on degradation of Rhodamine B: Fenton-photo hybrid process. *Chem. Eng. J.* 2013;229:57-65.
126. Sathishkumar P, Mangalaraja RV, Anandan S, Ashokkumar M. CoFe₂O₄/TiO₂ nanocatalysts for the photocatalytic degradation of Reactive Red 120 in aqueous solutions in the presence and absence of electron acceptors. *Chem. Eng. J.* 2013;220:302-10.
127. Muhammad S, Saputra E, Sun HQ, Ang HM, Tade MO, Wang SB. Removal of phenol using sulphate radicals activated by natural zeolite-supported cobalt catalysts. *Water Air Soil Poll.* 2013;224(12).
128. Shukla P, Sun HQ, Wang SB, Ang HM, Tade MO. Co-SBA-15 for heterogeneous oxidation of phenol with sulfate radical for wastewater treatment. *Catal. Today*. 2011;175(1):380-5.
129. Qi F, Chu W, Xu BB. Catalytic degradation of caffeine in aqueous solutions by cobalt-MCM41 activation of peroxymonosulfate. *Appl. Catal., B* 2013;134:324-32.
130. Huang ZF, Bao HW, Yao YY, Lu WY, Chen WX. Novel green activation processes and mechanism of peroxymonosulfate based on supported cobalt phthalocyanine catalyst. *Appl. Catal., B* 2014;154:36-43.
131. Sun HQ, Tian HY, Hardjono Y, Buckley CE, Wang SB. Preparation of cobalt/carbon-xerogel for heterogeneous oxidation of phenol. *Catal. Today*. 2012;186(1):63-8.

132. Shi PH, Dai XF, Zheng HG, Li DX, Yao WF, Hu CY. Synergistic catalysis of Co₃O₄ and graphene oxide on Co₃O₄/GO catalysts for degradation of Orange II in water by advanced oxidation technology based on sulfate radicals. *Chem. Eng. J.* 2014;240:264-70.
133. Shi PH, Su RJ, Wan FZ, Zhu MC, Li DX, Xu SH. Co₃O₄ nanocrystals on graphene oxide as a synergistic catalyst for degradation of Orange II in water by advanced oxidation technology based on sulfate radicals. *Appl. Catal., B* 2012;123:265-72.
134. Yao YJ, Xu C, Qin JC, Wei FY, Rao MN, Wang SB. Synthesis of magnetic cobalt nanoparticles anchored on graphene nanosheets and catalytic decomposition of orange II. *Ind. Eng. Chem. Res.* 2013;52(49):17341-50.
135. Saputra E, Muhammad S, Sun HQ, Ang HM, Tade MO, Wang SB. Different crystallographic one-dimensional MnO₂ nanomaterials and their superior Performance in catalytic phenol degradation. *Environ. Sci. Technol.* 2013;47(11):5882-7.
136. Wang YX, Sun HQ, Ang HM, Tade MO, Wang SB. 3D-hierarchically structured MnO₂ for catalytic oxidation of phenol solutions by activation of peroxymonosulfate: Structure dependence and mechanism. *Appl. Catal., B* 2015;164:159-67.
137. Saputra E, Muhammad S, Sun HQ, Ang HM, Tade MO, Wang SB. Shape-controlled activation of peroxymonosulfate by single crystal alpha-Mn₂O₃ for catalytic phenol degradation in aqueous solution. *Appl. Catal., B* 2014;154:246-51.
138. Saputra E, Muhammad S, Sun HQ, Ang HM, Tade MO, Wang SB. Manganese oxides at different oxidation states for heterogeneous activation of peroxymonosulfate for phenol degradation in aqueous solutions. *Appl. Catal., B* 2013;142:729-35.
139. Yao YJ, Xu C, Yu SM, Zhang DW, Wang SB. Facile synthesis of Mn₃O₄-reduced graphene oxide hybrids for catalytic decomposition of aqueous organics. *Ind. Eng. Chem. Res.* 2013;52(10):3637-45.
140. Tan CQ, Gao NY, Deng Y, Deng J, Zhou SQ, Li J, et al. Radical induced degradation of acetaminophen with Fe₃O₄ magnetic nanoparticles as heterogeneous activator of peroxymonosulfate. *J. Hazard. Mater.* 2014;276:452-60.
141. Wang YX, Sun HQ, Ang HM, Tade MO, Wang SB. Magnetic Fe₃O₄/carbon sphere/cobalt composites for catalytic oxidation of phenol solutions with sulfate radicals. *Chem. Eng. J.* 2014;245:1-9.
142. Liu J, Zhao ZW, Shao PH, Cui FY. Activation of peroxymonosulfate with magnetic Fe₃O₄-MnO₂ core-shell nanocomposites for 4-chlorophenol degradation. *Chem. Eng. J.* 2015;262:854-61.
143. Zhang T, Zhu HB, Croue JP. Production of sulfate radical from peroxymonosulfate induced by a magnetically separable CuFe₂O₄ spinel in water: Efficiency, stability, and mechanism. *Environ. Sci. Technol.* 2013;47(6):2784-91.

144. Guan YH, Ma J, Ren YM, Liu YL, Xiao JY, Lin LQ, et al. Efficient degradation of atrazine by magnetic porous copper ferrite catalyzed peroxymonosulfate oxidation via the formation of hydroxyl and sulfate radicals. *Water Res.* 2013;47(14):5431-8.
145. Ren YM, Lin LQ, Ma J, Yang J, Feng J, Fan ZJ. Sulfate radicals induced from peroxymonosulfate by magnetic ferrosphinel MFe_2O_4 ($M = Co, Cu, Mn, \text{ and } Zn$) as heterogeneous catalysts in the water. *Appl. Catal., B* 2015;165:572-8.
146. Saputra E, Muhammad S, Sun HQ, Wang SB. Activated carbons as green and effective catalysts for generation of reactive radicals in degradation of aqueous phenol. *RSC Adv.* 2013;3(44):21905-10.
147. Zhang J, Su DS, Zhang AH, Wang D, Schlogl R, Hebert C. Nanocarbon as robust catalyst: Mechanistic insight into carbon-mediated catalysis. *Angew. Chem. Int. Ed.* 2007;46(38):7319-23.
148. Zhang J, Liu X, Blume R, Zhang AH, Schlogl R, Su DS. Surface-modified carbon nanotubes catalyze oxidative dehydrogenation of n-butane. *Science.* 2008;322(5898):73-7.
149. Lee G, Cho K. Electronic structures of zigzag graphene nanoribbons with edge hydrogenation and oxidation. *Phys. Rev. B.* 2009;79(16).
150. Indrawirawan S, Sun HQ, Duan XG, Wang SB. Nanocarbons in different structural dimensions (0-3D) for phenol adsorption and metal-free catalytic oxidation. *Appl. Catal., B* 2015;179:352-62.
151. Peng WC, Liu SZ, Sun HQ, Yao YJ, Zhi LJ, Wang SB. Synthesis of porous reduced graphene oxide as metal-free carbon for adsorption and catalytic oxidation of organics in water. *J. Mater. Chem. A* 2013;1(19):5854-9.
152. Liu SZ, Peng WC, Sun HQ, Wang SB. Physical and chemical activation of reduced graphene oxide for enhanced adsorption and catalytic oxidation. *Nanoscale.* 2014;6(2):766-71.
153. Indrawirawan S, Sun HQ, Duan XG, Wang SB. Low temperature combustion synthesis of nitrogen-doped graphene for metal-free catalytic oxidation. *J. Mater. Chem. A* 2015;3(7):3432-40.
154. Zhao Y, Yang LJ, Chen S, Wang XZ, Ma YW, Wu Q, et al. Can boron and nitrogen co-doping improve oxygen reduction reaction activity of carbon nanotubes? *J. Am. Chem. Soc.* 2013;135(4):1201-4.
155. Liang J, Jiao Y, Jaroniec M, Qiao SZ. Sulfur and nitrogen dual-doped mesoporous graphene electrocatalyst for oxygen reduction with synergistically enhanced performance. *Angew. Chem. Int. Ed.* 2012;51(46):11496-500.

Every reasonable effort has been made to acknowledge the owners of copyright material. I would be pleased to hear from any copyright owner who has been omitted or incorrectly acknowledged.

Chapter 3. Insights into Heterogeneous Catalysis of Persulfate Activation on Dimensional-Structured Nanocarbons

Abstract

A variety of dimensional-structured nanocarbons were applied for the first time as metal-free catalysts to activate persulfate (PS) for catalytic oxidation of phenolics and dyes as well as their degradation intermediates. Single-walled carbon nanotubes (SWCNTs), reduced graphene oxide (rGO) and mesoporous carbon (CMK-8) demonstrated superior catalytic activities for heterogeneous PS activation, whereas fullerene (C₆₀), nanodiamonds, and graphitic carbon nitride (g-C₃N₄) presented low efficiencies. Moreover, the carbocatalysts presented even better catalytic performances than activated carbon and metal oxides, such as Fe₃O₄, CuO, Co₃O₄ and MnO₂. The activity of prepared rGO-900 was further competing to the most efficient electron donor of zero-valent iron (ZVI). Both characterization and oxidation results suggested that the catalytic performances of the nanocarbons are determined by the intrinsic atom arrangements of carbon hybridization, pore structure, defective sites, and functional groups (especially the carbonyl groups). Electron paramagnetic resonance (EPR) spectra revealed that carbocatalysts might act as an excellent electron bridge in activation of PS to oxidize adsorbed water directly to generate hydroxyl radicals, distinct from homogeneous and metal-based catalytic activation. This study discovers several efficient nanocarbons for heterogeneous PS activation, and presents new insights into the catalytic activation processes, providing a fascinating strategy to develop metal-free catalysts for green remediation.

3.1 Introduction

In recent decades, environmental deterioration issues such as sandy desertification, air pollution, soil and water contamination have interrupted the balance of harmonious co-existence between the nature and human beings. The excessive hazardous compounds in industrial wastewater and domestic sewage have been far beyond the natural degradation capability by the ecosystem. Therefore, state-of-the-art remediation technologies for adsorption and catalytic oxidation of aqueous pollutants have been intensively investigated.(1, 2) Notwithstanding adsorption presents great performance for phase separation, the adsorbed pollutants are not completely destroyed and the subsequent disposal or regeneration of adsorbents will likely give rise to secondary contamination.(3) On the other hand, advanced oxidation processes (AOPs), utilizing oxidants such as oxygen, ozone, and superoxides such as H_2O_2 , HSO_5^- and $\text{S}_2\text{O}_8^{2-}$, are able to completely decompose organics into harmless substances, water and carbon dioxide.(3) A conventional Fenton reaction applies ferrous ions to stimulate H_2O_2 to generate hydroxyl radicals for AOPs. However, the Fenton process suffers from drawbacks, such as strict pH requirements (~3) and production of large amounts of sludge. Meanwhile, it releases metal ions into the water body, making it both cost-ineffective and non-eco-friendly for industrial application. Compared to liquid H_2O_2 , persulfate (PS), a white crystal solid, is cheaper (\$0.74/kg vs \$1.5/kg of H_2O_2), more chemically stable and convenient to transport, storage and operation, and has triggered broad interests for pollutant removal.(4, 5)

PS itself presents a low oxidative potential for decomposition of organic compounds without activation processes. The bond distance and energy of O–O ($\text{SO}_4\text{--SO}_4$) bonding were estimated to be 1.497 Å and 140 kJ/mol, respectively.(6, 7) The symmetric structure of PS molecules and relatively high bonding energy make it more difficult to break the O–O bond and generate free radicals without external activation. Various approaches were then applied to activate PS either to generate free radicals such as sulfate ($\text{SO}_4^{\cdot-}$) and hydroxyl radicals ($\cdot\text{OH}$) or to induce non-radical process to conduct the oxidation processes.(5) Physical activation such as UV irradiation or heating is able to effectively stimulate PS to produce sulfate radicals for oxidation of pollutants.(8-10) Chemical activation such as bases, phenols, and quinones were

reported to be effective for activating PS for *in situ* chemical oxidation (ISCO).(11-13) Recent studies also applied electrochemical methods or electron donors (zero-valent iron or ferrous ion (II)) for PS activation.(14-17) Andrew et al. reported that silver (I) was active in catalytic activation of PS for oxidative decarboxylation of acids, and copper (II) could effectively enhance the catalytic reaction with co-catalysis.(18) All the above approaches require energy or chemical inputs, or discharge toxic substances into the water. However, effective heterogeneous PS activation has been less explored. Zhang and co-workers reported that copper oxide (CuO) can work as an efficient catalyst for PS activation under mild conditions via a non-radical process for oxidative degradation of 2,4-dichlorophenol (2,4-DCP).(5) PS tends to firstly interact with the outer sphere of CuO, which is supposed to be the rate-limit step, and then quickly reacts with the target organic pollutants.

We first discovered that chemically reduced graphene oxide (rGO) can work as an effective metal-free catalyst to activate peroxymonosulfate (PMS) to generate reactive radicals.(19) More recently, multi-walled carbon nanotubes (MWCNTs) further demonstrated superior performance for PS activation toward phenol oxidation.(20, 21) The sp^2 covalent carbon network and oxygen functional groups (CNT-C=O) at the defective edges of MWCNTs were suggested to conduct a redox cycle for electron transfer to PS to produce radicals, yet insight into the mechanism of carbocatalysis for PS activation is still lacking. It was reported that nanocarbons with different structure dimensions presented unique properties in charge transportation, electronic conductivity, mechanical strength, and porosity in supercapacitor electrodes.(22, 23) However, to the best of our knowledge, the effect of molecular dimensions of nanocarbons on heterogeneous catalysis has rarely been investigated. In this study, a wide variety of carbon allotropes in differently molecular dimensions, such as 0D fullerene and nanodiamonds, 1D SWCNTs and MWCNTs, 2D graphene and g-C₃N₄, and 3D CMK-8, were employed for PS activation for catalytic phenol oxidation. Activated carbon, iron powders and several classical metal oxides were utilized as reference materials. Electron paramagnetic resonance (EPR) was applied as a powerful *in-situ* characterization technique to facilitate the first insight into PS activation and radical evolution processes on nanocarbons.

3.2 Experimental Section

Chemicals and Materials. Potassium peroxydisulfate (PS, >99.0%), melamine (>99.0%), diamond nanopowder (>97.0%, <10 nm), and 5,5-dimethylpyrroline-oxide (DMPO, >99.0%) were purchased from Sigma-Aldrich. Phenol (>99.0%), 2,4-dichlorophenol (2,4-DCP, >99.0%), methylene blue (>99.0%), and methanol (absolute) were obtained from Chem-Supply. Fullerene (C₆₀, >99.5%) and 3D cubic-ordered mesoporous carbon (CMK-8, >99.6%) were purchased from XF Nano, Nanjing, China. The single-walled carbon nanotubes (SWCNTs) and multi-walled carbon nanotubes (MWCNTs) were obtained from Timesnano, Chengdu, China. Activated carbon (AC) was purchased from Picactive Co. Ltd, Indonesia. All carbon materials were used as received.

Synthesis of Reduced Graphene Oxide, g-C₃N₄ and Metal Oxides. Graphene oxide (GO) was synthesized via a modified Hummers' method as reported in our previous studies.(2, 19) To prepare the reduced graphene oxide (rGO), GO was ground finely and transferred to a quartz boat placed in a tubular furnace. Nitrogen was applied as the protection gas with a flow rate of 50 mL/min. After the quartz tube was purged by N₂ flow for 2 h, the temperature was elevated to 450 °C for 1 h with a heating rate of 5 °C/min to make GO fully expanded. The temperature was then raised to 900 °C and kept for 1 h to remove the oxygen groups and cooled down to room temperature naturally. The fluffy black powder was washed with water and ethanol several times and dried in an oven overnight at 60 °C. Thus, rGO was obtained and denoted as rGO-900. Graphitic carbon nitride (g-C₃N₄) was prepared by a one-pot thermal condensation method. Briefly, melamine (5.0 g) was placed in a crucible with a lid and transferred to a muffle furnace under static air atmosphere, annealing with a heating rate of 5 °C/min and kept at 550 °C for 2 h, then cooling down naturally. A yellow product was ground finely and collected for use. Preparation procedures of referenced metal oxides of Fe₃O₄, CuO, Co₃O₄ and MnO₂ can be found in references.

Characterization of Materials. Nitrogen sorption isotherms were acquired from a Tristar 3000 at -196 °C to evaluate the Brunauer-Emmett-Teller (BET) specific surface area. Porous structure and pore size distribution were estimated by the Barrett-Joiner-Halenda (BJH) method (desorption). Raman spectra were studied on an ISA dispersive

argon laser Raman spectrometer (514 nm). The surface elemental information was obtained from X-ray photoelectron microscopy (XPS, Thermo Escalab 250) under Al K α X-ray. The XPS spectra were fitted with CasaXPS software, calibrated to the binding energy of primary C 1s peak at 284.5 eV. The chemical component fitting was applied by the Voigt functions with the Shirley background and a 30% Lorentzian component.

Catalytic Activity Tests. The adsorption and catalytically oxidative degradation of phenol were carried out in a batch reactor. At each time interval, the reaction solution was withdrawn, filtered and injected into a vial. In catalytic oxidation, 0.5 mL of methanol as a radical scavenger was immediately injected to the vial to quench the oxidation reaction. The sample was analyzed by an UltiMate 3000 ultra-high performance liquid chromatography plus (UHPLC⁺) from Thermo-Fisher Scientific for monitoring phenol concentration and intermediates with UV lamp at 270 nm with a C18 column. The mobile phase was made of 30 wt.% acetonitrile and 70 wt.% ultrapure water at a flowrate of 1 mL/min. After each run, the carbocatalysts were recycled, washed by water and ethanol several times, and dried in an oven at 60 °C overnight for reuse. 2,4-DCP, catechol and 1,4-dihydroxybenzene were also tested using the similar protocols. Methylene blue was degraded and monitored by UV-visible spectroscopy. After each run, the carbocatalysts were collected and washed with ethanol and ultrapure water several times, and then dried in an oven at 60 °C overnight for reuse. The passivated catalysts after the third run was re-generated via thermal treatment. Briefly, the catalysts were first washed and dried, annealed in a muffle furnace (static atmosphere) at 350 °C for 1 h with a heating rate of 5 °C /min and cooled down naturally.

Mechanistic Study of Radical Evolution. An EMS-plus electron paramagnetic resonance (Bruker, Germany) was utilized to capture the generated active radicals with a spin trapping agent of 5,5-dimethylpyrroline-oxide. The instrument was operated in the following conditions: Center field: 3514.7 G; sweep width: 100 G; microwave frequency: 10.0 GHz; power setting: 18.88 mW; scan time: 30 s; scan number: 2. The EPR spectra were analyzed and exported by Bruker Xeon software. The DMPO radical adducts were identified by hyperfine splitting constants of DMPO-OH ($\alpha_N=14.8$, $\alpha_H=14.8$) and DMPO-SO₄ ($\alpha_N=13.2$, $\alpha_H=9.6$, $\alpha_H=1.48$, and $\alpha_H=0.78$).

3.3 Results and Discussions

The physicochemical properties of carbonaceous materials are displayed in Table 3.1. Most of the nanocarbons possessed high specific surface areas (SSAs) from 200 to 1000 m²/g and pore volumes at a range of 0.74 - 1.64 cm³/g. CMK-8 presented extremely large surface area (1072 m²/g) and pore volume (1.6 cm³/g) owing to the cubic-ordered mesoporous structure. However, the SSAs of C₆₀ and g-C₃N₄ were only about 4.8 and 11.7 m²/g, respectively, probably due to the aggregated particles and stacking layers. The pore structure of nanocarbons was primarily at mesoporous region (2 - 50 nm, data not shown here).

Table 3.1. Structure and surface chemistry of various nanocarbons.

	SSAs m ² /g	Pore volume cm ³ /g	Pore size nm	Raman I _D /I _G ratio	Oxygen content
C ₆₀	4.8	0.003	4.2	-	9.1%
SWCNTs	385.2	0.90	8.2	0.46	1.6%
MWCNTs	253.6	0.74	11.2	0.65	2.1%
g-C ₃ N ₄	11.7	0.04	9.5	-	1.1%
rGO-900	462.2	1.00	5.7	1.70	6.0%
Nanodiamond	315.5	0.96	8.4	-	4.1%
CMK-8	1071.9	1.64	5.1	1.49	8.8%

The I_D/I_G ratios (defective to graphitic degree) of Raman spectra are widely employed to evaluate the crystalline structure of carbon materials. RGO-900 has a much higher I_D/I_G value (1.70) than that of SWCNTs (0.46) and MWCNTs (0.65), due to the reconstruction of carbon network and the creation of defective sites during the synthesis process. XPS study was performed to investigate the surface chemistry and chemical states of the elements in the catalysts (data not shown here). It is well known that the edges of graphene and carbon nanotubes are terminated with hydrogen and oxygen atoms.(24) Most of nanocarbons contained certain amounts of oxygen groups such as hydroxyl (C-OH), carbonyl (C=O) and carboxyl (-COOH) groups, as indicated in Figure 3.S1. The relative high oxygen contents of C₆₀ (9.1%) might be ascribed to the adsorbed oxygen molecules and organic compounds from the synthesis process. After thermal treatment, most of the oxygen groups were removed from the surface of

GO and the oxygen level was reduced from 32.0% to 6.0%.

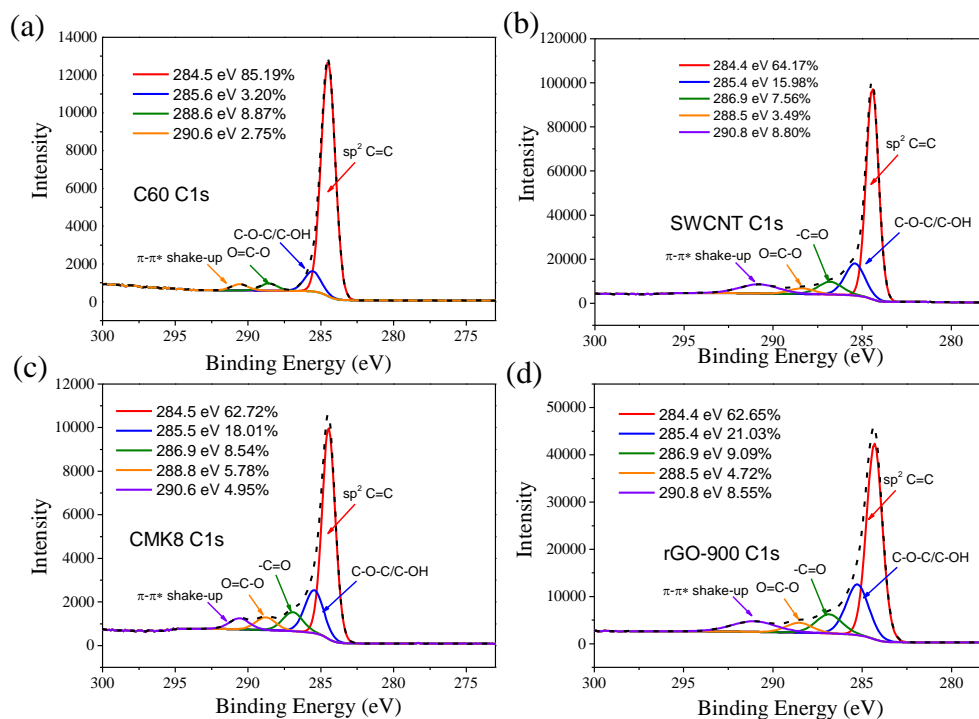


Figure 3.S1. C1s high resolution of (a) C₆₀, (b) SWCNT, (c) CMK-8, and (d) rGO-900.

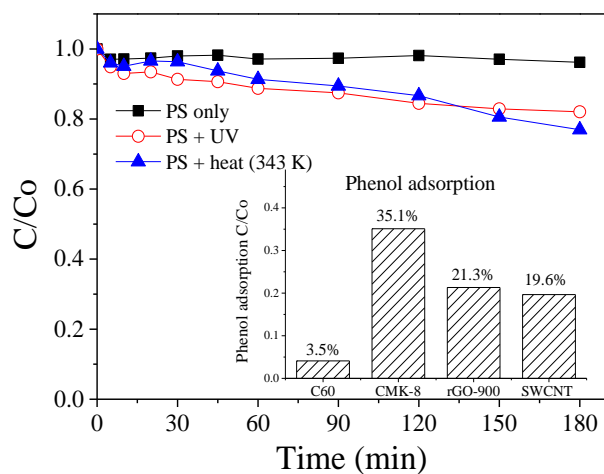


Figure 3.1. Phenol adsorption and PS activation under various conditions. [Catalyst] = 0.2 g/L; [Temp] = 25 °C; [PS] = 6.5 mM; [Phenol] = 20 ppm.

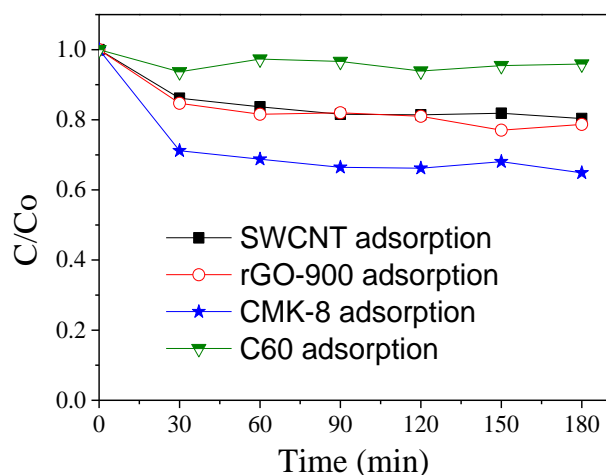


Figure 3.S2. Phenol adsorption on nanocarbons. [Temp] = 25 °C; [PS] = 0 mM; [phenol] = 20 ppm, [carbocatalysts] = 0.2 g/L

Control experiments of physical activation of PS and phenol adsorption on various nanocarbons were carried out. As shown in Figure 3.1, PS can hardly oxidize phenol without activation. Only 3.8% of phenol was degraded without the presence of a solid catalyst. Physical strategies such as ultraviolet light radiation and thermal activation (70 °C) provided 18.0% and 23.1% phenol removal accordingly. Phenol adsorption on various nanocarbons was tested as indicated in Figure 3.S2. Phenol removal efficiencies of C₆₀, SWCNTs, rGO-900, and CMK-8 were 3.5%, 19.6%, 21.3%, and 35.1%, respectively. It was suggested that the adsorption capacity of nanocarbons is closely related to the structure of nanocarbons, which follows an order: 0D < 1D ~ 2D < 3D. The nanocarbons with a higher molecular dimension possess more porous structures and larger specific surface areas, giving rising to higher phenol adsorption. Additionally, the versatile oxygen groups on the surface of carbon materials also played crucial roles to enhance the adsorption.

The catalytic activities of various nanocarbons toward PS activation were evaluated for phenol oxidation. Figure 3.2 shows that PS could barely be activated by C₆₀ and g-C₃N₄ producing only 3.8% and 4.0% phenol removal efficiencies, respectively. Around 39.5% and 92.5% of phenol were decomposed in 180 min on pristine nanodiamond and MWCNTs, respectively. It was found that SWCNTs, CMK-8 and rGO-900 presented outstanding performances for PS activation, providing complete phenol degradation in 90, 45 and 30 min, accordingly. The reaction intermediates

during the phenol oxidation were investigated and illustrated in Figure 3.3 to reveal the phenol degradation pathways. Several standard compounds were utilized to identify the intermediates (data not shown here). It can be suggested that phenol was first oxidized to 1,2-hydrobenzene and benzoquinone, and subsequently the benzene ring was opened and oxidized to small molecular acids such as malonic acid, malic acid and formic acid. Figure 3.4 further demonstrated that the nanocarbons presented a great efficiency for catalytic oxidation of other organic pollutants such as methylene blue (MB), 2,4-DCP, catechol, and 1,4-dihydroxybenzene, etc.

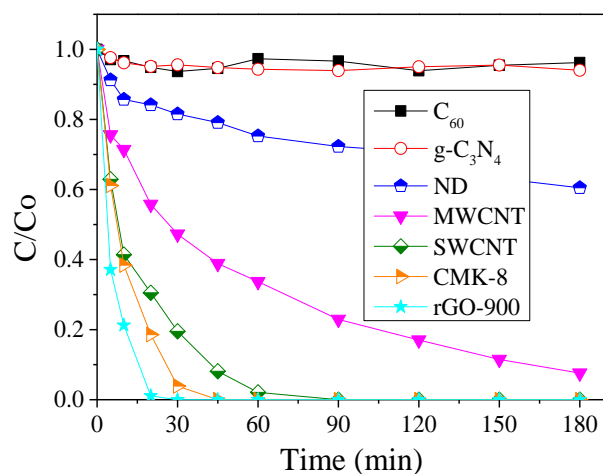


Figure 3.2. Phenol oxidative degradation on various nanocarbons. [Catalyst] = 0.2 g/L; [Temp] = 25 °C; [PS] = 6.5 mM; [Phenol] = 20 ppm.

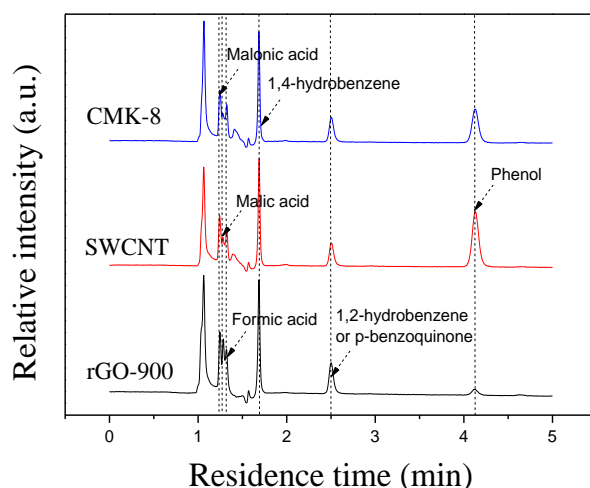


Figure 3.3. Intermediates detection in phenol oxidation on nanocarbons. [Temp] = 25 °C; [PS] = 6.5 mM; [Phenol] = 20 ppm; [Carbocatalyst] = 0.2 g/L, [Reaction time] = 30 min.

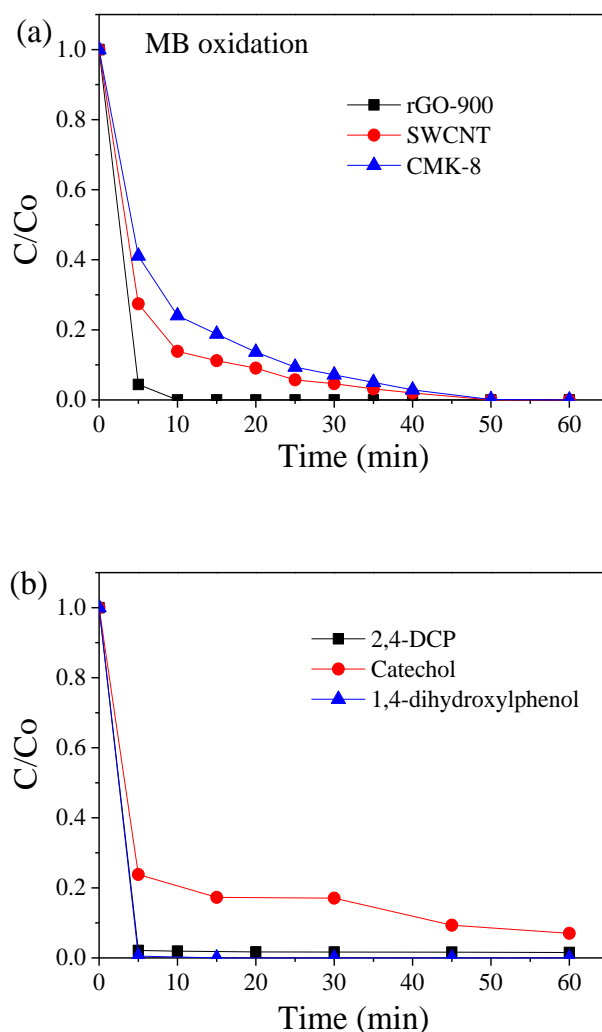


Figure 3.4. (a) Persulfate activation on nanocarbons for methylene blue degradation ($[MB] = 10$ ppm); (b) 2,4-DCP, catechol, 1,4-dihydroxybenzene oxidative degradation on rGO-900. ($[2,4-DCP] = 10$ ppm; $[Catechol]$ or $[1,4-dihydroxybenzene] = 20$ ppm) $[Temp] = 25$ °C; $[PS] = 6.5$ mM; $[Carbocatalyst] = 0.2$ g/L.

During synthesis of nanocarbons, metal impurities are always unavoidably introduced into the carbon materials in spite of physical and chemical post-treatments such as mechanical separation and acid washing.(25, 26) It is well reported that trace metal residues might significantly influence the carbocatalyst-based heterogeneous reactions.(25, 27-29) However, in this study, XPS survey confirmed that no significant metal elements were found in the XPS spectra of the nanocarbons (data not shown here). The effect of metal residues was further ruled out by employing the ash of nanocarbons as catalysts for phenol oxidation, which presented poor activities for PS

activation (data not shown here). Furthermore, the digested solutions of carbocatalysts after acid washing were employed for PS activation. The experimental results (not shown here) further exclude the influence of metal residuals. Herein, the outstanding catalytic activity was exclusively proven to derive from functional groups and active sites of nanocarbons in carbocatalysis for PS activation.

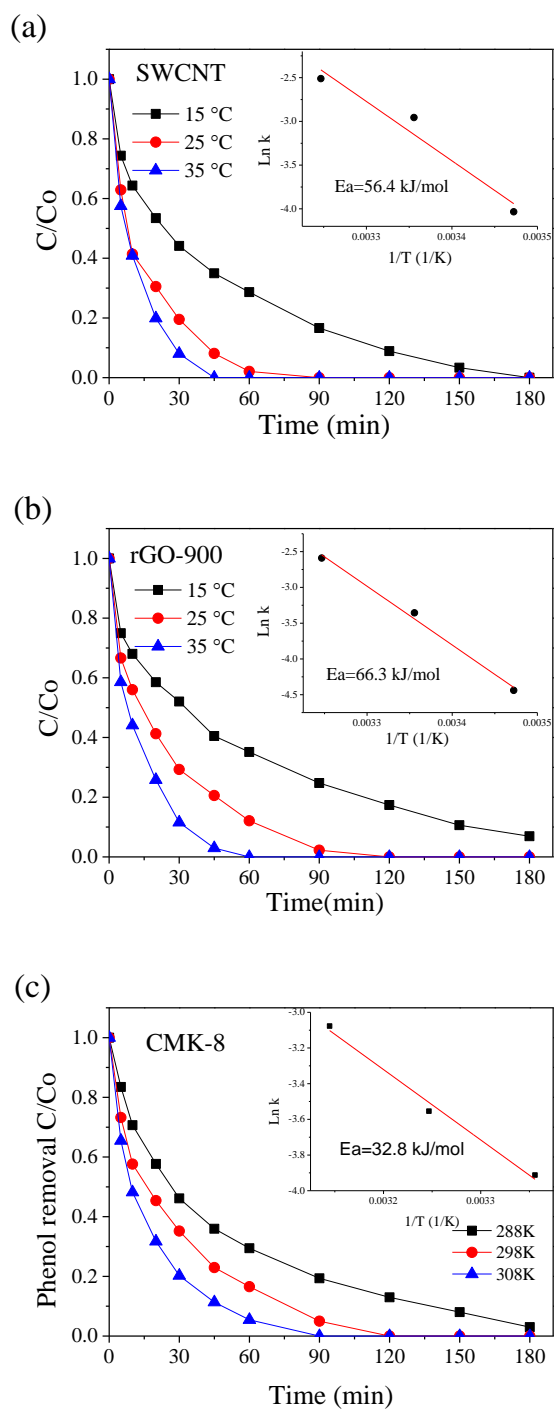


Figure 3.S3. Temperature effect on phenol removal on (a) SWCNT ([Catalyst] = 0.2 g/L), (b) rGO-900 ([Catalyst] = 0.1 g/L) [PS] = 6.5 mM; [Phenol] = 20 ppm.

Effect of reaction temperature on catalytic phenol oxidation over nanocarbons by PS activation was further investigated. Figure 3.S3a shows that SWCNTs could completely oxidize phenol in 180 min at 15 °C. The catalytic performances of the nanocarbons in PS activation were improved with elevated temperatures. The reaction time reduced to 120 and 60 min when the temperature increased to 25 and 35 °C, respectively. Figure 3.S3b demonstrated that around 96.7% phenol removal was achieved in 180 min on rGO-900 at 15 °C, and 100% phenol was decomposed at 25 and 35 °C in 120 and 60 min, respectively. CMK-8 provided complete phenol removal in 120 and 90 min at 25 and 35 °C and 97% phenol oxidation at 15 °C as shown in Figure 3.S3c. In general, elevated temperature would facilitate phenol adsorption and electron transfer from carbon materials to PS to produce reactive radicals, herein enhancing the phenol degradation. The activation energies were estimated based on first order kinetics and determined by the Arrhenius equation presented in the insets figures. The activation energies of SWCNTs, rGO-900, and CMK-8 were calculated to be 56.4, 66.3, and 32.8 kJ/mol, respectively.

Su and co-workers reported that improved catalytic activity for aerobic oxidation originated from the synergistic performance of the carboxylic groups and unconfined π electrons at the defective edges of graphene oxide (GO).⁽³⁰⁾ Frank et al. discovered that the ketonic and quinonic groups (C=O) at the edge of carbon nanotubes were rich in electrons and could work as Lewis basic sites for selectively oxidative dehydrogenation (ODH) of light alkanes to alkenes.^(31, 32) In environmental remediation, we first reported that rGO prepared by a hydrothermal method demonstrated an excellent activity to activate peroxymonosulfate (PMS) for organic pollutant oxidation.⁽¹⁹⁾ The surface acidity of GO was tuned by removal of oxygen groups with ammonia solution. The minor oxygen groups, especially the carbonyl (C=O) and edge defects, were suggested to present a high redox potential to facilitate electron transfer to PMS to generate free radicals. In a subsequent study, the rGO activated with CO₂ demonstrated a high specific surface area (SSA>1200 m²/g) and an enhanced activity toward PMS activation.⁽²⁾ Similar to PMS, the essence of PS activation depends on the abilities of breaking-up of SO-OS bond and conducting the electron transfer from catalysts or organic compounds to PS.

In this study, for the first time, we observed that nanocarbons such as SWCNTs, rGO-

900, and CMK-8 have superb catalytic activities to activate PS for phenol oxidation. However, C₆₀, g-C₃N₄, and nanodiamond presented poor performances. SWCNTs and MWCNTs are consisted of highly sp²-hybridized graphitic carbon structure with low defects and oxygen levels, confirming that the abundant free-flowing π electrons might be effective to activate PS to form reactive radicals. Additionally, the bent graphene sheets of CNTs contained partially delocalized π electrons and provide better access to the reactants (PS), thus further enhancing the catalytic activity.(24) Nanodiamond possesses a sp³-hybridized core and is coated with amorphous carbon, presenting no effectiveness for PS activation. However, CMK-8 (amorphous carbon) with high oxygen contents and defective degrees ($I_D/I_G=1.49$) demonstrates great performance for phenol oxidation, suggesting that the defective edges and oxygen groups can be active sites. This is further supported by the catalysis on chemically derived rGO-900, which has a sp² carbon lattice and the highest defective degrees ($I_D/I_G=1.70$) with plentiful zigzag edges, vacancy defects, non-hexagonal units and functional groups formed during the thermal annealing, and demonstrates the best performance for PS activation. Additionally, the porous structure of nanocarbons, which possess large pore volume and high specific surface area, not only facilitates the adsorption of phenol and enhances mass transfer process, but also provides more exposed active sites for surface catalytic reactions. To further probe the effective species, three kinds of small molecular catalysts (benzoquinone, 1,4-dicarboxybenzene and 1,2-dihydroxybenzene) were employed to mimic different oxygen groups of carbonyl groups (C=O), carboxyl groups (-COOH), and hydroxyl groups (-OH), respectively.(33, 34) The *in-situ* electron paramagnetic resonance (EPR) spectra in Figure 3.5 revealed that the carbonyl presented the strongest intensities and demonstrated much better performance to activate PS for reactive radical generation, suggesting C=O is the main active sites among the oxygen groups. It is interesting to note that graphene oxide possesses high oxygen contents (over 30 at.%), yet demonstrates very poor activity toward phenol adsorption and PS activation (data not shown here). The catalytic activity was dramatically enhanced after removing most of the oxygen groups via thermal annealing (rGO-900). The same phenomenon was also observed in our previous study for PMS activation.(19) As the electron transfer process is influenced by the relative electronic potential between the carbocatalysts and persulfate, the excess of oxygen contents will significantly affect the reducibility of graphene, which is not beneficial for the electron transfer from graphene to PMS or PS. Thus, for future design of

efficient carbocatalysts, both the oxygen level and species of oxygen groups should be optimized. The experimental results suggest that the relationship between dimensional effect and catalytic performance is poor. The catalytic activity of nanocarbons for PS activation indeed originates from the carbon-conjugated structure, defective sites, and proper amounts of functional groups.

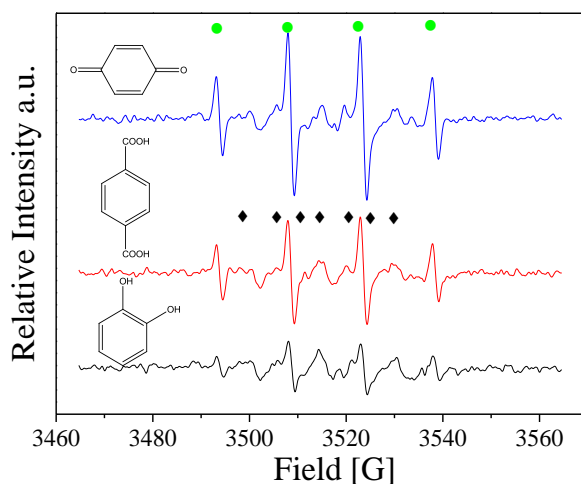


Figure 3.5. EPR spectra of PS activation on (a) benzoquinone, (b) 1,4-dicarboxybenzene, and (c) 1,2-dihydroxybenzene. (●: DMPO-OH, ◆: DMPO-SO₄) [Temp] = 25 °C; [PS] = 6.5 mM; [Catalyst] = 20 ppm; [DMPO] = 0.08 M.

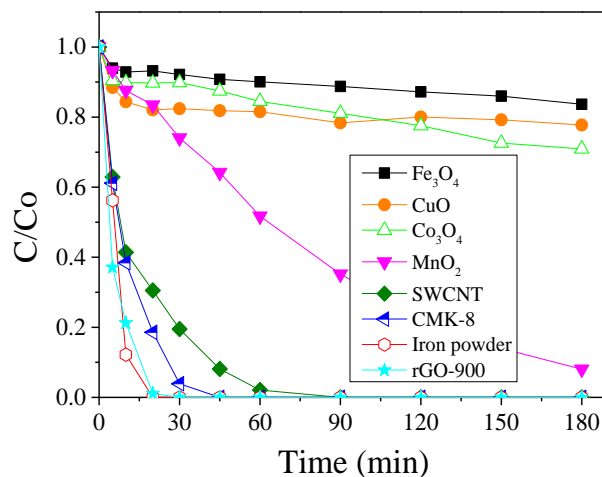


Figure 3.6. Comparison of metal and metal-free catalysts for PS activation. [Catalyst] = 0.2 g/L; [Temp] = 25 °C; [PS] = 6.5 mM; [Phenol] = 20 ppm.

Classic metal (Fe⁰) and metal oxides (Fe₃O₄, CuO, Co₃O₄ and MnO₂) were employed to compare with the metal-free catalysts. Figure 3.6 indicates that Fe₃O₄, CuO, and

Co₃O₄ presented poor catalytic activities, leading to 16.4%, 22.3%, and 29.1% phenol oxidation, respectively. MnO₂ was able to effectively activate PS with 92.0% phenol degradation in 180 min. The zero-valent iron (ZVI) worked as electron donors to stimulate PS (S₂O₈²⁻) to generate sulfate radicals (SO₄^{•-}), providing 100% phenol removal in 30 min. However, it can be seen that nanocarbons, such as MWCNTs, SWCNTs, and CMK-8, are more effective than most of the metal oxides for PS activation. rGO-900 was even comparable to the most efficient metal catalyst ZVI, completely avoiding the introduction of metal ions (Fe³⁺) to the water body.

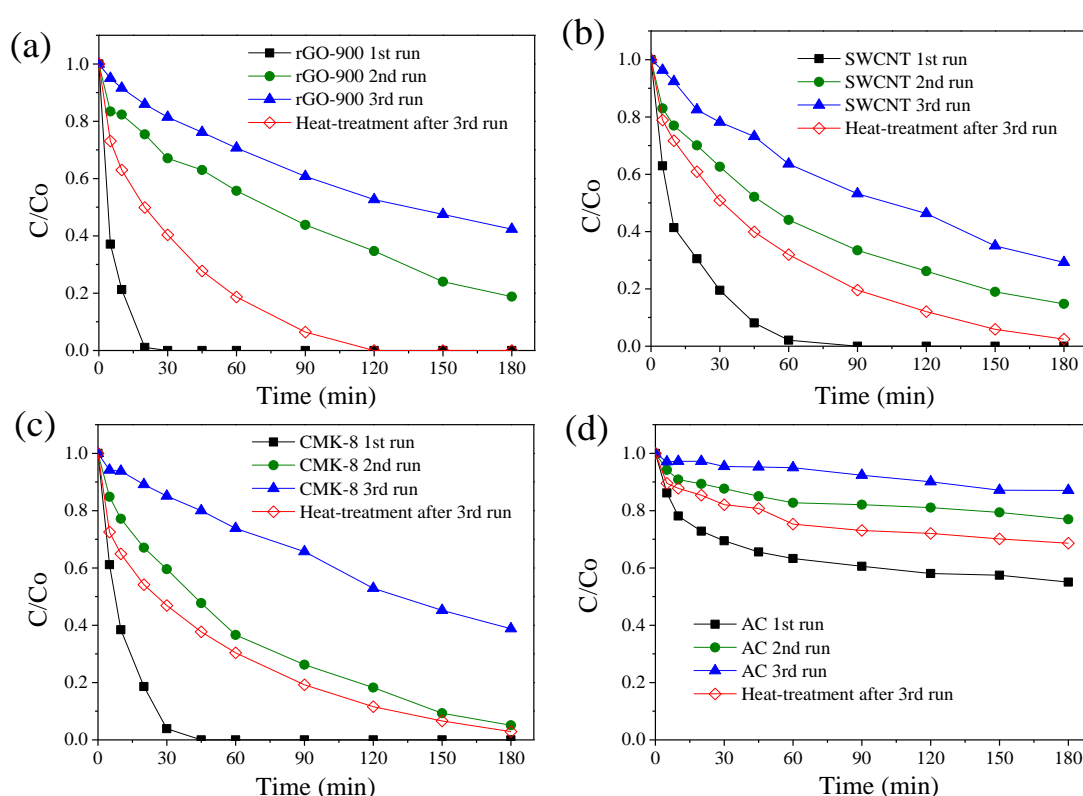


Figure 3.7. Stability and regeneration tests of (a) rGO-900, (b) SWCNTs, (c) CMK-8, and (d) activated carbon. [Catalyst] = 0.2 g/L; [Temp] = 25 °C; [PS] = 6.5 mM; [Phenol] = 20 ppm.

The stability tests of rGO-900, SWCNTs and CMK-8 were performed and shown in Figure 3.7. Fresh rGO-900 could completely decompose 20 ppm phenol in just 30 min, and 81.2% and 57.7% of phenol removals were achieved in 180 min, respectively, in the 2nd and 3rd runs. SWCNTs provided 100% phenol oxidation in the 1st run, and

85.2% and 70.7% for the 2nd and 3rd cycles. CMK-8 was able to obtain 100%, 94.9% and 61.3% of phenol decomposition for the three cycles. Yang et al. found that activated carbon could catalyze persulfate to degrade dyes.(35) An activated carbon (SSAs 821.3 m²/g, pore volume 0.011 cm³/g) was then tested, which provides 44.9%, 23.0% and 12.9% phenol removal for the 1st, 2nd and 3rd runs, respectively. It is well reported that the deactivation of metal oxides in heterogeneous catalysis was mainly due to changes of surface crystal structure and coverage of intermediates. In terms of ZVI, the surface of ZVI was quickly covered and wrapped by ferric hydroxide or ferrous sulfate in the activation of PS, thus preventing the further interaction of ZVI and PS.(36) However, the passivation of nanocarbons in activation of PS is different from metals and metal oxides.

Table 3.S1. Physicochemical properties of SWCNT and rGO-900 after 1st run.

	SSAs m ² /g	Pore volume cm ³ /g	Pore size nm	Oxygen content
SWCNT used	378.0	0.85	6.34	4.8%
rGO-900 used	241.4	0.50	4.85	10.7%

Table 3.S1 suggests that the pore structure and surface chemistry of rGO-900 and SWCNTs changed significantly after the 1st run, due to the re-construction of carbon structure and coverage of phenol and organic intermediates, which presented a strong interaction with the sp² hybridized carbon system. Interestingly, it can be seen that SWCNTs presented a better reusability than the chemically derived rGO, which was possibly ascribed to the more stable and highly graphitic shell structure.(37) The activated carbon possesses much larger SSAs than rGO-900 and SWCNTs and smaller pore volume than the CMK-8, but presenting the poorest catalytic activity and stability. At the current stage, the stability of emerging nanocarbons for AOPs might be not comparable to the commercially used metal-based catalysts used in oxidative dehydrogenation or electrochemical reactions. Nevertheless, carbon catalysts do have advantages such as a high efficiency for PS activation, a better stability than the ZVI, and the metal-free nature avoiding toxic metal leaching (iron, silver, or copper ions) to the waterbody. For carbocatalysts, the activity of deactivated catalysts could commonly be recovered by post-treatment such as thermal annealing or hydrogenation at a mild condition to remove the adsorbed intermediates and to retain the better

reductive degree from oxidation in practical applications.(38-40) Therefore, the passivated carbocatalysts after the 3rd run were re-activated via heat-treatment and the catalytic activities were partially recovered. More specifically, re-generated rGO provided complete phenol oxidation in 120 min and 97.5%, 97.2% and 31.4% phenol removal efficiencies were achieved on SWCNTs, CMK-8, and activated carbon in 180 min, respectively. This study presented novel ideas for green catalysis and raised a new and efficient metal-free catalytic system in activation of PS for pollutant degradation. Further investigations need to be done to improve the stability and develop efficient and robust metal-free catalysts in future applications.

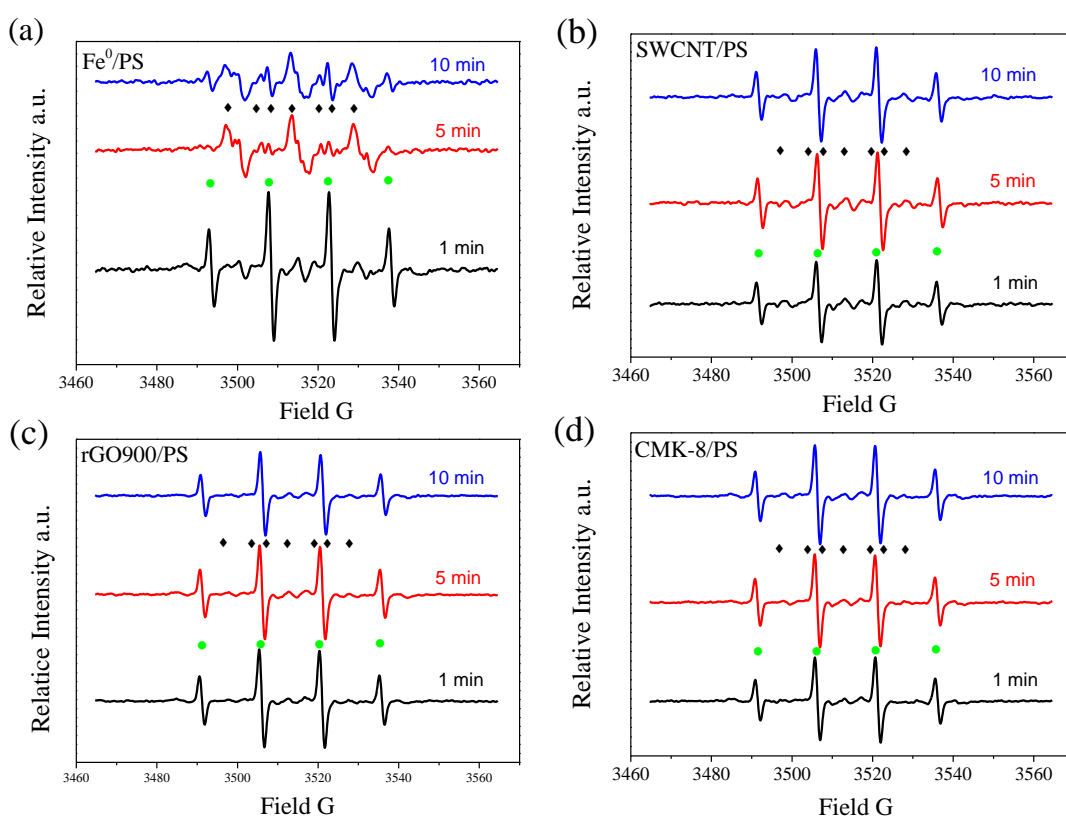
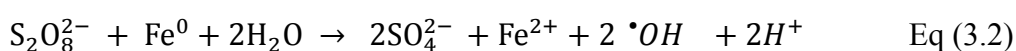


Figure 3.8. EPR spectra of (a) rGO-900, (b) SWCNTs, (c) CMK-8, and (d) activated carbon. (●: DMPO-OH, ◆: DMPO-SO₄) [Catalyst] = 0.2 g/L; [Temp] = 25 °C; [PS] = 6.5 mM; [Phenol] = 20 ppm; [DMPO] = 0.08 M.

Electron paramagnetic resonance was utilized as a powerful tool to probe the PS activation and radical revolution processes on nanocarbons. A classical spin-trapping agent, 5, 5-dimethylpyrroline-oxide (DMPO), was used to capture the free radicals

during the PS activation. Interestingly, we discovered that ZVI was able to activate PS to generate large amounts of hydroxyl radicals in the first 1 min, and subsequently generate sulfate radicals in 5 and 10 min (see Figure 3.8a). It has been well reported in many studies that iron ions mainly activated persulfate to generate sulfate radicals (Eq. 3.1), (14-17) which suggests that the PS activation on ZVI is different from that in Fe^{2+}/PS systems. As PS itself can hardly produce hydroxyl radicals, and inter-transfer between $SO_4^{\bullet-}$ to $\bullet OH$ only contributes to very small amounts of hydroxyl radicals, most of the hydroxyl radicals can be only originated from water. ZVI might be able to directly activate PS by oxidizing water via a four-electron pathway and ZVI itself works as the electron donor as well (Eq. 3.2). We suggest that the mechanisms of heterogeneous and homogeneous activations of persulfate are different. This is further verified by the nanocarbons catalysis, which preferably produce hydroxyl radicals $\bullet OH$. It is indicated in Figures 3.8 b-d that large amounts of $\bullet OH$ and small portion of $SO_4^{\bullet-}$ were generated in the SWCNT/PS, rGO-900/PS and CMK-8/PS systems throughout the reaction. Since sulfate radicals possesses higher oxidative potential (2.5~3.1 V) than hydroxyl radicals (2.7 V), O-O bond of persulfate is firstly activated and weakened on the active sites of carbocatalysts, following by directly oxidizing the adsorbed water or hydroxyl groups (OH^-) to generate hydroxyl radicals via one-step process. The mechanism of PS activation on carbocatalysts was illustrated in Scheme 3.1. It is suggested that the carbon matrix (similar to ZVI) can also work as an excellent electron bridge to facilitate the fast electron-transfer processes. Therefore, nanocarbons with various kinds of active sites and networks present different capabilities for PS activation, water and phenol adsorption, and electron transfer, thus presenting different performances in PS activation and phenol oxidation. It is also worthwhile noting that, different from metal-based systems, the highly covalent carbon network might play a crucial role to interact and activate the benzene ring of the organic matters, which helps the ring-open processes, and synergistically promotes the attack and oxidation by the reactive radicals.





Scheme 3.1. Proposed mechanism of PS activation on carbocatalysts.

3.4 Conclusions

In this study, various nanocarbons were tested as metal-free catalysts for catalytic oxidation of organic contaminants. For the first time, we found that SWCNTs, reduced graphene oxide and CMK-8 demonstrated superior efficiencies for PS activation, whereas C_{60} , $g-C_3N_4$ and nanodiamond presented poor activity. The carbocatalysts showed a much higher activity than the universally used metal oxides such as Fe_3O_4 , CuO , Co_3O_4 and MnO_2 . And rGO-900 was even comparable to the most efficient electron donor of ZVI. Meanwhile nanocarbons as catalysts completely avoid the metal leaching problems into the water body. Both the characterization and adsorption/oxidation results revealed that the structural dimension might affect the phenol adsorption capability, while catalytic activity of nanocarbons is strongly dependent on the conjugation of carbon network, defective sites, and proper amounts of functional groups (especially the carbonyl groups). More importantly, this is the first mechanistic study on PS activation on nanocarbons. The EPR results revealed that heterogeneous activation of PS is different from homogeneous systems and carbocatalysts can effectively activate PS molecules via directly oxidizing adsorbed water through the carbon bridge. Future study is still required to envisage further insights into the relationship between each active sites and its capability towards PS activation, water adsorption, and charge transfer processes. This study not only reports several green catalysts for PS activation, but also contributes to exploring new advanced oxidative systems for wastewater treatment without secondary

contamination. It is also inspiring to note that, as hydrogen peroxide is more difficult to be activated on heterogeneous catalysts (especially for nanocarbons) to generate hydroxyl radicals, this study might open up a brand new way using the metal-free catalysis for hydrogen peroxide-based systems such as Fenton reaction, photocatalysis, electrochemistry, and versatile selective oxidation processes.

References

1. Shukla PR, Wang SB, Sun HQ, Ang HM, Tade M. Activated carbon supported cobalt catalysts for advanced oxidation of organic contaminants in aqueous solution. *Appl. Catal., B* 2010; 100(3-4):529-34.
2. Peng WC, Liu SZ, Sun HQ, Yao YJ, Zhi LJ, Wang SB. Synthesis of porous reduced graphene oxide as metal-free carbon for adsorption and catalytic oxidation of organics in water. *J. Mater. Chem. A*. 2013; 1(19):5854-9.
3. Liu SZ, Peng WC, Sun HQ, Wang SB. Physical and chemical activation of reduced graphene oxide for enhanced adsorption and catalytic oxidation. *Nanoscale*. 2014; 6(2):766-71.
4. Hussain H, Green IR, Ahmed I. Journey describing applications of oxone in synthetic chemistry. *Chem. Rev.* 2013; 113(5):3329-71.
5. Zhang T, Chen Y, Wang Y, Le Roux J, Yang Y, Croué J-P. Efficient peroxydisulfate activation process not relying on sulfate radical generation for water pollutant degradation. *Environ. Sci. Technol.* 2014; 48(10):5868-75.
6. Kolthoff IM, Miller IK. The Chemistry of Persulfate. I. The kinetics and mechanism of the decomposition of the persulfate ion in aqueous medium¹. *J. Am. Chem. Soc.* 1951; 73(7):3055-9.
7. Yang SY, Wang P, Yang X, Shan L, Zhang WY, Shao XT, et al. Degradation efficiencies of azo dye Acid Orange 7 by the interaction of heat, UV and anions with common oxidants: Persulfate, peroxymonosulfate and hydrogen peroxide. *J. Hazard. Mater.* 2010; 179(1-3):552-8.
8. Yang Y, Pignatello JJ, Ma J, Mitch WA. Comparison of halide impacts on the efficiency of contaminant degradation by sulfate and hydroxyl radical-based advanced oxidation processes (AOPs). *Environmental Science & Technology*. 2014; 48(4):2344-51.
9. Kronholm J, Metsala H, Hartonen K, Riekkola ML. Oxidation of 4-chloro-3-methylphenol in pressurized hot water/supercritical water with potassium persulfate as oxidant. *Environ. Sci. Technol.* 2001; 35(15):3247-51.
10. Kronholm J, Riekkola ML. Potassium persulfate as oxidant in pressurized hot water. *Environ. Sci. Technol.* 1999; 33(12):2095-9.

11. Furman OS, Teel AL, Watts RJ. Mechanism of base activation of persulfate. *Environ. Sci. Technol.* 2010; 44(16):6423-8.
12. Ahmad M, Teel AL, Watts RJ. Mechanism of persulfate activation by phenols. *Environ. Sci. Technol.* 2013; 47(11):5864-71.
13. Fang GD, Gao J, Dionysiou DD, Liu C, Zhou DM. Activation of persulfate by quinones: free radical reactions and implication for the degradation of PCBs. *Environ. Sci. Technol.* 2013; 47(9):4605-11.
14. Cai C, Zhang H, Zhong X, Hou L. Electrochemical enhanced heterogeneous activation of peroxydisulfate by Fe–Co/SBA-15 catalyst for the degradation of Orange II in water. *Water Res.* 2014; 66(0):473-85.
15. Chen LC, Zeng XT, Si P, Chen YM, Chi YW, Kim DH, et al. Gold nanoparticle-graphite-like C₃N₄ nanosheet nanohybrids used for electrochemiluminescent immunosensor. *Anal. Chem.* 2014; 86(9):4188-95.
16. Drzewicz P, Perez-Estrada L, Alpatova A, Martin JW, El-Din MG. Impact of peroxydisulfate in the presence of zero valent iron on the oxidation of cyclohexanoic acid and naphthenic acids from oil sands process-affected water. *Environ. Sci. Technol.* 2012; 46(16):8984-91.
17. Ahn S, Peterson TD, Righter J, Miles DM, Tratnyek PG. Disinfection of ballast water with iron activated persulfate. *Environ. Sci. Technol.* 2013; 47(20):11717-25.
18. Anderson JM, Kochi JK. Silver(I)-catalyzed oxidative decarboxylation of acids by peroxydisulfate. Role of silver(II). *J. Am. Chem. Soc.* 1970; 92(6):1651-9.
19. Sun HQ, Liu SZ, Zhou GL, Ang HM, Tade MO, Wang SB. Reduced graphene oxide for catalytic oxidation of aqueous organic pollutants. *ACS Appl. Mater. Interfaces.* 2012; 4(10):5466-71.
20. Lee H, Lee HJ, Jeong J, Lee J, Park NB, Lee C. Activation of persulfates by carbon nanotubes: Oxidation of organic compounds by nonradical mechanism. *Chem. Eng. J.* 2015; 266:28-33.
21. Sun HQ, Kwan C, Suvorova A, Ang HM, Tade MO, Wang SB. Catalytic oxidation of organic pollutants on pristine and surface nitrogen-modified carbon nanotubes with sulfate radicals. *Appl. Catal., B* 2014; 154:134-41.
22. Yu Z, Tetard L, Zhai L, Thomas J. Supercapacitor electrode materials: Nanostructures from 0 to 3 dimensions. *Energ. Environ. Sci.* 2014.
23. Zhi MJ, Xiang CC, Li JT, Li M, Wu NQ. Nanostructured carbon-metal oxide composite electrodes for supercapacitors: a review. *Nanoscale.* 2013; 5(1):72-88.
24. Zhang JA, Su DS, Blume R, Schlogl R, Wang R, Yang XG, et al. Surface chemistry and catalytic reactivity of a nanodiamond in the steam-free dehydrogenation of ethylbenzene. *Angew. Chem. Int. Ed.* 2010; 49(46):8640-4.

25. Wu S, Wen G, Wang J, Rong J, Zong B, Schlogl R, et al. Nitrobenzene reduction catalyzed by carbon: does the reaction really belong to carbocatalysis? *Catal. Sci. Technol.* 2014; 4(12):4183-7.
26. Chen PR, Chew LM, Xia W. The influence of the residual growth catalyst in functionalized carbon nanotubes on supported Pt nanoparticles applied in selective olefin hydrogenation. *J. Catal.* 2013; 307:84-93.
27. Buchwald SL, Bolm C. On the role of metal contaminants in catalyses with FeCl₃. *Angew. Chem. Int. Ed.* 2009; 48(31):5586-7.
28. Banks CE, Crossley A, Salter C, Wilkins SJ, Compton RG. Carbon nanotubes contain metal impurities which are responsible for the "electrocatalysis" seen at some nanotube-modified electrodes. *Angew. Chem. Int. Ed.* 2006; 45(16):2533-7.
29. Zhang J, Comotti M, Schuth F, Schlogl R, Su DS. Commercial Fe- or Co-containing carbon nanotubes as catalysts for NH₃ decomposition. *Chem. Commun.* 2007(19):1916-8.
30. Su CL, Acik M, Takai K, Lu J, Hao SJ, Zheng Y, et al. Probing the catalytic activity of porous graphene oxide and the origin of this behaviour. *Nat. Commun.* 2012;3.
31. Frank B, Zhang J, Blume R, Schlogl R, Su DS. Heteroatoms increase the selectivity in oxidative dehydrogenation reactions on nanocarbons. *Angew. Chem. Int. Ed.* 2009; 48(37):6913-7.
32. Frank B, Blume R, Rinaldi A, Trunschke A, Schlogl R. Oxygen Insertion catalysis by sp(2) carbon. *Angew. Chem. Int. Ed.* 2011; 50(43):10226-30.
33. Wu SC, Wen GD, Liu XM, Zhong BW, Su DS. Model molecules with oxygenated groups catalyze the reduction of nitrobenzene: insight into carbocatalysis. *Chemcatchem.* 2014; 6(6):1558-61.
34. Wen GD, Wu SC, Li B, Dai CL, Su DS. Active sites and mechanisms for direct oxidation of benzene to phenol over carbon catalysts. *Angew. Chem. Int. Ed.* 2015;54(13):4105-9.
35. Yang SY, Yang X, Shao XT, Niu R, Wang LL. Activated carbon catalyzed persulfate oxidation of Azo dye acid orange 7 at ambient temperature. *J. Hazard. Mater.* 2011; 186(1):659-66.
36. Al-Shamsi MA, Thomson NR. Treatment of organic compounds by activated persulfate using nanoscale zerovalent iron. *Ind. Eng. Chem. Res.* 2013; 52(38):13564-71.
37. Duan XG, Sun HQ, Wang YX, Kang J, Wang SB. N-doping-induced nonradical reaction on single-walled carbon nanotubes for catalytic phenol oxidation. *ACS Catal.* 2014; 5(2):553-9.

38. Sun HQ, Wang YX, Liu SZ, Ge L, Wang L, Zhu ZH, et al. Facile synthesis of nitrogen doped reduced graphene oxide as a superior metal-free catalyst for oxidation. Chem. Commun. 2013; 49(85):9914-6.
39. Duan XG, Ao ZM, Sun HQ, Indrawirawan S, Wang YX, Kang J, et al. Nitrogen-doped graphene for generation and evolution of reactive radicals by metal-free catalysis. ACS Appl. Mater. Interfaces. 2015; 7(7):4169-78.
40. Duan XG, O'Donnell K, Sun HQ, Wang YX, Wang SB. Sulfur and nitrogen co-doped graphene for metal-free catalytic oxidation reactions. Small. 2015; 11(25):3036-44.

Every reasonable effort has been made to acknowledge the owners of copyright material. I would be pleased to hear from any copyright owner who has been omitted or incorrectly acknowledged.

Chapter 4. Controlled Generation of Reactive Radicals by Carbocatalysis on Nanodiamonds

Abstract

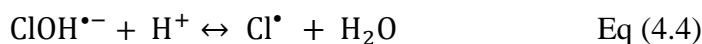
Production of radicals by metal-free catalysis is expected to offer a promising oxidative reaction for remediation of emerging contaminants. In this study, selective generation of hydroxyl radicals from novel metal-free activation of persulfate (PS) on annealed nanodiamonds (ANDs) was discovered, which demonstrated superior performances in decomposition of various pollutants to conventional metal-based catalysis. Comprehensive investigations on the effects of reaction parameters, such as solution pH, reaction temperature, initial phenol concentration, catalyst loading, PS usage, the presence of chlorine ions and humic acid, on phenol degradation were carried out. In addition, ND material optimization and reusability were also studied. Electron paramagnetic resonance (EPR) unraveled that the PS/AND system can selectively produce hydroxyl radicals ($\cdot\text{OH}$) other than sulfate radicals ($\text{SO}_4^{\cdot-}$), originated from oxidizing water molecules on the nanodiamond surface. The selective generation process was further verified by the findings that phenol decomposition was favored at a basic condition and phenol removal was enhanced at elevated solution pHs. The carbocatalysts served as an excellent electron tunnel to facilitate the charge transfer from water or hydroxide ions to PS to produce hydroxyl radicals. Electrochemical analyses in PS oxidant solution and oxygen reduction reaction (ORR) were carried out to understand O-O bond activation by the metal-free catalysis. This study provides an environmentally benign and highly efficient oxidative reaction system with hydroxyl radicals along with insights into the metal-free PS activation process.

4.1 Introduction

Ongoing environmental deterioration has motivated worldwide research in green and efficient remediation to pursue the sustainable development of human society.(1, 2) Green technologies integrating advanced oxidation processes (AOPs) have been developed to decompose organic contaminants using various superoxides to evolve reactive oxygen species especially for hydroxyl radicals ($\cdot\text{OH}$). For instance, Fenton reactions have been widely applied in wastewater treatment, in which hydrogen peroxide (H_2O_2) is decomposed by ferrous ions (Fe^{2+}) to produce hydroxyl radicals ($\cdot\text{OH}$) for AOPs. However, conventional Fenton reactions encounter some issues, for example, the instability of chemicals, pH restriction (pH~3), metal leaching and flocculation.(3) In pursuit of an alternative to Fenton reaction with less inputs of chemicals and energy, extensive trials have been attempted to employ peroxymonosulfate (PMS) or persulfate (PS) salts to generate sulfate radicals, which possess a higher oxidative potential ($\text{SO}_4^{\cdot-}$, 2.5-3.1 V vs $\cdot\text{OH}$, 2.7 V) and non-selectivity for oxidation.(4) As PS is stable and much cheaper than PMS and H_2O_2 , more attention has been attracted for developing an outstanding PS-based oxidation process.(5) A variety of physical and chemical approaches have been explored to activate PS to generate sulfate radicals.(6-9) Ferrous ions, zero-valent iron (ZVI),(10, 11) copper oxide (CuO) and biochar with persistent free radicals (PFRs)(5, 12) have been reported for PS activation. Nanocarbons were first discovered by our group to activate PMS and PS to produce reactive species for degradation of organic contaminants (phenolics, dyes, and antibiotics).(13-15) The PS/carbocatalyst also demonstrated a better controllable manner than metal-based catalysis.(16) However, this emerging catalysis is still lack of insight into the activation mechanism. The poor stability of the nanocarbons in AOPs also impedes the future applications.(17)

On the other hand, industrial and domestic wastewaters usually contain high levels of salinity and diverse natural organic matters. The diversity of the contaminants requires a controllable and selective remediation. For instance, sulfate radicals ($\text{SO}_4^{\cdot-}$) would first react with Cl^- in natural wastewater to form Cl^\cdot at a high reaction rate (Eq 4.1, $k_{\text{for}} = 3.0 \times 10^8 \text{ M}^{-1} \text{ s}^{-1}$), and then the Cl^\cdot rapidly combine with another chloride ion to produce a chlorine radical ($\text{Cl}_2^{\cdot-}$, Eq 4.2).(18, 19) The chlorine radicals with a redox potential of 2.1 V are more selective to attack the electron-rich compounds via one-

electron extraction, thus the efficiency would be reduced in treating electron-poor contaminants such as cyclohexanol and alkanes.(20, 21) The stubborn issue of sulfate radicals with background Cl⁻ ions is insignificant for hydroxyl radicals at neutral and basic pHs and Cl₂^{•-} generation becomes remarkable only at low pHs (Eqs 4.4 and 4.5).(20, 21) Therefore, solutions to the above problems of both hydroxyl and sulfate radicals for practical wastewater treatment as a challenging mission have to be found out.



Recently, nanodiamond (ND) with excellent catalytic performances and biocompatibility has become a candidate for metal-free catalysis.(22-24) In its heterogeneous catalysis, electrochemical reduction of nitrogen,(25) photocatalytic water splitting,(26) direct oxidation of benzene to phenol,(27) and oxidative dehydrogenation reactions (ODH)(28-30) have been reported. Further studies also indicated that modification of the sp² curved concentric shells of NDs with nitrogen or phosphorus could significantly enhance the catalytic activity and selectivity for ODH and selective oxidation.(22, 31) Herein, for the first time, we applied annealed nanodiamonds as superb carbocatalysts to activate persulfate, and conducted mechanistic studies targeting feasible wastewater remediation. The kinetic studies at varying reaction temperature, catalyst loading, PS dosage and initial phenol concentration were carried out. The mechanism of PS activation and radical revolution were investigated, and the possible degradation pathway was revealed by identification of the reaction intermediates. Moreover, the effects of pH, natural organic matters, and radical scavengers on oxidation efficiencies were systematically investigated. This study dedicates to providing a green, novel, and highly-efficient PS activation technology to tackle the issues in Fenton reaction and sulfate radical-based oxidation.

4.2 Experimental Sections

Materials Preparation and Characterization. All chemicals were obtained from Sigma-Aldrich. For carbon modification, pristine nanodiamonds (NDs, particle size < 10 nm) were transferred to a quartz tube and annealed at 600 – 1000 °C under nitrogen atmosphere for one hour to get annealed samples, denoted as AND-X (X = 600, 700, 800, 900, and 1000). Some metal oxides, Fe₃O₄, Co₃O₄, and CuO, were also prepared. (16) Ga₂O₃ and Fe₂O₃ were prepared via a hydrothermal method with GaCl₃ or FeCl₃ in basic conditions (pH=10, adjusted by ammonium solution) at 180 °C for 20 h. The morphology and crystal structure of the nanodiamonds were revealed by a JEOL 2100 TEM instrument. FTIR spectra were obtained from a Bruker spectrometer. Thermo-gravimetric analysis (TGA) was recorded on a Perkin Elmer thermal analyzer. The pore structures of the carbocatalysts were estimated by the Barrett-Joyner-Halenda (BJH) method and the specific surface areas (SSAs) were calculated using the Brunauer-Emmett-Teller (BET) equation from N₂ adsorption isotherms on a TriStar II instrument. The surface chemistry of the as-made catalysts was analyzed by X-ray photoelectron spectroscopy (XPS) on a Kratos AXIS Ultra DLD machine with a monochromated Al K α X-ray gun. Shirley background was utilized for peak fitting with C 1s calibrated to 284.5 eV for all the spectra.

Experimental Procedure. Activation of persulfate by nanodiamonds and metal oxides was carried out for oxidizing various aqueous pollutants. A typical reaction was conducted in a 250 mL batch reactor with fixed amounts of phenol, persulfate and nanodiamonds in solution ([catalyst] = 0.2 g/L, [PS] = 6.5 mM, [T] = 25 °C, [Phenol] = 20 mg/L, and [pH]_{initial} = 5.9 \pm 0.1 without a buffer solution) unless specified elsewhere. A water bath with a temperature controller was used to maintain the constant reaction temperature. Reaction solutions were withdrawn and injected into a HPLC vial through a 0.45 μ m filter and mixed with ethanol (V_{Solution}/V_{EtOH} = 2:1) at vigorously shaking to scavenge the excessive radicals. Then, the solutions were analyzed using an UltiMate 3000 UHPLC system with an OA column (150 \times 4 mm, 5 μ m) and an UV detector set at 270 nm for phenol and catechol and 228 nm for benzoic acid. A RSLC C18 column (100 \times 2 mm, 2.2 μ m) was applied for evaluating the concentration of an antibiotic, sulfachloropyridazine (SCP). Methylene blue (MB) was determined on a JASCO UV-vis spectrophotometer at a wavelength of 664 nm. After

each run, the passivated catalysts were recycled and washed with water and ethanol for 4 times each and dried in an oven at 60 °C overnight for reuse. Data in key figures were obtained from three parallel experiments to estimate the mean value and standard deviation. The initial rate constants were determined by a pseudo-first-order kinetic model in first 30 min before severe deactivation of the carbocatalysts.

Identification of Reactive Radicals. Electron paramagnetic resonance (EPR, Bruker) was utilized to probe the radical generation process during PS activation and the reactive radicals were trapped by 5, 5-dimethylpyrroline-oxide (DMPO, 0.08 M). The EPR instrument was operated at the center field of 3514.8 G, sweep width of 100.0 G and power of 18.7 mW with sweeping time of 30 s.

Electrochemical Measurement. The electrochemical study was performed in an O₂-saturated KOH (0.1 M) solution. A standard three-electrode configuration was utilized with a Ag/AgCl (4 M KCl) as a reference electrode, a platinum wire as a counter electrode, and a catalyst-coated glassy carbon rotating disk electrode as a working electrode (GC-RDE, 0.196 cm², Pine Research Instrumentation, USA). Electrochemical data were obtained on a CHI instrument (CHI 760E series Bipotentiostat, USA). Cyclic voltammogram (CVs) measurements were conducted at a scan rate of 100 mV s⁻¹ from 0.2 to -1.0 V vs. Ag/AgCl. Linear sweep voltammograms (LSVs) were acquired at a scan rate of 5 mV s⁻¹ from 0.2 to -0.6 V vs. Ag/AgCl on the RDE (1600 rpm). Electrochemical impedance spectroscopy (EIS) was carried out utilizing a 5 mV amplitude AC voltage (frequency range from 10⁵ to 10⁻¹ Hz) and acquired at -0.3 V vs. Ag/AgCl.

4.3 Results and Discussions

Characterization of NDs. TEM images in Figures 4.1 a and b demonstrate that after removal of amorphous carbon layers, smaller size particles with a characteristic core/shell structure were obtained for the annealed nanodiamond. The fingerprints in diamond crystals indicated a d-spacing of 2.06 Å, which was in a good agreement of the selected area electron diffraction (SAED) patterns (inset) and the sharp peak at the 2θ of 42.5° in XRD spectra corresponding to the (111) diamond facet as indicated in Figure 4.1c. Electron energy loss spectroscopy (EELS) was applied to further probe

the carbon type of the annealed nanodiamond with the carbon K-edge spectra at the diamond core and graphitic shell (Figure 4.1d). The σ^* transition peak at 293.3 eV originated from C 1s electrons of the sp^3 hybridized diamond core structure, whereas the peak at 285.5 eV can be attributed to the π^* transition of the sp^2 hybridized graphitic shell, confirming the hybrids of AND-1000.(32, 33) The SSAs (specific surface areas, Table 4.S1) and adsorption volume (Figure 4.2a) slightly increased for AND-1000, while the thermal stability of the nanodiamonds decreased after pyrolysis in nitrogen (Figure 4.2b), due to the transformation of the core structure. Thermal annealing of nanodiamonds consists of complicated processes including the decomposition of surface functional groups, collapse of diamond-edge plane (001) and reconstruction into graphitic plane (001), and formation of novel nanohybrid structure.(31, 34) FTIR spectra in Figure 4.2c suggest that most of functional groups on pristine NDs were removed after the pyrolysis. X-ray photoelectron spectroscopy (XPS) surveys (Figure 4.2d) indicate that the oxygen level decreases after the thermal treatment due to the removal of excess functional groups. The minor nitrogen impurity was introduced during the denotation process of ND manufacture.

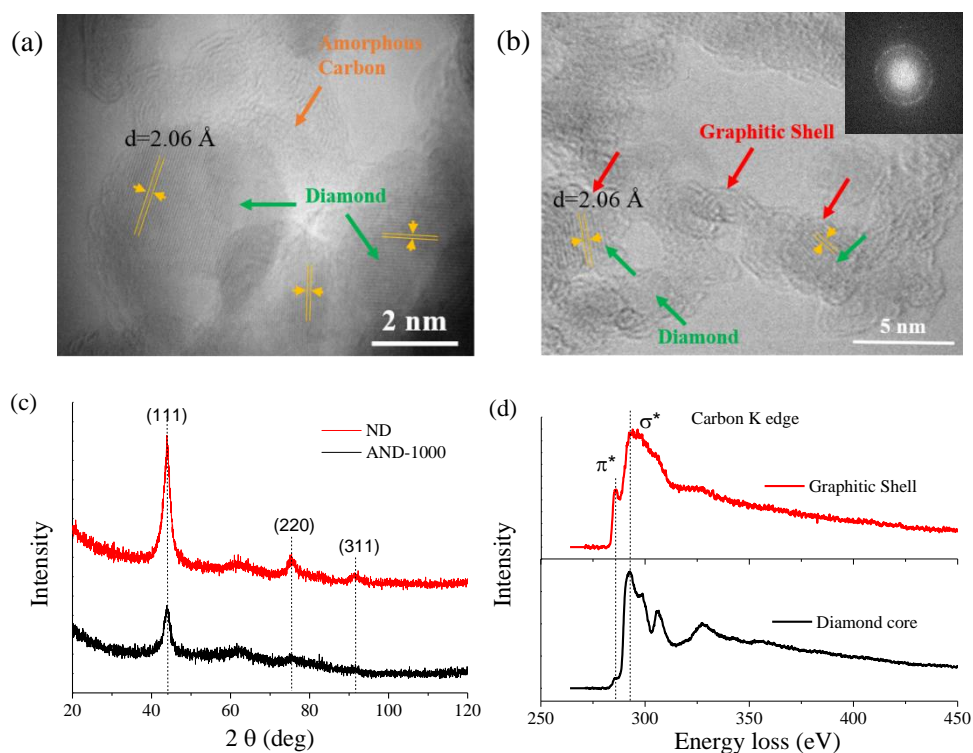


Figure 4.1. HRTEM images of (a) ND and (b) AND-1000 (SAED pattern, inset), (c) XRD patterns of ND and AND-1000, (d) EELS carbon K-edge spectra of the core and shell structures of AND-1000.

Table 4.S1. Structure and surface chemistry information of ND and AND-1000, and AND-1000 used (after first run).

	$S_{\text{BET}}, \text{m}^2/\text{g}$	$V_{\text{pore}},$	$\text{C}, \text{at.}\%$	$\text{O}, \text{at.}\%$	$\text{N}, \text{at.}\%$
AND-1000	364.4	1.1	92.7	5.7	1.5
AND-1000	354.7	1.04	89.4	8.8	1.5
ND	315.5	1.0	94.8	3.6	1.6

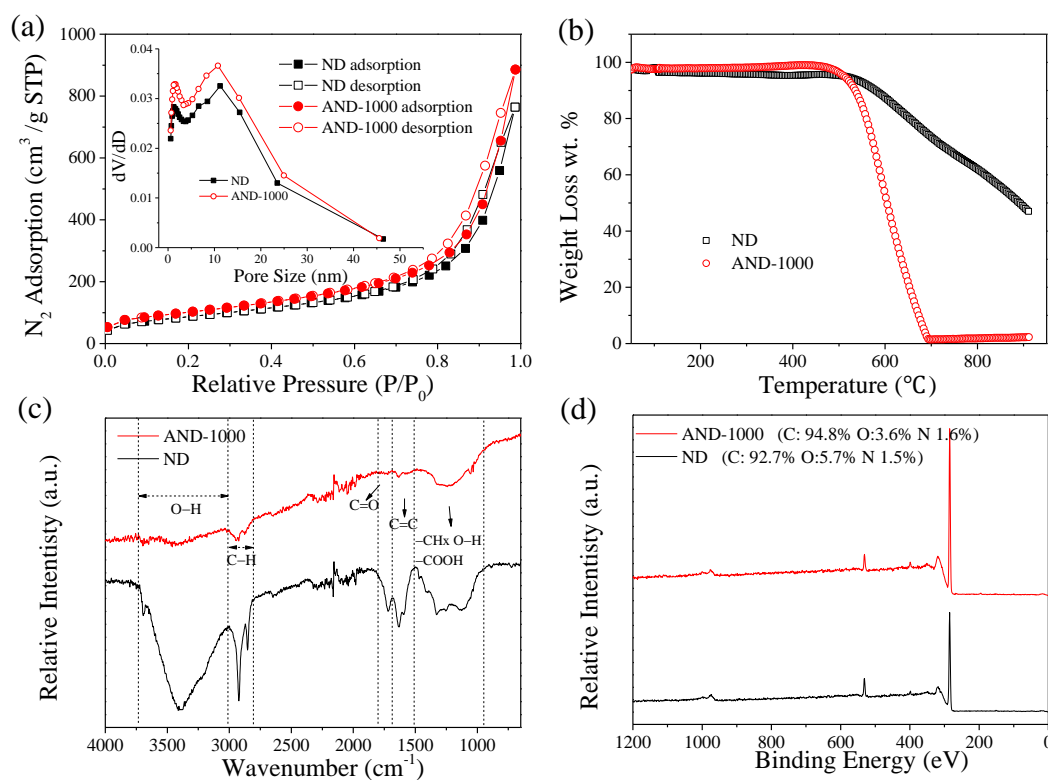


Figure 4.2. (a) Nitrogen sorption profiles and pore size distributions, (b) TGA curves, (c) FTIR spectra, and (d) XPS surveys of pristine ND and AND-1000.

Catalytic Evaluation of NDs and Metal Oxides. In the oxidative reaction, persulfate without activation is ineffective for phenol degradation. As illustrated in Figure 4.3a, phenol oxidation was dramatically enhanced on modified NDs compared to that on pristine NDs. The initial rate constants of pristine ND and AND-1000 were estimated to be 0.004 and 0.084 min^{-1} (Figure 4.S1), and a 21-fold enhancement in the activity was achieved on the AND-1000. The reaction pathways were revealed by identification of reaction intermediates (Figure 4.S2), e.g. 1,4-hydroquinone, benzoquinone, and mineral acids. This is further confirmed by the decreased pH of the reaction solution from 5.9 (initial) to 3.3 when phenol was completely oxidized as

shown in Figure 4.S3. It is worth pointing out that the catalytic oxidation of phenol on AND-1000 with PS activation was much better than most popular metal oxides as indicated in Figure 4.3b. Nevertheless, the reaction rate of zero valent iron (ZVI) is slightly faster than that of AND-1000 with 100% phenol oxidation in 20 min, the severe deactivation (seen in Figure 4.S4) due to surface coverage of ferric hydroxide and irreversible leaching of excessive iron ions from ZVI significantly impede the application for green remediation. Such metal-free catalytic oxidation can also be used for effective degradation of an antibiotic (sulfachloropyridazine, SCP), dye (methylene blue, MB), and catechol (Figure 4.S5). Besides, total organic carbon (TOC) removal was evaluated in phenol solution and a simulated wastewater matrix (SW) as shown in Figure 4.S6, which indicated the great performance for organic mineralization in the AND-1000/PS system.

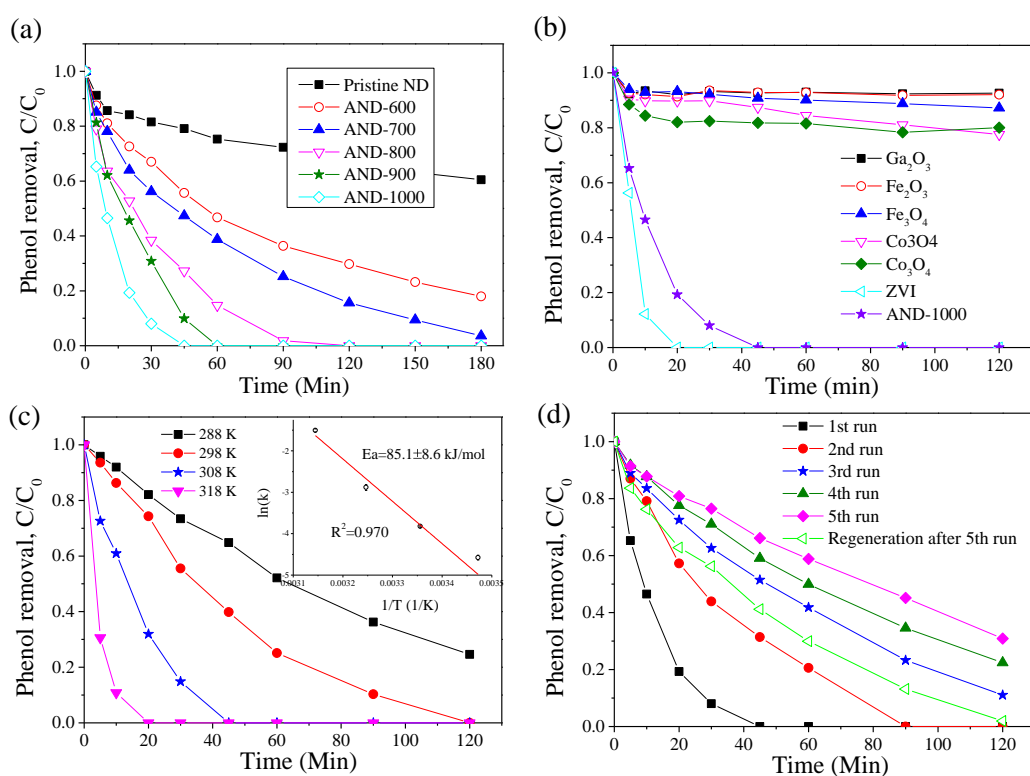


Figure 4.3. (a) Phenol oxidation with carbocatalysts, (b) PS activation on AND-1000, ZVI, and various metal oxides, (c) Influence of temperature on phenol oxidation (catalyst=0.1 g/L), and (d) Recyclability tests of AND-1000.

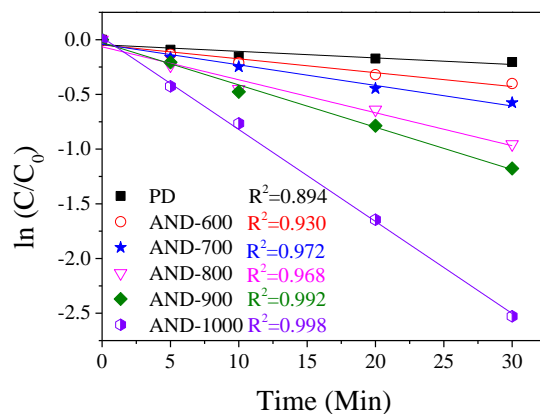


Figure 4.S1. Phenol oxidation with PS on various carbocatalysts.

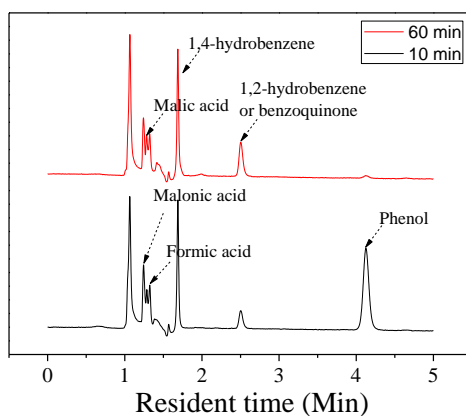


Figure 4.S2. Identification of intermediates during phenol oxidation with PS on AND-1000.

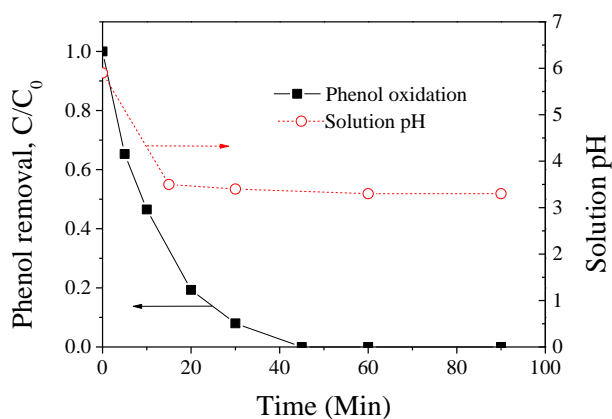


Figure 4.S3. Variation of pH in phenol solution during the oxidation in AND-1000.

The pristine nanodiamonds produced from the detonation method present a characteristic core/shell structure which is partially covered with soots and amorphous carbon and can be modified with versatile functional groups.(35, 36) The thermal

annealing processes are believed to be capable of removing the inert coatings, facilitating the formation of an onion-like graphitic shell due to the collapse and transformation of the diamond (001) surface.(31) The unique sp^3/sp^2 hybrids possess the chemical properties of graphene with various surface defects and can induce intricate interactions with the diamond core, thus having demonstrated excellent catalytic performances in various redox reactions such as oxygen reduction reaction (ORR), selective oxidation and oxidative dehydrogenation reactions.(28, 30, 31, 33) In this study, pristine NDs present a poor activity for PS activation. The dramatic improvement was achieved after the thermal annealing, suggesting that the graphitic shell structure of AND-1000 functionalized with the surface defects can effectively interact with PS for activation of O-O bond and generation of reactive species.

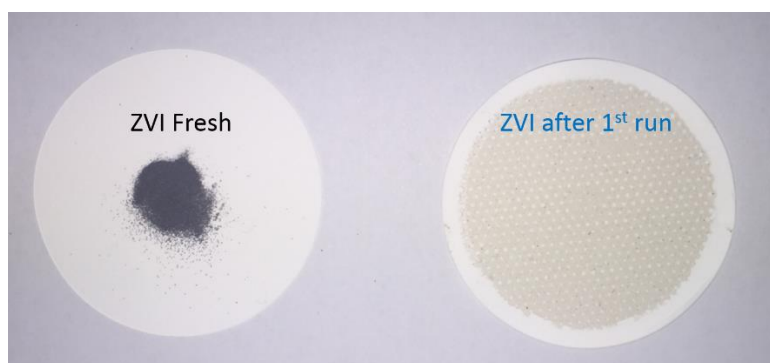


Figure 4.S4. ZVI deactivation after 1st run in activation of persulfate.

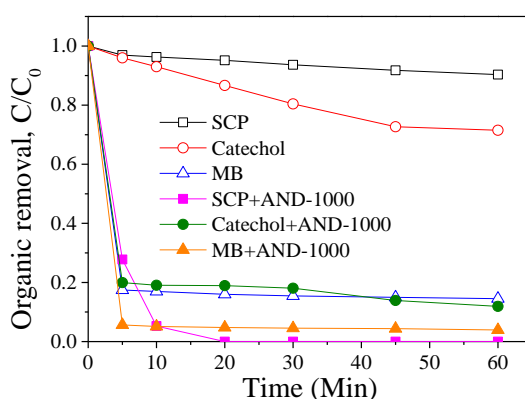


Figure 4.S5. Oxidative degradation of various organics by PS with and without AND-1000.

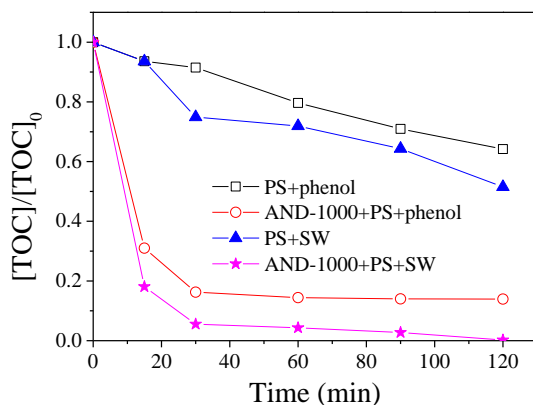


Figure 4.S6. Total organic carbon removal of AND-1000/PS in phenol solution ([phenol] = 20 ppm) and a simulated wastewater (SW) matrix ([phenol] = [SCP] = 10 ppm; [K⁺] = 6.5 mM; [Na⁺] = 3 mM; [NH₄⁺] = 2 mM; [NO₃⁻] = 2 mM; [Cl⁻] = [HCO₃⁻] = [H₂PO₄⁻] = 1 mM)

Electrochemical measurement was performed to probe the charge transfer process at the interface of water/PS/nanodiamond and compare the redox potential on different carbocatalysts. Electrochemical impedance spectroscopy (EIS) analysis in Figure 4.S7a indicates that AND-1000 presented a smaller semicircle diameter, suggesting the thermal annealing process considerably improved the charge transfer capability of the nanodiamond due to the formation of the sp²-hybridized graphitic shell. The cyclic voltammetry (CV) performance of nanodiamonds in Figure 4.S7b further demonstrates that AND-1000 presented a greater reduction capacity for chemical reactions and redox processes in PS (6.5 mM) and Na₂SO₄ (0.1 M) solutions.(37) Moreover, it is supposed that the PS activation process by NDs is similar to ORR on carbocatalysts, in which the O-O bonds in oxygen molecules are first activated by the carbon surface and then break up by obtaining electrons from the electrode to form H₂O₂ (two-electron pathway) or OH⁻ (four-electron pathway).(38, 39) The promoted ORR performance on the AND-1000 (Figure 4.S8) also confirmed the enhanced catalysis in charge transfer and O-O bond activation.

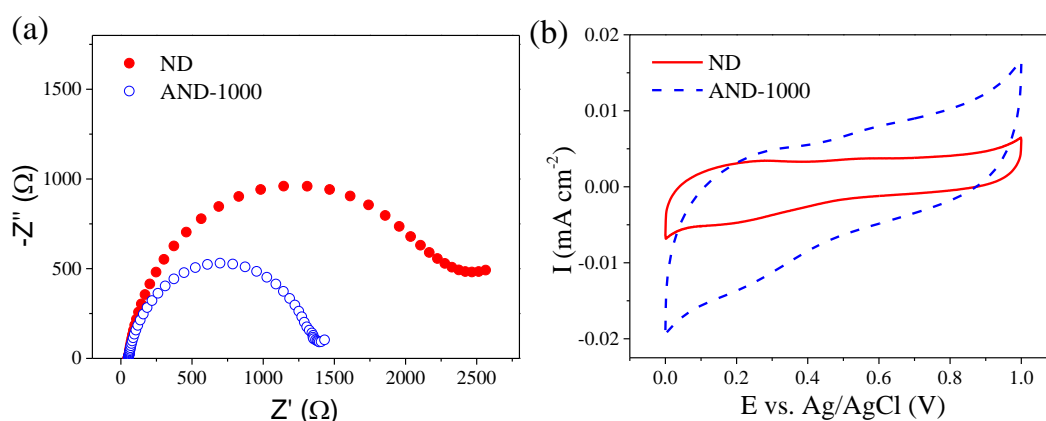


Figure 4.S7. (a) EIS plots of ND and AND-1000 electrodes recorded at -0.3 V vs. Ag/AgCl under the influence of an AC voltage of 5 mV amplitude in 0.1 M KOH solution; (b) CVs of ND and AND-1000 catalysts in PS and Na_2SO_4 solution after 10 cycles. (Scan rate: 50 mV s^{-1} , $[\text{Na}_2\text{SO}_4] = 0.1$ M, $[\text{PS}] = 6.5$ mM, RDE rotating rate: 0 rpm, N_2 saturated)

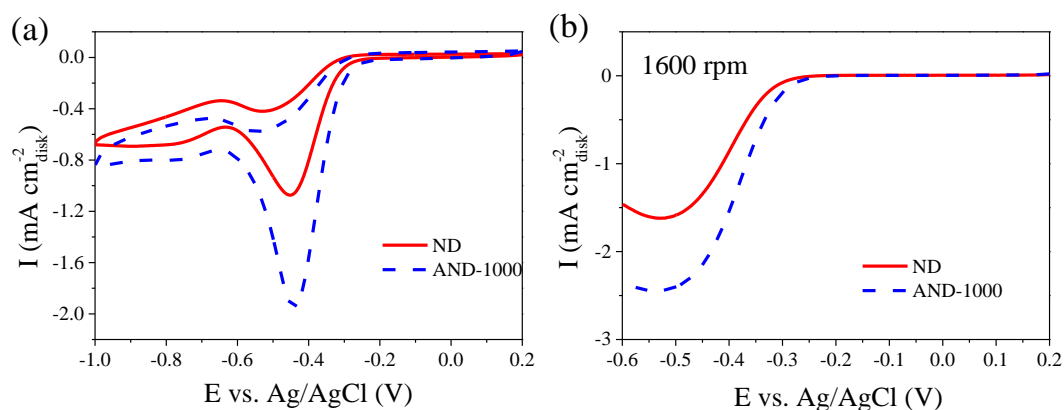
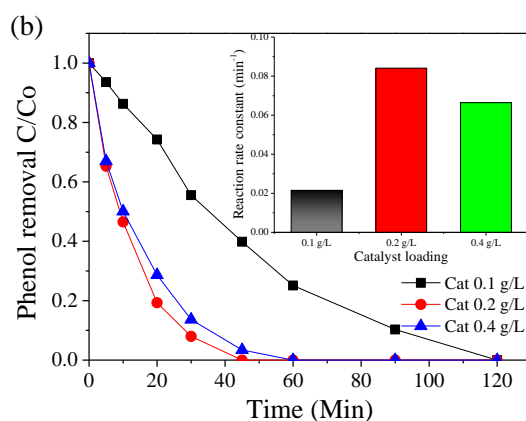
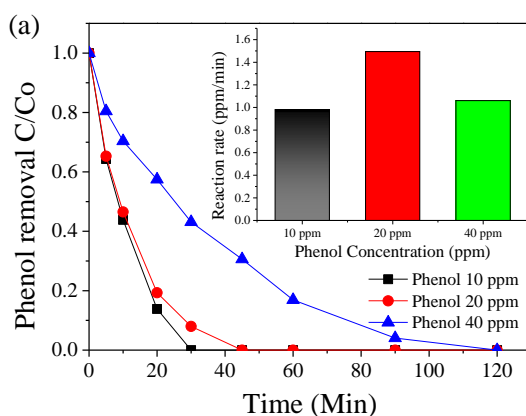


Figure 4.S8. (a) CVs of ORR on ND and AND-1000 catalysts in O_2 -saturated KOH solution. (Scan rate: 100 mV s^{-1} , $[\text{KOH}] = 0.1$ M) (b) LSVs of ORR on ND and AND-1000 catalysts in O_2 -saturated KOH solution. (Scan rate: 5 mV s^{-1} , RDE rotating rate: 1600 rpm, $[\text{KOH}] = 0.1$ M)

The effects of initial phenol concentration, catalyst loading, and dosage of PS on phenol degradation in corresponding kinetic behaviors are shown in Figures 4.S9. Different from initial phenol concentration and catalyst loading, the increase of PS loading shows a negligible influence on the degradation efficiency. As expected, the reaction rate increased with a higher phenol concentration (from 10 to 20 ppm), yet dropped slightly when excess phenol (40 ppm) was induced owing to the insufficiency

of the oxidant (PS). When the catalyst loading increased from 0.1 to 0.2 g/L, the reaction rate constant raised from 0.021 to 0.084 min^{-1} , then decreased to 0.066 min^{-1} at a loading 0.4 g/L catalyst. Generally, increasing the catalyst dosage can bring in more active sites, and then remarkably enhance the catalytic performance. In the AOPs, when over-abundant active sites are introduced, the oxidant (PS) can be rapidly activated to generate tremendous reactive radicals in a very short time. The excessive radicals will give rise to chain termination reactions by self-quenching, herein slowing down the degradation efficiency. Interestingly, different from initial phenol concentration and catalyst loading, the increase of PS shows a negligible influence on the degradation efficiency. This might be ascribed to the limited active sites (defects) on nanodiamonds during PS activation



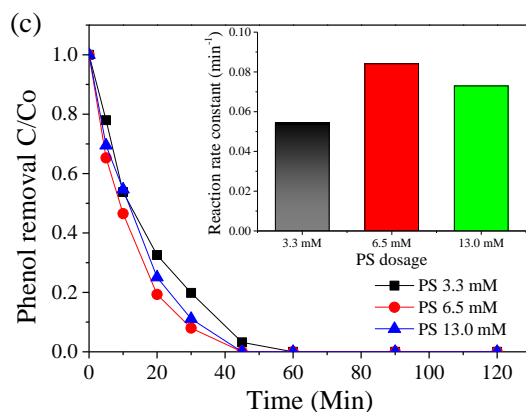


Figure 4.S9. Effects of (a) initial phenol concentration, (b) catalyst loading, and (c) dosage of PS on phenol removal.

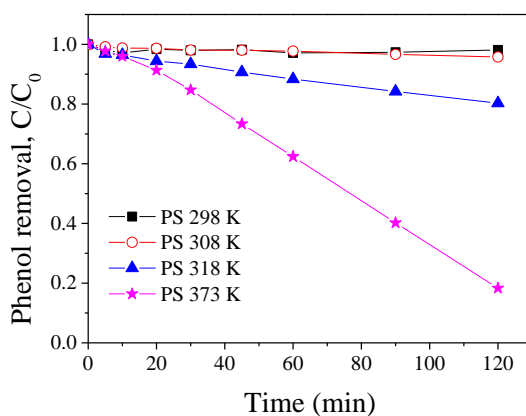


Figure 4.S10. Effect of temperature for PS activation without carbocatalysts.

Figure 4.3c indicates that 75.4% phenol removal was attained at 288 K in 120 min, while complete phenol oxidation was attained on AND-1000 at 298 K, and the time for complete phenol decomposition reduced to 45 and 20 min at 308 and 318 K, respectively. The influence of reaction temperature on PS activation by annealed nanodiamonds is more significant than that by graphene-based materials and carbon nanotubes reported before.(13, 15) The activation energy of phenol degradation on AND-1000 was evaluated to be 85.1 ± 8.1 kJ/mol, which is higher than that on the multi-walled carbon nanotubes (44.6 kJ/mol).(15) As physical approaches such as heat or UV are reported to be capable of activating PS to generate sulfate radicals for oxidation, the effect of reaction temperature without carbocatalysts is also provided in Figure 4.S10. It can be seen that the influence of temperature is insignificant giving 1.9 and 4.4% phenol oxidation in 120 min at 298 and 308 K, respectively, while 19.6

and 81.7% phenol removals were yielded at 318 and 373 K, respectively. Therein, the improved oxidative effectiveness at low temperature was mostly attributed to the enhanced catalytic effect of AND-1000/PS system. The sp^3 -hybridized core demonstrated a superior thermal conductance from the diamond core to the shell and was beneficial for endothermic processes for phenol adsorption and oxidation, meanwhile facilitating the electron conduction from the core to shell and charge transfer on the nanodiamond surface.(28)

In the previous studies, the reusability of metal catalysts for PS activation was rarely discussed, due to the irreversibility of homogeneous metal ions, severe metal-leaching and surface coverage of ferrous sulfate or ferric hydroxide on ZVI-based heterogeneous catalysts.(11, 40) The deactivation of the carbocatalysts is mainly due to the coverage of adsorbed intermediates, altered surface chemistry, minor change of pore structure, and oxidation or destruction of carbocatalysts in the highly oxidative environment with hydroxyl radicals.(41-43) Both XPS and FTIR spectra confirmed the increased oxygen level of the carbocatalyst (data not shown here) after the first run due to the surface oxidation and intermediates adsorption, meanwhile the SSA and pore volume slightly decreased owing to the change of pore structure and coverage of active sites. We recently observed that carbon nanotubes demonstrated excellent activity and reusability in PMS activation owing to the highly graphitic and curved graphene shell structure.(44) In this study, the AND-1000 demonstrated an excellent reusability providing 100% phenol oxidation in the 2nd run. Moreover, 89.0, 77.6, and 69.1% phenol removal efficiencies were attained in 120 min in the 3rd, 4th, and 5th runs, respectively (Figure 4.3d). The stability of the surface-tuned nanodiamond is much better than chemically modified graphene, carbon nanotubes, cubic ordered mesoporous carbon (CMK-8) and activated carbon.(16) The excellent stability of the annealed nanodiamonds might be ascribed to the robust core-shell (sp^3/sp^2) hybrid structure, which exhibits a great resistance to oxidation. The deactivated AND-1000 after the 5th run was regenerated with a thermal treatment (annealing at 573 K under nitrogen atmosphere for 1 h). The activity of passivated carbocatalyst was recovered with 98.1% phenol removal in 120 min due to the removal of adsorbed intermediates and tuning of oxidized diamond surface.

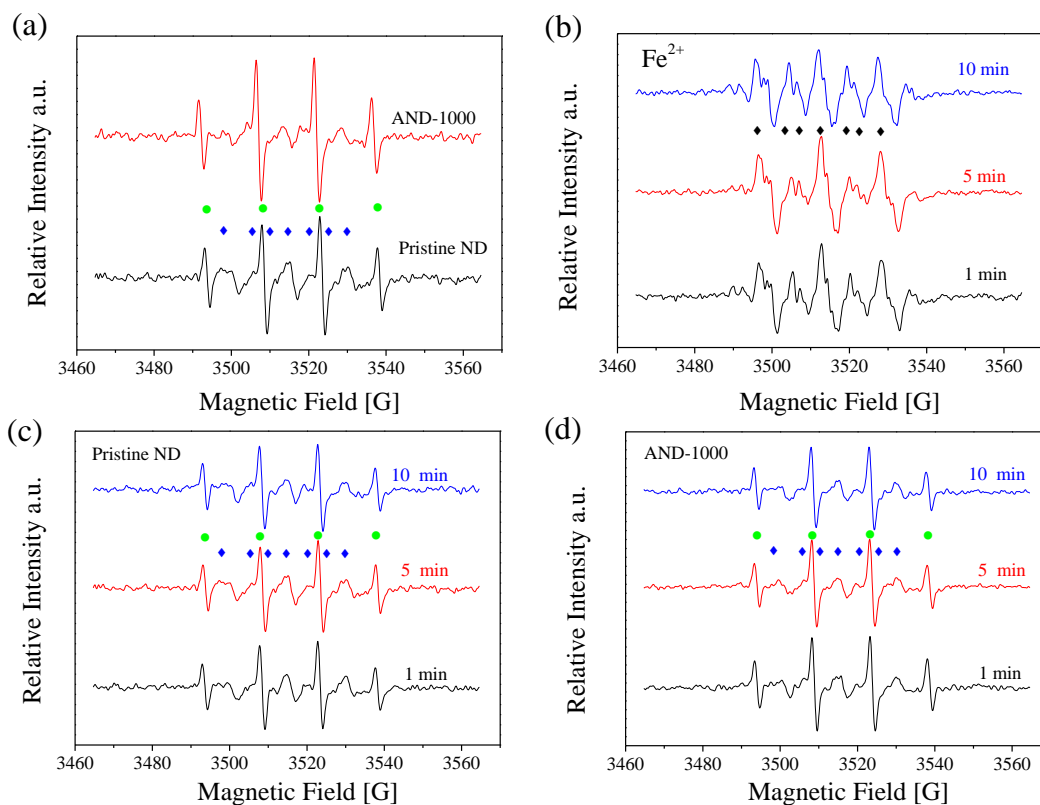
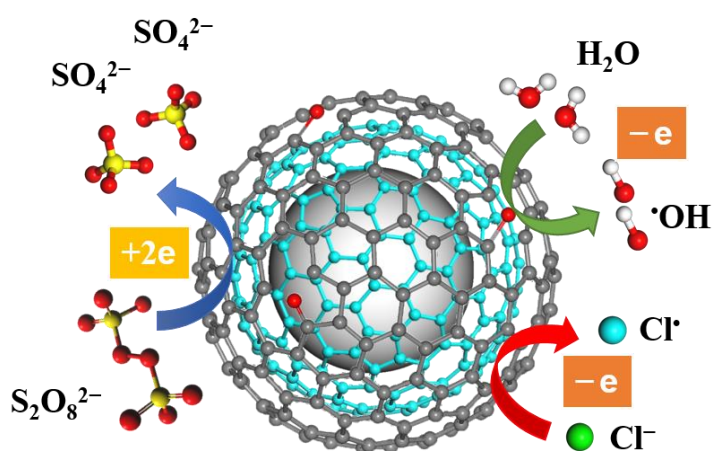


Figure 4.4. (a) Comparison of EPR spectra of PS activation on pristine nanodiamond and AND-1000. EPR spectra of active radicals induced by (b) homogeneous PS activation with Fe^{2+} and heterogeneous activation on (c) pristine NDs and (d) AND-1000. (●: DMPO-OH, ◆: DMPO-SO₄)

EPR was employed to *in situ* detect the active species produced from PS activation on nanodiamonds. Figure 4.4a indicates that the radical intensity of AND-1000 is higher than that of pristine nanodiamond, suggesting a better capability of the AND-1000 to activate PS to generate free radicals. It was already known that homogeneous Fe^{2+} /PS reaction would primarily produce sulfate radicals ($\text{SO}_4^{\bullet-}$) (Figure 4.4b). The persulfate radicals may also contribute to organic oxidation especially in the presence of O_2 which cannot be ruled out in this study.⁽⁴⁵⁾ Huang et al. also reported that EPR spectra in persulfate activated system change significantly due to the variation of PS/catalyst concentration and transition of major radical species ($\cdot\text{OH}$ and $\text{SO}_4^{\bullet-}$) along with the reaction time.⁽⁴⁶⁾ However, the nanodiamonds in this study were able to activate PS to mainly produce hydroxyl radicals ($\cdot\text{OH}$) and only minor amount of sulfate radicals were detected throughout the reaction (Figures 4.4 c and d). Since persulfate ($\text{SO}_3\text{-O-}$

O-SO₃) can be only decomposed to produce SO₄^{•-} and the transition from SO₄^{•-} to [•]OH should only contribute to a small portion of the produced [•]OH, the generation of hydroxyl radicals should be induced from water oxidation. We suppose that PS may be first activated by the graphitic shell and then oxidizes adsorbed water directly via one-electron transfer to generate hydroxyl radicals, while PS can get two electrons from carbocatalysts to produce two sulfate ions (SO₄²⁻) without the generation of sulfate radicals (SO₄^{•-}) as illustrated in Scheme 4.1. The phenomenon is intrinsically distinct from ferrous ions and ZVI systems.(16) In a recent study, we first carried out density functional theory (DFT) calculations to reveal the PS activation process on carbocatalysts.(47) We found that when water was presented adjacent to a persulfate molecule on the surface of carbocatalyst, the H-O bond in H₂O was significantly lengthened with greater tendency to donate electrons to the carbon matrix, meanwhile the persulfate molecule demonstrated enhanced adsorption energy, prolonged O-O bond, more charge transfer from the catalyst, suggesting the oxidation of water by PS and generation of hydroxyl radicals.



Scheme 4.1. Proposed mechanism of persulfate activation on annealed nanodiamonds.

To further verify the proposed process, the effect of solution pH on PS activation was investigated. Figure 4.5a shows that phenol degradation on AND-1000/PS system is favored at the basic condition and phenol oxidation efficiency enhances with the elevated pH values. Since a hydroxide ion with bare extra electrons is more easily to donate an electron to PS without activation of H-O bond compared with water molecules to form hydroxyl radicals, the higher pH is favorable for PS activation on a carbocatalyst. Moreover, AND-1000 remained a high catalytic activity for PS

activation in a much wider pH range (pH 2-11), compared with the conventional Fenton reactions (H_2O_2 , $\text{pH}<3$), ozone- (O_3), and peroxydisulfate- (neutral and basic conditions) based oxidative reactions.(18, 48, 49) It should be pointing out that the basic condition was also reported to be able to facilitate PS activation, not significant for phenol oxidation in this study though.(6) Besides, the formation of phenoate species in the basic condition may impact the reactivity of phenol and intermediates in the oxidative processes.

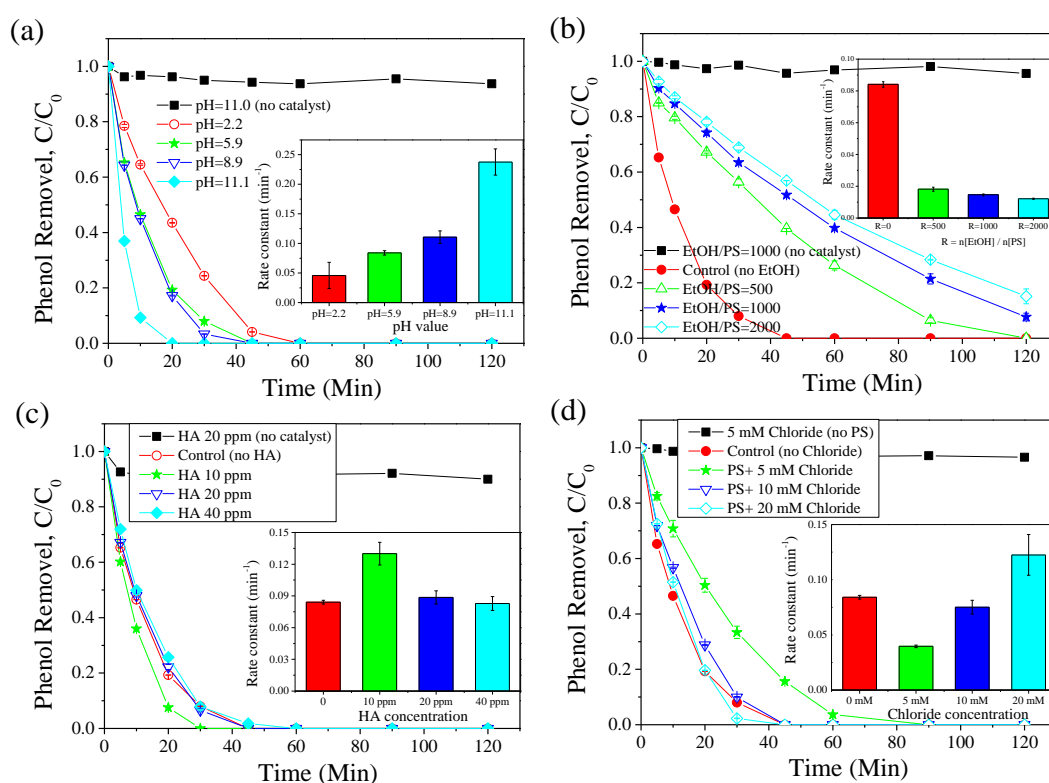


Figure 4.5. Influences of (a) pH, (b) ethanol, (c) humic acid, and (d) chloride on phenol oxidation with PS/AND-1000.

Recent studies indicated that nonradical oxidation might occur in PMS and PS activation and the existence of radical quenching agents did not remarkably affect the performances of organic decomposition in the oxidative systems.(44, 50) Figure 4.5b shows that phenol removal efficiency and reaction rate constants decreased dramatically at high ratios of ethanol (a scavenger of hydroxyl radicals), suggesting the critical roles of radicals in the oxidation. Moreover, when the aqueous solution was completely replaced with ethanol (only 1% water remaining introduced in phenol stock solution), the oxidation was almost completely terminated which is intrinsically

distinctive from the nonradical dominated processes (Figure 4.S11). It should be noteworthy that ethanol might also function as an electron donor (competing with water) to prevent the radical formation rather than a radical scavenger to donate one electron transfer to persulfate via AND surface, hereby slowing down the oxidation rate.

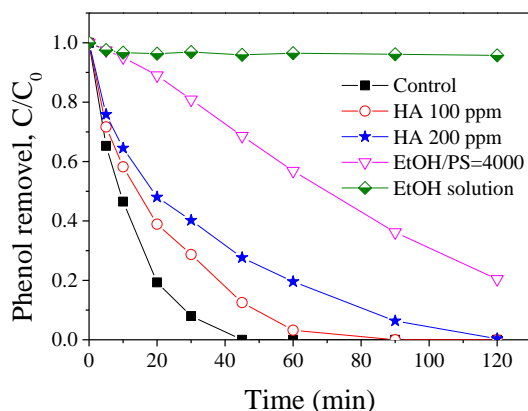


Figure 4.S11. Effects of high dose of HA and EtOH on phenol oxidation by PS activation AND-1000.

In a real wastewater matrix, the background organic matters and various radical scavengers would severely affect the organic degradation effectiveness.(20) Natural organic matters (NOMs), such as humic acid (HA), are rich in electrons and can serve as an oxidant scavenger to react with the reactive radicals, thus significantly decreasing the oxidation efficiency toward target contaminants. On the other hand, the NOMs with semiquinone radicals (phenols, quinones, and hydroquinones) are also reported to be able to mediate PMS and PS to generate $\cdot\text{OH}$ and $\text{SO}_4^{\cdot-}$.(8, 9, 12, 49) Figure 4.5c indicates that the presence of HA at low concentrations presented a marginal impact on PS activation and phenol oxidation on AND-1000. The PS/AND-1000 system showed high-efficiency in phenol removal from wastewater in the presence of natural organic matters though the hydroxyl radicals were reported to be non-selective.(20, 51) The PS/AND-1000 can generate a myriad of free radicals that are capable of attacking phenol and HA simultaneously. Moreover, the phenol removal efficiency degraded gradually with increasing addition of HA (Figure 4.S11) due to the competing reaction of HA with hydroxyl radicals (Figure 4.S12) and insufficiency of the oxidants.

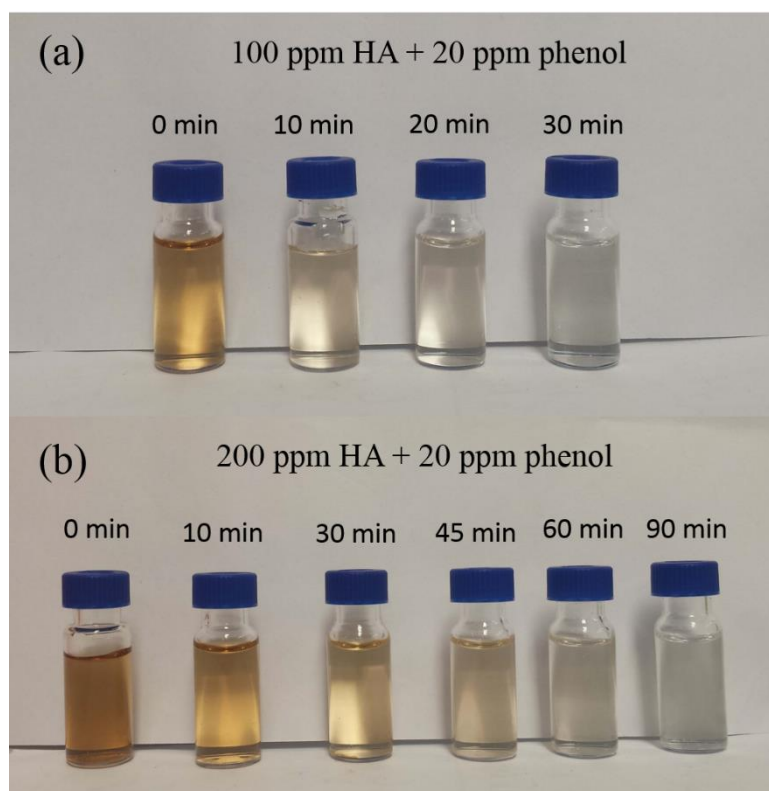


Figure 4.S12. Decolorization of HA and phenol solutions with PS on AND-1000. (Pure phenol solution is transparent)

The influence of chloride ions in solution on catalytic phenol degradation is shown in Figure 4.5d. The presence of a minor amount of chloride ions results in a declined efficiency of phenol degradation because the chloride ions scavenge most of the sulfate radicals and a small part of hydroxyl radicals to form Cl^\bullet and $\text{Cl}_2^{\bullet-}$, which are less reactive than $\text{SO}_4^{\bullet-}$ and $^\bullet\text{OH}$. However, superabundant chloride ions (Cl^-) in the solution will not only shield $\text{SO}_4^{\bullet-}$ and $^\bullet\text{OH}$, but also compete with the adsorbed water molecules to donate electrons on the carbon surface to PS to form Cl^\bullet (as indicated in Scheme 4.1) that subsequently combines another Cl^- to produce $\text{Cl}_2^{\bullet-}$. This procedure is similar to the hydroxyl radical generation via oxidizing water with PS on the carbocatalysts. Besides, the generated myriad amounts of $^\bullet\text{OH}$ can also react with Cl^- to produce Cl^\bullet and $\text{Cl}_2^{\bullet-}$ (Eq 4.3 ~ Eq 4.5) in an acid condition. The excess $\text{Cl}_2^{\bullet-}$ can mineralize the electron-rich phenol and intermediates such as diphenols and benzoquinone, giving rise to enhanced efficiency of phenol removal via H-abstraction and one-electron oxidation.(19-21) It should be pointing out that the halogenated compounds such as dichlorophenols and trichlorophenols, which are produced from phenol mineralization and similar to disinfection byproducts, are highly toxic and more

resistant to be degraded in the advanced oxidation. The process should be controlled and optimized in future applications.

4.4 Conclusions

In summary, annealed nanodiamonds were discovered to be able to activate PS to selectively produce hydroxyl radicals via water oxidation. Such emerging catalysis demonstrated potentials for overcoming the demerits of both sulfate and hydroxyl radical-based reactions. The annealed graphitic core-shell structure with versatile defects of ANDs provides a fantastic environment for oxygen and PS activation by serving as a superb bridge for charge transfer. Besides, the intricate interactions of sp^2 and sp^3 interfaces via conjugation effects are able to induce electron conduction from the nanodiamond core to shell surface, further enhancing the O-O breakup efficiency. Thus, AND/PS provides an excellent route for organic oxidation, which can be applied for contaminant decomposition and selective oxidation reactions by carbocatalysis. As ANDs are mainly synthesized via a detonation method and modified with thermal treatments, the high-cost of the carbocatalysts compared with conventional transition metals or metal oxides severely limits their wide application to environmental engineering. Thus, state-of-the-art strategies are still needed to be developed for preparation of efficient and cheap diamond-based carbocatalysts. In regard to future environmental implications, the novel oxidative system (PS/AND) should be evaluated for degradation of versatile persistent contaminants such as antibiotics (e.g. SCP in this study), pharmaceuticals, personal-care products, and endocrine disruption compounds. Moreover, the interference and impact of various natural organic matters (e. g. HA), radical scavengers (halogen ions) and potential byproducts should also be evaluated in the future studies.

References

1. Navalon S, Martin R, Alvaro M, Garcia H. Gold on diamond nanoparticles as a highly efficient fenton catalyst. *Angew. Chem. Int. Ed.* 2010; 49(45):8403-7.
2. Ensing B, Buda F, Blochl P, Baerends EJ. Chemical involvement of solvent water molecules in elementary steps of the fenton oxidation reaction. *Angew. Chem. Int. Ed.* 2001; 40(15):2893-5.

3. Liu XW, Sun XF, Li DB, Li WW, Huang YX, Sheng GP, et al. Anodic Fenton process assisted by a microbial fuel cell for enhanced degradation of organic pollutants. *Water Res.* 2012; 46(14):4371-8.
4. Anipsitakis GP, Dionysiou DD. Degradation of organic contaminants in water with sulfate radicals generated by the conjunction of peroxymonosulfate with cobalt. *Environ. Sci. Technol.* 2003; 37(20):4790-7.
5. Zhang T, Chen Y, Wang YR, Le Roux J, Yang Y, Croue JP. Efficient peroxydisulfate activation process not relying on sulfate radical generation for water pollutant degradation. *Environ. Sci. Technol.* 2014; 48(10):5868-75.
6. Furman OS, Teel AL, Watts RJ. Mechanism of base activation of persulfate. *Environ. Sci. Technol.* 2010; 44(16):6423-8.
7. Kronholm J, Riekkola ML. Potassium persulfate as oxidant in pressurized hot water. *Environ. Sci. Technol.* 1999; 33(12):2095-9.
8. Fang GD, Gao J, Dionysiou DD, Liu C, Zhou DM. Activation of persulfate by quinones: free radical reactions and implication for the degradation of PCBs. *Environ. Sci. Technol.* 2013; 47(9):4605-11.
9. Ahmad M, Teel AL, Watts RJ. Mechanism of persulfate activation by phenols. *Environ. Sci. Technol.* 2013; 47(11):5864-71.
10. Ahn S, Peterson TD, Righter J, Miles DM, Tratnyek PG. Disinfection of ballast water with iron activated persulfate. *Environ. Sci. Technol.* 2013; 47(20):11717-25.
11. Drzewicz P, Perez-Estrada L, Alpatova A, Martin JW, El-Din MG. Impact of peroxydisulfate in the presence of zero valent iron on the oxidation of cyclohexanoic acid and naphthenic acids from oil sands process-affected water. *Environ. Sci. Technol.* 2012; 46(16):8984-91.
12. Fang GD, Liu C, Gao J, Dionysiou DD, Zhou DM. Manipulation of persistent free radicals in biochar to activate persulfate for contaminant degradation. *Environ. Sci. Technol.* 2015; 49(9):5645-53.
13. Duan XG, Ao ZM, Sun HQ, Indrawirawan S, Wang YX, Kang J, et al. Nitrogen-doped graphene for generation and evolution of reactive radicals by metal-free catalysis. *ACS Appl. Mater. Interfaces.* 2015; 7(7):4169-78.
14. Sun HQ, Liu SZ, Zhou GL, Ang HM, Tade MO, Wang SB. Reduced graphene oxide for catalytic oxidation of aqueous organic pollutants. *ACS Appl. Mater. Interfaces.* 2012; 4(10):5466-71.
15. Sun HQ, Kwan C, Suvorova A, Ang HM, Tade MO, Wang SB. Catalytic oxidation of organic pollutants on pristine and surface nitrogen-modified carbon nanotubes with sulfate radicals. *Appl. Catal., B.* 2014; 154:134-41.
16. Duan XG, Sun HQ, Kang J, Wang YX, Indrawirawan S, Wang SB. Insights into heterogeneous catalysis of persulfate activation on dimensional-structured nanocarbons. *ACS Catal.* 2015; 5(8):4629-36.

17. Sun HQ, Wang YX, Liu SZ, Ge L, Wang L, Zhu ZH, et al. Facile synthesis of nitrogen doped reduced graphene oxide as a superior metal-free catalyst for oxidation. *Chem. Commun.* 2013; 49(85):9914-6.
18. Yang Y, Jiang J, Lu X, Ma J, Liu Y. Production of sulfate radical and hydroxyl radical by reaction of ozone with peroxymonosulfate: a novel advanced oxidation process. *Environ. Sci. Technol.* 2015; 49(12):7330-9.
19. Anipsitakis GP, Dionysiou DD, Gonzalez MA. Cobalt-mediated activation of peroxymonosulfate and sulfate radical attack on phenolic compounds. Implications of chloride ions. *Environ. Sci. Technol.* 2006; 40(3):1000-7.
20. Grebel JE, Pignatello JJ, Mitch WA. Effect of halide ions and carbonates on organic contaminant degradation by hydroxyl radical-based advanced oxidation processes in saline waters. *Environ. Sci. Technol.* 2010; 44(17):6822-8.
21. Yang Y, Pignatello JJ, Ma J, Mitch WA. Comparison of halide impacts on the efficiency of contaminant degradation by sulfate and hydroxyl radical-based advanced oxidation processes (AOPs). *Environ. Sci. Technol.* 2014; 48(4):2344-51.
22. Sun X, Ding Y, Zhang B, Huang R, Chen D, Su DS. Insight into the enhanced selectivity of phosphate-modified annealed nanodiamond for oxidative dehydrogenation reactions. *ACS Catal.* 2015; 5(4):2436-44.
23. Osswald S, Yushin G, Mochalin V, Kucheyev SO, Gogotsi Y. Control of sp²/sp³ carbon ratio and surface chemistry of nanodiamond powders by selective oxidation in air. *J. Am. Chem. Soc.* 2006; 128(35):11635-42.
24. El Tall O, Hou YF, Abou-Hamad E, Raja IU, Hedhili MN, Peng W, et al. Direct functionalization of nanodiamonds with maleimide. *Chem. Mater.* 2014; 26(9):2766-9.
25. Zhu D, Zhang LH, Ruther RE, Hamers RJ. Photo-illuminated diamond as a solid-state source of solvated electrons in water for nitrogen reduction. *Nat. Mater.* 2013; 12(9):836-41.
26. Jang DM, Myung Y, Im HS, Seo YS, Cho YJ, Lee CW, et al. Nanodiamonds as photocatalysts for reduction of water and graphene oxide. *Chem. Commun.* 2012; 48(5):696-8.
27. Wen GD, Wu SC, Li B, Dai CL, Su DS. Active sites and mechanisms for direct oxidation of benzene to phenol over carbon catalysts. *Angew. Chem. Int. Ed.* 2015; 54(13):4105-9.
28. Zhang JA, Su DS, Blume R, Schlogl R, Wang R, Yang XG, et al. Surface chemistry and catalytic reactivity of a nanodiamond in the steam-free dehydrogenation of ethylbenzene. *Angew. Chem. Int. Ed.* 2010; 49(46):8640-4.
29. Zhang J, Su DS, Zhang AH, Wang D, Schlogl R, Hebert C. Nanocarbon as robust catalyst: Mechanistic insight into carbon-mediated catalysis. *Angew. Chem. Int. Ed.* 2007; 46(38):7319-23.

30. Liu X, Frank B, Zhang W, Cotter TP, Schlogl R, Su DS. Carbon-catalyzed oxidative dehydrogenation of n-butane: selective site formation during sp(3)-to-sp(2) lattice rearrangement. *Angew. Chem. Int. Ed.* 2011; 50(14):3318-22.
31. Lin YM, Su DS. Fabrication of nitrogen-modified annealed nanodiamond with improved catalytic activity. *ACS Nano.* 2014; 8(8):7823-33.
32. Turner S, Lebedev OI, Shenderova O, Vlasov II, Verbeeck J, Van Tendeloo G. Determination of size, morphology, and nitrogen impurity location in treated detonation nanodiamond by transmission electron microscopy. *Adv. Funct. Mater.* 2009; 19(13):2116-24.
33. Lin YM, Pan XL, Qi W, Zhang BS, Su DS. Nitrogen-doped onion-like carbon: a novel and efficient metal-free catalyst for epoxidation reaction. *J. Mater. Chem. A.* 2014; 2(31):12475-83.
34. Kuznetsov VL, Chuvilin AL, Butenko YV, Stankus SV, Khairulin RA, Gutakovskii AK. Closed curved graphite-like structures formation on micron-size diamond. *Chem. Phys. Lett.* 1998; 289(3-4):353-60.
35. Mochalin VN, Shenderova O, Ho D, Gogotsi Y. The properties and applications of nanodiamonds. *Nat. Nanotechnol.* 2012; 7(1):11-23.
36. Krueger A. The structure and reactivity of nanoscale diamond. *J. Mater. Chem.* 2008; 18(13):1485-92.
37. Ren YM, Lin LQ, Ma J, Yang J, Feng J, Fan ZJ. Sulfate radicals induced from peroxydisulfate by magnetic ferromagnetic spinel MFe₂O₄ (M = Co, Cu, Mn, and Zn) as heterogeneous catalysts in the water. *Appl. Catal., B* 2015; 165:572-8.
38. Zheng Y, Jiao Y, Chen J, Liu J, Liang J, Du A, et al. Nanoporous graphitic-C₃N₄@carbon metal-free electrocatalysts for highly efficient oxygen reduction. *J. Am. Chem. Soc.* 2011; 133(50):20116-9.
39. Zhao Y, Yang LJ, Chen S, Wang XZ, Ma YW, Wu Q, et al. Can boron and nitrogen co-doping improve oxygen reduction reaction activity of carbon nanotubes? *J. Am. Chem. Soc.* 2013; 135(4):1201-4.
40. Al-Shamsi MA, Thomson NR. Treatment of Organic Compounds by activated persulfate using nanoscale zerovalent iron. *Ind. Eng. Chem. Res.* 2013; 52(38):13564-71.
41. Duan XG, O'Donnell K, Sun HQ, Wang YX, Wang SB. Sulfur and nitrogen co-doped graphene for metal-free catalytic oxidation reactions. *Small.* 2015; 11(25):3036-44.
42. Hou WC, BeigzadehMilani S, Jafvert CT, Zepp RG. Photoreactivity of unfunctionalized single-wall carbon nanotubes involving hydroxyl radical: chiral dependency and surface coating effect. *Environ. Sci. Technol.* 2014; 48(7):3875-82.

43. Radich JG, Krenselewski AL, Zhu JD, Kamat PV. Is Graphene a stable platform for photocatalysis? mineralization of reduced graphene oxide with uv-irradiated TiO₂ nanoparticles. Chem. Mater. 2014; 26(15):4662-8.
44. Duan XG, Sun HQ, Wang YX, Kang J, Wang SB. N-doping-induced nonradical reaction on single-walled carbon nanotubes for catalytic phenol oxidation. ACS Catal. 2015; 5(2):553-9.
45. Clarke K, Edge R, Land EJ, Navaratnam S, Truscott TG. The sulphate radical is not involved in aqueous radiation oxidation processes. Radiat. Phys. Chem. 2008; 77(1):49-52.
46. Huang ZF, Bao HW, Yao YY, Lu WY, Chen WX. Novel green activation processes and mechanism of peroxymonosulfate based on supported cobalt phthalocyanine catalyst. Appl. Catal., B 2014; 154:36-43.
47. Duan X, Ao Z, Sun H, Zhou L, Wang G, Wang S. Insights into N-doping in single-walled carbon nanotubes for enhanced activation of superoxides: a mechanistic study. Chem. Commun. 2015; 51(83):15249-52.
48. Zhang T, Zhu HB, Croue JP. Production of Sulfate Radical from peroxymonosulfate induced by a magnetically separable CuFe₂O₄ spinel in water: efficiency, stability, and mechanism. Environ. Sci. Technol. 2013; 47(6):2784-91.
49. Guan YH, Ma J, Ren YM, Liu YL, Xiao JY, Lin LQ, et al. Efficient degradation of atrazine by magnetic porous copper ferrite catalyzed peroxymonosulfate oxidation via the formation of hydroxyl and sulfate radicals. Water Res. 2013; 47(14):5431-8.
50. Lee H, Lee HJ, Jeong J, Lee J, Park NB, Lee C. Activation of persulfates by carbon nanotubes: Oxidation of organic compounds by nonradical mechanism. Chem. Eng. J. 2015; 266:28-33.
51. Lee H, Yoo HY, Choi J, Nam IH, Lee S, Lee S, et al. Oxidizing capacity of periodate activated with iron-based bimetallic nanoparticles. Environ. Sci. Technol. 2014; 48(14):8086-93.

Every reasonable effort has been made to acknowledge the owners of copyright material. I would be pleased to hear from any copyright owner who has been omitted or incorrectly acknowledged.

Chapter 5. Nitrogen-Doped Graphene for Generation and Evolution of Reactive Radicals by Metal-Free Catalysis

Abstract

N-doped graphene (NG) nanomaterials were synthesized by directly annealing graphene oxide (GO) with a novel nitrogen precursor of melamine. A high N doping level, 8-11 at.%, was achieved at a moderate temperature. The sample of NG-700, obtained at a calcination temperature of 700 °C, showed the highest efficiency in degradation of phenol solutions by metal-free catalytic activation of peroxymonosulfate (PMS). The catalytic activity of the nitrogen doped rGO (NG-700) was about 80 times higher than un-doped rGO in phenol degradation. Moreover, the activity of NG-700 was 18.5 times higher than the most popular metal-based catalyst of nanocrystalline Co_3O_4 in PMS activation. Theoretical calculations using spin-unrestricted density functional theory (DFT) were carried out to probe the active sites for PMS activation on N-doped graphene. In addition, experimental detection of generated radicals using electron paramagnetic resonance (EPR) and competitive radical reactions were performed to reveal the PMS activation processes and pathways of phenol degradation on nanocarbons. It was observed that both $\cdot\text{OH}$ and $\text{SO}_4^{\cdot-}$ existed in the oxidation processes and played critical roles in phenol oxidation.

5.1 Introduction

In the past two decades, nanocarbons such as carbon nanotubes (CNTs), graphene oxide (GO), reduced graphene oxide (rGO), graphene, graphitic carbon nitride (g-C₃N₄) and other graphene-like materials have attracted worldwide attention, owing to the large theoretical surface area, high thermal conductivity, unique electronic property, and sp²-hybridized carbon configuration.(1-3) Studies on metal-free catalysis have demonstrated that nanocarbons can play promising roles in various catalytic processes for energy and environmental applications.(4-6) The employment of nanocarbons in water treatment as an alternative to metal-based catalysts, such as Co, Fe or Mn, is expected to completely avoid metal leaching and the associated secondary contamination. However, current applications of metal-free catalysis are mainly for energy and chemical synthesis,(7, 8) and metal-free remediation has been less explored.

As one of advanced oxidation processes (AOPs), catalytic oxidation by sulfate radicals (SO₄^{•-}) from peroxymonosulfate (PMS) has been applied to decompose the hazardous organic compounds in wastewater. Compared to hydroxyl radicals (•OH) in Fenton reaction, SO₄^{•-} demonstrated a higher oxidative potential (2.5-3.1 V vs 2.7 V of •OH), and can adapt to a wide pH range.(9) Homogeneous Co(II)/PMS and Mn(II)/PMS systems have been proven to be highly effective to generate active radicals for the AOPs.(9, 10) Nevertheless, the loss of toxic metals leads to severe environmental issues, giving rise to high risks to human beings. Heterogeneous catalysis using cobalt oxides,(11) supported cobalt oxides,(12) or manganese oxides(13) has been investigated, yet leaching is still inevitable. Therefore, novel metal-free catalysts with high catalytic efficiency are urgently required in terms of green catalysis for wastewater remediation.

In pioneering studies, we found that rGO prepared by a hydrothermal method can effectively promote PMS activation to generate active radicals for degradation of phenol, chlorophenols, and dyes in aqueous solution.(14) It was also found that the zigzag edges and ketonic groups (C=O) on the edges of graphene might be the active sites for PMS activation. The delocalized electrons at the zigzag edges and little amount of oxygen-containing groups with rich electrons can present a great potential for the redox process.(15, 16) To improve the catalytic performance, structural

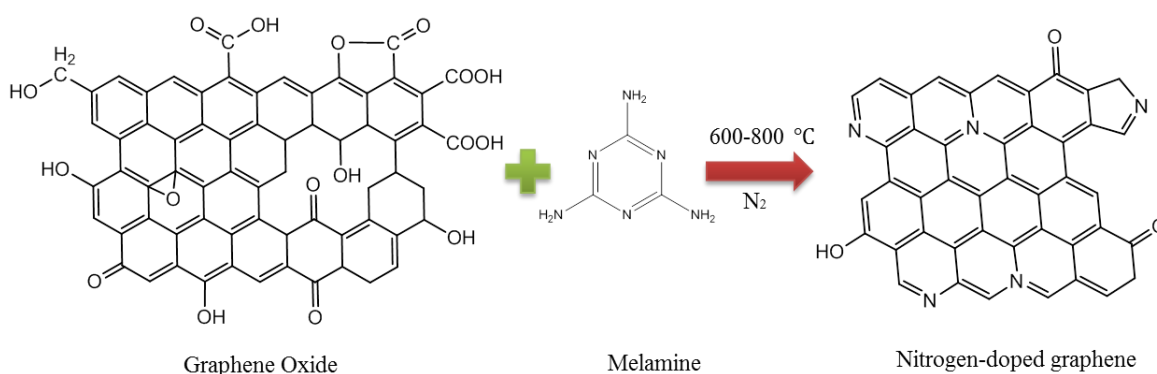
modification was carried out by physical and/or chemical activation of rGO.(17, 18) The specific surface area (SSA) of rGO can be increased from 200 to 1200 m²/g and the activated porous rGO demonstrated to be highly effective for adsorptive and oxidative removal of phenol and methylene blue (MB) in water. The studies also suggested that both oxygen groups and SSA played key roles in adsorption and catalytic oxidation of MB.(17)

It was expected that chemically compositional modification would bring out instinct changes to nanocarbons, more significant than structural modification. It has been reported that doping heteroatoms (e.g. N, B and P) into the carbon honeycomb network can create more active sites and bring in new properties such as increasing the electrochemical catalytic activity, hydrophilicity, and higher selectivity towards oxidative dehydrogenation (ODH) reaction and oxygen reduction reaction (ORR).(16, 19) In environmental remediation, we proved that modification of rGO and pristine multi-walled carbon nanotubes (MWCNTs) with nitrogen atoms using ammonium nitrate as the N precursor can dramatically boost the performance of PMS activation.(20, 21) The SSA of N-rGO-350 was found to be as low as 64.1 m²/g, and the nitrogen doping level was 5.61 at.%.

In this study, we presented a simple thermal process for synthesis of rGO with both structural and compositional modification. The prepared N-doped graphene (NG) presented a larger SSA (227.5 m²/g) and a higher N doping level (9.68 at.%). A stunning 80-fold enhancement was achieved on NG-700 in catalytic oxidation of phenol solutions compared with unmodified rGO. N-doped rGO also showed superior performance to g-C₃N₄, graphene nanosheets (GNs), rGO, single-walled carbon nanotube (SWCNT), N-doped graphene and carbon nanotube utilizing ammonium nitrate as a nitrogen precursor, and a typical metal-based catalyst of crystalline Co₃O₄. Computational studies, electron paramagnetic resonance (EPR) spectra and competitive radical reactions facilitated the first insights into the mechanism of PMS activation by the nanocarbons and the evolution of sulfate radicals in phenol oxidation.

5.2 Experimental Section

Materials and Chemicals. Graphite powder (purity 99.9995%), potassium permanganate (KMnO_4), sulphuric acid (95-97%), and potassium peroxydisulfate ($2\text{KHSO}_5 \cdot 3\text{KHSO}_4 \cdot \text{K}_2\text{SO}_4$, Oxone[®]) were purchased from Sigma-Aldrich. Hydrogen peroxide (30%, H_2O_2) was obtained from Chem-Supply. Phenol was obtained from Ajax Finechem. 5,5-Dimethyl-1-pyrroline (DMPO, >99.0%) was obtained from Fluka. The multi-walled carbon nanotubes (MWCNTs), single-walled carbon nanotubes (SWCNTs) and graphene nanosheets (GNs) were purchased from Chengdu Organic Chemical, China. All chemicals were used as received without further purification.



Scheme 5.1. Synthesis procedure of N-doped graphene.

Synthesis of Nitrogen-Doped Graphene. Graphite oxide (GO) was synthesized through a modified Hummers' method (22) and used for preparation of N-doped rGO. The preparation procedure is shown in Scheme 5.1. In a typical synthesis, GO (1.0 g) was dissolved in 50 mL of ethanol, stirred for 30 min and sonicated for another 30 min. Then melamine (1.0 g) was added to the mixed solution and then the suspension was heated to 50 °C on a hotplate to evaporate the ethanol gradually whilst stirring. The dried mixture was first heated in a muffle furnace at 450 °C and then in a tubular furnace for further calcination at 600, 700, and 800 °C for 1 h under N_2 atmosphere to obtain NG-600, -700 and -800, respectively. The samples were washed with ultrapure water and ethanol for several times and dried in an oven at 60 °C overnight. Thus, the nitrogen-doped graphene (NG) was obtained.

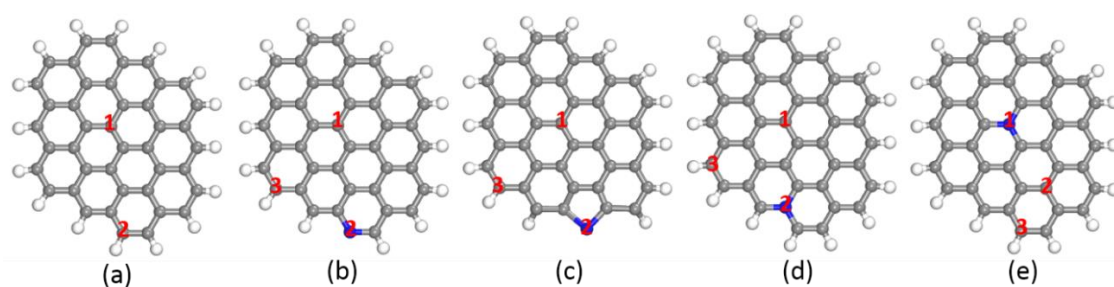
Characterization of Materials. X-ray diffraction (XRD) patterns were acquired on a D8-Advanced diffractometer system from Bruker with $\text{Cu-K}\alpha$ radiation ($\lambda=1.5418 \text{ \AA}$).

Fourier transform infrared spectra (FTIR) were obtained from a Bruker instrument with ATR correction mode. Thermogravimetric-differential thermal analysis (TG-DTA) was recorded on a Perkin-Elmer Diamond thermal analyzer with a heating rate of 10 °C/min in air. The Brunauer-Emmett-Teller (BET) equation and Barrett-Joyner-Halenda (BJH) method were utilized to evaluate the specific surface area and pore size distribution of the carbon materials, respectively. Total organic carbon (TOC) was measured on a Shimadzu TOC-vcph analyzer. Raman spectra were obtained by using an ISA argon-laser Raman spectrometer. X-ray photoelectron microscopy (XPS) was conducted on a Thermo Escalab 250 using an Al-K α X-ray source to detect the elemental composition of carbon materials. The morphological information of scanning electronic microscopy (SEM) image was analyzed on a Zeiss Neon 40EsV FIBSEM. Electron paramagnetic resonance (EPR) from a Bruker EMS-plus was applied to probe the reactive radicals generated during activation of PMS captured by a spin trapping agent 5,5-dimethylpyrroline-oxide (DMPO), operating with center field of 3515G, sweep width of 100G, microwave frequency of 9.86 GHz, power setting of 18.75 mW, and scan number of 3. The EPR spectra were analyzed by the spin-fitting package of Bruker Xeon software.

Evaluation of Phenol Catalytic Oxidation. The catalytic oxidation of phenol was performed in a 250 mL conical flask with phenol solution (20 ppm), catalyst (0.1 g/L) and PMS (2 g/L) in a constant temperature controlled water bath for the kinetic study. During each time interval, 1 mL solution was withdrawn by a syringe, filtered by a 0.45 μ m Millipore film, and injected into a vial. Then 0.5 mL of methanol was also injected into the reaction solution as a quenching reagent. The mixed solution was analyzed by a high performance liquid chromatography (HPLC, Varian). The organics were separated by a C-18 column and analyzed by a UV detector (270 nm). The mobile phase was made of 30% acetonitrile and 70% ultrapure water and at a flowrate of 1 mL/min. The intermediates tests were carried out with a flowrate of 0.1 mL/min at 220 nm.

Computational Models and Methodology. The spin-unrestricted density functional theory (DFT) calculations were carried out using the Dmol³ package.⁽²³⁾ Exchange-correlation functions were taken as generalized gradient approximation

(GGA) with Perdew–Burke–Ernzerhof (PBE).(24) Double numerical plus polarization (DNP) was employed as the basis set. The convergence tolerance of energy of 10^{-5} Hartree was applied (1 Hartree = 27.21 eV), and the maximal allowed force and displacement were 0.002 Hartree/Å and 0.005 Å, respectively. In the simulation, non-periodic graphene cluster was employed in the calculation, as shown in Scheme 5.2 below. The DFT+D method within the Grimme scheme(25) was used in all calculations to take the van der Waals forces into account.



Scheme 5.2 Atomic structures of graphene before and after N doping. Pristine graphene (a) and graphene with different doping types ((b)-pyridinic N, (c)-pyrrolic N, and (d), (e)-graphitic N) are considered. The numbers indicate the adsorption sites of the H atom we considered. In this figure, the grey, white and blue balls are C, H and N atoms, respectively.

5.3 Results and Discussions

5.3.1 Characterization of Carbon Materials.

XRD patterns of GO and nitrogen doped rGO samples are shown in Figure 5.1. The strong peak at $2\theta = 10.2^\circ$ is corresponding to the graphene oxide (002) reflection, demonstrating that a well-ordered and layered structure of GO is formed. The interlayer space (0.86 nm) is larger than that of pristine graphite (0.34 nm), indicating that the oxygen groups were introduced into the graphitic layer and the C=C double bonds were formed. After reduction, the peak at $2\theta = 10.2^\circ$ disappeared and a small sharp peak at $2\theta = 25.1^\circ$ emerged. The XRD patterns also showed that the degree of crystallinity (peak intensity) of the nitrogen-doped graphene increased with elevated temperature, while the peak was shifted to a higher 2θ degree, implying a better reducibility owing to removal of surface functional groups and that nitrogen atoms were successfully doped into the graphitic system.(26)

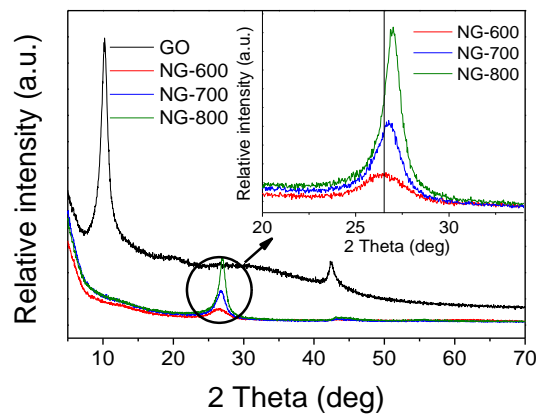


Figure 5.1. XRD patterns of GO and N doped rGO. Inset: high-resolution of graphite phase.

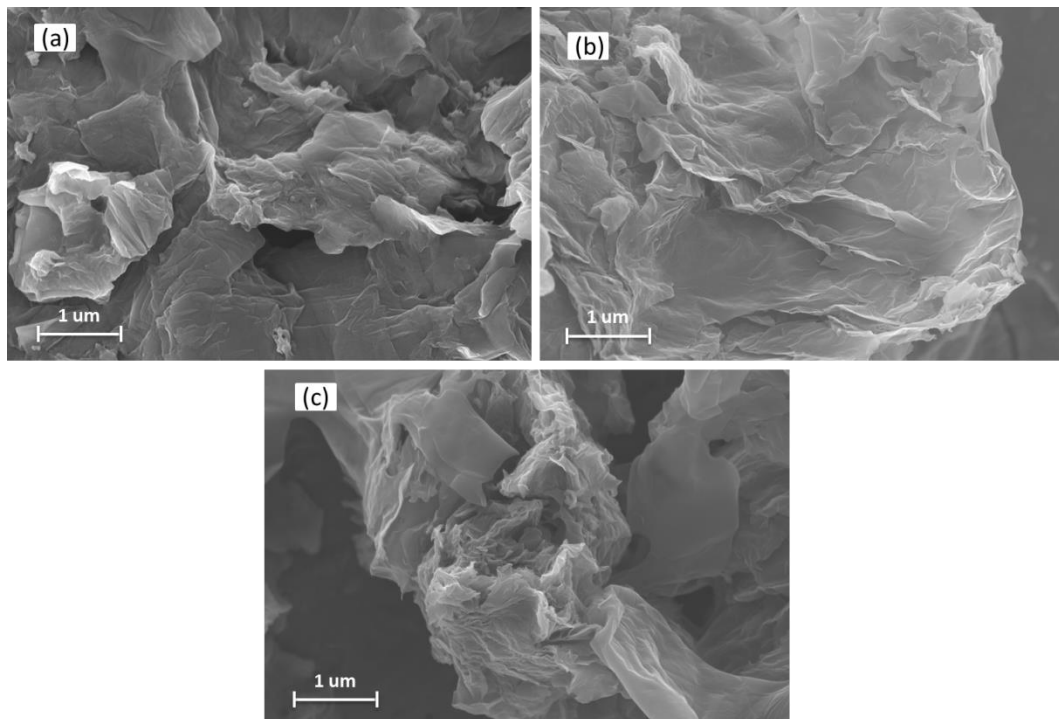


Figure 5.2. SEM images of GO (a), rGO-700 (b), and NG-700 (c).

Figure 5.2 presents SEM images of GO, rGO-700, and NG-700. It can be seen that exfoliated layers were found in rGO-700 and NG-700. Compared with the silk veil-like morphology of rGO-700, partially aggregated and crinkled structure was obtained at the end of doped graphene sheets, originated from the created defective sites after nitrogen atoms incorporated into the graphene layer. It was reported that the GO layers would re-fabricated when annealing at high temperatures and can be influenced by the heteroatom doping process.(27)

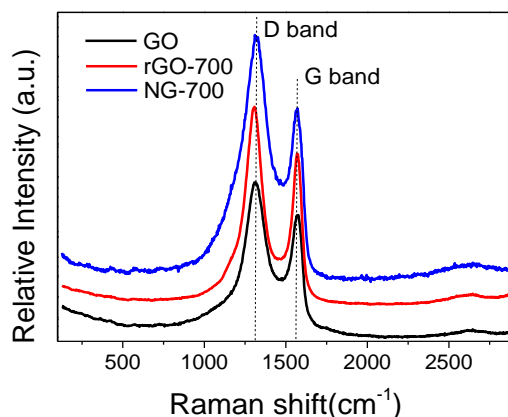


Figure 5.3. Raman spectra of GO, rGO-700, and NG-700.

Raman spectra have been widely used to investigate the degree of graphitization, number of layers, and doping status of graphene.(28) Figure 5.3 displays the Raman spectra of GO, rGO-700 and NG-700. The integrated intensity ratio of D band versus G band (I_D/I_G) is a significant parameter to reflect the defect and disorder level in the graphitic carbon layers.(29) The I_D/I_G value of NG-700 (1.34) is higher than GO (1.22) and rGO-700 (1.28), indicating that more defective sites were created through the incorporation of nitrogen atoms into the carbon network. The strong D band indicated that the N-doping would significantly enhance the defect density. It was reported that width of G band would be changed when doping with heteroatoms.(30, 31) In this study, the G band width came along with an order as NG-700 > GO > rGO-700, suggesting that N atoms were doped into the sp^2 carbon networks.

Figure 5.4 shows nitrogen sorption isotherm, pore size distribution and BET surface area of three NG samples doped at varying temperatures. It can be seen that NG-700 has a higher surface area (227.5 m^2/g) than NG-600 (64.4 m^2/g) and NG-800 (104.9 m^2/g). For carbon materials, high annealing temperature usually brings about porous structure, smaller nanocrystalline graphene sheets, and larger surface area, hereby creating more edges and defects.(17) However, the decreased surface area for NG-800 may be ascribed to the collapse of the carbon skeleton structure when the temperature is over 700 °C. Figure 5.4 (b) indicates that the pore structures of the NG catalysts prepared are primarily consisted of micro- and meso-pores (0~5 nm).

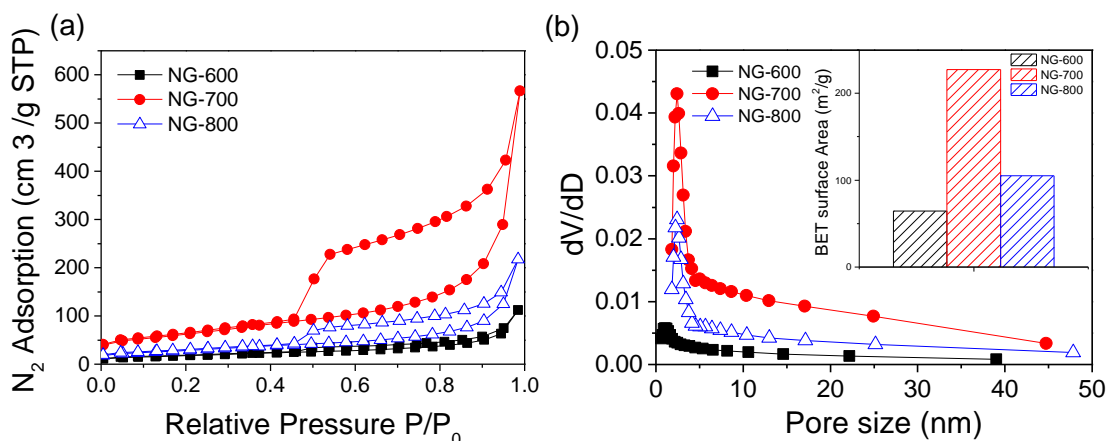


Figure 5.4. (a) N₂ sorption isotherms, and (b) pore size distributions and BET surface area of NG-600, -700 and -800.

Figure 5.5a displays XPS survey (0-1000 eV) of N-doped graphene to explore the elemental compositions. Figure 5.5(a) shows that the O/C ratios (oxygen versus carbon) of NG-600, -700, and -800 were measured to be 3.28, 3.11, and 2.41%, respectively, which were much lower than that of GO with a O/C ratio of 45%.⁽³²⁾ It has been reported that the acid oxygen groups like carboxyl and lactone began to decompose into CO₂ at about 250 °C, and the neutral and weak basic surface groups such as epoxide, quinone, phenol, and carbonyl would be volatilized into CO and CO₂ between 450 and 900 °C.^(33, 34) The desorption and decomposition properties of GO, NGs and the N precursor (melamine) were shown in Figure 5.S1. The quick weight loss before 300 °C can be ascribed to the decomposition of the functional groups in GO. After 500 °C, the carbon skeleton started to break down due to combustion. It is worthwhile to note that melamine was completely combusted in air at 340 °C, suggesting that most melamine was burnt and doped into the graphene during the process of annealing in the muffle furnace at 450 °C. Previous research also revealed that certain surface oxides at edges and defect sites of GO might play a crucial role as the active sites in reaction with nitrogen precursors (the amino groups and the carbon nitride intermediates produced by thermal polymerization) for C-N bond formation, affording N-doping into the graphene layers, which is consistent with XPS and Raman spectra results.^(33, 35, 36)

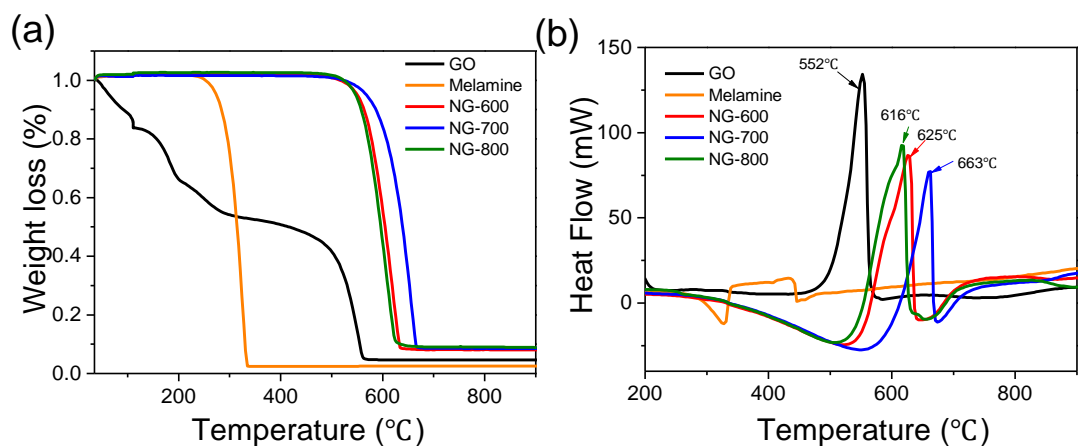


Figure 5.S1. TGA (a) and DTA (b) curves of graphene oxide melamine and nitrogen-doped graphene

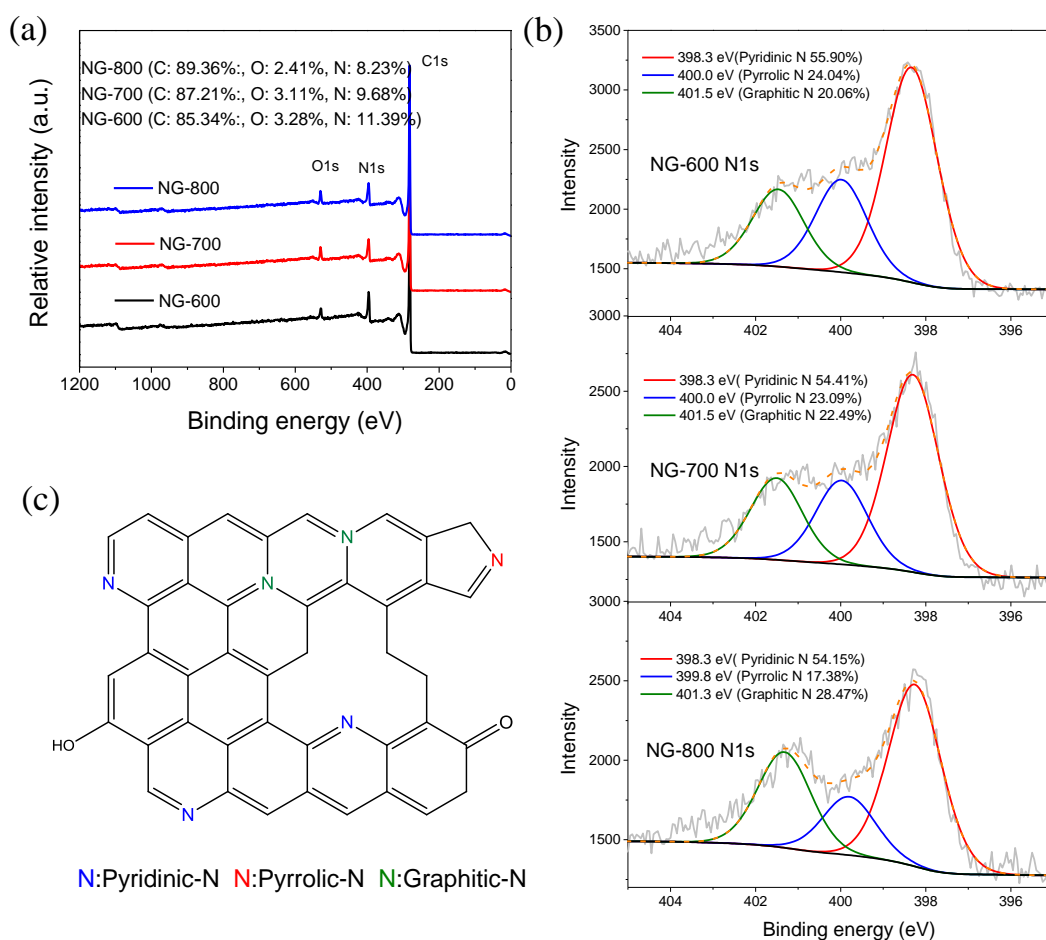


Figure 5.5. (a) XPS survey of NG-600, NG-700 and NG-800, (b) N1s scan of NG-600, NG-700, and NG-800, (c) Different types of N-doping.

The N1s peak at the binding energy of around 400 eV was observed on all the NG-600, -700 and -800, presenting 11.39, 9.68 and 8.23 at.% nitrogen doping levels, respectively. Nitrogen contents in the graphene layer would reduce at an elevated temperature due to the breakup of C-N bonds.(33, 34) In this study, the catalysts had a high N-doping level (8.23-11.39 at.%), compared to those obtained from other reported methods such as the enhanced chemical vapor deposition (CVD) (5.0 at.%(37)), plasma method (5.8 at.%(32)), annealing GO with NH₃ at 300-1100 °C (3-5 at.%(33)), and with ammonium nitrate at 350 °C (5.61 at.%(21)), suggesting that the melamine could act as a novel and efficient N precursor.

Figure 5.5b displays the high-resolution N1s XPS spectra in a narrow range (393-407 eV). N signals were fitted into three components: 398.3, 400.0 and 401.5 eV, corresponding to pyridinic N (nitrogen in a six-atom heterocyclic ring), pyrrolic N (nitrogen in a five-atom heterocyclic ring), and quaternary N (or graphitic N, sp²-hybridized N neighbored with three sp²-C), respectively.(5, 21, 32, 38) The structures of different N species are shown in Figure 5.5c. It can be seen that, with elevated annealing temperature from 600 to 800 °C, more graphitic N incorporated into the graphene basal plane from 20.06 to 28.47% due to the better thermal stability compared to pyrrole-like N.(33, 35, 39) Thus, the nitrogen compositional species and doping content could be controlled by synthesis conditions.

3.3.2 Catalytic Performance of Carbon Materials in Phenol Degradation.

The catalytic activities of various carbocatalysts were investigated in catalytic activation of PMS for phenol oxidation in aqueous solution. Figure 5.6a shows that PMS itself can hardly generate active radicals for phenol degradation without a solid catalyst. Meanwhile, without the addition of PMS, only around 4% phenol was removed on NG-700 due to adsorption. Moreover, the GO and g-C₃N₄ (product from melamine polymerization) were not able to effectively activate PMS for the phenol oxidation reactions, indicating that the doped nitrogen was the active sites. Figure 5.6b reveals that NG-700 exhibited a greater catalytic performance to activate PMS for phenol degradation, compared to other nanocarbons such as graphene nanosheets (GNs), single-walled carbon nanotubes (SWCNTs), rGO-700, N-doped rGO and MWCNTs using ammonium nitrate as the N precursor (NG-350 and N-CNT-350,

respectively) and a typical metal catalyst, Co_3O_4 . A pseudo first order reaction was employed to estimate the kinetic rates as shown below:

$$\ln\left(\frac{C}{C_0}\right) = -kt \quad \text{Eq. (5.1)}$$

The reaction rate constants (k) of phenol oxidation on NG-700, rGO-700, GNs, SWCNTs, NG-350, N-CNT-350, and crystalline Co_3O_4 were then evaluated to be 0.319, 0.004, 0.00138, 0.00697, 0.00995, 0.00851 and 0.0173 min^{-1} , respectively. Upon nitrogen doping, the activity of rGO obtained from reduction at 700 °C with the same method can be enhanced by about 80 times. NG-700 not only showed a higher efficiency than other carbon allotropes, but superior to the popular metal-based catalyst of crystalline Co_3O_4 with more than 18 times enhancement.

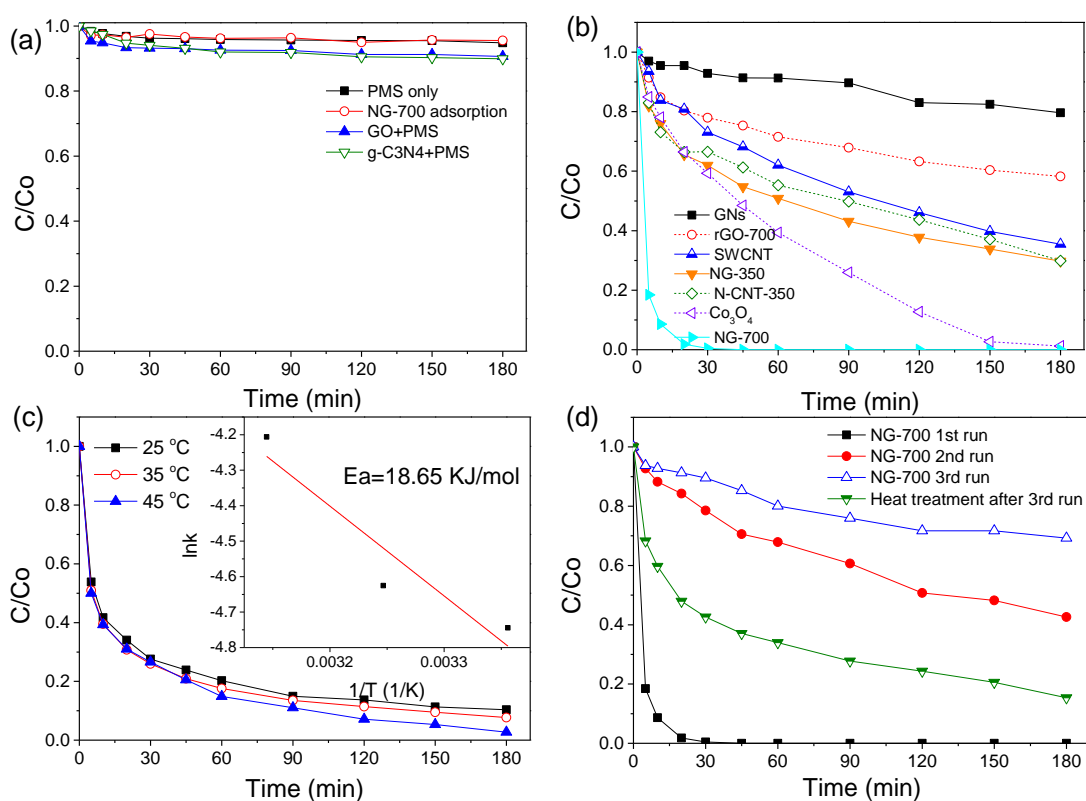


Figure 5.6. (a) Phenol degradation under various reaction conditions, (b) PMS activation under various catalysts, (c) Effect of temperature on phenol removal. (Catalyst=0.05 g/L) (d) Stability and recyclability studies of NG-700. (Catalyst: 0.1 g/L; PMS: 6.5 mM, Phenol: 20 mg/L, T: 25 °C)

Figure 5.S2 further shows that all the samples of NG-600, -700, and -800 can completely degrade 20 ppm phenol within 15 min. In the same reaction conditions, they demonstrated much better catalytic performance than the carbon-based catalysts such as graphene (70% phenol removal in 180 min), N-doped graphene (annealing GO with ammonium nitrate at 350 °C), and N-modified multi-walled CNTs with complete removal of phenol in 45 min in previous studies.(14, 20, 21) Approximate 75% TOC removal was achieved on NG-700 in 60 min (data not shown here).

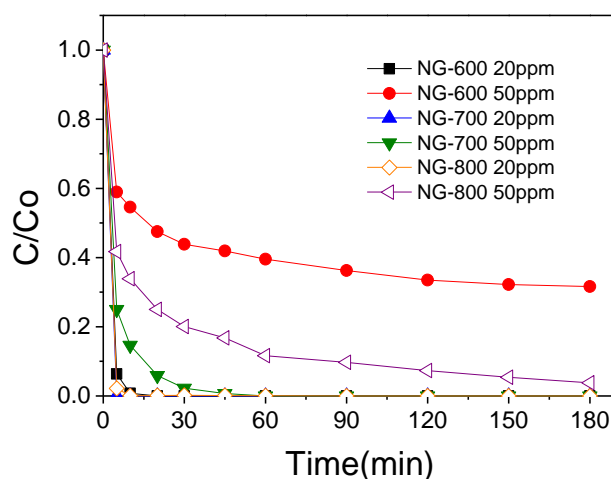


Figure 5.S2. Catalytic oxidation of phenol on NG-600, NG-700 and NG-800 (catalyst: 0.2 g/L, PMS: 6.5 mM, T: 25 °C)

NG-700 shows the best performance among the NGs, thus it was chosen for subsequent kinetic and stability studies. The influence of reaction temperature on phenol degradation is presented in Figure 5.6c. Interestingly, it was found that temperature presented only a marginal effect on the process of catalytic oxidation of phenol solution, which was also discovered in another study employing the N-doped carbon nanotube (N-CNT) as an effective catalyst for organic pollutant removal.(14) It suggests that the N-doping modification might lead to this effect, compared with rGO-700 without doping (data not shown here). The activation energy of NG-700 for catalytic oxidation of phenol was calculated to be 18.6 kJ/mol, lower than the reported value of CNT (33.3 kJ/mol), N-CNT (39.2 kJ/mol), and graphene (84.0 kJ/mol).(14, 21) The induced N atoms could significantly activate the sp^2 carbon system and reduce the activation energy for electron transfer from graphene surface to PMS, and impose a more significant impact on the processes of PMS activation.

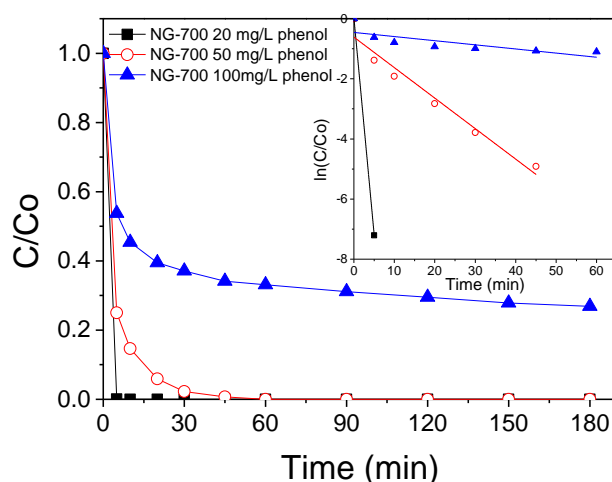


Figure 5.S3. Effect of phenol initial concentration on phenol degradation. (Catalyst=0.2 g/L, PMS=6.5 mM, T=25 °C)

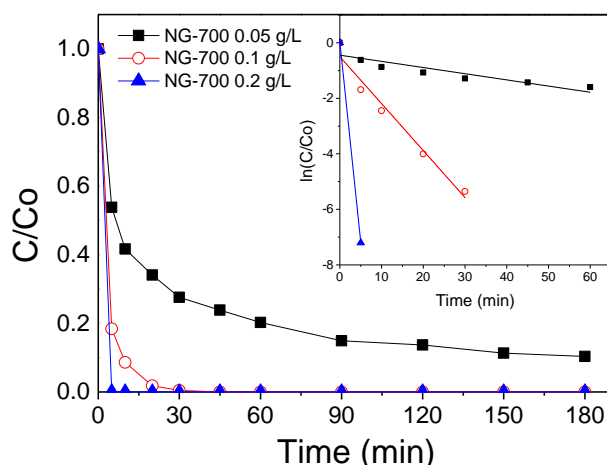


Figure 5.S4. Effect of catalyst dosage on phenol degradation (phenol=20 mg/L, PMS=6.5 mM, T=25 °C)

Figure S3 displays the effect of initial phenol concentration on its degradation rate. It was found that phenol degradation efficiency tended to drop quickly with increasing initial phenol contents in solution. It can be seen that 100% phenol was degraded in 5 min and 60 min for 20 and 50 mg/L, respectively, whereas only 75% phenol was degraded in 180 min at phenol concentration of 100 mg/L. The adsorbed phenol molecules and intermediates would cover the active sites of the catalyst, then hinder the activation of PMS. Moreover, the insufficient PMS might also be a limiting factor for degradation of high concentration of phenol solutions. Figure 5.S4 reveals the effect of catalyst dosage on phenol removal. At 0.05 g/L, 90% of phenol removal can

be achieved in 180 min, which can be significantly reduced to 30 and 5 min on a loading of 0.1 and 0.2 g/L, respectively. The increase of catalyst dosage will bring in more active sites to activate PMS, giving rise to the enhancement of catalytic efficiency.

The stability and reusability were evaluated as shown in Figure 5.6. Around 58 and 31% of phenol were removed after 180 min in the second and third runs, respectively, compared to 100% decomposition of phenol in 45 min for the fresh catalyst. A thermal treatment was applied to burn the covered intermediates on the active sites and edges of the catalyst. The activity was partially recovered through the thermal annealing and 85% phenol removal was achieved, compared 31% removal at 3rd run in 180 min. The long-term stability of the metal-free NG is not comparable to most metal catalysts, which was also reported in other heterogeneous catalytic systems.(21, 40, 41) As shown in Table 5.S1 and Figure 5.S5, the specific surface area decreased from 227.5 to 202.8 m²/g and the pore volume reduced from 0.67 to 0.46 cm³/g after 1st run, while no apparent changes were found in average pore size. Moreover, the XPS spectra revealed a great increase of oxygen level to 13.74 at.% and a decrease of N-doping level to 1.56 at.% on the used catalysts. The deactivation of the catalyst might be ascribed to intricate influences of surface chemistry and structural changes, including the adsorption of intermediates, coverage of surface active sites, changes of pore structures, and dopants re-fabrication in graphene network. The activity of passivated catalysts could be recovered via thermal annealing (Figure 5.6d) or hydrogenation at a mild condition to remove the adsorbed intermediates and to create a better reductive degree of graphene. Recently, we discovered that N-doped carbon nanotubes presented a much better stability than rGO, owing to that the surface chemistry of the rolled graphene shells of CNTs was more stable and robust than the chemically derived graphene with a highly defective degree.(6) It was indicated that nitrogen doped graphene with a robust structure and a higher doping level could be more stable in metal-free catalysis.

Table 5.S1. Nitrogen sorption results of SNG before and after reaction

	BET surface	Pore volume	Average pore
NG-700	227.5	0.67	5.3
NG-700 after 1 st	202.8	0.46	5.3

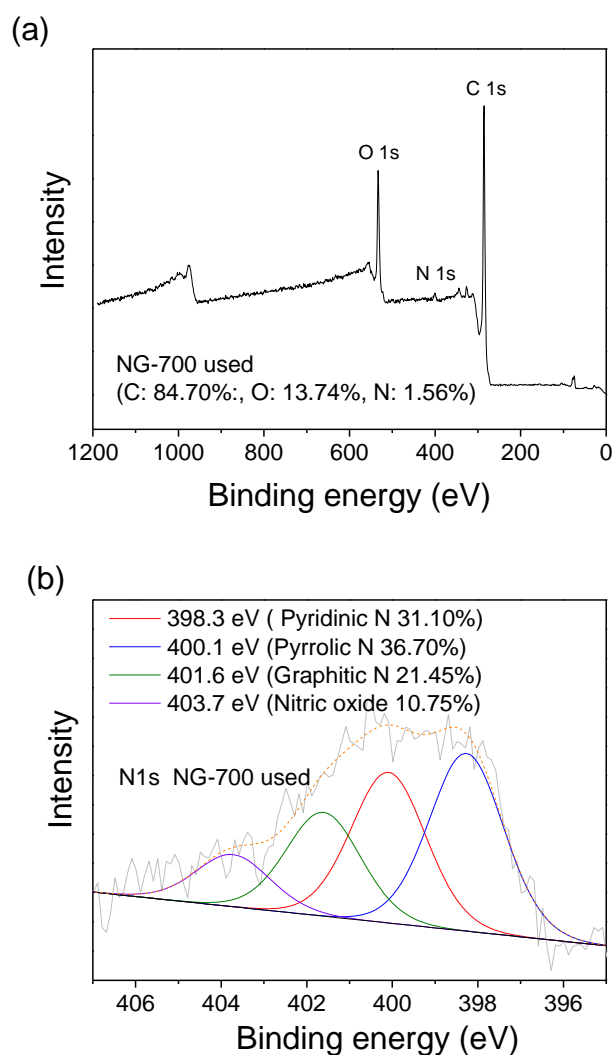


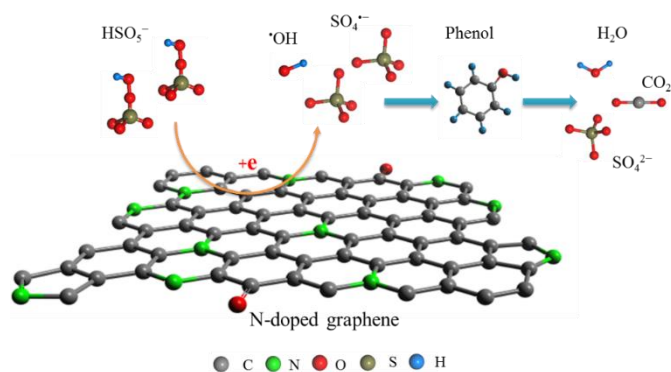
Figure 5.S5. (a) XPS survey and (b) N 1s high resolution spectra of NG-700 after 1st run.

5.3.3. Mechanism of Generation and Evolution of Active Radicals and Reaction Pathways.

Nanocarbons have demonstrated a promising activity for PMS activation for organic pollutant removal, yet the mechanism of activation processes has not been clearly illustrated (14, 42, 43). It was suggested that sp^2 carbon, zigzag edges, and electron rich-containing oxides such as carboxyl and quinone might work as the real active sites to activate PMS for the advanced oxidation processes.(14, 17, 18) It was further suggested that substantial modification with nitrogen can dramatically enhance the catalytic performance of rGO and MWCNTs.(20, 21)

It was well reported that the introduction of heteroatoms into graphene layers would disrupt sp^2 -hybridized carbon configuration and modulate the physical, chemical, and electrical properties of graphene, meanwhile create new active sites for various reactions.(4, 7, 44) Theoretical studies indicated that the graphitic N, with a smaller covalent radius and higher electronegativity than C atom, can induce electron transfer from adjacent carbon atoms to nitrogen, thus breaking the chemical inertness of sp^2 carbon layer and altering the catalytic activity of graphene.(29, 39, 45) Luo et al.(46) demonstrated that pyridinic N, with a pair of lone electrons, is able to effectively alter the valance band of graphene and improve the π states of Fermi level. Long and co-workers(38) found that the quaternary N could be the metal-free active sites for selectively catalytic oxidation of benzylic alcohol. Both theoretical and experimental investigations have shown that the graphitic nitrogen sites may lead to high charge density and asymmetric spin density and present extraordinary electron-catalytic activity towards oxygen reduction reaction (ORR), and more active sites can then be created with the enhancing nitrogen contents.(47-50)

The proposed mechanism of PMS activation on N-doped graphene is illustrated in Scheme 5.3. We proposed that delocalized electrons from the zigzag edges of graphene would be able to demonstrate a high chemical activity and could be transferred to activate the PMS to generate radicals.(15, 51, 52) The Lewis basic sites with lone electrons such as ketonic groups, pyridinic, and pyrrolic N can present an extraordinary potential for the redox process.(16) Moreover, sp^2 -hybridized C in the graphene can be further activated by substantial doping of nitrogen atoms (graphitic N). In this study, a high N doping level (8-11 at.%) and large portion of substitutional doping (graphitic N, 20-28%) were achieved by a facile one-pot doping strategy. Both characterization and experimental results indicated that the catalytic activation of N-rGO does not simply rely on the N contents, but on the structure of graphene and N species. The graphitic N might play a dominant role for PMS activation as the positively charged adjacent carbon atoms presented greater potential for the chemical adsorption of HSO_5^- and breaking up the O-O bond ($HO-SO_4^-$) to generate active radicals.



Scheme 5.3. Proposed mechanism of PMS activation and phenol oxidation on N-doped graphene.

Table 5.1. DFT calculation results for PMS activation on different graphene models.

	Position	E_{tot} (Ha)	E_{b} (eV)	Q (e)
Graphene (Panel a, $E_{\text{tot}} = -1608.94$ Ha)	1	-2383.41	-1.69	-0.556
	2	-2383.41	-1.62	-0.543
N-doped graphene (Panel b, $E_{\text{tot}} = -1624.97$ Ha)	1	-2399.45	-1.59	-0.536
	2	-2399.45	-1.54	-0.519
	3	-2399.45	-1.54	-0.523
N-doped graphene (Panel c, $E_{\text{tot}} = -1586.22$ Ha)	1	-2360.70	-1.81	-0.565
	2	-2360.71	-1.93	-0.438
	3	-2360.61	0.69	-0.516
N-doped graphene (Panel d, $E_{\text{tot}} = -1625.53$ Ha)	1	-2400.04	-2.67	-0.888
	2	-2400.06	-2.98	-0.855
	3	-2400.04	-2.49	-0.767
N-doped graphene (Panel e, $E_{\text{tot}} = -1625.53$ Ha)	1	-2400.05	-2.77	-0.831
	2	-2400.05	-2.69	-0.887
	3	-2400.04	-2.46	-0.889

Theoretical calculations were then applied to give further insights into PMS activation process on graphene and N-doped graphene in different systems as shown in Scheme 5.2. The minimum energy of each system was set as the basis energy when calculating the relative total energy (E_{tot}). The adsorption energy of PMS (E_{b}) on graphene was calculated by $E_{\text{b}} = E_{\text{graphene+PMS}} - E_{\text{graphene}} - E_{\text{PMS}}$, where $E_{\text{graphene+PMS}}$, E_{graphene} , and E_{PMS} are total energies of graphene with PMS adsorption, graphene only, and free PMS molecule, respectively. Q is the electron transfer between PMS and graphene. It was observed from Table 5.1 that, compared with pristine graphene (panel a), the adsorption enhancement for PMS was mainly induced by the graphitic N (panel d and e), where a higher adsorption energy was found and more electrons were transferred

from graphene to PMS. For the other two types of N doping with pyridinic N (panel b) and pyrrolic N (panel c), the changes of adsorption energy and electron transfer were not significant. Therefore, the graphitic N doping can enhance the interaction between PMS and graphene, possibly inducing a higher activity for PMS adsorption and activation via getting electrons from graphene system and producing active radicals.

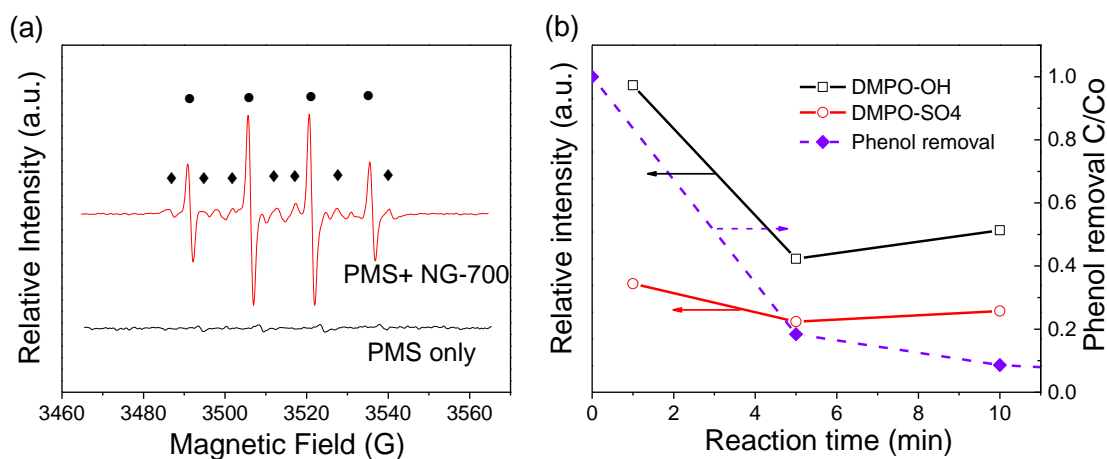


Figure 5.7. (a) EPR spectra of DMPO adducts under different conditions (●: DMPO-OH, ◆: DMPO-SO₄). (b) Intensity changes of DMPO adducts (Catalyst: 0.1 g/L; PMS: 6.5 mM; phenol: 20 mg/L; T: 25 °C; and DMPO: 0.16 mol/L)

EPR spectra were acquired to experimentally probe the PMS activation processes. Figure 5.7a indicates that very few active radicals were generated by PMS itself without a catalyst and NG-700 presents excellent performance in PMS activation. Two types of radicals, $\cdot\text{OH}$ and $\text{SO}_4^{\cdot-}$, were detected during the activation and oxidation processes. The quantitative information of DMPO-SO₄ adducts ($\alpha_{\text{H}}=0.78$, $\alpha_{\text{H}}=1.48$, $\alpha_{\text{H}}=9.6$, and $\alpha_{\text{N}}=13.2$) and DMPO-OH adducts ($\alpha_{\text{H}}=14.8$, $\alpha_{\text{N}}=14.8$) was presented in Figure 5.7b. Huang et al.(53) reported that the sulfate radicals served as the primary active species for catalytic oxidation of organic pollutants, whereas the initially produced hydroxyl radicals tended to activate PMS to produce sulfate radicals. In this study, lots of $\cdot\text{OH}$ were generated in the first 1 min, then its amount quickly dropped and raised again after 5 min, and the $\text{SO}_4^{\cdot-}$ presented the same trend with relatively lower amounts. It was suggested that the NGs are able to effectively activate PMS to produce sulfate and hydroxyl radicals. The rapid drop of $\cdot\text{OH}$ amount was due to the consumption by phenol oxidation and the inter-conversion to $\text{SO}_4^{\cdot-}$ (Eq. 5.3). An

upward trend after 5 min might be ascribed to the accumulation of $\cdot\text{OH}$ produced from PMS and transformation of $\text{SO}_4^{\cdot-}$ (Eqs.5.2 and 5.6) as most of phenol molecules have been decomposed in the meantime. Sulfate radicals were consumed for oxidation of phenol and transferred to $\cdot\text{OH}$ (Eqs. 5.7 and 5.6) during the whole reaction. The EPR results strongly proved that NG-700 can effectively activate PMS to produce sulfate and hydroxyl radicals, and large quantity of $\cdot\text{OH}$ generated initially might play a crucial role for phenol degradation in the first few minutes. The competitive radical tests shown in Figure 5.S6 suggested that sulfate radicals also played a critical role for complete decomposition of phenol. It can be deduced that both $\cdot\text{OH}$ and $\text{SO}_4^{\cdot-}$ work as active radicals to attack phenol compound during the oxidation process, and the generation of $\text{SO}_4^{\cdot-}$ might have a close relationship with the initial existence of $\cdot\text{OH}$ in PMS activation. Scheme 5.S4 shows the possible degradation pathways, and the related intermediates were shown in Figures 5.S7.

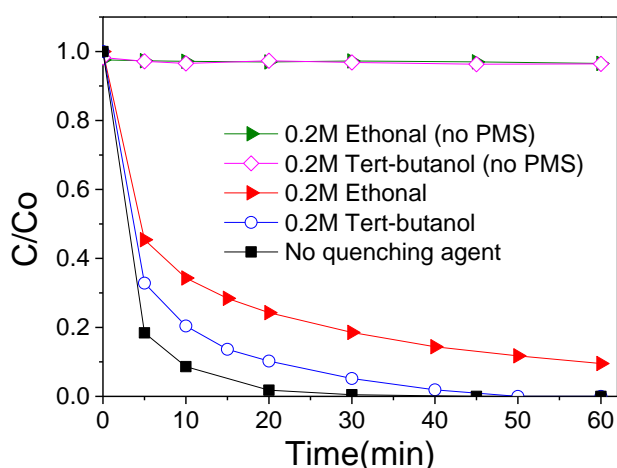
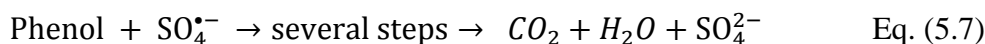
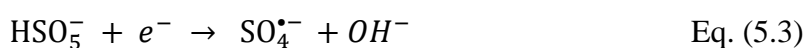
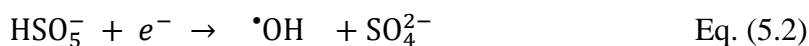


Figure 5.S6 Effects of ethanol and tert-butanol on the PMS activation for phenol degradation.

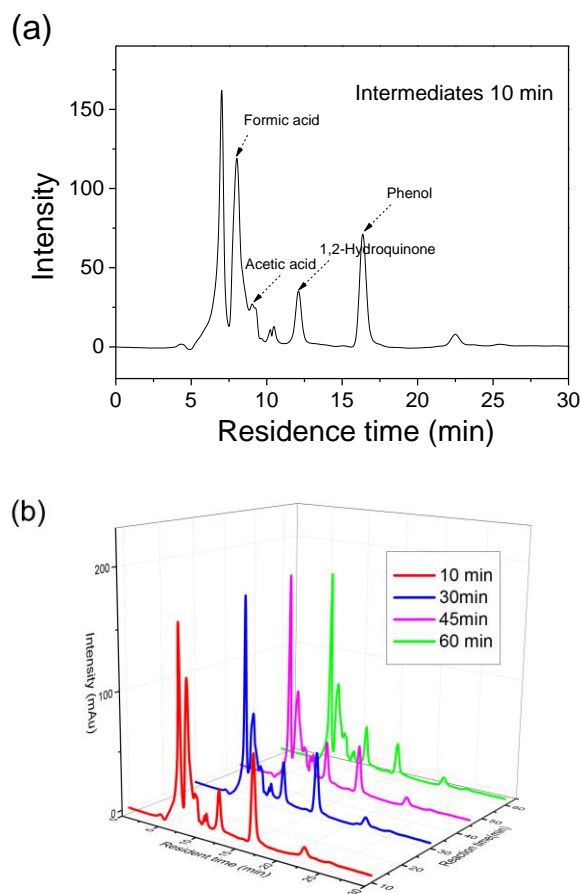
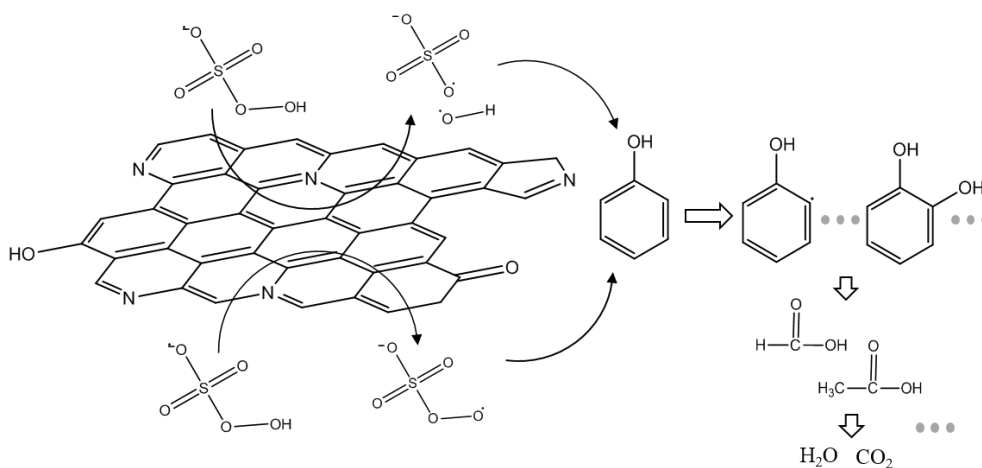


Figure 5.S7 (a) Several typical intermediates during phenol degradation, (b) variation of intermediates in the phenol oxidation process.



Scheme 5.S4 Proposed reaction pathways of phenol oxidative degradation on N-rGO with PMS.

5.4 Conclusions

Nitrogen-doped reduced graphene oxide with both structural and compositional modifications was synthesized by a one-pot method. The prepared N-doped graphene had larger SSAs and higher nitrogen contents. N-doped graphene showed outstanding performance in catalytic activation of PMS for oxidation of phenol, and was superior to many other carbon allotropes and a typical metal-based catalyst of Co_3O_4 . Kinetic studies indicated that the initial phenol concentration and catalyst dosage will influence the kinetic rate, whereas the temperature does not show a strong effect. Theoretical calculations illustrated that quaternary N is able to dramatically reduce the adsorption energy and facilitate electron transfer for PMS activation on graphene sheets. EPR spectra and competitive radical tests suggested that both $\cdot\text{OH}$ and $\text{SO}_4^{\cdot-}$ were generated during the activation processes and played key roles in phenol degradation. The reaction pathways were illustrated by identification of the intermediates. This study not only provided an excellent metal-free catalyst, but also, for the first time, illustrated the PMS activation and phenol degradation on nanocarbons. This metal-free catalysis will be significantly contributing to the pursuit of a sustainable remediation technology without any secondary contamination. With the development of state-of-the-art technology to synthesize low-cost and large-scale GO and graphene in the near future, this study will significantly contribute to development of highly robust and effective carbocatalysts for practical applications in aqueous reactions including water treatment.

References

1. Geim AK, Novoselov KS. The rise of graphene. *Nat. Mater.* 2007; 6(3):183-91.
2. Zhu YW, Murali S, Cai WW, Li XS, Suk JW, Potts JR, et al. Graphene and graphene oxide: synthesis, properties, and applications. *Adv. Mater.* 2010; 22(35):3906-24.
3. Loh KP, Bao QL, Ang PK, Yang JX. The chemistry of graphene. *J. Mater. Chem.* 2010; 20(12):2277-89.
4. Su DS, Perathoner S, Centi G. Nanocarbons for the development of advanced catalysts. *Chem. Rev.* 2013; 113(8):5782-816.

5. Lai LF, Potts JR, Zhan D, Wang L, Poh CK, Tang CH, et al. Exploration of the active center structure of nitrogen-doped graphene-based catalysts for oxygen reduction reaction. *Energ. Environ. Sci.* 2012; 5(7):7936-42.
6. Duan X, Sun H, Wang Y, Kang J, Wang S. N-doping-induced nonradical reaction on single-walled carbon nanotubes for catalytic phenol oxidation. *ACS Catal.* 2014; 5(2):553-9.
7. Su DS, Zhang J, Frank B, Thomas A, Wang XC, Paraknowitsch J, et al. Metal-free heterogeneous catalysis for sustainable chemistry. *Chemsuschem.* 2010; 3(2):169-80.
8. Chizari K, Deneuve A, Ersen O, Florea I, Liu Y, Edouard D, et al. Nitrogen-doped carbon nanotubes as a highly active metal-free catalyst for selective oxidation. *Chemsuschem.* 2012; 5(1):102-8.
9. Anipsitakis GP, Dionysiou DD. Degradation of organic contaminants in water with sulfate radicals generated by the conjunction of peroxymonosulfate with cobalt. *Environ. Sci. Technol.* 2003; 37(20):4790-7.
10. Anipsitakis GP, Dionysiou DD, Gonzalez MA. Cobalt-mediated activation of peroxymonosulfate and sulfate radical attack on phenolic compounds. Implications of chloride ions. *Environ. Sci. Technol.* 2006; 40(3):1000-7.
11. Anipsitakis GP, Stathatos E, Dionysiou DD. Heterogeneous activation of oxone using Co₃O₄. *J. Phys. Chem. B.* 2005; 109(27):13052-5.
12. Liang HW, Sun HQ, Patel A, Shukla P, Zhu ZH, Wang SB. Excellent performance of mesoporous Co₃O₄/MnO₂ nanoparticles in heterogeneous activation of peroxymonosulfate for phenol degradation in aqueous solutions. *Appl. Catal., B* 2012; 127:330-5.
13. Saputra E, Muhammad S, Sun HQ, Ang HM, Tade MO, Wang SB. Different crystallographic one-dimensional mno₂ nanomaterials and their superior performance in catalytic phenol degradation. *Environ. Sci. Technol.* 2013; 47(11):5882-7.
14. Sun HQ, Liu SZ, Zhou GL, Ang HM, Tade MO, Wang SB. Reduced graphene oxide for catalytic oxidation of aqueous organic pollutants. *ACS Appl. Mater. Inter.* 2012; 4(10):5466-71.
15. Enoki T, Fujii S, Takai K. Zigzag and armchair edges in graphene. *Carbon.* 2012; 50(9):3141-5.
16. Frank B, Zhang J, Blume R, Schlogl R, Su DS. Heteroatoms increase the selectivity in oxidative dehydrogenation reactions on nanocarbons. *Angew. Chem. Int. Ed.* 2009; 48(37):6913-7.
17. Liu SZ, Peng WC, Sun HQ, Wang SB. Physical and chemical activation of reduced graphene oxide for enhanced adsorption and catalytic oxidation. *Nanoscale.* 2014; 6(2):766-71.

18. Peng WC, Liu SZ, Sun HQ, Yao YJ, Zhi LJ, Wang SB. Synthesis of porous reduced graphene oxide as metal-free carbon for adsorption and catalytic oxidation of organics in water. *J. Mater. Chem. A* 2013; 1(19):5854-9.
19. Zhang J, Liu X, Blume R, Zhang AH, Schlogl R, Su DS. Surface-modified carbon nanotubes catalyze oxidative dehydrogenation of n-butane. *Science*. 2008; 322(5898):73-7.
20. Sun HQ, Kwan C, Suvorova A, Ang HM, Tade MO, Wang SB. Catalytic oxidation of organic pollutants on pristine and surface nitrogen-modified carbon nanotubes with sulfate radicals. *Appl. Catal., B* 2014; 154:134-41.
21. Sun HQ, Wang YX, Liu SZ, Ge L, Wang L, Zhu ZH, et al. Facile synthesis of nitrogen doped reduced graphene oxide as a superior metal-free catalyst for oxidation. *Chem. Commun.* 2013;49(85):9914-6.
22. Hummers WS, Offeman RE. Preparation of graphitic oxide. *J. Am. Chem. Soc.* 1958;80(6):1339-.
23. Delley B. From molecules to solids with the DMol(3) approach. *J. Chem. Phys.* 2000; 113(18):7756-64.
24. Perdew JP, Burke K, Ernzerhof M. Generalized gradient approximation made simple. *Phys Rev Lett.* 1996;77(18):3865-8.
25. Grimme S. Semiempirical GGA-type density functional constructed with a long-range dispersion correction. *J. Comput. Chem.* 2006; 27(15):1787-99.
26. Qu LT, Liu Y, Baek JB, Dai LM. Nitrogen-doped graphene as efficient metal-free electrocatalyst for oxygen reduction in fuel cells. *ACS Nano*. 2010; 4(3):1321-6.
27. Su YZ, Zhang Y, Zhuang XD, Li S, Wu DQ, Zhang F, et al. Low-temperature synthesis of nitrogen/sulfur co-doped three-dimensional graphene frameworks as efficient metal-free electrocatalyst for oxygen reduction reaction. *Carbon*. 2013; 62:296-301.
28. Ferrari AC, Meyer JC, Scardaci V, Casiraghi C, Lazzeri M, Mauri F, et al. Raman spectrum of graphene and graphene layers. *Phys. Rev. Lett.* 2006; 97(18).
29. Choi CH, Park SH, Woo SI. Binary and ternary doping of nitrogen, boron, and phosphorus into carbon for enhancing electrochemical oxygen reduction activity. *ACS Nano*. 2012; 6(8):7084-91.
30. Berciaud S, Ryu S, Brus LE, Heinz TF. Probing the intrinsic properties of exfoliated graphene: raman spectroscopy of free-standing monolayers. *Nano Lett.* 2009; 9(1):346-52.
31. Casiraghi C, Pisana S, Novoselov KS, Geim AK, Ferrari AC. Raman fingerprint of charged impurities in graphene. *Appl. Phys. Lett.* 2007; 91(23):Doi 10.1063/1.2818692.

32. Kumar NA, Nolan H, McEvoy N, Rezvani E, Doyle RL, Lyons MEG, et al. Plasma-assisted simultaneous reduction and nitrogen doping of graphene oxide nanosheets. *J. Mater. Chem. A*. 2013; 1(14):4431-5.
33. Li XL, Wang HL, Robinson JT, Sanchez H, Diankov G, Dai HJ. Simultaneous nitrogen doping and reduction of graphene oxide. *J. Am. Chem. Soc.* 2009; 131(43):15939-44.
34. Kinoshita K. *Carbon: electrochemical and physicochemical properties* 1988. Medium: X; Size: Pages: 541 p.
35. Sheng ZH, Shao L, Chen JJ, Bao WJ, Wang FB, Xia XH. Catalyst-free synthesis of nitrogen-doped graphene via thermal annealing graphite oxide with melamine and its excellent electrocatalysis. *ACS Nano*. 2011; 5(6):4350-8.
36. Lin ZY, Waller G, Liu Y, Liu ML, Wong CP. Facile Synthesis of nitrogen-doped graphene via pyrolysis of graphene oxide and urea, and its electrocatalytic activity toward the oxygen-reduction reaction. *Adv. Energ. Mater.* 2012; 2(7):884-8.
37. Wang CD, Zhou YA, He LF, Ng TW, Hong G, Wu QH, et al. In situ nitrogen-doped graphene grown from polydimethylsiloxane by plasma enhanced chemical vapor deposition. *Nanoscale*. 2013; 5(2):600-5.
38. Long JL, Xie XQ, Xu J, Gu Q, Chen LM, Wang XX. Nitrogen-doped graphene nanosheets as metal-free catalysts for aerobic selective oxidation of benzylic alcohols. *ACS Catal.* 2012; 2(4):622-31.
39. Deng DH, Pan XL, Yu LA, Cui Y, Jiang YP, Qi J, et al. Toward n-doped graphene via solvothermal synthesis. *Chem. Mater.* 2011; 23(5):1188-93.
40. Kong XK, Sun ZY, Chen M, Chen CL, Chen QW. Metal-free catalytic reduction of 4-nitrophenol to 4-aminophenol by N-doped graphene. *Energ. Environ. Sci.* 2013; 6(11):3260-6.
41. Kong XK, Chen CL, Chen QW. Doped graphene for metal-free catalysis. *Chem. Soc. Rev.* 2014; 43(8):2841-57.
42. Saputra E, Muhammad S, Sun HQ, Wang SB. Activated carbons as green and effective catalysts for generation of reactive radicals in degradation of aqueous phenol. *Rsc Adv.* 2013; 3(44):21905-10.
43. Wang SB, Sun HQ, Ang HM, Tade MO. Adsorptive remediation of environmental pollutants using novel graphene-based nanomaterials. *Chem. Eng. J.* 2013; 226:336-47.
44. Liu HT, Liu YQ, Zhu DB. Chemical doping of graphene. *J. Mater. Chem.* 2011; 21(10):3335-45.
45. Gong KP, Du F, Xia ZH, Durstock M, Dai LM. Nitrogen-doped carbon nanotube arrays with high electrocatalytic activity for oxygen reduction. *Science*. 2009; 323(5915):760-4.

46. Luo ZQ, Lim SH, Tian ZQ, Shang JZ, Lai LF, MacDonald B, et al. Pyridinic N doped graphene: synthesis, electronic structure, and electrocatalytic property. *J. Mater. Chem.* 2011; 21(22):8038-44.
47. Lu ZJ, Bao SJ, Gou YT, Cai CJ, Ji CC, Xu MW, et al. Nitrogen-doped reduced-graphene oxide as an efficient metal-free electrocatalyst for oxygen reduction in fuel cells. *RCS Adv.* 2013; 3(12):3990-5.
48. Geng DS, Chen Y, Chen YG, Li YL, Li RY, Sun XL, et al. High oxygen-reduction activity and durability of nitrogen-doped graphene. *Energ. Environ. Sci.* 2011; 4(3):760-4.
49. Nagaiah TC, Kundu S, Bron M, Muhler M, Schuhmann W. Nitrogen-doped carbon nanotubes as a cathode catalyst for the oxygen reduction reaction in alkaline medium. *Electrochem. Commun.* 2010; 12(3):338-41.
50. Zhang LP, Niu JB, Li MT, Xia ZH. Catalytic mechanisms of sulfur-doped graphene as efficient oxygen reduction reaction catalysts for fuel cells. *J. Phys. Chem. C* 2014; 118(7):3545-53.
51. Lee G, Cho K. Electronic structures of zigzag graphene nanoribbons with edge hydrogenation and oxidation. *Phys. Rev. B* 2009; 79(16).
52. Jiang DE, Sumpter BG, Dai S. Unique chemical reactivity of a graphene nanoribbon's zigzag edge. *J. Chem. Phys.* 2007; 126(13).
53. Huang ZF, Bao HW, Yao YY, Lu WY, Chen WX. Novel green activation processes and mechanism of peroxydisulfate based on supported cobalt phthalocyanine catalyst. *Appl. Catal., B* 2014; 154:36-43.

Every reasonable effort has been made to acknowledge the owners of copyright material. I would be pleased to hear from any copyright owner who has been omitted or incorrectly acknowledged.

Chapter 6. Sulfur and Nitrogen Co-Doped Graphene for Metal-Free Catalytic Oxidation Reactions

Abstract

Sulfur and nitrogen co-doped reduced graphene oxide (rGO) was synthesized by a facile method and demonstrated remarkably enhanced activities in metal-free activation of peroxymonosulfate (PMS) for catalytic oxidation of phenol. Based on a first-order kinetic model, S-N co-doped rGO (SNG) presented an apparent reaction rate constant of $0.043 \pm 0.002 \text{ min}^{-1}$, which was 86.6, 22.8, 19.7, and 4.5-fold as high as that over graphene oxide (GO), rGO, S-doped rGO (S-rGO) and N-doped rGO (N-rGO), respectively. A variety of characterization techniques and density functional theory (DFT) calculations were employed to investigate the synergistic effect of sulfur and nitrogen co-doping. Co-doping of rGO at an optimal sulfur loading can effectively break the inertness of carbon systems, activate the sp^2 -hybridized carbon lattice and facilitate the electron transfer from covalent graphene sheets for PMS activation. Moreover, both electron paramagnetic resonance (EPR) spectroscopy and classical quenching tests were employed to investigate the generation and evolution of reactive radicals on the SNG sample for phenol catalytic oxidation. This study presented a novel metal-free catalyst for green remediation of organic pollutants in water.

6.1 Introduction

Graphene, a sp^2 -hybridized honeycomb lattice carbon, has emerged as a novel nanocarbon in recent years. Unique electronic, physical, and chemical properties have made it a promising candidate for versatile applications in solar cells, lithium ion batteries, biosensors, and supercapacitors.(1-5) Several research has demonstrated that graphene can be employed as a metal-free catalyst for various heterogeneous reactions of oxygen-reduction reaction (ORR), oxidative dehydrogenation (ODH) of alkanes, chemical synthesis, and environmental remediation, opening up a new material platform towards green and sustainable catalysis.(6-9)

Graphene can be obtained through micromechanical exfoliation, chemical vapor deposition (CVD) or reduction of chemically exfoliated graphene oxide platelets.(10) The zero band-gap of pristine graphene was suggested to greatly limit the catalytic activity and has hindered its further applications.(11) Chemical doping has demonstrated to be an excellent strategy to break the inertness of the graphene layer and to modulate the electronic and chemical properties by tailoring the electron states (charge or/and spin density) within the graphene basal plane.(12)

Substitutional doping with adventitious B, P, N, or S atoms into the carbon framework can modulate the chemical properties, create new active sites and dramatically enhance the catalytic activity of graphene.(5, 13, 14) Furthermore, co-doping by two or three elements with different electronegativities can give rise to a unique electron distribution and then result in a synergistic effect.(12) Zhao et al.(15) indicated that simultaneous introduction of B and N to adjacent positions of the carbon nanotube (CNT) honeycomb lattice created a neutralization effect between the electron donator (N) and acceptor (B). Zheng et al.(16) incorporated B atoms into N-doped graphene and discovered that the guest dopants were able to significantly enhance the activity of pyridinic N through a B-C-N bridge, resulting in synergistic coupling between the dopants (B and N).

Notwithstanding that nanocarbons have been intensively investigated in many catalytic processes, very few studies have been focused on graphene materials for aqueous phase catalytic reactions. In a pioneer study, we first reported that reduced

graphene oxide exhibited notable catalysis in peroxydisulfate (PMS) activation.(17) It was proposed that sp^2 carbon with abundant free-flowing electrons and unconfined π electrons at the zigzag edges can effectively react with PMS to produce reactive radicals for phenol decomposition.(18) Further physical and chemical activation approaches were applied to modify the microstructure and surface features of graphene material.(19, 20) The specific surface area (SSA) was increased to a large extent and more defect sites were created for improving adsorption and catalysis. It was further found that compositional modification with nitrogen atoms doped into graphene can produce more significant enhancement for catalytically oxidative phenol degradation.(9) The doped nitrogen with a lone-pair electrons and higher electronegativity could act as the Lewis basic sites (pyridinic and pyrrolic N) to effectively activate the positively charged neighbouring sp^2 carbon atoms via charge transfer (quaternary N) and disrupt the chemically inert nature of graphene network.(21)

Significant improvements in ORR via co-doping motivated us to investigate whether co-doping of other heteroatoms (B, P, S, or I) with N could bring about new properties and further promote the catalysis on nitrogen doped graphene.(22-24) Our previous study found that co-doping with trace amounts of boron (0.1 wt% B_2O_3) was able to slightly improve the catalytic activity of N-doped graphene for phenol oxidative degradation, whereas co-doping with phosphorus did not show any effect.(9) It can be also observed that co-doping with iodine cannot further improve the activity for phenol oxidation (data not shown here). In this study, we employed various graphene derivatives as metal-free catalysts for PMS activation. Co-doping with sulfur greatly enhanced the catalytic efficiency of nitrogen doped graphene, suggesting that sulfur can act as a promising co-dopant to further improve the activity of chemically modified graphene toward PMS activation.

6.2 Experimental Section

6.2.1 Catalyst Preparation. All the chemicals were purchased from Sigma-Aldrich and used as received without further purification. Graphene oxide (GO) was prepared by a modified Hummers' method.(25) Graphite was oxidized by concentrated H_2SO_4 and $KMnO_4$, and then the produced slurry was reacted with H_2O_2 . Details can be found

in our previous reports.(9, 17) For modified graphene synthesis, finely grounded GO (1.0 g) was dissolved in 100 mL ethanol, stirred for 30 min and sonicated for 30 min to form a well-dispersed solution. Ammonium nitrate (1.0 g) and diphenyl disulfide (DDS 0.3 g, unless noted elsewhere) were added to the mixture and stirred to dry at 323 K. The product was grounded to fine particles and transferred to a muffle furnace for annealing at 623 K for one hour. The obtained black powder was washed with ultrapure water and ethanol for several times and dried in an oven overnight. Thus S and N co-doped graphene (SNG) sample was obtained. Single nitrogen or sulfur doped graphene (N-rGO or S-rGO-0.3) was prepared by the same procedure above without addition of DDS (or ammonium nitrate). Reduced graphene oxide (rGO) was prepared without addition of any dopant precursors.

6.2.2 Materials Characterization. The morphological information of pristine and modified graphene was investigated by a ZEISS NEON 40EsB scanning electron microscopy (SEM) and a JEOL-2011 transmission electron microscopy (TEM). Raman spectra were acquired on an ISA (Dilor) argon-laser Raman spectrometer. X-ray photoelectron spectroscopy (XPS) was performed on a Kratos AXIS Ultra DLD system with monochromated Al-K α X-rays (1486.7 eV) under UHV conditions ($< 1 \times 10^{-9}$ mBar). Spectra were fitted with Kratos Vision software and CasaXPS software and calibrated to yield a primary C 1s component at 284.5 eV. A Shirley background was applied, fitting with Voigt functions (30% Lorentzian component). N₂ sorption isotherms were obtained by a Micromeritics Tristar 3000 instrument to determine surface area and pore size distribution. Before analysis, the samples were degassed in vacuum at 373 K overnight. Electron paramagnetic resonance (EPR) was employed on a Bruker EMS-plus instrument to probe the free radicals. The radicals were trapped with 5, 5-dimethyl-1-pyrroline N-oxide (DMPO) and the quantitative information was analyzed by Xeon software (Bruker) with hyperfine splitting constants DMPO-OH: $\alpha_N=14.9$ G, $\alpha_H=14.9$ G; DMPO-SO₄: $\alpha_N=13.2$ G, $\alpha_H=9.6$ G, $\alpha_H=1.48$ G, $\alpha_H=0.78$ G.

6.2.3 Catalytic Oxidation Procedure. Phenol oxidation was carried out in a 500 mL conical flask with 20 mg/L phenol solution and dipped in a constant-temperature water bath (298 K). The catalyst (0.2 g/L) was first added to the solution and stirred for 5 min and then PMS (6.5 mM) was added to the solution to start the reaction. At each time interval, 1 mL of solution was withdrawn by a syringe, filtered by a 0.45 μ m

Millipore film, and injected into a HPLC (high performance liquid chromatography) vial. The sample was mixed immediately with 0.5 mL of methanol to quench the reactive radicals, and then analyzed on a Varian HPLC using a UV detector ($\lambda = 270$ nm) and a C18 column. The statistical analyses were obtained via performing three parallel experiments on the different carbocatalysts.

6.2.4 Computational Methodology. A $C_{54}H_{18}$ cluster was used as a model graphene sheet for density functional theory (DFT) calculations. Sulfur was doped at the edge to give two single bonds to adjacent carbons as demonstrated experimentally using XPS.(26) For simplification, only graphitic N doping was considered. For co-doping, the relative positions of S and N were based on a previously reported model for investigation of ORR with various distances from S to N.(26) Electronic structure calculations were carried out using the FHI-aims all-electron DFT code(27) using numerical atom-centred orbitals as a basis set. The default “tight” orbital set was used. Calculations were performed at the gamma point using the PBE exchange-correlation functional(28) to a SCF convergence tolerance of 1×10^{-6} eV. Structures were fully relaxed to a force tolerance of 5×10^{-3} eV/ang. On-site charges were computed using the Bader analysis via the Bader code. (29) Spin isosurfaces ($n_{\text{up}} - n_{\text{down}}$) were shown with an isosurface value of 0.007 electrons/ang³. Electrostatic potential were shown with an isosurface value of 0.105 electrons/ang³.

6.3 Results and Discussion

6.3.1 Characterization of Materials.

The morphologies and structure of GO and SNG were obtained from SEM and TEM images. Figure 6.1a shows that, different from the smooth surface of GO, silk-like wrinkled flakes and several stacked layers were observed on SNG. It was reported that the wrinkled sheets were originated from the reconstruction of graphene during thermal annealing. Moreover, the defective sites produced by the heteroatom doping process would further influence the re-fabrication procedure, leading to more compacted and disoriented features of graphene.(30, 31) TEM image in Figure 6.1b also revealed the stacked aggregates of SNG with wrinkled graphene sheets and the selected area electron diffraction (SAED) spot rings can be assigned to the hexagonal structure of honeycomb carbon lattice and graphite planes.(17, 32) The interlayer

spacing reduced from 0.83 nm (GO) to 0.34 nm (SNG) as indicated in XRD spectra (data not shown here). During the doping process, more oxygen groups were removed and a better reducibility was achieved, leading to stronger π - π stacking between sp^2 -hybridized graphene basal planes. The changes in chemical compositions and surface groups were also revealed by the following characterizations such as XRD and XPS studies. Moreover, enhanced catalytic performances were obtained owing to such modifications.(33)

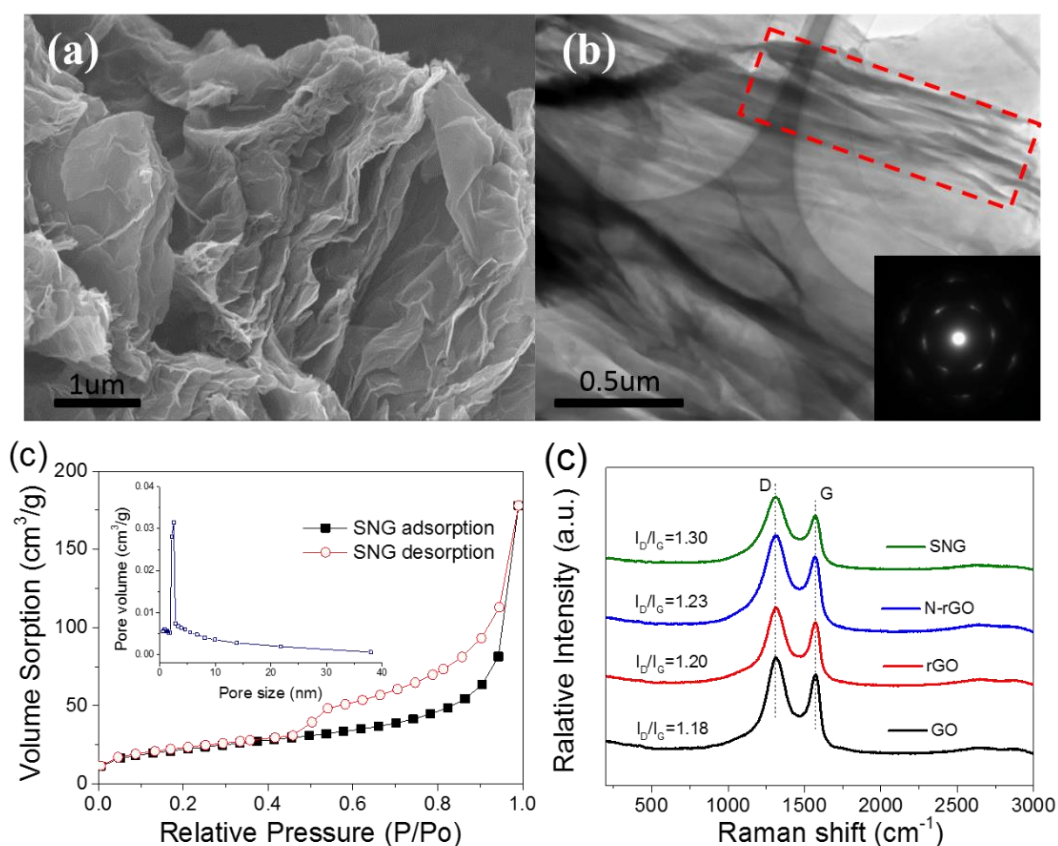


Figure 6.1. (a) SEM image and (b) TEM image of S-N co-doped graphene and SAED (inset), (c) N_2 sorption and pore size distribution of SNG, and (d) Raman spectra of GO, rGO, N-rGO, and SNG.

Figure 6.1c displays that the pore structure of SNG mainly had a mesopore distribution. The specific surface areas (SSAs) of GO, rGO, N-rGO, and SNG were 29.9, 255.4, 81.5, and 69.1 m^2/g , respectively. The SSA of rGO increased significantly after thermal annealing owing to the expansion and exfoliation of graphene layers. Heat treatment can contribute to expanding graphene layers, removing surface oxides and reducing the interaction between layers due to the removal of water and functional

groups at the surface and edges of graphene. However, the SSA of rGO decreased to some extents after doping with nitrogen and sulfur atoms, which was in consistent with the distortion and multi-layered structure presented in the SEM and TEM images. The decreased SSA of doped samples might be due to the lower exfoliation degree induced by the reduction/annealing processes with the presence of nitrogen and sulfur precursors. The intercalation of dopants resulted in the highly mis-orientated and crinkled structure to graphene planes, also prevented the formation of few layered structure.(34)

Raman spectroscopy is a very powerful tool to evaluate the structure of nanocarbons and the quantity of exposed edges.(35, 36) Two peaks at 1310 and 1570 cm^{-1} observed in Figure 6.1d are corresponding to the D band and G band, respectively, and no obvious shifts were found. The D band usually results from the defects and distortion of carbon layers while the G band is closely related to the crystalline and graphitic structure.(34, 37) Therefore, the intensity ratio of D to G (I_D/I_G) can clearly indicate the defect degrees of carbon materials. Generally, introducing heteroatoms into the graphene network would create more defective sites and then increase the I_D/I_G ratio.(38) Specifically, the I_D/I_G value of rGO (1.20) is slightly higher than the GO (1.18), which was possibly attributed to the decays in graphene sheets and creation of more active edges during the thermal reduction process.(20) Compared with rGO, I_D/I_G ratios were enhanced after incorporating with N atoms (N-rGO, 1.23) and co-doping with N and S atoms (SNG, 1.30) into the graphene sheets. Co-doping of sulfur with nitrogen resulted in more defective sites and further interrupted the graphitic carbon configuration as well as electronic structure of graphene sheets.

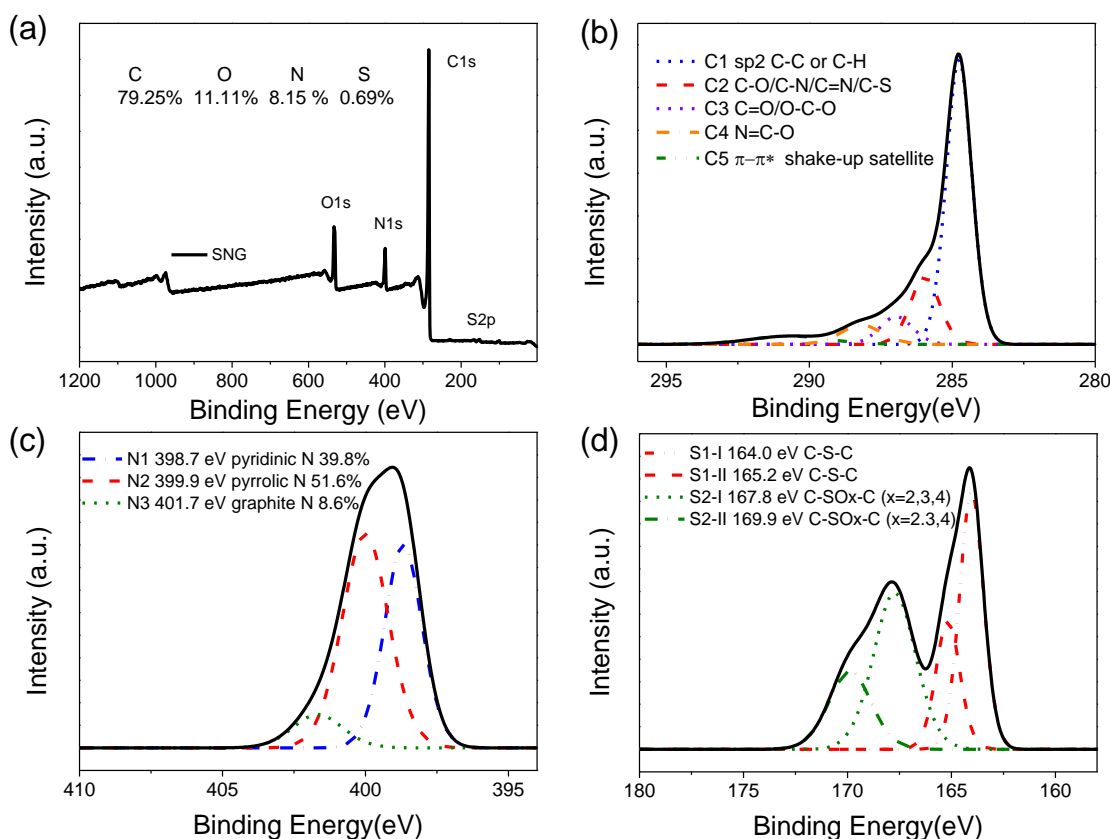


Figure 6.2. (a) XPS survey of SNG, and high resolution XPS (b) C1s, (c) N1s, and (d) S 2p.

Figure 6.2a displays the elemental composition from XPS analysis. Oxygen content was reduced from 31 at.% of GO to 11.11 at.% of rGO because of the decomposition of oxygen functional groups. A nitrogen doping level at 8.15 at.% was achieved, which was higher than that of 3~5 at.% via annealing in NH_3 atmosphere and 5.8 at.% by a plasma-assisted method.(39, 40) Besides, a sulfur doping level of 0.69 at.% was obtained. The relatively low S content was attributed to the larger atom radius (1.03\AA vs 0.71\AA of N and 0.75\AA of C), which makes it more difficult to be incorporated into the graphene layer.

The strong peak at the binding energy of 284.8 eV was corresponding to the sp^2 -hybridized carbon atoms in the honeycomb lattice. Figure 6.2b reveals that the C1s can be fitted into five components. The main peak at 284.8 eV was assigned to the sp^2 carbon, suggesting that most of the carbon atoms still remained in the conjugated graphene system,(41) which was further confirmed by the broad peak of shake-up

satellite at the binding energy of 290.7 eV. The peak at 284.8 eV (C2) was assigned to the sp^2 -carbon bonded with heteroatoms such as C-O, C-N, C=N, and C-S, while the peak at binding energy of 287.0 eV (C3) could be attributed to carbon atoms double-bonded with oxygen atoms such as C=O and/or O-C-O. The peak with a higher binding energy of 288.2 eV was possibly from the carbon atoms that bonded with N and O at the same time (N=C-O).(42)

High resolution XPS N1s was obtained to investigate the doped N species (Figure 6.2c). It is noted that three types of nitrogen: pyridine-like, pyrrole-like, and quaternary N (also known as graphitic N), were found in SNG with a level of 39.8, 51.6, and 8.6 at.% in overall N dopants, respectively. It is well known that a higher temperature could afford more instinct doping of N into the graphene basal plane, whereas elevated temperatures could also break up the C-N bond and result in the loss of nitrogen.(39, 43) Besides, the oxygen groups on GO can serve as active sites and bonding reconstruction are necessary for N atoms to be incorporated into the highly conjugated graphene lattice.(36, 37, 39) Figure 6.S1 shows the thermal analysis of the samples, indicating that the temperature of removal and decomposition of oxygen-functional groups was at the range of nitrogen doping process.

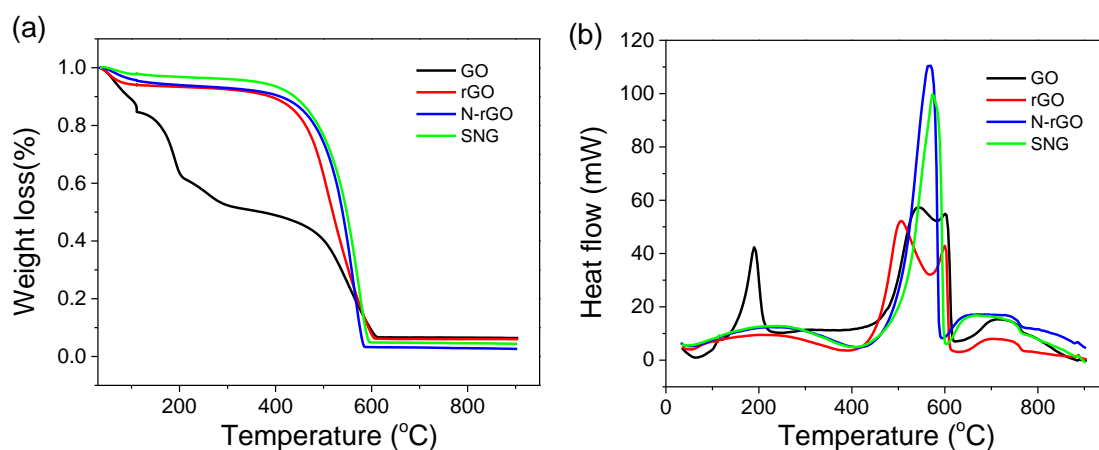


Figure 6.S1. TGA (a) and DSC (b) curves of carbon materials. Thermal stability was improved for rGO, N-rGo and SNG due to removal of functional groups. It is noted that only one great exothermal peak appears after doping.

Chemical states of sulfur dopants were illustrated in Figure 6.2d. Usually the S p2 peak would split into two linked peaks S p1/2 and S p3/2. The two adjacent peaks at 164.0 and 165.2 eV were assigned to the C-S-C, whereas the peaks at the bind energy of around 167.8 and 169.9 eV were attributable to C-SO_x-C (x = 2, 3, 4).^(14, 44) The XPS indicated that sulfur atoms were successfully doped into the graphene layer. It is worthwhile noting that the S-doping was achieved in this study by a facile method without any critical synthesis conditions widely used in the previous studies such as chemical vapor deposition (CVD) or thermal annealing at high temperature.^(31, 45)

6.3.2 Phenol Oxidative Degradation on Nanocarbons.

The adsorption and catalytic oxidation profiles of phenol on various nanocarbons are shown in Figure 6.3. It is noted that PMS could rarely oxidize phenol and only 12% of phenol was removed in 180 min. About 15% of phenol removal was achieved by the adsorption of SNG-0.3. The SNG was able to completely degrade phenol in 90 min and demonstrated the best performance for phenol removal. The SNG was more efficient than the rGO prepared by a hydrothermal method and multi-walled carbon nanotubes with 71% and 76% phenol removal, respectively, within 180 min in previous studies.^(17, 46) A first-order kinetic model was applied for the evaluation of catalytic phenol oxidation on graphene samples (Eq. 6.1).

$$\ln\left(\frac{c}{c_0}\right) = -k_{obs} \cdot t \quad \text{Eq (6.1)}$$

SNG-0.3 was found to have an apparent reaction rate constant of $0.043 \pm 0.002 \text{ min}^{-1}$, which was 86.6, 22.8, 19.7, and 4.5 folds higher than that of GO, rGO, S-rGO-0.3 and N-rGO, respectively. The reaction rate of SNG for phenol degradation was estimated to be $0.860 \pm 0.040 \text{ ppm/min}$, which was much higher than Co-SBA-15/PMS (0.175 ppm/min) and Co-ZSM-5/PMS (0.019 ppm/min) systems.^(47, 48) In a pioneering study, a N-doped rGO was demonstrated to effectively activate PMS for phenol oxidation with a superior degradation efficiency comparable to the most popular metal oxides, such as $\alpha\text{-MnO}_2$ and Co_3O_4 .⁽⁹⁾ It can be seen that co-doping with nitrogen and sulfur into the graphene layer would further enhance the catalytic performance in phenol oxidation.

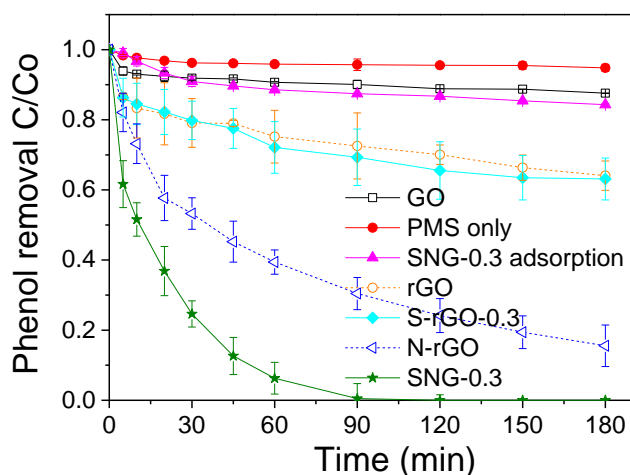


Figure 6.3. Phenol removal efficiencies on various carbon catalysts.

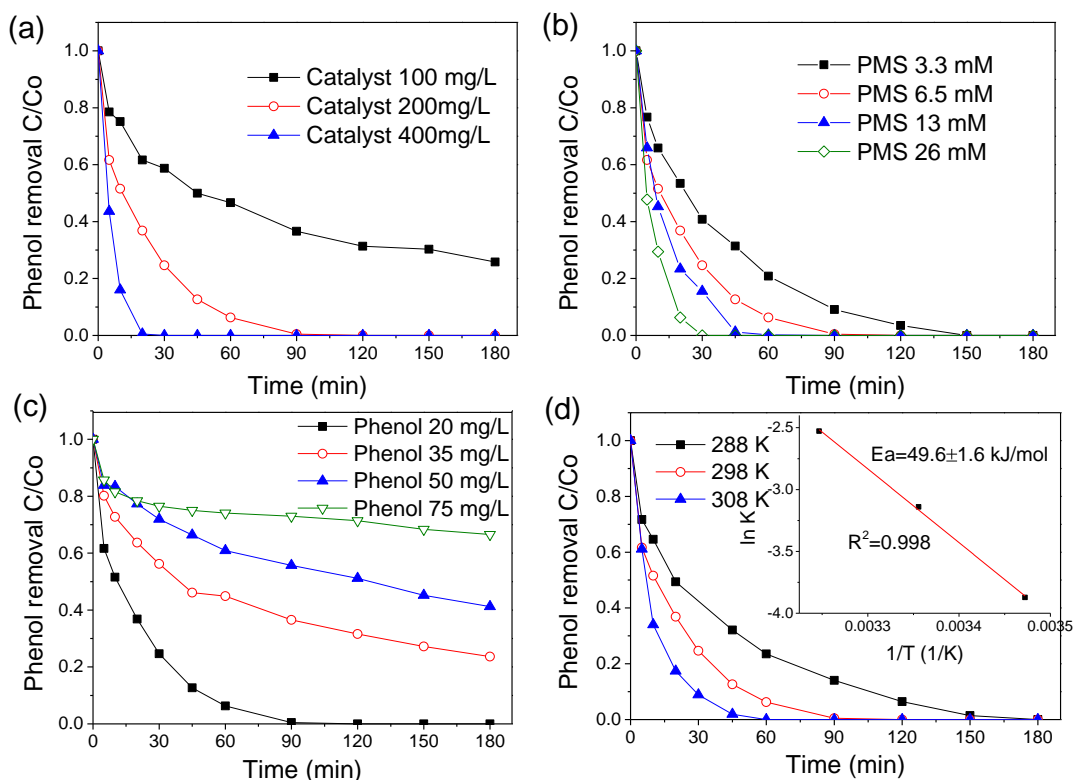


Figure 6.4. Effects of (a) catalyst loading, (b) PMS dosage, (c) initial phenol concentration, and (d) reaction temperature on phenol oxidation on S-N-G.

Figure 6.4a presents the effect of the catalyst loading on PMS activation. It is well known that an increase of catalyst dosage can bring out more active sites to react with PMS, hereby dramatically promote the generation of active radicals. More specifically,

75% of phenol was decomposed in 180 min at 0.1 g/L catalysts, while 100% phenol removal was obtained in 90 and 20 min when the catalyst amount was increased to 0.2 and 0.4 g/L, respectively.

Phenol removal efficiency was also influenced by the dosage of PMS as shown in Figure 6.4b. The total duration for 100% phenol degradation was reduced from 150 to 30 min with the addition of PMS from 3.3 to 26 mM. It was found that in the $\text{Co}_3\text{O}_4/\text{PMS}$ system, further increase of PMS loading (more than 6.5 mM) would decrease the phenol removal efficiency, owing to the extra SO_5^- in solution reacting with $\text{SO}_4^{\bullet-}$ to generate SO_5^- , which possesses a lower oxidative potential (1.1 V) than the $\text{SO}_4^{\bullet-}$ (2.5-3.1 V).^(48, 49) However, compared with the metal catalyst, SNG presented greater potential for catalytically activating large amounts of PMS for phenol decomposition.

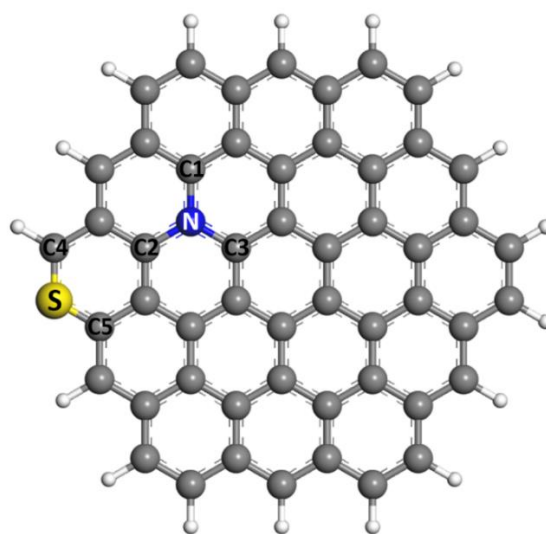
The influence of initial phenol concentration from 20 to 75 mg/L was presented in Figure 6.4c. As expected, the phenol degradation efficiency dropped with the increasing phenol concentration. The apparent reaction rate constants decreased from $0.043 \pm 0.002 \text{ min}^{-1}$ ($R^2 = 0.993$) to $(9.1 \pm 0.8) \times 10^{-3} \text{ min}^{-1}$ ($R^2 = 0.930$), $(6.2 \pm 0.4) \times 10^{-3} \text{ min}^{-1}$ ($R^2 = 0.941$) and $(3.1 \pm 0.5) \times 10^{-3} \text{ min}^{-1}$ ($R^2 = 0.905$) with the addition of phenol from 20 to 35, 50, 75 mg/L, accordingly. It is deduced that the excess adsorption of phenol could cover the active sites of the catalysts, giving rise to the low catalytic activity for PMS activation. Moreover, the low reaction efficiency of phenol oxidation was also possibly due to the deficiency of PMS as the produced active radicals would be quickly consumed by the excess radical inhibitor (phenol and intermediates), thereby slowing down its own consumption by radicals.

Reaction temperature also acts as a significant factor in phenol removal. Figure 6.4d indicates that a higher reaction rate was achieved at an elevated temperature. For instance, complete phenol degradation was obtained in 60 min at the reaction temperature of 308 K ($k_{\text{obs}} = 0.080 \pm 0.005 \text{ min}^{-1}$, $R^2 = 0.977$), compared with 90 min and 180 min of phenol removal at 298 K ($k_{\text{obs}} = 0.043 \pm 0.002 \text{ min}^{-1}$, $R^2 = 0.993$) and 288 K ($k_{\text{obs}} = 0.021 \pm 0.005$, $R^2 = 0.987$), respectively. Based on the Arrhenius equation, the activation energy (E_a) of SNG for catalyzed phenol oxidative degradation was

estimated to be 49.6 ± 1.6 kJ/mol, which was lower than that of pristine graphene (68.4 ± 3.6 kJ/mol), S-rGO (86.2 ± 2.5 kJ/mol) (data not shown here) and typical cobalt based catalysts ($59.7\sim 69.7$ kJ/mol(17, 47, 50)), yet similar to that of N-rGO (48.8 ± 1.9 kJ/mol). The effect of sulfur level on phenol oxidation is shown in Figure 6.S8 , indicating that sulfur dopant also affected the catalytic activity of rGO.

6.3.3 Catalytic Mechanism of PMS Activation on Graphene.

It was reported that the more electronegative N atoms (3.04 vs 2.55 of carbon) can effectively facilitate electron transfer from the neighbouring C and lead to a high charge density of carbon atoms. On the other hand, sulfur has a close electronegativity (2.58) to carbon and can reduce the energy difference of graphene between the highest unoccupied molecular orbital (HOMO) and the lowest unoccupied molecular orbital (LUMO) after doping and alter the electron configuration of sp^2 carbon system.(26, 51, 52) Yang and co-workers suggested that the spin density played the dominant role for promoting ORR performance of the S-doped graphene.(14) Zhang et al. (53) reported that S-doped graphene clusters (sulfur or sulfur oxide) distributed at the zigzag edges would induce a larger spin and charge density to neighbouring carbon and create more active sites for the ORR reaction. Long et al. (37) suggested quaternary N to be the active sites for selective oxidation of benzylic alcohol. Recent studies also demonstrated that S-N co-doping presented a synergistic effect owing to the re-distribution of spin and charge densities and newly created more active sites. (26, 42, 45)



Scheme 6.1. Molecular model of S-, N-dual doped graphene.

Table 6.1. Charge density of atoms in graphene model.

Atom Number	Graphene	S-doped graphene	N-doped graphene	S-,N- doped graphene	S-, S-, N- Graphene
N	--	--	-0.65	-0.65	-0.68
S	--	0.12	--	1.23	0.58
C1	0.16	0.11	0.29	0.26	0.08
C2	-0.09	0.08	0.29	0.36	0.17
C3	-0.07	0.02	0.58	0.56	0.49
C4	-0.01	-0.38	-0.10	-0.42	0.00
C5	0.05	0.12	0.22	0.06	-0.31

Density functional theory (DFT) calculations were carried out to give further insights into the effects of dopants on the electron states of carbon atoms in a graphene sheet model (Scheme 6.1). Figures 6.S2 shows the molecular structures and spin densities of pure and modified graphene materials. As seen in Table 6.1, negligible charge transfer among the involving carbon atoms was found in the S-doped graphene, while N doping induces a high positive charge density to the adjacent carbons (C1, C2, and C3). Co-doping of S into the N-doped graphene further increases the charge density of the C2 from 0.31 to 0.48. The electrostatic potential mapping in Figure 6.5 revealed that the doping process would significantly break the chemical inertness of pristine graphene and change the electron distribution and surface chemistry. The theoretical calculations were consistent with the experimental findings that single sulfur doping presented a poor activity for PMS activation, while N-rGO demonstrated a better performance for phenol removal. Sulfur and nitrogen co-doping demonstrated a greater catalytic activity than pristine graphene and S- or N-doped rGO. We supposed that positively charged carbon sites might be the active sites to facilitate the adsorption of HSO_5^- and break up O-O bond (HO-SO_4^-) in PMS activation.⁽⁵⁴⁾ The synergistic effect of S and N co-doping can effectively break the inertness of carbon systems, activate the sp^2 -hybridized carbon lattice and facilitate the electron transfer from covalent graphene sheets to PMS for radical generation.

The effect of co-doped sulfur amount was investigated and the enhancement of catalysis is shown in Figure 6.6. The activity increased with the addition of BDS from the level of 0.05 ~ 0.3 g/g GO and dropped when the BDS/GO was increased to 0.5

g/g, yet still higher than the N-rGO. It was suggested that increasing sulfur amount in a certain range can improve the catalytic performance of phenol oxidative decomposition, yet the synergistic effect would be weakened when superabundant sulfur atoms were introduced into the graphene framework. The excess sulfur might break the charge balance of the covalent graphene electron system and disrupt the charge re-distribution when S became the dominant dopant as sole S-doping, presenting a poor catalytic activity as evidenced in Figure 6.S3. This is further verified by theoretical calculations that the charge density of C1, C2, C3 decreased from 0.26, 0.36 and 0.56 (S-N-G) to 0.08, 0.17, and 0.49 (S-S-N-G), respectively, and that the positive charged area reduced significantly when one more sulfur atom was introduced into the S-N-graphene model (S-S-N-G, Figure 6.5e). It can be suggested that, compared with metal-based catalysts, the overall catalytic performance for PMS activation on graphene is not simply relying on the increasing of N and S active sites but the contributions from intricately synergistic coupling interactions between the dopants. The same phenomenon was also reported in B and N dual-doped systems.(16)

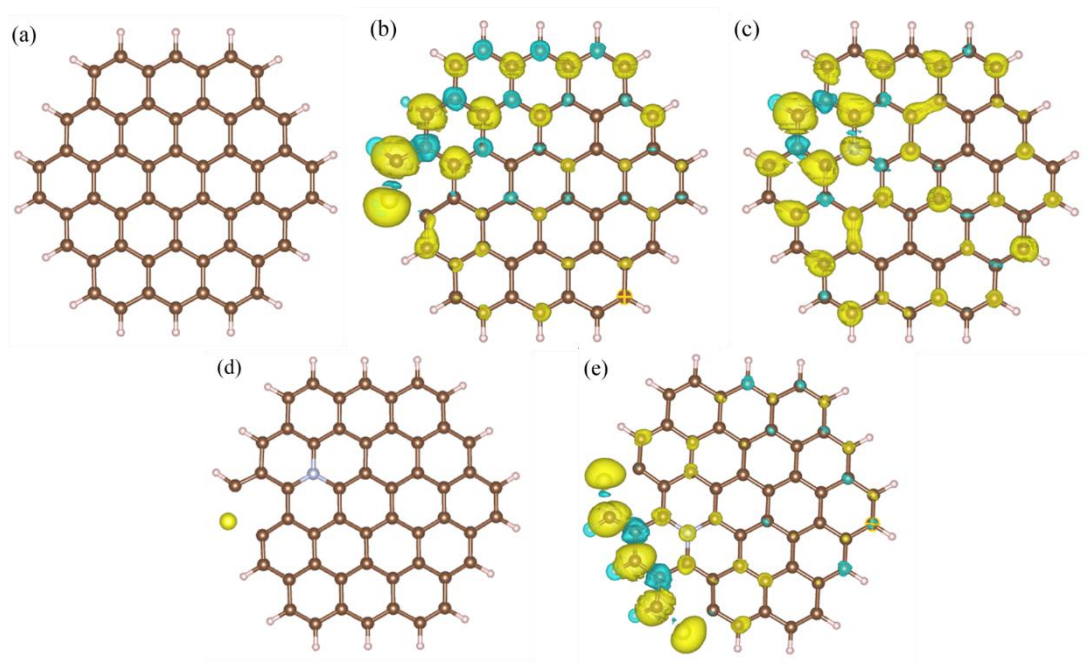


Figure 6.S2. Spin density isosurface for (a) undoped model graphene, (b) S-G, (c) N-G, (d) S-N-G, and (e) S-S-N-G.

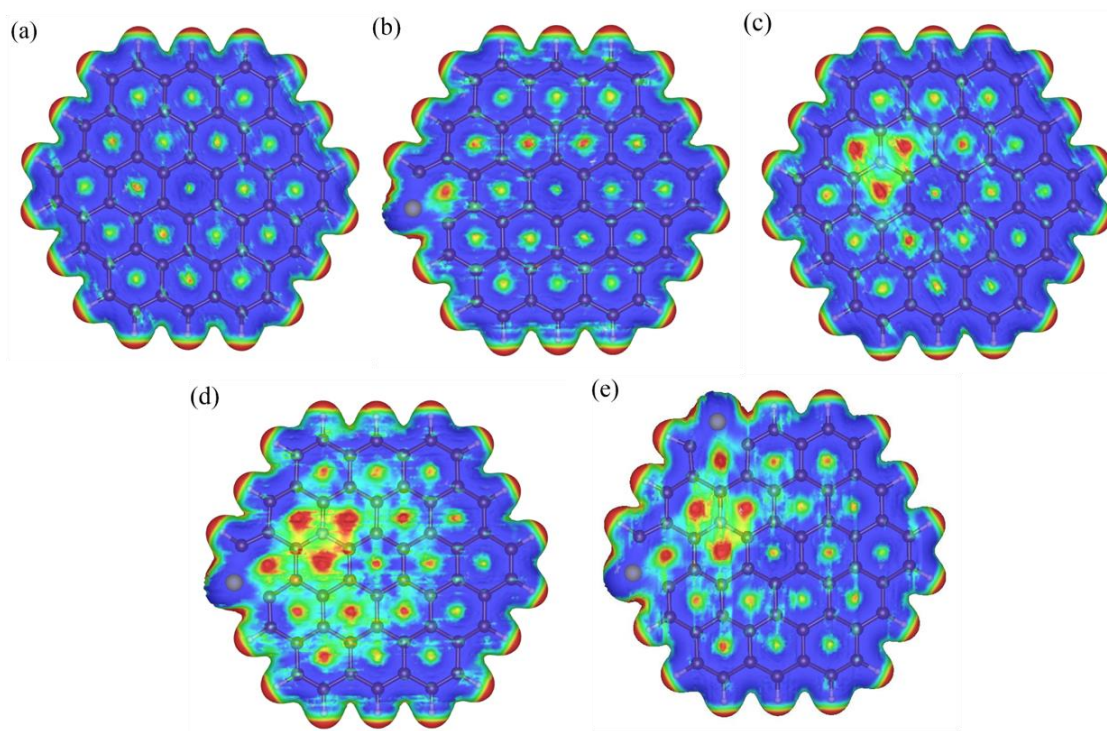


Figure 6.5. Electrostatic potential mapping from charge density matrix for (a) undoped model graphene, (b) S-G, (c) N-G, (d) S-N-G, and (e) S-S-N-G.

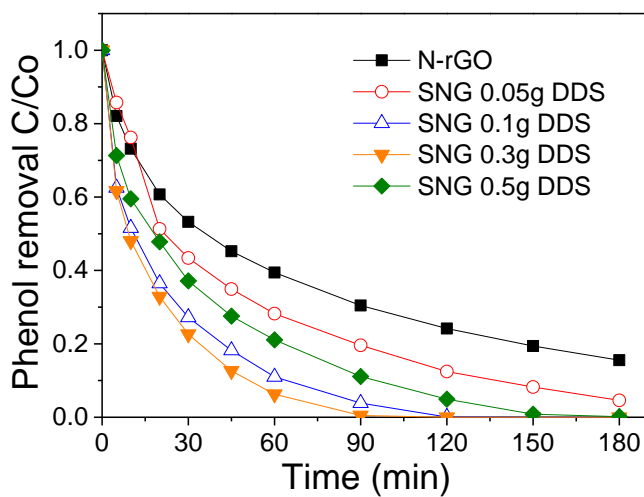


Figure 6.6. Phenol removal on N-rGO and S, N co-doped rGO with different contents of sulfur precursor (per gram GO) (catalyst: 0.2 g/L; PMS: 6.5 mM; phenol: 20 mg/L; T: 298K)

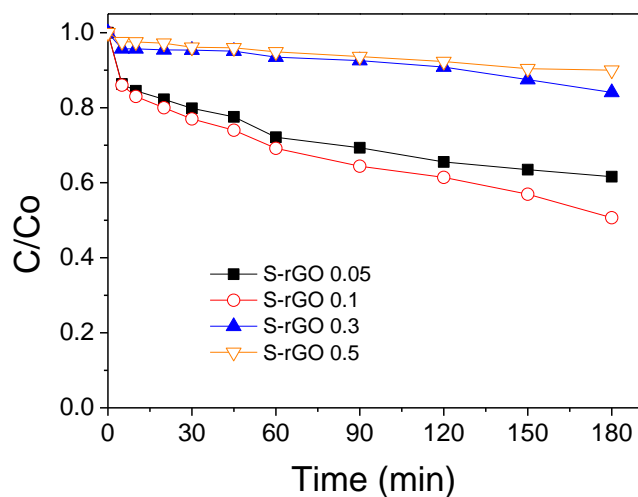
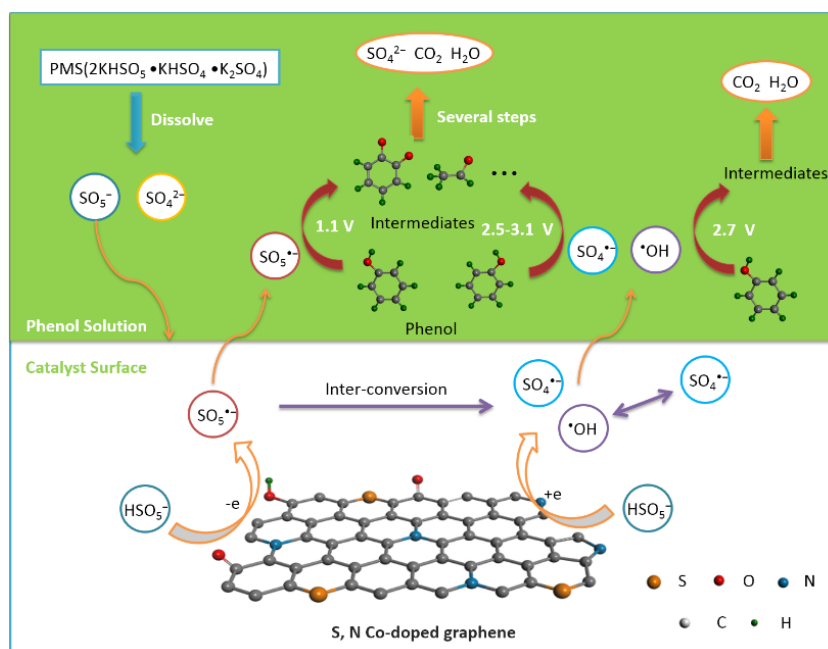


Figure 6.S3. Phenol removal on S-doped rGO with different contents of sulfur precursor (catalyst: 0.2 g/L; PMS: 6.5 mM; phenol: 20 mg/L; T: 298 K)



Scheme 6.S1. Proposed reaction pathways of phenol oxidation by PMS activation on SNG.

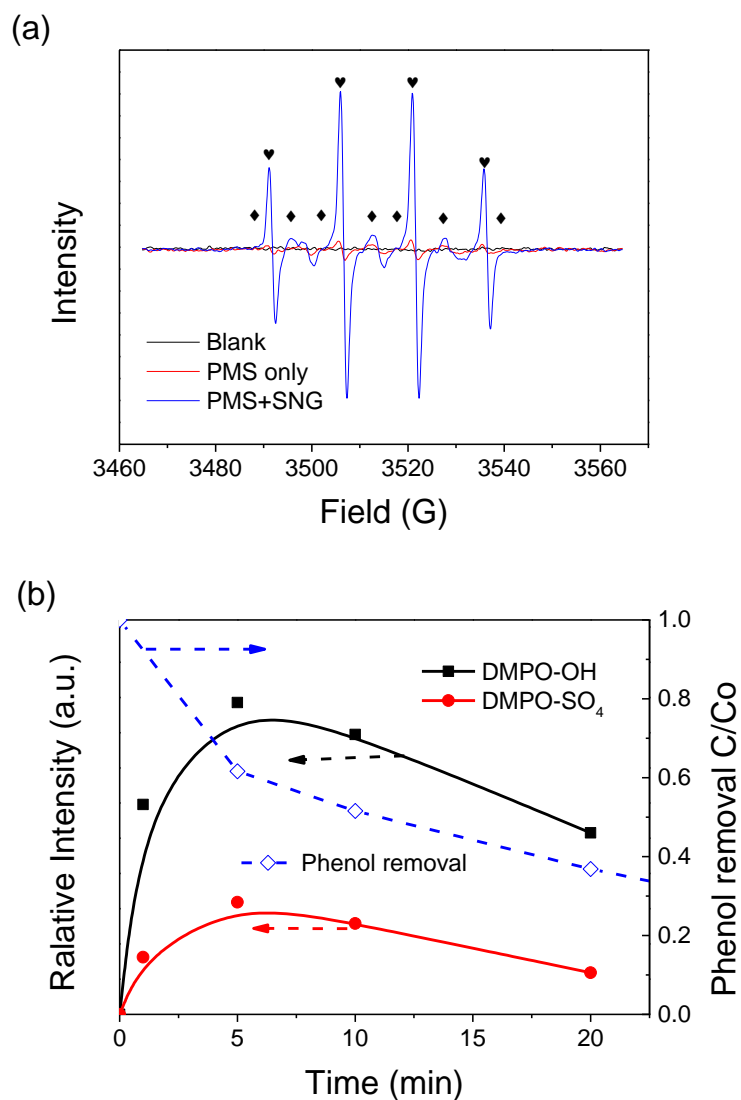


Figure 6.7. (a) EPR spectra of PMS activation under different conditions. (♥: DMPO-OH, ♦: DMPO-SO₄) (b) Radicals evolution during the PMS activation on SNG. (Catalyst: 0.2 g/L; PMS: 6.5 mM; phenol: 20 mg/L; T: 298 K; DMPO: 0.08 M)

To experimentally probe the PMS activation processes, EPR was employed to identify the reactive radicals using DMPO as a spin trapping agent. Figure 6.7a shows that SNG demonstrated an excellent performance for activating PMS to generate active radicals. Radical evolution in Figure 6.7b reveals that both SO₄^{•-} and [•]OH were quickly produced in the first five minutes. Their intensities then gradually went down owing to the consumption by phenol oxidation. Huang and co-workers (55, 56) applied Fe₃O₄ nanoparticles to activate PMS and found that only [•]OH was initially generated in the first few minutes and the concentration of SO₄^{•-} climbed up afterwards. The same phenomena also occurred in a CoPc/PMS system. It can be suggested that the

radical generation process on nanocarbons might be different from that on metal-based catalysts. Chemically modified graphene can activate PMS to produce both sulfate and hydroxyl radicals effectively for pollutants degradation. It is noted that the relative intensity of DMOP-OH is much higher than that of DPMO-SO₄, suggesting that •OH might play a critical role in phenol degradation, especially in the first few minutes. The competitive radical quenching tests (Figure 6.S4) indicate that sulfate radicals also presented a great effect in the whole process of phenol oxidation.

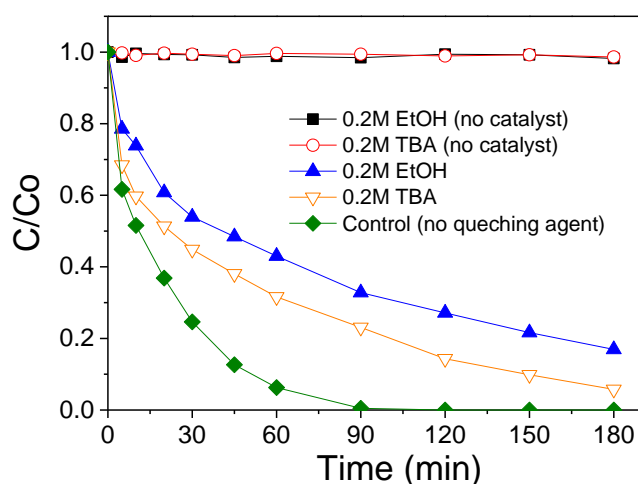


Figure 6.S4. Competitive radical tests under various conditions. (Catalyst: 0.2 g/L; PMS: 6.5 mM; phenol: 20 mg/L; T: 298 K) Ethanol (EtOH) and tert-butanol (TBA) are two classical radical scavengers to identify the reactive radicals. Ethanol can quickly react sulphate ($k_{\text{SO}_4^{\cdot-}} = (1.6-7.7) \times 10^9 \text{ M}^{-1}\text{s}^{-1}$) and hydroxyl radicals ($k_{\cdot\text{OH}} = (1.2-2.8) \times 10^9 \text{ M}^{-1}\text{s}^{-1}$), whereas tert-butanol (TBA) indicates different reaction rates towards sulfate ($k_{\text{SO}_4^{\cdot-}} = (4.0-9.1) \times 10^5 \text{ M}^{-1}\text{s}^{-1}$) and hydroxyl radicals ($k_{\cdot\text{OH}} = (3.8-7.6) \times 10^8 \text{ M}^{-1}\text{s}^{-1}$)

Figure 6.S5 shows the stability of SNG in repeated uses. It should be noted that the stability of the SNG was not comparable to conventional metal-based catalysts. The poor reusability of nanocarbons applied under high oxidant concentration was also found in rGO, N-rGO, and BNG in our previous studies.(9, 17) Figures 6.S6 and Table 6.S1 indicate the possible deactivation mechanism with changed surface chemistry and pore structures, which was due to the strong oxidation process and coverage of adsorbed phenol and intermediates which tend to block the pores and interact with sp²-hybridized carbon lattice. Future studies need be done to design efficient and robust

carbocatalysts to improve the stability for practical application. Based on above studies, the degradation mechanism was proposed in Scheme 6.S1. This will provide informative results for future studies on the reusability enhancement.

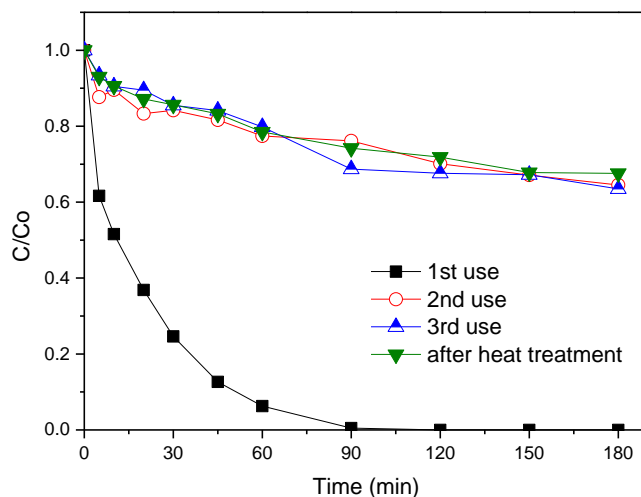


Figure 6.S5. Stability and recyclability test of S-N-doped graphene. (Catalyst: 0.2 g/L; PMS: 6.5 mM; phenol: 20 mg/L; T: 298 K) The catalytic activity of SNG reduced significantly after the 1st use. Interestingly, it was found that the catalysts stabilized for the 2nd and 3rd use and almost no further active sites were recovered after heat treatment.

Table 6.S1. Nitrogen sorption results of SNG before and after reaction

	BET surface area	Pore volume	Average pore size
SNG	69.1	0.17	9.1
SNG used	43.8	0.12	12.0

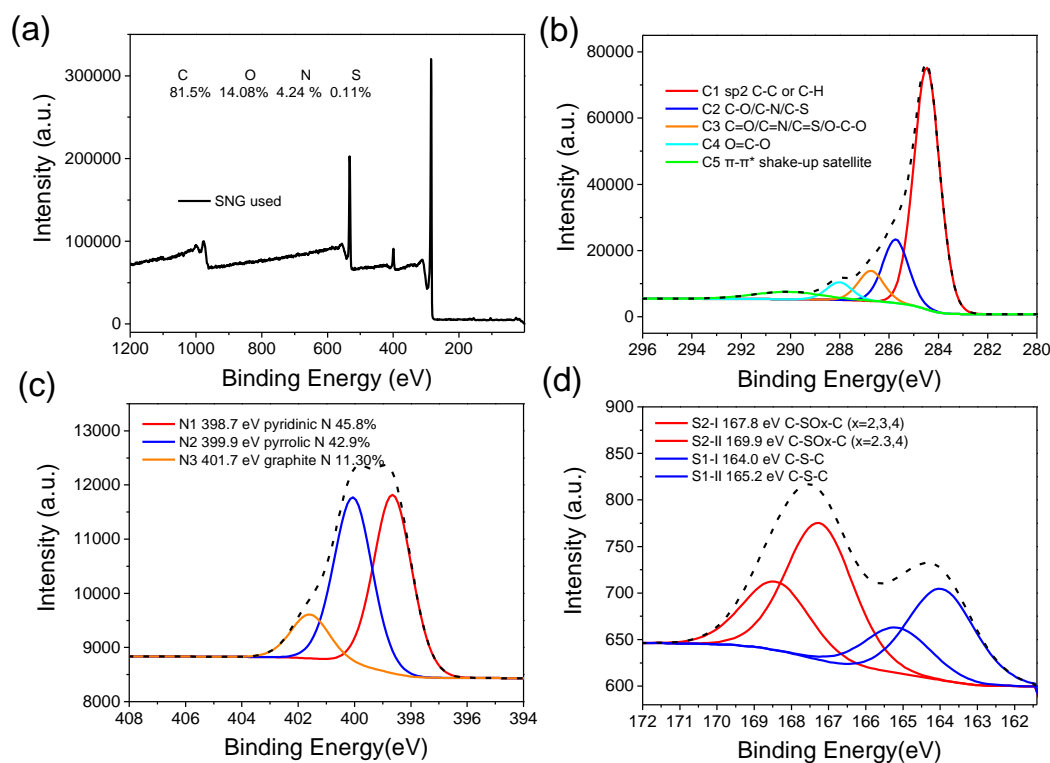


Figure 6.S6. (a) XPS survey and high resolution spectra of (b) C1s, (c) N1s, (d) S2p for SNG after 1st run.

6.4 Conclusions

We developed a facile one-pot strategy to successfully incorporate sulfur and nitrogen atoms into graphene sheets. Both experimental and theoretical studies demonstrated that co-dopants (S and N) presented synergistically catalytic activity to enhance the PMS activation compared to the pristine and N- (or S-) sole-doped graphene. Kinetic studies indicated that catalyst loading, PMS dosage, initial phenol concentration and reaction temperature would pose significant influences on the phenol removal efficiencies. EPR spectra and competitive radical tests suggested that both hydroxyl and sulfate radicals were generated and played critical roles in phenol oxidative decomposition. The theoretical calculations also suggested that introducing sulfur into N-doped graphene can significantly change the surface charge distribution and electrostatic potential of graphene. Experimental results demonstrated that, compared with boron, phosphorus, and iodine, sulfur can function as an effective co-dopant to further enhance catalytic activity of N-doped graphene for phenol degradation with

radicals. This study suggested that chemically modified graphene is able to be utilized as a superior metal-free catalyst for sustainable environmental remediation.

References

1. Lin TQ, Huang FQ, Liang J, Wang YX. A facile preparation route for boron-doped graphene, and its CdTe solar cell application. *Energ. Environ. Sci.* 2011; 4(3):862-5.
2. Li N, Chen ZP, Ren WC, Li F, Cheng HM. Flexible graphene-based lithium ion batteries with ultrafast charge and discharge rates. *P. Natl. Acad. Sci.* 2012; 109(43):17360-5.
3. El-Kady MF, Strong V, Dubin S, Kaner RB. Laser scribing of high-performance and flexible graphene-based electrochemical capacitors. *Science.* 2012;335(6074):1326-30.
4. Wood KN, O'Hayre R, Pylypenko S. Recent progress on nitrogen/carbon structures designed for use in energy and sustainability applications. *Energ. Environ. Sci.* 2014; 7(4):1212-49.
5. Wang HB, Maiyalagan T, Wang X. Review on recent progress in nitrogen-doped graphene: synthesis, characterization, and its potential applications. *ACS Catal.* 2012 ;2(5):781-94.
6. Wang SY, Zhang LP, Xia ZH, Roy A, Chang DW, Baek JB, et al. BCN graphene as efficient metal-free electrocatalyst for the oxygen reduction reaction. *Angew. Chem. Int. Ed.* 2012; 51(17):4209-12.
7. Su DS, Zhang J, Frank B, Thomas A, Wang XC, Paraknowitsch J, et al. Metal-free heterogeneous catalysis for sustainable chemistry. *Chemsuschem.* 2010; 3(2):169-80.
8. Dreyer DR, Jia HP, Bielawski CW. Graphene Oxide: A convenient carbocatalyst for facilitating oxidation and hydration reactions. *Angew. Chem. Int. Ed.* 2010; 49(38):6813-6.
9. Sun HQ, Wang YX, Liu SZ, Ge L, Wang L, Zhu ZH, et al. Facile synthesis of nitrogen doped reduced graphene oxide as a superior metal-free catalyst for oxidation. *Chem. Commun.* 2013; 49(85):9914-6.
10. Zhu YW, Murali S, Cai WW, Li XS, Suk JW, Potts JR, et al. Graphene and graphene oxide: synthesis, properties, and applications. *Adv. Mater.* 2010; 22(35):3906-24.
11. Huang CC, Li C, Shi GQ. Graphene based catalysts. *Energ. Environ. Sci.* 2012;5(10):8848-68.
12. Kong XK, Chen CL, Chen QW. Doped graphene for metal-free catalysis. *Chem. Soc. Rev.* 2014;43(8):2841-57.

13. Frank B, Zhang J, Blume R, Schlogl R, Su DS. Heteroatoms increase the selectivity in oxidative dehydrogenation reactions on nanocarbons. *Angew. Chem. Int. Ed.* 2009;48(37):6913-7.
14. Yang Z, Yao Z, Li GF, Fang GY, Nie HG, Liu Z, et al. Sulfur-doped graphene as an efficient metal-free cathode catalyst for oxygen reduction. *ACS Nano.* 2012;6(1):205-11.
15. Zhao Y, Yang LJ, Chen S, Wang XZ, Ma YW, Wu Q, et al. Can boron and nitrogen co-doping improve oxygen reduction reaction activity of carbon nanotubes? *J. Am. Chem. Soc.* 2013;135(4):1201-4.
16. Zheng Y, Jiao Y, Ge L, Jaroniec M, Qiao SZ. Two-step boron and nitrogen doping in graphene for enhanced synergistic catalysis. *Angew. Chem. Int. Ed.* 2013; 52(11):3110-6.
17. Sun HQ, Liu SZ, Zhou GL, Ang HM, Tade MO, Wang SB. Reduced graphene oxide for catalytic oxidation of aqueous organic pollutants. *ACS Appl. Mater. Interfaces.* 2012;4(10):5466-71.
18. Jiang DE, Sumpter BG, Dai S. Unique chemical reactivity of a graphene nanoribbon's zigzag edge. *J. Chem. Phys.* 2007; 126(13).
19. Liu SZ, Peng WC, Sun HQ, Wang SB. Physical and chemical activation of reduced graphene oxide for enhanced adsorption and catalytic oxidation. *Nanoscale.* 2014; 6(2):766-71.
20. Peng WC, Liu SZ, Sun HQ, Yao YJ, Zhi LJ, Wang SB. Synthesis of porous reduced graphene oxide as metal-free carbon for adsorption and catalytic oxidation of organics in water. *J. Mater. Chem. A.* 2013;1(19):5854-9.
21. Deng DH, Pan XL, Yu LA, Cui Y, Jiang YP, Qi J, et al. Toward n-doped graphene via solvothermal synthesis. *Chem. Mater.* 2011; 23(5):1188-93.
22. Choi CH, Park SH, Woo SI. Binary and ternary doping of nitrogen, boron, and phosphorus into carbon for enhancing electrochemical oxygen reduction activity. *ACS Nano.* 2012; 6(8):7084-91.
23. Choi CH, Chung MW, Jun YJ, Woo SI. Doping of chalcogens (sulfur and/or selenium) in nitrogen-doped graphene-CNT self-assembly for enhanced oxygen reduction activity in acid media. *RCS Adv.* 2013; 3(30):12417-22.
24. Paraknowitsch JP, Thomas A. Doping carbons beyond nitrogen: an overview of advanced heteroatom doped carbons with boron, sulphur and phosphorus for energy applications. *Energ. Environ. Sci.* 2013; 6(10):2839-55.
25. Hummers Jr WS, Offeman RE. Preparation of graphitic oxide. *J. Am. Chem. Soc.* 1958; 80(6):1339-.
26. Liang J, Jiao Y, Jaroniec M, Qiao SZ. Sulfur and nitrogen dual-doped mesoporous graphene electrocatalyst for oxygen reduction with synergistically enhanced performance. *Angew. Chem. Int. Ed.* 2012; 51(46):11496-500.

27. Blum V, Gehrke R, Hanke F, Havu P, Havu V, Ren XG, et al. Ab initio molecular simulations with numeric atom-centered orbitals. *Comput. Phys. Commun.* 2009; 180(11):2175-96.
28. Perdew JP, Burke K, Ernzerhof M. Generalized gradient approximation made simple. *Phys. Rev. Lett.* 1996; 77(18):3865-8.
29. Tang W, Sanville E, Henkelman G. A grid-based Bader analysis algorithm without lattice bias. *J. Phys. Condens. Mat.* 2009;21(8).
30. Su YZ, Zhang Y, Zhuang XD, Li S, Wu DQ, Zhang F, et al. Low-temperature synthesis of nitrogen/sulfur co-doped three-dimensional graphene frameworks as efficient metal-free electrocatalyst for oxygen reduction reaction. *Carbon.* 2013; 62:296-301.
31. Yang SB, Zhi LJ, Tang K, Feng XL, Maier J, Mullen K. Efficient synthesis of heteroatom (n or s)-doped graphene based on ultrathin graphene oxide-porous silica sheets for oxygen reduction reactions. *Adv. Funct. Mater.* 2012; 22(17):3634-40.
32. Yeh TF, Syu JM, Cheng C, Chang TH, Teng HS. Graphite oxide as a photocatalyst for hydrogen production from water. *Adv. Funct. Mater.* 2010; 20(14):2255-62.
33. Li Y, Zhao Y, Cheng HH, Hu Y, Shi GQ, Dai LM, et al. Nitrogen-doped graphene quantum dots with oxygen-rich functional groups. *J. Am. Chem. Soc.* 2012; 134(1):15-8.
34. Qu LT, Liu Y, Baek JB, Dai LM. Nitrogen-doped graphene as efficient metal-free electrocatalyst for oxygen reduction in fuel cells. *ACS Nano.* 2010; 4(3):1321-6.
35. Geng DS, Chen Y, Chen YG, Li YL, Li RY, Sun XL, et al. High oxygen-reduction activity and durability of nitrogen-doped graphene. *Energ. Environ. Sci.* 2011; 4(3):760-4.
36. Sheng ZH, Shao L, Chen JJ, Bao WJ, Wang FB, Xia XH. Catalyst-free synthesis of nitrogen-doped graphene via thermal annealing graphite oxide with melamine and its excellent electrocatalysis. *ACS Nano.* 2011; 5(6):4350-8.
37. Long JL, Xie XQ, Xu J, Gu Q, Chen LM, Wang XX. Nitrogen-doped graphene nanosheets as metal-free catalysts for aerobic selective oxidation of benzylic alcohols. *ACS Catal.* 2012; 2(4):622-31.
38. Ismagilov ZR, Shalagina AE, Podyacheva OY, Ischenko AV, Kibis LS, Boronin AI, et al. Structure and electrical conductivity of nitrogen-doped carbon nanofibers. *Carbon.* 2009; 47(8):1922-9.
39. Li XL, Wang HL, Robinson JT, Sanchez H, Diankov G, Dai HJ. Simultaneous nitrogen doping and reduction of graphene oxide. *J. Am. Chem. Soc.* 2009; 131(43):15939-44.

40. Kumar NA, Nolan H, McEvoy N, Rezvani E, Doyle RL, Lyons MEG, et al. Plasma-assisted simultaneous reduction and nitrogen doping of graphene oxide nanosheets. *J. Mater. Chem. A* 2013;1(14):4431-5.
41. Park JE, Jang YJ, Kim YJ, Song MS, Yoon S, Kim DH, et al. Sulfur-doped graphene as a potential alternative metal-free electrocatalyst and Pt-catalyst supporting material for oxygen reduction reaction. *Phys. Chem. Chem. Phys.* 2014; 16(1):103-9.
42. Wohlgemuth SA, White RJ, Willinger MG, Titirici MM, Antonietti M. A one-pot hydrothermal synthesis of sulfur and nitrogen doped carbon aerogels with enhanced electrocatalytic activity in the oxygen reduction reaction. *Green Chem.* 2012; 14(5):1515-23.
43. Kinoshita K. *Carbon: electrochemical and physicochemical properties.* 1988.
44. Yan Y, Yin YX, Xin S, Guo YG, Wan LJ. Ionothermal synthesis of sulfur-doped porous carbons hybridized with graphene as superior anode materials for lithium-ion batteries. *Chem. Commun.* 2012; 48(86):10663-5.
45. Xu JX, Dong GF, Jin CH, Huang MH, Guan LH. Sulfur and nitrogen co-doped, few-layered graphene oxide as a highly efficient electrocatalyst for the oxygen-reduction reaction. *Chemsuschem.* 2013; 6(3):493-9.
46. Sun HQ, Kwan C, Suvorova A, Ang HM, Tade MO, Wang SB. Catalytic oxidation of organic pollutants on pristine and surface nitrogen-modified carbon nanotubes with sulfate radicals. *Appl. Catal., B* 2014; 154:134-41.
47. Shukla P, Wang SB, Singh K, Ang HM, Tade MO. Cobalt exchanged zeolites for heterogeneous catalytic oxidation of phenol in the presence of peroxymonosulphate. *Appl. Catal., B* 2010; 99(1-2):163-9.
48. Shukla P, Sun HQ, Wang SB, Ang HM, Tade MO. Co-SBA-15 for heterogeneous oxidation of phenol with sulfate radical for wastewater treatment. *Catal. Today.* 2011; 175(1):380-5.
49. Saputra E, Muhammad S, Sun HQ, Ang HM, Tade MO, Wang SB. Manganese oxides at different oxidation states for heterogeneous activation of peroxymonosulfate for phenol degradation in aqueous solutions. *Appl. Catal., B* 2013; 142:729-35.
50. Shukla PR, Wang SB, Sun HQ, Ang HM, Tade M. Activated carbon supported cobalt catalysts for advanced oxidation of organic contaminants in aqueous solution. *Appl. Catal., B* 2010; 100(3-4):529-34.
51. Glenis S, Nelson AJ, Labes MM. Sulfur doped graphite prepared via arc discharge of carbon rods in the presence of thiophenes. *J. Appl. Phys.* 1999; 86(8):4464-6.
52. Kurita N, Kobayashi K, Kumahora H, Tago K, Ozawa K. Molecular-Structures, Binding-Energies and Electronic-Properties of Dopyballs C59x (X = B, N and S). *Chem. Phys. Lett.* 1992; 198(1-2):95-9.

53. Zhang LP, Niu JB, Li MT, Xia ZH. Catalytic mechanisms of sulfur-doped graphene as efficient oxygen reduction reaction catalysts for fuel cells. *J. Phys. Chem. C* 2014;118(7):3545-53.
54. Duan X, Sun H, Wang Y, Kang J, Wang S. N-doping-induced nonradical reaction on single-walled carbon nanotubes for catalytic phenol oxidation. *ACS Catal.* 2014; 5(2):553-9.
55. Tan C, Gao N, Deng Y, Deng J, Zhou S, Li J, et al. Radical induced degradation of acetaminophen with Fe₃O₄ magnetic nanoparticles as heterogeneous activator of peroxymonosulfate. *J. Hazard. Mater.* 2014; 276(0):452-60.
56. Huang ZF, Bao HW, Yao YY, Lu WY, Chen WX. Novel green activation processes and mechanism of peroxymonosulfate based on supported cobalt phthalocyanine catalyst. *Appl. Catal., B* 2014;154:36-43.

Every reasonable effort has been made to acknowledge the owners of copyright material. I would be pleased to hear from any copyright owner who has been omitted or incorrectly acknowledged.

Chapter 7. Effect of Nitrogen-Doping on Single-Walled Carbon Nanotubes on Activation of Superoxide O-O Bond for Enhanced Metal-Free Oxidation

Abstract

Metal-free materials have demonstrated to be promising alternatives to conventional metal-based catalysts. Comparable catalysis on nanocarbons against cobalt- or manganese-based catalysts in peroxymonosulfate (PMS) activation has been achieved, yet the catalyst stability has to be addressed and the mechanism is also needed to be elucidated. In this study, N-doped carbon nanotubes was employed as a metal-free catalyst for phenol catalytic oxidation with sulfate radicals, and more importantly, detailed mechanism in PMS activation and the roles of nitrogen heteroatoms were comprehensively investigated. For the first time, a non-radical pathway accompanying with radical generation ($\cdot\text{OH}$ and $\text{SO}_4^{\cdot-}$) in phenol oxidation with PMS was discovered upon nitrogen heteroatom doping. The NoCNTs presented an excellent stability due to the emerging non-radical processes. Moreover, emerging characteristics upon nitrogen-doping was differentiated in activation of superoxides over single-walled carbon nanotubes. Both experimental and theoretical studies revealed that enhanced peroxymonosulfate (PMS) activation is ascribed to a nonradical process while persulfate (PS) activation is accelerated via direct oxidizing water, yet hydrogen peroxide (H_2O_2) activation is inert to N-doping. This study dedicates the first insights into versatile N-doping in carbocatalysis for organic oxidation in sustainable remediation. The findings can be used for design of efficient and robust metal-free catalysts with both superior catalytic performance and high stability for various heterogeneous catalytic processes.

Part 1. N-Doping-Induced Nonradical Reaction on Single-Walled Carbon Nanotubes for Catalytic Phenol Oxidation

7.1 Introduction

Modern chemistry and chemical engineering heavily rely on catalytic processes that have dramatically initiated and sustained global industrialization.(1) Most homogeneous and heterogeneous catalytic processes are based on either noble,(2) transition,(3) and rare-earth(4) metals or their oxides. The issues of metal-based catalysts, such as the scarcity in nature, deactivation, high cost in disposal of waste catalysts and secondary pollution, have been experienced in terms of sustainable development. Moreover, the inherent chemical complexity of metal-based catalysts, including various forms of polyvalent states,(5) bridging and terminal of lattice oxygen,(6) and side reactions,(7) has imposed a variety of difficulties in the mechanistic studies.(1, 8) Therefore, novel metal-free materials are highly desirable as alternatives to metal-based catalysts.

In environmental remediation, advanced oxidation processes (AOPs) have been widely employed owing to the complete destruction of organic pollutants to water and carbon dioxide.(9) Most AOPs such as Fenton reaction,(10) catalytic ozonation,(11) photocatalysis(12) and oxidation with sulfate radicals,(13, 14) are based on catalytic processes. In most cases, metal-based catalysts were used to mediate the formation of reactive radicals. Hydroxyl radicals ($\cdot\text{OH}$) have been observed in the most of above AOPs, and demonstrated high efficiencies and almost non-selectivity to organic pollutants. The demerits of hydroxyl radicals are low pH 3-4 (Fenton), use of specific instruments (ozonation and photocatalysis), and secondary contamination of sludge and metal leaching. (15)

In 1956, Ball and Edward(16) discovered that peroxymonosulfuric acid (Caro's acid) was highly reactive and able to facilitate degradation of pollutants in water. The involved sulfate radicals not only are flexible to a wide pH range up to natural and basic conditions, but also have a higher redox potential of 2.5-3.1 V than 1.8-2.7 V of

hydroxyl radicals, indicating a more powerful oxidation capability.(17, 18) Homogeneous metal ions(13, 14) and heterogeneous metal oxides(5, 15, 19, 20) have been recently applied to activate peroxydisulfate (PMS) to generate sulfate radicals for decomposition of organic pollutants. The main problem of these catalytic oxidation processes was toxic metal leaching.

Recently, metal-free materials have attracted increasing attention as sustainable alternatives to metal-based catalysts. In energy conversion or chemical synthesis, metal-free catalysts are expected to reduce the cost, prevent deactivation and facilitate mechanistic studies.(21-23) For environmental catalysis, metal-free catalysts can provide an extra advantage of non-secondary contamination especially in water remediation. For the first time, we reported that chemically reduced graphene oxide (rGO) is able to activate PMS to produce sulfate radicals for phenol oxidation.(24) Physical and chemical modifications were able to create porous structures and tune the surface acidity/alkalinity, and then improve the adsorption and catalytic activity of rGO.(25, 26) Further studies also suggested that nitrogen doping can significantly enhance the efficiencies of nanocarbons in PMS activation.(27, 28) Though oxygen functional groups, defective edges and heteroatoms in sp^2 carbon framework were suggested to be the active sites, solid and insightful mechanism of PMS activation on nanocarbons is still lacking. Moreover, the stability of metal-free materials is required to enable the practical applications.

In this study, we developed a one-pot synthesis of N-doped nanocarbon (NoCNT-700) using single-walled carbon nanotubes (oCNTs) with a novel N precursor of melamine at 700 °C. This synthesis was free of critical conditions such as vacuum, plasma and high temperature above 900 °C, and toxic/explosive nitrogen precursors like NH_3 and ammonium nitrate.(27-29) The high degree of graphitic structure and low oxygen content in CNTs would make it possible to identify the roles of doped nitrogen. Electron paramagnetic resonance (EPR) and classical radical quenching tests were used to investigate the PMS activation and phenol oxidation. Unlike other AOPs in which free radicals are the keys for organic degradation, non-radical processes were, for the first time, observed on the modified CNT samples upon nitrogen doping. Non-radical processes were identified in Fenton or Gif chemistry (selective hydrocarbon activation chemistry),(30-32) yet have been barely reported in AOPs. Very recently,

Zhang et al.(33, 34) indicated that ozonation or peroxydisulfate (PDS) activation without radical generation can degrade organic pollutants in water. CuO was essential in the ozonation and PDS activation. Nevertheless, the non-radical oxidation has never been reported in carbocatalysis for heterogeneous oxidation. The observation of non-radical processes of PMS activation upon nitrogen doping in this study significantly contributed to mechanistic studies on the active sites of metal-free catalysts and suggested an efficient strategy for improving the catalytic stability of such catalysts.

7.2 Experimental Section

7.2.1 Synthesis of Nitrogen Modified Single-Walled Carbon Nanotubes (SWCNTs). Commercial SWCNTs (1.0 g, 99.9%) were firstly mixed with nitric acid (100 mL, 70 wt.%) and stirred on a hotplate at 100 °C for 4 h to remove any metal residuals to get metal-free CNT(oCNT). The material was filtered and washed with ultrapure water and dried in an oven at 60 °C overnight. Melamine was added to the oCNT/ethanol suspension, and stirred at 50 °C to evaporate ethanol to obtain a homogenous mixture of oCNT and melamine. The dried mixture was transferred to a tube furnace for annealing at 700 °C for 1 h under N₂ (40 mL/min) atmosphere. The sample was collected and washed with ultrapure water several times and dried at 60 °C in an oven overnight. Thus, nitrogen-doped carbon nanotubes (NoCNT-700) were obtained. oCNT-700 was prepared with the same procedure without melamine. NoCNT-350 was prepared using ammonium nitrate as a N precursor for annealing at 350 °C.

7.2.2 Characterization of Materials. X-ray diffraction (XRD) patterns were obtained on a Bruker D8-Advanced X-ray instrument using Cu-K α radiation with λ at 1.5418 Å. Raman spectra were acquired on an ISA dispersive Raman spectrometer using argon ion lasers (514 nm). X-ray photoelectron spectroscopy (XPS) was performed on a Kratos AXIS Ultra DLD system under UHV condition with Al-K α X-ray to investigate the composition and chemical states. Data were analyzed with Kratos Vision and CasaXPS software.

7.2.3 Evaluation of the Catalytic Performance. The catalytic activity of the materials was evaluated in catalytic oxidation of phenol. The reactions were carried out in phenol

aqueous solution (20 ppm, 500 mL) with a catalyst (100 mg/L) and PMS (6.5 mM) at 25 °C. During each interval, 1 mL solution was withdrawn by a syringe and filtered by a 0.45 µm film, and injected into a vial that was priorly filled with 0.5 mL methanol for quenching the reaction. The sample was analyzed by a high performance liquid chromatography (HPLC, Varian) with a C-18 column. After each run, the used catalyst was collected by ultrasonic washing for 5 min and washed with ultrapure water (500 mL) 3 times, filtered and dried in an oven for reuse.

7.2.4 Mechanistic Studies of the Catalytic Processes. An EMS-plus EPR instrument from Bruker was employed to detect the free radicals captured by 5,5-dimethyl-1-pyrroline (DMPO, >99.0%) during PMS activation, operating at the following conditions: center field: 3515G; sweep width: 100G; microwave frequency: 9.87GHz; power setting: 18.75mW; and scan number: 3. The radical quantitative information was acquired from the Spin Fitting from Bruker Xenon Software Package. Identification of major radicals as well as the radical vs non-radical processes were investigated by classical quenching tests. The procedure was similar to the typical phenol degradation mentioned above, but the reactions were carried out with addition of different amounts of ethanol.

7.3 Results and Discussion

XRD patterns of pristine and modified SWCNTs are illustrated in Figure 7.1.1a. The strong diffraction peak at 25.9 ° and weak peak at 43.0 ° were, respectively, assigned to the (002) and (111) reflections of the hexagonal graphitic structure of carbon nanotube.(35, 36) Thermal treatment and nitrogen doping at 350 or 700 °C did not significantly change the XRD patterns, indicating the stable crystal structure of the CNTs.

Raman spectra of CNTs are displayed in Figure 7.1.1b. The characteristic D band (1319 cm⁻¹), G band (1580 cm⁻¹), and 2D band (2623 cm⁻¹) were observed. The D band to G band ratios (I_D/I_G) can be used to evaluate the structural disorder of carbon materials.(37) The I_D/I_G values of oCNT, oCNT-700, NoCNT-350, and NoCNT-700 were estimated to be 0.205, 0.212, 0.247, and 0.354, respectively. It could be found that the defective degree of oCNT and oCNT-700 was at a low level. Also, N doping

could bring about great interruption to the well-ordered sp^2 hybridized and curved honeycomb nanosheets. It was worthwhile to note that the I_D/I_G of NoCNT was much lower than the doped graphene (commonly >1),⁽³⁷⁻³⁹⁾ suggesting that after doping the graphitic structure of CNTs still remained very well, which can also be confirmed by the results of XRD, SEM (scanning electron microscopy), and TEM (transition electron microscopy)(Figure 7.1.S1). (40)

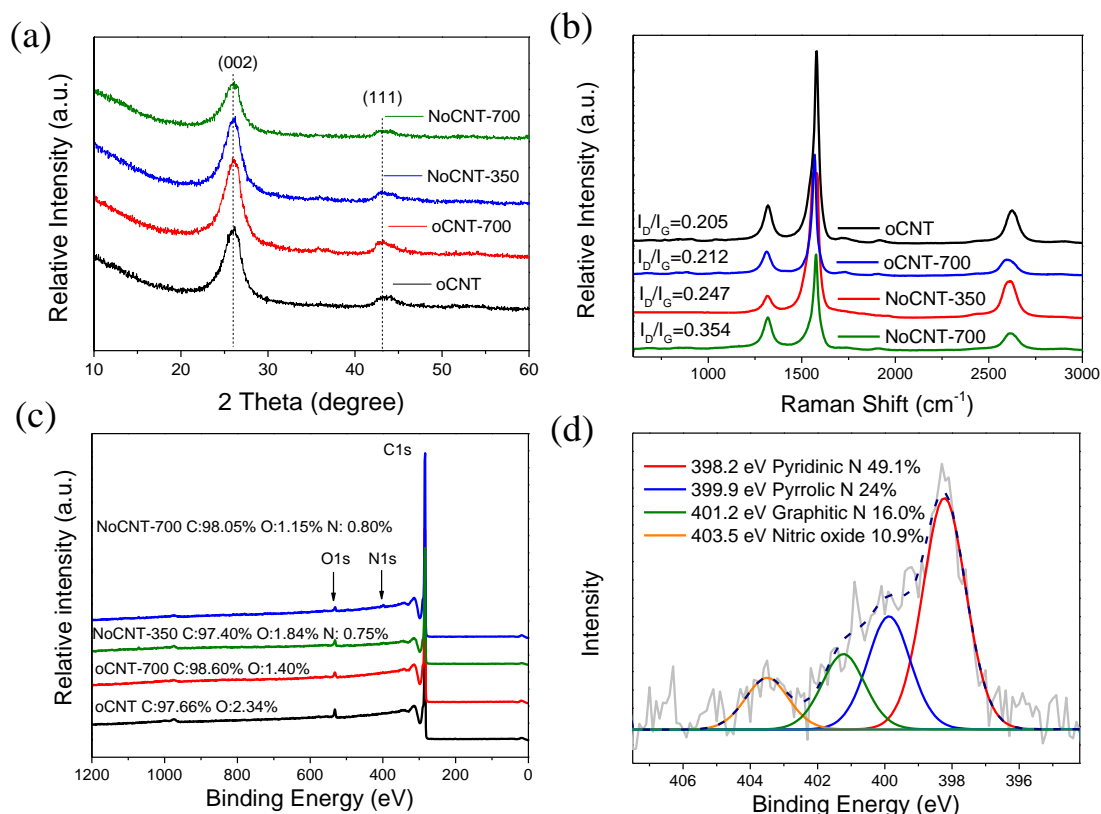


Figure 7.1.1. (a) XRD patterns of oCNT, oCNT-700, NoCNT-350 and NoCNT-700, (b) Raman spectra of CNTs samples, (c) XPS survey of CNTs samples, (d) N1s spectra of NoCNT-700.

XPS studies were carried out to give insights into the composition and chemical states of nitrogen-doped CNTs. As shown in Figure 7.1.1c, 2.34 at.% of oxygen was presented on the pristine CNTs due to the pre-treatment using nitric acid. The oxygen level was subsequently reduced to 1.40 at.%, 1.84 at.% and 1.15 at.% on oCNT-700 after thermal annealing, NoCNT-350 (low-temperature doping) and NoCNT-700 (high-temperature doping), respectively. The oxygen contents in the CNTs samples were much lower than rGO (14.44 at.%) and N-rGO (11.53 at.%) derived from

reduction of graphite oxide,(27) therefore, the effect of oxygen functional groups on catalytic performance was minimized. It is well known that oxides (carboxyl and lactone) started to decompose at the elevated temperatures and the oxygen functional groups played a significant role in reacting with the nitrogen precursors to form C-N bond in the doping process.(37, 41, 42) In this study, N doping at around 0.75 at.% and 0.80 at.% was achieved on the NoCNT-350 and NoCNT-700, respectively. The relative low doping levels compared with N-rGO (5.61 at.%(27) was ascribed to the highly stable structure of the rolled graphene sheets, as rGO usually underwent a self-reconstruction and re-fabrication process during the thermal annealing and doping processes.(28, 43) High resolution XPS N1s spectrum of NoCNT-700 in Figure 7.1.1d was fitted into four peaks with the binding energies at 398.2, 399.9, 401.2, and 403.5 eV, corresponding to the pyridinic, pyrrolic, graphitic (or quaternary) N, and nitrogen oxides, respectively.(37, 41, 42) Substitutional nitrogen doping was achieved at a portion of 16.0 at.% in the overall nitrogen dopants. On the other hand, only pyridinic and pyrrolic nitrogen species were found in NoCNT-350 (data not shown here) due to the low annealing temperature.(28) It was well believed that higher annealing temperature can produce more graphitic nitrogen in the carbon network.(37, 42, 44)

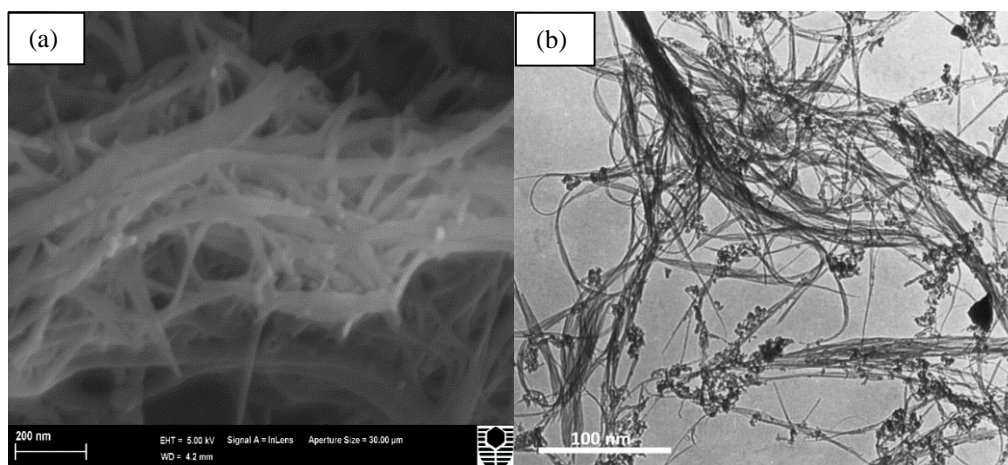


Figure 7.1.S1. (a)SEM (b)TEM image of NoCNT-700.

The catalytic performances of the metal-free nanocarbon materials were evaluated in catalytic activation of PMS for phenol degradation in water solutions. As shown in Figure 7.1.2a, PMS itself could barely degrade phenol indicating that ambient temperature is not able to activate PMS to produce sulfate radicals. Without PMS, only 10% phenol was removed due to adsorption. Undoped oCNT showed a moderate

activity in PMS activation, and 56.5% phenol was decomposed in 180 min with sulfate radicals. It was found that both high-temperature annealing and nitrogen doping can significantly improve the catalytic activity of CNT samples. Phenol removal at 100% was achieved on NoCNT-700, NoCNT-350, and oCNT-700 in 20, 45 and 150 min, respectively. The reaction rate constants for the oCNT, oCNT-700 and NoCNT-700 were estimated to be 0.0043, 0.0231 and 0.2466 min^{-1} , respectively, and the NoCNT-700 presented 57.4- and 10.7-fold enhancement over oCNT and oCNT-700, respectively. The catalytic activities of CNTs samples were compared with two most popular metal-based catalysts in the same conditions. $\alpha\text{-MnO}_2$ and Co_3O_4 provided 93.3% and 100% phenol removal in 180 min, respectively, and the degradation rate of NoCNT-700 was 16.9 and 15.6 times higher than $\alpha\text{-MnO}_2$ and Co_3O_4 accordingly, implying that the metal-free catalyst demonstrated a superior efficiency in PMS activation for phenol degradation.

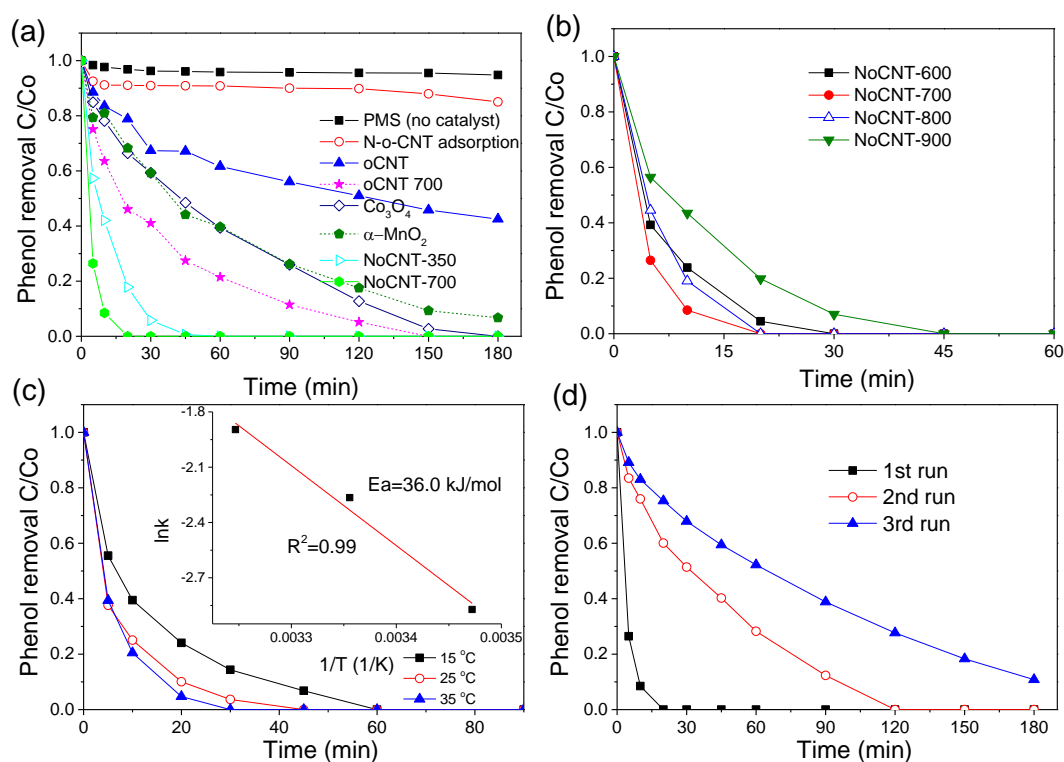


Figure 7.1.2. (a) Phenol removal in various conditions, (b) effect of N-doping temperature on catalytic activity, (c) effect of reaction temperature on phenol degradation and estimation of activation energy (inset) (catalyst = 50 mg/L) and (d) stability tests of PMS/NoCNT-700. Reaction conditions: phenol = 20 ppm, catalyst = 100 mg/L, PMS = 6.5 mM, temperature = 25 °C.

Figure 7.1.2b presented the catalytic performances of N-doped CNTs derived at different annealing temperatures. It was found that the best catalytic performance was achieved on NoCNT-700. It was well reported that high annealing temperature could generate more quaternary nitrogen, which is more thermally stable than the pyrrolic N, into the carbon lattice during the re-construction of graphene sheets under annealing. However, even higher temperature would give rise to the break-up of C-N bond and nitrogen removal.(37, 42, 44) The effect of solution temperature on PMS activation on NoCNT-700 is shown in Figure 7.1.2c. It can be seen that the phenol degradation efficiency slightly increased at the elevated temperatures. Specifically, 100% phenol removal was achieved in 60 min at 15 °C (catalyst = 50 mg/L), and the reaction time for the same phenol removal efficiency decreased to 45 and 30 min at 25 and 35 °C, respectively. The activation energy was reduced from 43.8 kJ/mol (on oCNT-700, data not shown here) to 36.0 kJ/mol (on NoCNT-700) after nitrogen modification.

Reusability tests were also carried out on NoCNT-700 and the results are shown in Figure 7.1.2d. The fresh sample (first run) was able to completely decompose phenol in 20 min and phenol removals at 100% and 89% were attained in 120 min and 180 min for the 2nd and 3rd runs, respectively. In a similar study, MnO₂ supported cobalt catalyst decomposed 100% phenol in 90 min in the first run,(45) and the time for complete phenol removal increased to 150 and 180 min at the second and third runs, respectively. In another study,(15) the time for complete phenol oxidation on 3D MnO₂ in the 1st, 2nd and 3rd runs was 30, 45 and 60 min, respectively. It can be seen that the deactivation on metal-free NoCNT-700 was not as good as cobalt- and manganese-based catalysts. Nevertheless, the catalytic stability of NoCNT-700 was much higher than rGO,(24) which achieved complete decomposition of phenol in 150 min in 1st run, yet only 58% and 25% phenol removals were achieved in 180 min for the 2nd and 3rd runs, respectively. On nitrogen doped rGO,(27) 100% phenol removal required 45 min in 1st run. However, in 2nd run, only 56.0% phenol removal was achieved in 180 min. The high stability of NoCNT-700 will be discussed below in mechanistic studies.

Different from the polyvalent metal sites, the catalytic performance of nanocarbons in heterogeneous systems is closely related to the intricate electronic states and spin

culture of the covalent carbon system.(24) PMS activation indeed relies on the electron transfer from the catalyst to PMS to break up $\text{O}_3\text{SO—OH}$ bond and generate active radicals. The abundant free-flowing electrons in the sp^2 hybridized graphene shell could present great potential to facilitate electron transport to HSO_5^- (PMS) to generate sulfate ($\text{SO}_4^{\cdot-}$) and hydroxyl ($\cdot\text{OH}$) radicals. Unlike the flat sp^2 hybridizations of 2D graphene, the π orbitals of curved 1D carbon nanotubes contain a certain numbers of s electrons with p electrons, probably resulting in higher chemical activities.(46) Besides, the defective sites such as vacancies and non-six-carbon rings, zigzag edges with unconfined π electrons, and Lewis basic groups such as ketonic and quinone groups (C=O) at the defective edges of nanocarbons played more important roles in presenting catalytic potential to induce a redox process.(21, 22, 24, 25, 47) The promoted catalytic performance of oCNT-700 was possibly due to the removal of excess of surface functional groups (the oxygen contents decreased from 2.34 to 1.40 at.%), which might interfere the electron transfer from the CNT sp^2 hybridized carbon system. Decline in oxygen content would also lead to a better reducibility of carbon substrate, tuning the surface charge density, and creating new defective sites during the thermal annealing process. Further doping of N atoms dramatically promoted the catalytic process. In a previous study, we found that nitric oxide (NO_x) demonstrated poor enhancement toward PMS activation.(28) The NoCNT-350 obtained a 21.4-fold enhancement over oCNT in PMS activation with a similar N doping level, yet in that case only pyridinic and pyrrolic N were formed at the defective sites other than substitutional doping in the carbon framework. NoCNT-700 successfully afforded quaternary N into the rolled graphene sheets and presented a stunning reaction rate of 57.4 times faster than oCNT, suggesting that the graphitic N might play a key role in PMS activation. It was reported that the quaternary N has a higher electronegativity and smaller covalent radius to facilitate the electron-transfer from neighbouring C, giving rise to high asymmetric spin and charge density to the adjacent carbon atoms.(44, 48)

It was suggested that metal-based catalysts can activate PMS to produce both hydroxyl and sulfate radicals.(49-51) However, PMS activation processes on metal-free materials have never been investigated. Here, we first employ electron paramagnetic resonance (EPR) to probe the generation and evolution of reactive radicals using 5,5-dimethyl-1-pyrroline (DMPO) as a radical spin trapping agent. Figure 7.1.3a

demonstrates that NoCNT-700 was able to effectively activate PMS to generate both $\text{SO}_4^{\cdot-}$ and $\cdot\text{OH}$. Figure 7.1.3b further illustrates that the active radicals were produced rapidly showing higher concentration in the first few minutes and then dropping gradually due to the consumption in phenol oxidation.

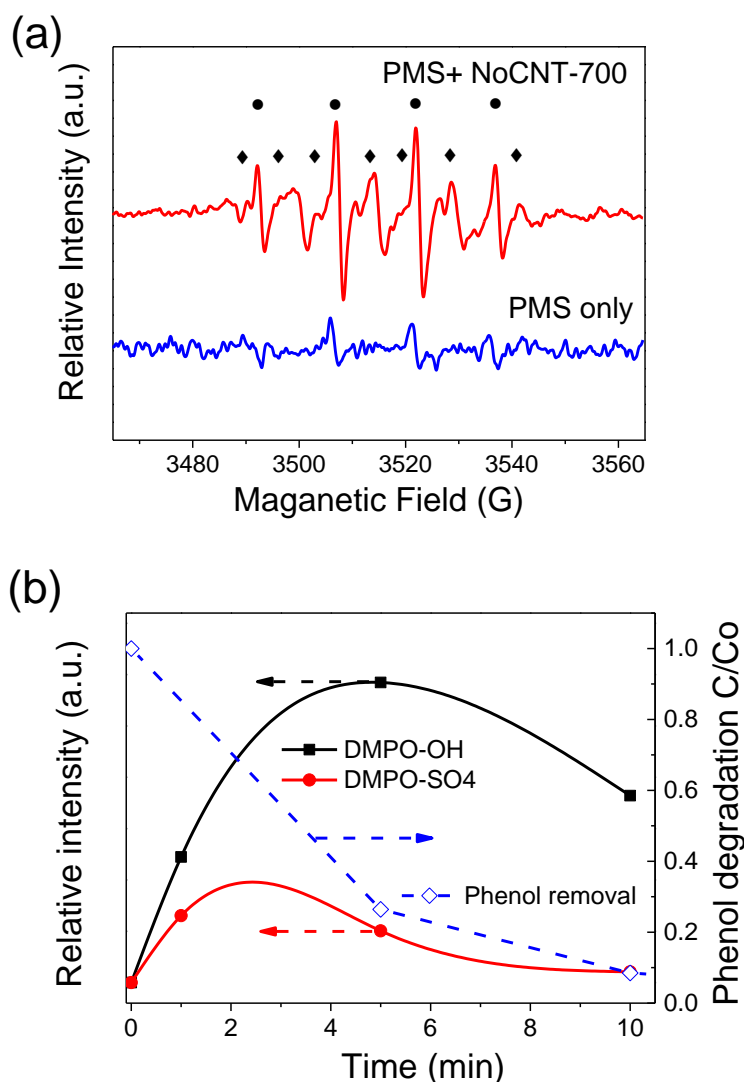


Figure 7.1.3. (a) EPR spectra of PMS activation with NoCNT-700 (●: DMPO-OH, ◆: DMPO-SO₄), (b) Radical evolution during PMS activation on NoCNT-700.

Ethanol was applied as a radical scavenger to quickly react with both hydroxyl and sulfate radical species ($k_{\text{SO}_4^{\cdot-}} = 1.6\sim 7.8 \times 10^7 \text{ M}^{-1} \text{ s}^{-1}$, $k_{\cdot\text{OH}} = 1.2\sim 2.8 \times 10^9 \text{ M}^{-1} \text{ s}^{-1}$) generated in the activation process.(52) In most AOPs, the radicals are essential for the organic degradation reactions. Therefore, if the quenching reagent of ethanol is present in solutions, the degradation would be significantly reduced or prevented.

Control experiments were carried out to compare the catalytic performances with addition of the quenching reagent of ethanol on Co_3O_4 , oCNTs and N-doped CNTs, respectively. Figure 7.1.4a shows the effect of ethanol on phenol catalytic oxidation over a conventional catalyst of cobalt oxide. In the standard condition, 20 ppm phenol was completely removed in 180 min. When ethanol was added into the reaction solution at a molar ratio of 500: 1 (ethanol: PMS), phenol degradation efficiency declined significantly. In 180 min, only around 40% phenol was decomposed. The more ethanol in solution, the lower phenol degradation is. When all water was replaced by ethanol, no phenol degradation was observed, indicating that all generated radicals were quenched rapidly by ethanol before reacting with phenol molecules. Figure 7.1.4b examined the behavior of phenol degradation on oCNT-700 in the presence of ethanol. Similar results were obtained as those of Co_3O_4 , and no phenol degradation occurred in ethanol solution, suggesting the same degradation pathways of oCNT-700 with metal-based catalyst, Co_3O_4 .

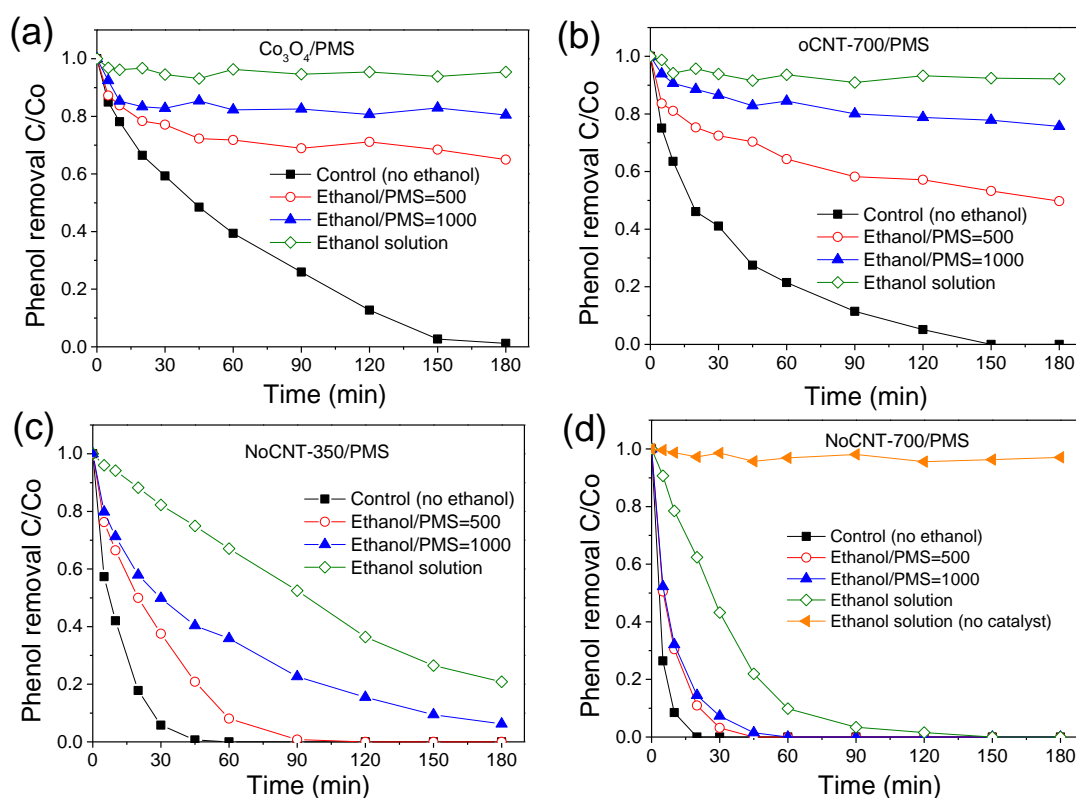
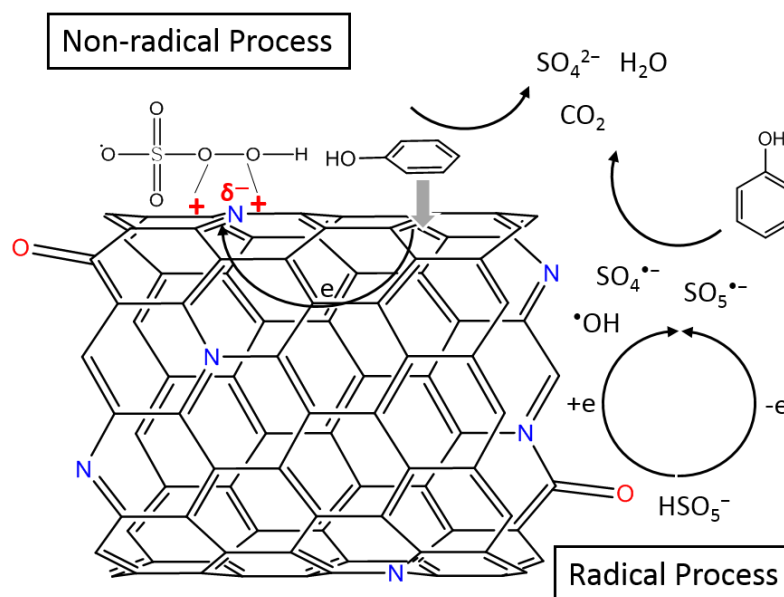


Figure 7.1.4. Effect of radical quenching on phenol degradation, (a) $\text{Co}_3\text{O}_4/\text{PMS}$, (b) oCNT-700/PMS, (c) NoCNT-350/PMS, and (d) NoCNT-700/PMS. Reaction

conditions: phenol = 20 ppm, catalyst = 100 mg/L, PMS = 6.5 mM, temperature = 25 °C.

However, intrinsic difference in the quenching effect on phenol degradation was observed after heteroatom doping in CNTs. Figures 7.1.4 c and d show that NoCNT-350 and NoCNT-700 still maintained excellent phenol degradation efficiency under high concentration of radical quenching agent with PMS. Even in ethanol solution, 79.0% and 100% phenol removal efficiencies were achieved in 180 and 150 min on NoCNT-350 and NoCNT-700, respectively. The results strongly suggested that nitrogen doping has changed the reaction mechanism and induced a new degradation pathway in metal-free NoCNT/PMS systems.



Scheme 7.1.1. Mechanisms of PMS activation on N-doped CNTs.

Previously, few investigations have found non-radical mechanism in Fenton-like reactions. In a previous study,(33) ceria supported CuO was applied to catalytic ozonation of oxalate. The oxalate degradation was dependent on neither hydroxyl radical oxidation nor acid assistance, which were common pathways in such a system. The Cu(II) formed on catalyst surface was suggested to be an active site in coordination with oxalate and then creating a multi-dentate surface complex, which would lead to the oxalate decomposition by intra-molecular electron transfer. More recently, it was reported that PDS could be activated by CuO via a non-radical process

through outer-sphere interaction, followed by a rapid reaction with the model compound of 2,4-dichlorophenol (2,4-DCP).(34)

In this investigation, non-radical process of phenol degradation was found to occur upon N doping in CNTs. The non-radical processes observed in CuO catalysis can be a plausible pathway for phenol degradation on nitrogen doped CNT samples. In the non-radical process, the oxidant (PMS) would first bonded with the sp^2 hybridized system and then reacted with the adsorbed phenol molecules as shown in Scheme 7.1.1. The highly covalent π electrons could activate the O-O bond in PMS and nitrogen dopants (especially for the quaternary N) would further activate the adjacent carbons and dramatically enhance the catalytic performance.

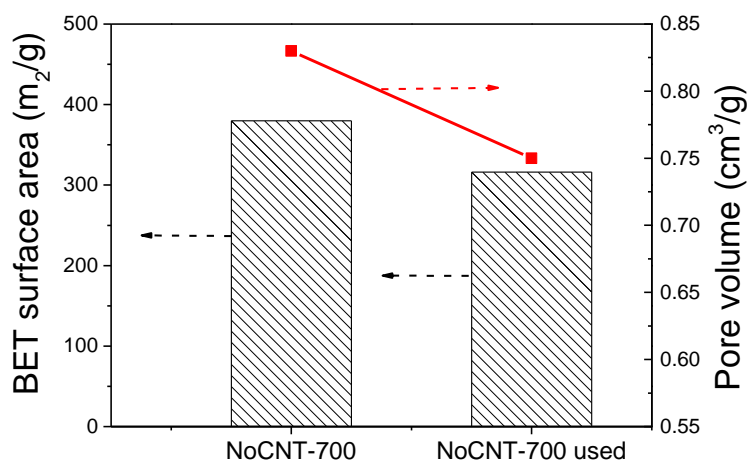
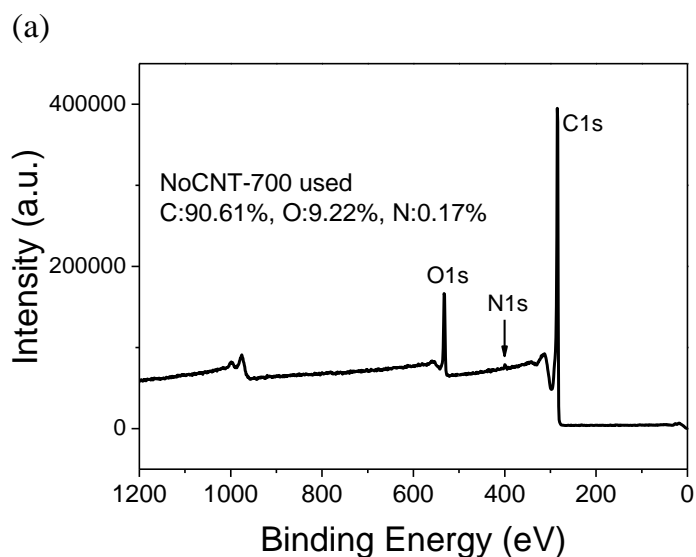


Figure 7.1.S2. BET surface area and pore volume for fresh catalyst and catalyst after 1st run.

Interestingly, it was found that the effect of reaction temperature on NoCNTs catalysis was not as significant as PMS activation on the undoped oCNT-700 and metal-based catalysts. The same phenomenon was also reported in the N-MWCNT(28) and nitrogen modified graphene. Nitrogen heteroatoms in CNT might greatly enhance both the radical and non-radical pathways, which gave rise to a more significant effect than the reaction temperature that controls the electron transfer in the typical radical generation process. Accordingly, the enhanced catalytic performance can be ascribed to both the radical and non-radical processes, which were significantly promoted by

nitrogen doping. Besides, it is worthwhile noting that the stability of NoCNT samples was much better than rGO and N-doped graphene in our previous studies.(24, 27) It was deduced that the defective sites at the carbon edges and functional groups, which played a crucial role in the radical generation, might be covered by the adsorbed phenol and intermediates during the reaction (Figure 7.1.S2).(27) The deactivation process was ascribed to modulation of the charge distribution and functional groups on CNT surface and reconstruction of the dopants (Figure 7.1.S3). As carbon structure in the curved graphene shell of CNT was much more stable, it was more difficult to change the structure and surface chemistry of the rolled CNT than the chemically derived graphene sheets. Since the non-radical processes mainly rely on the activated sp^2 carbon network which was induced by the substantial N-doping, the N-doped carbon nanotubes remain high activity and stability in reuses.



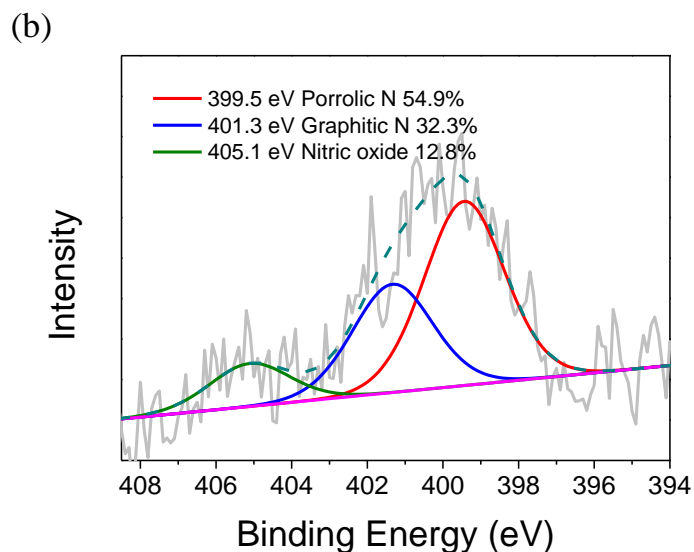


Figure 7.1.S3. (a) XPS survey and (b) N1s high resolution of NoCNT-700 after 1st run.

7.4 Conclusions

In conclusion, chemical modification of SWCNTs with substitutional N-incorporation to the rolled graphene sheets was achieved. NoCNT-700 presented an extraordinarily high catalytic activity for phenol removal by PMS activation with a 57.4-fold enhancement to oCNT, as well as 16.9- and 15.6-fold towards the most effective metal catalysts, α -MnO₂ and Co₃O₄, respectively. The mechanism of PMS activation on carbon nanotube was illustrated. For the first time, we discovered that both radical and non-radical pathways contribute to the phenol degradation on NoCNT with PMS activation. Among the N dopants, graphitic N plays a key role in the non-radical based oxidation process. It was also found that the temperature slightly affects the catalytic efficiency after nitrogen modification and the as-made catalysts presented a much better stability for reuse. Since in this study the nitrogen doping level is low, future studies may be required to investigate on the effect of nitrogen doping levels on the enhanced catalytic performance and reusability. This study provided insights into the roles of nitrogen heteroatoms of nanocarbons for enhanced catalysis, and more importantly, presented a novel view for improving the reusability of metal-free catalysts.

Part 2. Insights into N-Doping in Single-Walled Carbon Nanotubes for Enhanced Activation of Superoxides: A Mechanistic Study

7.5 Introduction

In recent years, water pollution has become one of the key issues in environmental deterioration which triggers worldwide concerns. Sustainable water resources from domestic sewage and industrial wastewater can be exploited through advanced oxidative processes (AOPs). Various superoxides such as ozone (O_3), hydrogen peroxide (H_2O_2), persulfate ($S_2O_8^{2-}$, PS), and peroxymonosulfate (HSO_5^- , PMS) are activated to produce reactive radicals to decompose toxic organic compounds into carbon dioxide, water and mineralized acids. For example, conventional Fenton reactions employ ferrous ions as an efficient homogeneous catalyst to activate H_2O_2 to generate hydroxyl radicals. However, this process requires strict acidic condition (pH~3) and produces a lot of sludge due to coagulation.(53) Metal-based heterogeneous catalysts, such as MnO_2 ,(54) CuO ,(34) $CuFe_2O_4$,(55) and zero valent iron (ZVI)(56), have been used to activate PMS and PS to conduct sulfate radical based oxidation, yet the stubborn toxic metal leaching severely limits the future practical applications.

Emerging carbocatalysis is able to completely avoid the secondary contamination from the metal leaching owing to its metal-free nature.(25, 57) However, the efficiencies of pristine nanocarbons in activation of superoxides are very low. We first discovered that reduced graphene oxide (rGO) can effectively activate PMS and further proved that nitrogen doping can remarkably enhanced the catalytic oxidation.(24, 27) Heteroatom doping has been proven to effectively break the inertness of graphene carbon matrix and induce novel physicochemical and electronic properties for enhanced catalysis.(38, 58-62) More recently, we observed that nitrogen-doping would induce a non-radical pathway in catalytic oxidation with PMS.(63, 64) However, the origin of the emerging features from nitrogen doping is not clear in PMS activation yet, and even more blurred in PS and H_2O_2 activation.

In this study, experimental results and theoretical calculations are integrated to reveal the effect of nitrogen doping on the radical generation processes over single-walled carbon nanotubes (SWCNTs). The pristine SWCNTs was thoroughly refluxed in concentrated nitric acid to remove any potential metal impurities (denoted as o-SWCNT). The purified o-SWCNT was then heated at 700 °C in N₂ to remove excess functional groups (denoted as SWCNT-700), or annealed with melamine as a N-precursor to produce nitrogen-doped sample (denoted as N-SWCNT).⁽⁶⁴⁾ The physical and chemical properties of prepared carbocatalysts are displayed in Table 7.2.S1. The nitrogen modified SWCNTs were designed with a highly crystallized structure ($I_D/I_G=0.35$) and a low oxygen level (1.15 at.%) to minimize the system complexity from defects and functional groups. Effect of nitrogen doping on activation of PMS, PS, and H₂O₂ was evaluated by phenol oxidation.

Table 7.2.S1. Physicochemical properties and reaction rate of superoxides activation for the carbocatalysts.

	S_{BET}	V_{Pore}	I_D/I_G	C	O	N	Reaction rate ppm•min ⁻¹		
	m ² /g	cm ³ /g					PMS	PS	H ₂ O ₂
oSWCNT	407.4	0.58	0.20	97.66	2.34	-	0.09	0.32	0.01
SWCNT-700	445.9	0.95	0.21	98.60	1.40	-	0.46	0.42	0.03
N-SWCNT	379.7	0.54	0.35	98.05	1.15	0.80	4.93	0.60	0.02

7.6 Theoretical Calculation Section

The spin-unrestricted density functional theory (DFT) calculations were carried out by using the Dmol³ package. Generalized gradient approximation (GGA) with Perdew–Burke–Ernzerhof (PBE) is taken as the exchange–correlation function. All electron core treatment is implemented for relativistic effects. Double numerical plus polarization (DNP) is employed as the basis set. The convergence tolerance of energy of 10⁻⁵ Hartree is taken (1 Hartree = 27.21 eV), and the maximal allowed force and displacement are 0.002 Hartree/Å and 0.005 Å, respectively. The DFT-D method within the Grimme schemeⁱ is used in all calculations to consider the van der Waals forces. In the simulation, three-dimensional periodic boundary conditions are taken. In this work, (6,6) single wall carbon nanotubes (SWCNTs) is taken as an example to consider the catalytic effect for pollution molecules activation. The size of the

simulation cell is $a \times b \times c = 30 \times 30 \times 9.838 \text{ \AA}$. The much bigger a, b are taken to minimize the interaction among different SWCNTs. The k -point is set to $6 \times 6 \times 1$, and all atoms are allowed to relax. To understand the catalytic effect on activation of some pollution molecules, such as PMS, H_2O_2 , PS molecules, their adsorption on SWCNTs is studied by DFT calculations.

7.7 Results and discussion

Figure 7.2.1 shows that the super-oxidants can hardly oxidize phenol without a catalyst. The catalytic performance of the modified SWCNTs for PMS activation is illustrated in Figure 7.2.1a. The o-SWCNT can provide 56.5% phenol removal in 180 min, while SWCNT-700 and N-SWCNT achieved complete phenol degradation in 180 and 45 min, respectively.(64) The initial reaction rates of o-SWCNT, SWCNT-700, and NoCNT were calculated to be 0.09, 0.46, and 4.93 $\text{ppm} \cdot \text{min}^{-1}$, respectively, based on pseudo first-order kinetics. The observations on carbon nanotubes-based materials were consistent with those of rGO, which is more efficient for PMS activation than GO with excess oxygen groups but less active than nitrogen doped rGO.(24, 27, 63) We further combined experimental design and computational studies to reveal that substitutional N-doping (graphitic N) can effectively break the chemical inertness of conjugated graphene network and facilitate charge transfer from adjacent carbon atoms to graphitic nitrogen atoms, giving rise to positively charged sites which can effectively improve the adsorption capability of PMS and weaken the O-O (HO-SO_4) bond.(63, 65)

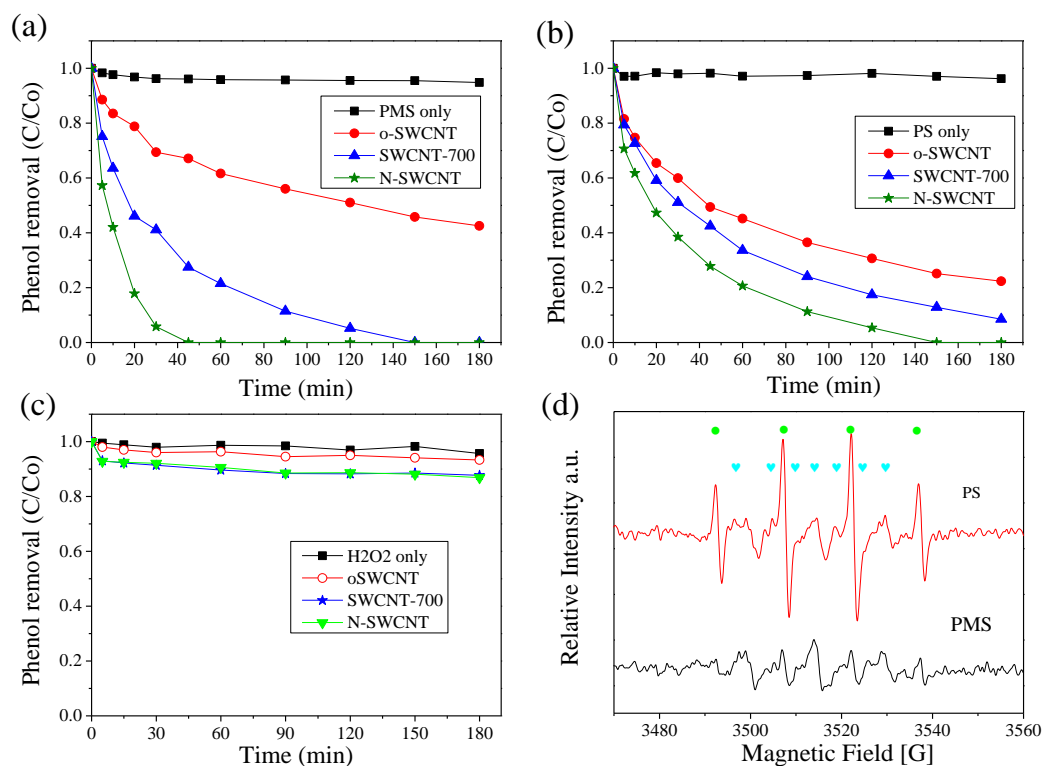


Figure 7.2.1. Phenol oxidation with (a) PMS (6.5 mM), (b) PS (6.5 mM) and (c) H₂O₂ (30 mM) under various conditions. [Phenol] = 20 ppm, [Catalyst] = 0.1 g/L, [Temperature] = 25 °C. (d) EPR spectra of PMS and PS activation on N-SWCNT (●: DMPO-OH, ♥: DMPO-SO₄).

The influence of annealing temperature of N-SWCNTs on PS activation is illustrated in Figure 7.2.S1. N-SWCNT under 700 °C presents the best catalytic activity among 600 ~ 900 °C, which is in well consistent with our previous studies on PMS activation on N-rGO and N-SWCNT.(63, 64) Rising annealing temperature gives a lower N concentration owing to the breakup of C-N bonds, meanwhile attaining a higher graphitic N proportion due to its better thermal stability. The experimental results suggests that both N- doping level and nitrogen species synergistically affect the carbocatalysis for peroxides activation. Additionally, the stability of the carbocatalysts were evaluated as shown in Figure 7.2.S2. The N-SWCNT after 1nd and 2rd cycles provided 73.2% and 53.0% phenol removal, respectively. The deactivation of the carbocatalysts can be ascribed to the alteration of surface charges and detaches of N dopants during the oxidation processes.

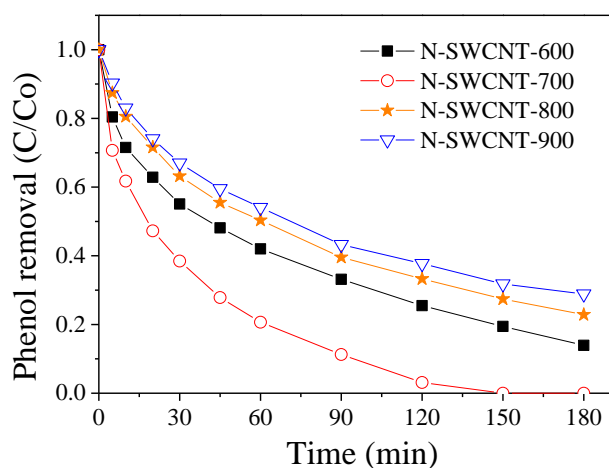


Figure 7.2.S1. Effect of annealing temperature of N-SWCNTs on PS activation. [Phenol] = 20 ppm, [Catalyst] = 0.1 g/L, [Temperature] = 25 °C, [PS] = 6.5 mM.

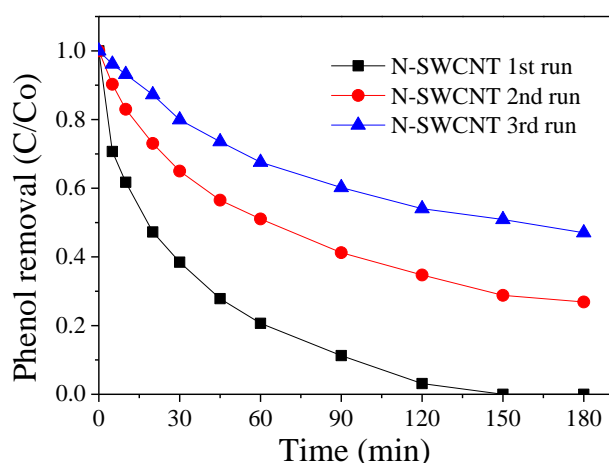


Figure 7.2.S2. Stability test of N-SWCNT for PS activation. [Phenol] = 20 ppm, [Catalyst] = 0.1 g/L, [Temperature] = 25 °C, [PS] = 6.5 mM.

N-doping for potentially enhanced PS and H₂O₂ activation is presented in Figures 7.2.1 b and c. It was found that N-doping can slightly improve the catalytic performance in PS activation, however, is ineffective for H₂O₂ activation. More specifically, o-SWCNT, SWCNT-700, and N-SWCNT attained 77.8, 91.6, and 100% phenol degradation with PS in 180 min and the initial reaction rates were estimated to be 0.32, 0.42, and 0.60 ppm•min⁻¹ accordingly. It is interesting to note that, though o-SWCNT is more efficient for PS activation than PMS, nitrogen-doped sample does not show the same trend, suggesting that the intrinsic mechanism of PS and PMS activation on N-SWCNT might be different. Figure 7.2.1c indicates poor effectiveness for H₂O₂

activation on both SWCNT-700 and N-SWCNT with only 12.3 and 13.1% phenol oxidation in 180 min, compared with 6.7% phenol removal on o-SWCNT. Recently, Yang et al. reported that ozone can react with PMS to generate sulfate and hydroxyl radicals,(66) which motivated us to explore if such a synergistic effect exists in the PMS/H₂O₂ or PS/H₂O₂ systems. However, as illustrated in Figure 7.2.S3, we found that both PMS and PS cannot work as efficient initiators to improve the activation of H₂O₂ on N-SWCNT. Moreover, the presence of H₂O₂ lowered the phenol oxidation efficiency on PMS/N-SWCNT and PS/N-SWCNT.

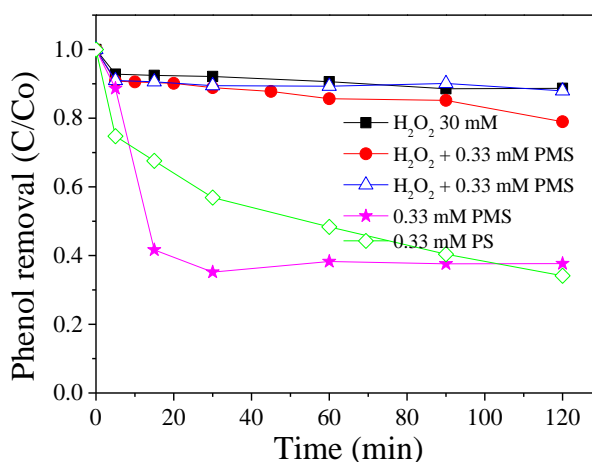


Figure 7.2.S3. Effect of H₂O₂ activation on N-SWCNT with PS and PMS. [Phenol] = 20 ppm, [Catalyst] = 0.1 g/L, [Temperature] = 25 °C, [H₂O₂]=30 mM.

We employed *in-situ* electron paramagnetic resonance (EPR) to investigate the radical generation process during PMS and PS activation on the carbocatalysts. As the generated free radicals usually have a very short lifetime and then quickly react with the organic compounds or are quenched through coupling with another radical molecule, the free-radicals were captured by a spin-trapping agent, 5,5-dimethyl-1-pyrroline N-oxide (DMPO), to form relative stable adducts and detected by EPR for the mechanistic study. As illustrated in Figure 7.2.1d, N-SWCNT can activate both PMS and PS to generate sulfate radicals (SO₄^{•-}) and hydroxyl radicals (•OH). Nevertheless, the PMS/N-SWCNT system is much more efficient than PS/N-SWCNT for phenol oxidation, the intensity of generated radicals from PS activation is much higher than that from PMS. In the AOPs, the reactive radicals play crucial roles in attacking and decomposing organics into oxidized products. The intrinsic distinction

of PMS and PS activation on N-SWCNTs for radical generation and phenol oxidation implies the completely different reaction pathways.

We further carried out density functional theory (DFT) calculations to discover the intricate interactions between the superoxides and carbocatalysts. The corresponding O-O bond lengths (l'_{O-O}) in free PMS, H₂O₂ and PS are 1.326, 1.471, and 1.222 Å, respectively. Table 7.2.1 suggests that the adsorption of PMS and PS on both SWCNT and N-doped SWCNT is quite strong, which induces relatively large electron transfer between the oxidant molecules and SWCNT (or N- SWCNT). The O-O bond length (l_{O-O}) of SO₃-OH in PMS and SO₄-SO₄ in PS increased remarkably comparing with that of free PMS and PS. However, the adsorption of H₂O₂ is very weak, mirrored by the low adsorption energy and near zero charge transfer. Therefore, SWCNT is theoretically proven to have excellent performance to activate PMS and PS molecules to be dissociated into -SO₃ and -OH groups, or two -SO₄ groups. The noticeable electron transfer tendency (Q) possibly suggests the generation of free radicals and anions. After N incorporation into SWCNT, the catalytic performance increases with a higher adsorption energy, more rapid charge transfer, and larger l_{O-O} value. Such changes were not observed in H₂O₂ activation. Thus, the theoretical calculations were in good accordance with the experimental results.

Table 7.2.1. The adsorption energy E_{ads} , electrons transfer between SWCNT and the adsorbed molecule Q , and the O-O bond length (l_{O-O}) of SO₃-OH in PMS, SO₄-SO₄ in PS, and HO-OH in H₂O₂ from different adsorption configurations in Figure 7.2.S4.

Type of CNT	Molecules	E_{ads} (eV)	Q (e)	l_{O-O} (Å)
Free molecule	PMS	-	-	1.326
	PS	-	-	1.222
	H ₂ O ₂	-	-	1.471
SWCNT	PMS	-2.05	-0.455	1.402
	PS	-1.74	-0.693	1.295
	H ₂ O ₂	-0.30	0	1.469
N-doped SWCNT	PMS	-2.98	-0.757	1.459
	PS	-2.99	-0.945	1.344
	H ₂ O ₂	-0.26	0.007	1.471

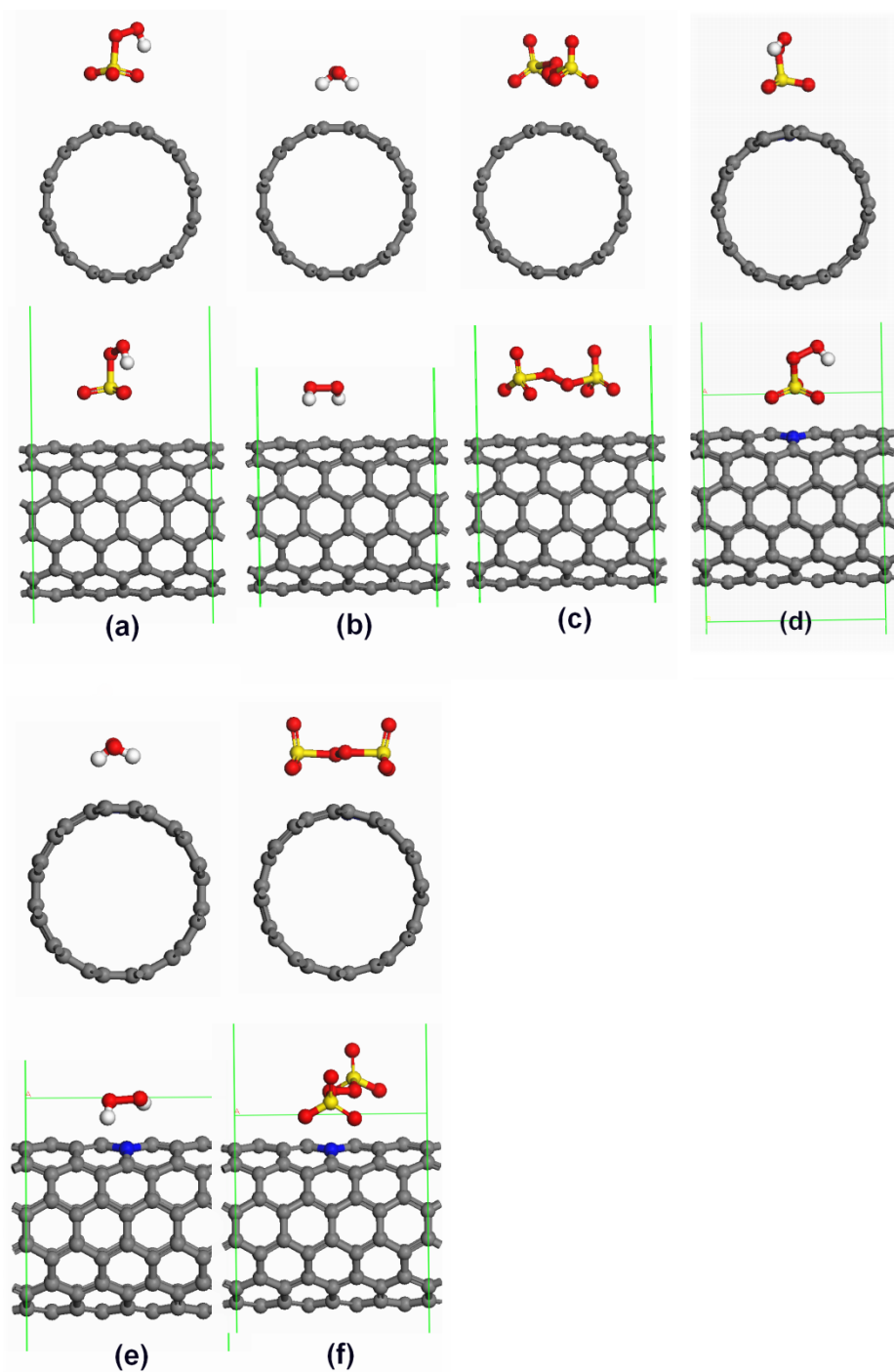


Figure 7.2.S4. The favourite adsorption configuration of PMS, H₂O₂, and PS on SWCNT and N-doped SWCNT, respectively. Both the front view and side view are shown here. (a) PMS on SWCNT, (b) H₂O₂ on SWCNT, (c) PS on SWCNT, (d) PMS on N-doped SWCNT, (e) H₂O₂ on N-doped SWCNT, (f) PS on N-doped SWCNT. The grey, blue, red, yellow, and white atoms are C, N, O, S, and H atoms, respectively.

Nevertheless the calculations revealed that nitrogen doping has a more remarkable enhancement for PS activation than PMS (reflected by more significant increases in E_{ads} , Q , and l_{O-O}), the catalytic oxidation did not follow this theoretical expectation. Based on the experiments and DFT calculations, we suggest that PMS and PS activation processes on N-SWCNT might be different. In a previous study, we first discovered that N-doping can induce nonradical reactions which co-exist with the radical pathway during catalytic phenol oxidation with PMS.(64) The PMS molecules are first adsorbed and interacted with activated sp^2 -conjugated carbon network due to nitrogen-doping, and then reacted rapidly with the target organics via a nonradical-generated oxidation process. The same phenomenon was also found in a PS/CuO system. PS first interacts with the outer-sphere of CuO electronic shell, which is the rate-limiting step, and then decomposes 2, 4-chlorophenol directly.(34) In order to investigate if such non-radical processes occur in the PS/N-SWCNT system as well, ethanol (EtOH), which can quickly quench both the sulfate and hydroxyl radicals, was utilized as a radical scavenger to quench the reactive species produced from PS activation.(52) The degradation efficiency decreased significantly with the rising ratio of ethanol in PS/SWCNT-700 and PS/N-SWCNT systems (Figures 7.2.2 a and b). The initial reaction rates were estimated (Figure 7.2.2c) and reduced significantly when the water was completely replaced by ethanol (only around 1% water remaining introduced during preparation of phenol solution), which is intrinsically different from the PMS/N-SWCNT system in which very high phenol removal efficiency still maintained in the ethanol solution.(64) The oxidation reaction was almost terminated with high concentration of ethanol in PS/N-SWCNT systems, suggesting that the generation of reactive radical was essential for phenol oxidation with PS and non-radical process was almost absent in the PS/N-SWCNT system.

It is also noteworthy that N-SWCNT can effectively activate PS to generate large amounts of hydroxyl radicals ($\cdot OH$) as indicated in the EPR spectra (Figure 7.2.1d). To the best of our knowledge, persulfate ($S_2O_8^{2-}$) cannot generate hydroxyl radicals itself and the large amounts of hydroxyl radicals can exclusively be devolved from water. We suppose that PS might be able to oxidize water directly on N-SWCNT to generate hydroxyl radicals for phenol degradation, shown in Figure 7.2.2d. A theoretical model was built up to modulate this process as presented in Figures 7.2.3 a and b. As one can see from Figure 7.2.3c and Table 7.2.S2, the adsorption of H_2O

molecules on nitrogen-doped SWCNT is minor due to the weak adsorption energy, little electron transfer from H₂O to SWCNT, and the O-H bond length rarely changes after adsorption. However, if a PS molecule presents together with a water molecule on the N-SWCNT (Figure 7.2.3b), the H₂O molecule adsorption enhances remarkably, where the adsorption energy increases almost 3 times, the charge transfer becomes 7 times faster, and the O-H bond length also is prolonged greatly (Table 7.2.S2). The adsorption capability of PS is also enhanced with a longer O-O bond length and faster electron transfer (Figure 7.2.3d).

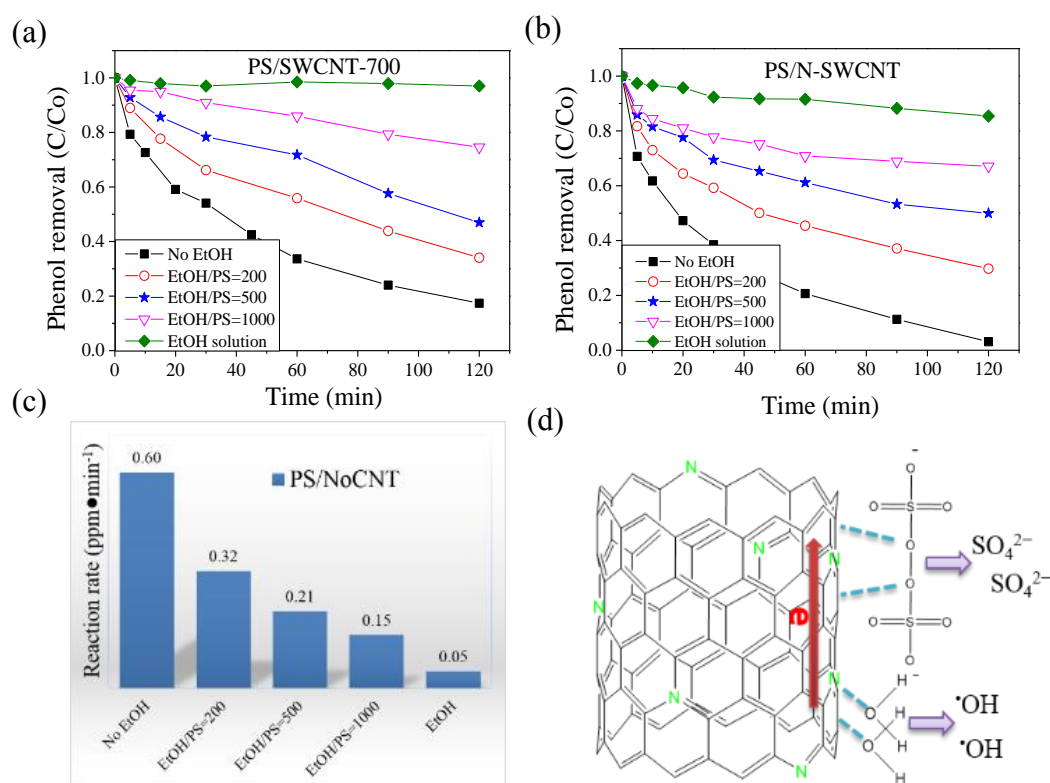


Figure 7.2.2. Effects of radical scavenger (EtOH) on phenol degradation in (a) PS/SWCNT-700, and (b) PS/N-SWCNT systems. (c) Reaction rates of phenol oxidation with PS on N-SWCNT under different ratios of EtOH. ([Phenol] = 20 ppm, [Catalyst] = 0.1 g/L, [Temperature] = 25 °C, [PS]=6.5 mM.) (d) Proposed mechanism of PS activation on N-SWCNT.

Therefore, the presence of PS can promote the dissociation of H₂O and facilitate the generation of ·OH group to form hydroxyl radicals. N-doped carbon nanotubes can activate H₂O molecules via acting as a fascinating bridge for electron transfer from H₂O to PS as proposed in Figure 7.2.2d. Besides, PS might be converted into sulfate

ions directly due to its great ability to extract electrons from the carbon matrix on N-SWCNT (Figure 7.2.3d and Table 7.2.S2) when it co-exists with adsorbed water, as no obvious signal of sulfate radical can be found in EPR spectra in Figure 7.2.1d. Distinct from PS and H₂O₂, the asymmetric structure of PMS (HO-SO₄) and the relative weak adsorption and oxidation ability on N-SWCNT might contribute to the emerging nonradical reaction for PMS activation.

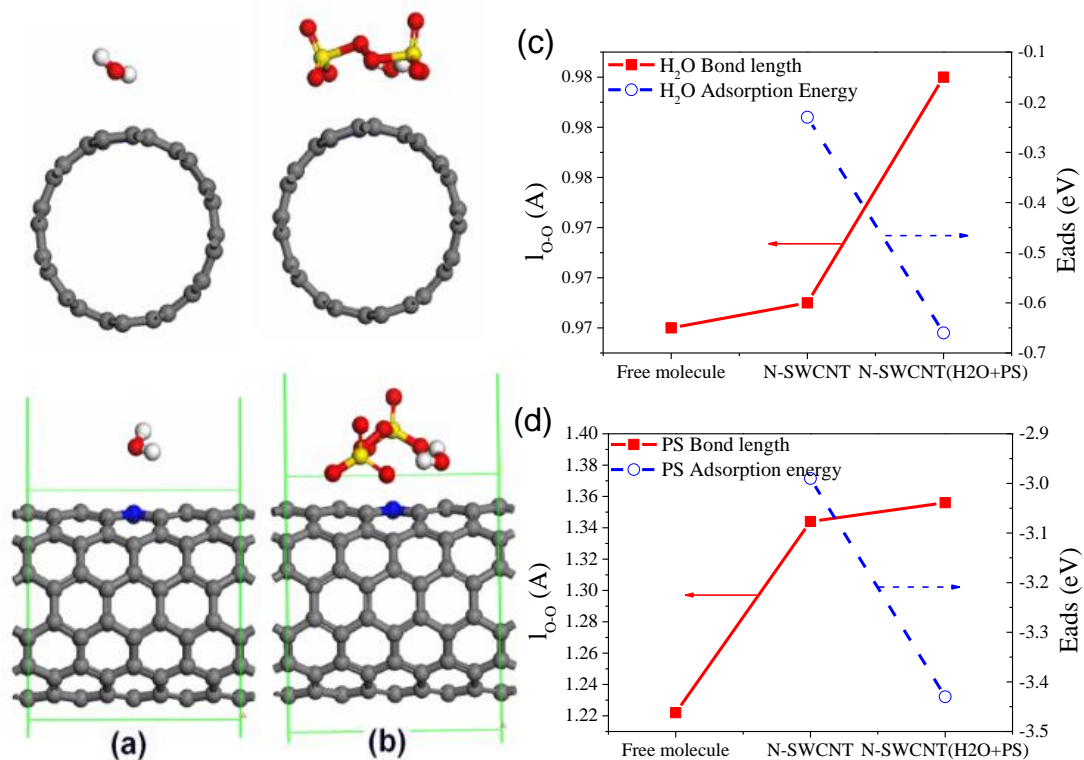


Figure 7.2.3. (a) H₂O adsorption on N-SWCNT, (b) PS and H₂O adsorbed on the N-SWCNT. (The grey, blue, red, yellow, and white atoms are C, N, O, S, and H atoms, respectively. The O-O bond length (l_{O-O}) and adsorption energy of (c) H₂O and (d) PS under different conditions: free molecule, adsorption alone on N-SWCNT, and co-adsorbed on N-SWCNT.

Table 7.2.S2. The adsorption energy E_{ads} , electrons transfer between SWCNT and the adsorbed molecule Q , and the O-O bond length of free molecule, PS or H_2O_2 adsorbed on N-SWCNT and PS adsorbed on N-SWCNT together with H_2O_2 .

Type of CNT	Molecules	E_{ads} (eV)	Q (e)	$l_{\text{O-O}}$ (Å)
Free molecule	PS	-	-	1.222
	H_2O	-	-	0.970
N-doped SWCNT	PS	-2.99	-0.945	1.344
	H_2O	-0.23	0.008	0.971
N-SWCNT with H_2O and PS	PS	-3.43	-1.021	1.356
	H_2O	-0.66	0.059	0.980

7.8 Conclusions

In summary, we investigated the effect of N-doping on activation of various superoxides including PMS, PS, and H_2O_2 . Both experimental results and theoretical calculations proved that N-doping can enhance PMS and PS activation, yet is not effective for H_2O_2 activation. N-doping can induce nonradical oxidation in PMS activation, whereas works as an excellent electron-bridge to facilitate PS to oxidize adsorbed water to generate hydroxyl radicals for catalytic oxidation. This study concludes new insights into N-doping in carbocatalysis for oxidative processes.

References

1. Behrens M, Studt F, Kasatkin I, Kuhl S, Havecker M, Abild-Pedersen F, et al. The active site of methanol synthesis over Cu/ZnO/ Al_2O_3 Ind. Catal. Sci. 2012;336(6083):893-7.
2. Chen MS, Kumar D, Yi CW, Goodman DW. The promotional effect of gold in catalysis by palladium-gold. Science. 2005;310(5746):291-3.
3. Liu SW, Yu JG, Jaroniec M. Tunable Photocatalytic Selectivity of Hollow TiO_2 microspheres composed of anatase polyhedra with exposed {001} facets. J. Am. Chem. Soc. 2010;132(34):11914-6.
4. Ishikawa A, Takata T, Kondo JN, Hara M, Kobayashi H, Domen K. Oxysulfide $\text{Sm}_2\text{Ti}_2\text{S}_2\text{O}_5$ as a stable photocatalyst for water oxidation and reduction under visible light irradiation ($\lambda \leq 650$ nm). J. Am. Chem. Soc. 2002;124(45):13547-53.
5. Saputra E, Muhammad S, Sun HQ, Ang HM, Tade MO, Wang SB. Manganese oxides at different oxidation states for heterogeneous activation of peroxydisulfate for phenol degradation in aqueous solutions. Appl. Catal., B 2013;142:729-35.

6. Montoya JF, Bahnemann DW, Peral J, Salvador P. Catalytic role of TiO₂ terminal oxygen atoms in liquid-phase photocatalytic reactions: oxidation of aromatic compounds in anhydrous acetonitrile. *Chemphyschem*. 2014;15(11):2311-20.
7. Besson M, Gallezot P. Selective oxidation of alcohols and aldehydes on metal catalysts. *Catal. Today*. 2000;57(1-2):127-41.
8. Zhang JA, Su DS, Blume R, Schlogl R, Wang R, Yang XG, et al. Surface chemistry and catalytic reactivity of a nanodiamond in the steam-free dehydrogenation of ethylbenzene. *Angew. Chem. Int. Ed*. 2010;49(46):8640-4.
9. Andreozzi R, Caprio V, Insola A, Marotta R. Advanced oxidation processes (AOP) for water purification and recovery. *Catal. Today*. 1999;53(1):51-9.
10. Zazo JA, Casas JA, Mohedano AF, Gilarranz MA, Rodriguez JJ. Chemical pathway and kinetics of phenol oxidation by Fenton's reagent. *Environ. Sci. Technol*. 2005;39(23):9295-302.
11. Yang L, Hu C, Nie YL, Qu JH. Catalytic Ozonation of selected pharmaceuticals over mesoporous alumina-supported manganese oxide. *Environ. Sci. Technol*. 2009;43(7):2525-9.
12. Zhao W, Ma WH, Chen CC, Zhao JC, Shuai ZG. Efficient degradation of toxic organic pollutants with Ni₂O₃/TiO_{2-x}B_x under visible irradiation. *J. Am. Chem. Soc*. 2004;126(15):4782-3.
13. Anipsitakis GP, Dionysiou DD, Gonzalez MA. Cobalt-mediated activation of peroxymonosulfate and sulfate radical attack on phenolic compounds. Implications of chloride ions. *Environ. Sci. Technol*. 2006;40(3):1000-7.
14. Anipsitakis GP, Dionysiou DD. Radical generation by the interaction of transition metals with common oxidants. *Environ. Sci. Technol*. 2004;38(13):3705-12.
15. Wang Y, Sun H, Ang HM, Tadé MO, Wang S. 3D-hierarchically structured MnO₂ for catalytic oxidation of phenol solutions by activation of peroxymonosulfate: Structure dependence and mechanism. *Appl. Catal., B*. 2015;164(0):159-67.
16. Ball DL, Edwards JO. The kinetics and mechanism of the decomposition of Caro's acid. I. *J. Am. Chem. Soc*. 1956;78(6):1125-9.
17. Buxton GV, Greenstock CL, Helman WP, Ross AB. Critical review of rate constants for reactions of hydrated electrons, hydrogen atoms and hydroxyl radicals ($\cdot\text{OH}/\text{O}^-$) in aqueous solution. *J. Phys. Chem. Ref. Data*. 1988;17(2):513-886.
18. Neta P, Huie RE, Ross AB. Rate constants for reactions of inorganic radicals in aqueous-solution. *J. Phys. Chem. Ref. Data*. 1988;17(3):1027-284.
19. Saputra E, Muhammad S, Sun HQ, Ang HM, Tade MO, Wang SB. Different Crystallographic One-dimensional MnO₂ nanomaterials and their superior performance in catalytic phenol degradation. *Environ. Sci. Technol*. 2013;47(11):5882-7.

20. Anipsitakis GP, Stathatos E, Dionysiou DD. Heterogeneous activation of oxone using Co_3O_4 . *J. Phys. Chem. B* 2005;109(27):13052-5.
21. Frank B, Blume R, Rinaldi A, Trunschke A, Schlogl R. Oxygen insertion catalysis by sp^2 carbon. *Angew. Chem., Int. Ed.* 2011;50(43):10226-30.
22. Frank B, Zhang J, Blume R, Schlogl R, Su DS. Heteroatoms increase the selectivity in oxidative dehydrogenation reactions on nanocarbons. *Angew. Chem., Int. Ed.* 2009;48(37):6913-7.
23. Zhang J, Liu X, Blume R, Zhang AH, Schlogl R, Su DS. Surface-modified carbon nanotubes catalyze oxidative dehydrogenation of n-butane. *Science*. 2008;322(5898):73-7.
24. Sun HQ, Liu SZ, Zhou GL, Ang HM, Tade MO, Wang SB. Reduced graphene oxide for catalytic oxidation of aqueous organic pollutants. *ACS Appl. Mater. Interfaces*. 2012;4(10):5466-71.
25. Cui W, Liu Q, Cheng NY, Asiri AM, Sun XP. Activated carbon nanotubes: a highly-active metal-free electrocatalyst for hydrogen evolution reaction. *Chem. Commun.* 2014;50(66):9340-2.
26. Peng WC, Liu SZ, Sun HQ, Yao YJ, Zhi LJ, Wang SB. Synthesis of porous reduced graphene oxide as metal-free carbon for adsorption and catalytic oxidation of organics in water. *J. Mater. Chem. A* 2013;1(19):5854-9.
27. Sun HQ, Wang YX, Liu SZ, Ge L, Wang L, Zhu ZH, et al. Facile synthesis of nitrogen doped reduced graphene oxide as a superior metal-free catalyst for oxidation. *Chem. Commun.* 2013;49(85):9914-6.
28. Sun HQ, Kwan C, Suvorova A, Ang HM, Tade MO, Wang SB. Catalytic oxidation of organic pollutants on pristine and surface nitrogen-modified carbon nanotubes with sulfate radicals. *Appl. Catal., B* 2014;154:134-41.
29. Bepete G, Tetana ZN, Lindner S, Rummeli MH, Chiguvare Z, Coville NJ. The use of aliphatic alcohol chain length to control the nitrogen type and content in nitrogen doped carbon nanotubes. *Carbon*. 2013;52:316-25.
30. Shi F, Tse MK, Li ZP, Beller M. Controlling iron-catalyzed oxidation reactions: from non-selective radical to selective non-radical reactions. *Chem. Europ. J.* 2008;14(29):8793-7.
31. Deguillaume L, Leriche M, Chaurnerliac N. Impact of radical versus non-radical pathway in the Fenton chemistry on the iron redox cycle in clouds. *Chemosphere*. 2005;60(5):718-24.
32. Nunes GS, Alexiou ADP, Toma HE. Catalytic oxidation of hydrocarbons by trinuclear μ -oxo-bridged ruthenium-acetate clusters: Radical versus non-radical mechanisms. *J. Catal.* 2008;260(1):188-92.

33. Zhang T, Li WW, Croue JP. A non-acid-assisted and non-hydroxyl-radical-related catalytic ozonation with ceria supported copper oxide in efficient oxalate degradation in water. *Appl. Catal., B* 2012;121:88-94.
34. Zhang T, Chen Y, Wang Y, Le Roux J, Yang Y, Croué J-P. Efficient peroxydisulfate activation process not relying on sulfate radical generation for water pollutant degradation. *Environ. Sci. Technol.* 2014;48(10):5868-75.
35. Zhao AQ, Masa J, Xia W, Maljusch A, Willinger MG, Clavel G, et al. Spinel Mn-Co oxide in N-doped carbon nanotubes as a bifunctional electrocatalyst synthesized by oxidative cutting. *J. Am. Chem. Soc.* 2014;136(21):7551-4.
36. Chen PR, Yang FK, Kostka A, Xia W. Interaction of cobalt nanoparticles with oxygen- and nitrogen-functionalized carbon nanotubes and impact on nitrobenzene hydrogenation catalysis. *ACS Catal.* 2014;4(5):1478-86.
37. Long JL, Xie XQ, Xu J, Gu Q, Chen LM, Wang XX. Nitrogen-doped graphene nanosheets as metal-free catalysts for aerobic selective oxidation of benzylic alcohols. *ACS Catal.* 2012;2(4):622-31.
38. Wang SY, Zhang LP, Xia ZH, Roy A, Chang DW, Baek JB, et al. BCN graphene as efficient metal-free electrocatalyst for the oxygen reduction reaction. *Angew. Chem., Int. Ed.* 2012;51(17):4209-12.
39. Zheng Y, Jiao Y, Ge L, Jaroniec M, Qiao SZ. Two-step boron and nitrogen doping in graphene for enhanced synergistic catalysis. *Angew. Chem., Int. Ed.* 2013;52(11):3110-6.
40. Higgins DC, Hoque MA, Hassan F, Choi J-Y, Kim B, Chen Z. Oxygen reduction on graphene-carbon nanotube composites doped sequentially with nitrogen and sulfur. *ACS Catal.* 2014;4(8):2734-40.
41. Sheng ZH, Shao L, Chen JJ, Bao WJ, Wang FB, Xia XH. Catalyst-free synthesis of nitrogen-doped graphene via thermal annealing graphite oxide with melamine and its excellent electrocatalysis. *ACS Nano.* 2011;5(6):4350-8.
42. Li XL, Wang HL, Robinson JT, Sanchez H, Diankov G, Dai HJ. Simultaneous nitrogen doping and reduction of graphene oxide. *J. Am. Chem. Soc.* 2009;131(43):15939-44.
43. Yang Z, Yao Z, Li GF, Fang GY, Nie HG, Liu Z, et al. Sulfur-doped graphene as an efficient metal-free cathode catalyst for oxygen reduction. *ACS Nano.* 2012;6(1):205-11.
44. Deng DH, Pan XL, Yu LA, Cui Y, Jiang YP, Qi J, et al. Toward N-doped graphene via solvothermal synthesis. *Chem. Mater.* 2011;23(5):1188-93.
45. Liang HW, Sun HQ, Patel A, Shukla P, Zhu ZH, Wang SB. Excellent performance of mesoporous $\text{Co}_3\text{O}_4/\text{MnO}_2$ nanoparticles in heterogeneous activation of peroxydisulfate for phenol degradation in aqueous solutions. *Appl. Catal., B* 2012;127:330-5.

46. Kong XK, Chen CL, Chen QW. Doped graphene for metal-free catalysis. *Chem. Soc. Rev.* 2014;43(8):2841-57.
47. Jiang DE, Sumpter BG, Dai S. Unique chemical reactivity of a graphene nanoribbon's zigzag edge. *J. Chem. Phys.* 2007;126(13).
48. Zhao Y, Yang LJ, Chen S, Wang XZ, Ma YW, Wu Q, et al. Can boron and nitrogen co-doping improve oxygen reduction reaction activity of carbon nanotubes? *J. Am. Chem. Soc.* 2013;135(4):1201-4.
49. Bennett JE, Gilbert BC, Stell JK. Mechanisms of peroxide decomposition. EPR studies of the one-electron oxidation of the peroxy monosulphate anion (HOOSO_3^-) and the reactions of $\text{SO}_5^{\cdot-}$. *J. Chem. Soc, Perkin Trans 2* 1991(8):1105-10.
50. Gilbert BC, Stell JK. Mechanisms of Peroxide Decomposition. An ESR study of the reactions of the peroxomonosulphate anion (HOOSO_3^-) with Ti(III), Fe(II), and alpha-oxygen-substituted radicals. *J. Chem. Soc, Perkin Trans 2.* 1990(8):1281-8.
51. Gilbert BC, Stell JK. Mechanisms of peroxide decomposition: an electron paramagnetic resonance study of the reaction of the peroxomonosulphate anion (HOOSO_3^-) with Cu(I). A marked contrast in behaviour with that Ti(III) and Fe(II). *J. Chem. Soc, Faraday Trans* 1990;86(19):3261-6.
52. Anipsitakis GP, Dionysiou DD. Degradation of organic contaminants in water with sulfate radicals generated by the conjunction of peroxy monosulfate with cobalt. *Enviro. Sci. Technol.* 2003;37(20):4790-7.
53. Liu XW, Sun XF, Li DB, Li WW, Huang YX, Sheng GP, et al. Anodic Fenton process assisted by a microbial fuel cell for enhanced degradation of organic pollutants. *Water Res.* 2012;46(14):4371-8.
54. Saputra E, Muhammad S, Sun H, Ang HM, Tade MO, Wang S. Different crystallographic one-dimensional MnO_2 nanomaterials and their superior performance in catalytic phenol degradation. *Enviro. Sci. Technol.* 2013;47(11):5882-7.
55. Zhang T, Zhu H, Croue J-P. Production of sulfate radical from peroxy monosulfate induced by a magnetically separable CuFe_2O_4 spinel in water: efficiency, stability, and mechanism. *Environ. Sci. Technol.* 2013;47(6):2784-91.
56. Drzewicz P, Perez-Estrada L, Alpatova A, Martin JW, El-Din MG. Impact of peroxydisulfate in the presence of zero valent iron on the oxidation of cyclohexanoic acid and naphthenic acids from oil sands process-affected water. *Enviro. Sci. Technol.* 2012;46(16):8984-91.
57. Cheng NY, Liu Q, Tian JQ, Xue YR, Asiri AM, Jiang HF, et al. Acidically oxidized carbon cloth: a novel metal-free oxygen evolution electrode with high catalytic activity. *Chem. Commun.* 2015;51(9):1616-9.
58. Kim Y, Shanmugam S. Polyoxometalate reduced graphene oxide hybrid catalyst: synthesis, structure, and electrochemical properties. *ACS Appl. Mater. Interfaces.* 2013;5(22):12197-204.

59. Sanetuntikul J, Hang T, Shanmugam S. Hollow nitrogen-doped carbon spheres as efficient and durable electrocatalysts for oxygen reduction. *Chem. Commun.* 2014;50(67):9473-6.
60. Wu Z-S, Yang S, Sun Y, Parvez K, Feng X, Muellen K. 3D Nitrogen-doped graphene aerogel-supported Fe₃O₄ nanoparticles as efficient electrocatalysts for the oxygen reduction reaction. *J. Am. Chem. Soc.* 2012;134(22):9082-5.
61. Li Y, Zhao Y, Cheng H, Hu Y, Shi G, Dai L, et al. nitrogen-doped graphene quantum dots with oxygen-rich functional groups. *J. Am. Chem. Soc.* 2012;134(1):15-8.
62. Liang J, Jiao Y, Jaroniec M, Qiao SZ. Sulfur and nitrogen dual-doped mesoporous graphene electrocatalyst for oxygen reduction with synergistically enhanced performance. *Angew. Chem. Int. Ed.* 2012;51(46):11496-500.
63. Duan XG, Ao ZM, Sun HQ, Indrawirawan S, Wang YX, Kang J, et al. Nitrogen-doped graphene for generation and evolution of reactive radicals by metal-free catalysis. *ACS Appl. Mater. Interfaces.* 2015;7(7):4169-78.
64. Duan XG, Sun HQ, Wang YX, Kang J, Wang SB. N-doping-induced nonradical reaction on single-walled carbon nanotubes for catalytic phenol oxidation. *ACS Catal.* 2015;5(2):553-9.
65. Duan X, O'Donnell K, Sun H, Wang Y, Wang S. Sulfur and nitrogen co-doped graphene for metal-free catalytic oxidation reactions. *Small.* 2015;11(25):3036-44.
66. Yang Y, Jiang J, Lu X, Ma J, Liu Y. Production of sulfate radical and hydroxyl radical by reaction of ozone with peroxymonosulfate: A novel advanced oxidation process. *Environ. Sci. Technol.* 2015;49(12):7330-39.

Every reasonable effort has been made to acknowledge the owners of copyright material. I would be pleased to hear from any copyright owner who has been omitted or incorrectly acknowledged.

Chapter 8. Conclusions and Perspectives

8.1 Conclusions

Surface-modified nanocarbons have demonstrated superior performances toward heterogeneous activation of persulfate (PS) and peroxymonosulfate (PMS) for organic degradation. Nanocarbons such as reduced graphene oxide (rGO), mesoporous carbon, single-walled carbon nanotubes (SWCNTs), and annealed nanodiamond (AND) are excellent carbocatalysts to activate persulfate to produce hydroxyl radicals for catalytic oxidation. The carbocatalysts perform as a superb electron-transfer tunnel to activate PS via oxidizing surface adsorbed water molecules to produced hydroxyl radicals. Nitrogen-doping can significantly promote the catalytic activity of graphene for PMS activation, and co-doping with proper amount of sulfur is able to manipulate the surface chemistry of N-graphene and further enhances the catalytic performance. Moreover, non-radical oxidation pathway was discovered upon N-doping on SWCNTs for aqueous oxidation with PMS. The comprehensive mechanism studies of PS and PMS activation with carbocatalysis are illuminated with experimental design and theoretical calculation. This study not only discovers several metal-free nanocarbon catalysts for PS and PMS activation, but also contributes to exploring new advanced oxidative systems for wastewater treatment without secondary contamination and facilitating new insights into heterogeneous carbocatalysis.

8.1.1 Insights into heterogeneous catalysis of persulfate activation on dimensional-structured nanocarbons

- ❖ Various nanocarbons were tested as metal-free catalysts for catalytic oxidation of organic contaminants. For the first time, we found that SWCNTs, reduced graphene oxide and CMK-8 demonstrated superior efficiencies for PS activation, whereas C_{60} , g- C_3N_4 and nanodiamond presented poor performances.
- ❖ The carbocatalysts showed a much higher activity than the universally used metal oxides such as Fe_3O_4 , CuO, Co_3O_4 and MnO_2 . And rGO-900 was even comparable to the most efficient electron donor of ZVI.

- ❖ Both the characterization and adsorption/oxidation results revealed that the structural dimension of carbon might affect the phenol adsorption capability, while catalytic activity of nanocarbons is strongly dependent on the conjugation of carbon network, defective sites, and proper amounts of functional groups (especially the carbonyl groups).
- ❖ The EPR results suggested that heterogeneous activation of PS is different from homogeneous systems and carbocatalysts can effectively activate PS molecules via directly oxidizing adsorbed water through the carbon bridge.

8.1.2 Controlled generation of reactive radicals by carbocatalysis on nanodiamonds

- ❖ Annealed nanodiamonds were discovered to be able to activate PS to selectively produce hydroxyl radicals via water oxidation. Such emerging catalysis demonstrated potentials for overcoming the demerits of both sulfate and hydroxyl radical-based reactions.
- ❖ The annealed graphitic core-shell structure with versatile defects of ANDs provides a fantastic environment for oxygen and PS activation by serving as a superb bridge for charge transfer. Besides, the intricate interactions of sp^2 and sp^3 interfaces via conjugation effects are able to induce electron conduction from the nanodiamond core to shell surface, further enhancing the O-O breakup efficiency.
- ❖ AND/PS provides an excellent technology for organic oxidation, which can be applied for contaminant decomposition and selective oxidation reactions by carbocatalysis.

8.1.3 Nitrogen-doped graphene for generation and evolution of reactive radicals by metal-free catalysis

- ❖ Nitrogen-doped reduced graphene oxide with both structural and compositional modification was synthesized by a one-pot method with larger SSAs and higher nitrogen contents.

- ❖ N-doped graphene showed outstanding performance in catalytic activation of PMS for oxidation of phenol, and was superior to many other carbon allotropes and a typical metal-based catalyst of Co_3O_4 .
- ❖ Theoretical calculations illustrated that quaternary N is able to dramatically reduce the adsorption energy and facilitate electron transfer for PMS activation on graphene sheets. EPR spectra and competitive radical tests suggested that both $\cdot\text{OH}$ and $\text{SO}_4^{\cdot-}$ were generated during the activation processes and played key roles in phenol degradation.

8.1.4 Sulfur and nitrogen co-doped graphene for metal-free catalytic oxidation reactions

- ❖ This study developed a facile one-pot strategy to successfully incorporate sulfur and nitrogen atoms into graphene sheets. Both experimental and theoretical studies demonstrated that co-dopants (S and N) presented synergistically catalytic activity to enhance the PMS activation compared to the pristine and N- (or S-) sole-doped graphene.
- ❖ Kinetic studies indicated that catalyst loading, PMS dosage, initial phenol concentration and reaction temperature would pose significant influences on the phenol removal efficiencies.
- ❖ The theoretical calculations also suggested that introducing sulfur into N-doped graphene can significantly change the surface charge distribution and electrostatic potential of the graphene. Experimental results demonstrated that, compared with boron, phosphorus, and iodine, sulfur can function as an effective co-dopant to further enhance catalytic activity of N-doped graphene for phenol degradation with radicals.

8.1.5 Effect of nitrogen-doped single-walled carbon nanotubes on activation of superoxide O-O bond for enhanced metal-free oxidation

- ❖ Emerging characteristics upon nitrogen-doping was differentiated in activation of superoxides such as PMS, PS and H₂O₂ over single-walled carbon nanotubes.
- ❖ Nitrogen-doped SWCNTs (NoCNT-700) presented an extraordinarily high catalytic activity for phenol removal by PMS activation with a 57.4-fold enhancement to pristine SWCNT, as well as 16.9- and 15.6-fold towards the most effective metal catalysts, α -MnO₂ and Co₃O₄, respectively.
- ❖ For the first time, we discovered that both radical and non-radical pathways contribute to the phenol degradation on NoCNT with PMS activation. Among the N dopants, graphitic N plays a key role in the non-radical based oxidation process.
- ❖ It was also found that the temperature slightly affects the catalytic efficiency for PMS activation on SWCNTs after nitrogen modification and the as-made catalysts presented a much better stability for reuse.
- ❖ Both experimental results and theoretical calculations proved that N-doping can enhance PMS and PS activation, yet is not effective for H₂O₂ activation.

8.2 Perspectives and suggestions for future research

Despite the fact that carbocatalysts have demonstrated great potential for metal-free environmental catalysis, nanocarbons such as graphene, carbon nanotubes, and nanodiamond are still of high-cost for practical application and show a relatively low stability under oxidative condition in AOPs. Therefore, it is of great importance to design cheap and efficient nanocarbon catalysts from large-scale production and with a controlled structure and stable surface chemistry.

The PMS and PS activation on nanocarbon is a complicated process, and may involve other oxidative species such as HSO₅^{•-}, SO₃^{•-}, HO₂[•], or O₂^{•-}, in addition to [•]OH and SO₄^{•-}. In future studies, comprehensive investigations applying *in situ* EPR

technology, various radical trapping methods, and competitive radical reactions can be used to identify the predominant reactive species and probe the mechanism. Besides, the adsorption and interaction between carbocatalyst and target organic may also played crucial roles in the catalytic oxidation processes with the generated reactive radicals, and should be revealed by rationally experimental design and theoretical modelling.

In the real water matrix, solution pH, versatile metal and inorganic ions, and natural organic matters (NOMs) can significantly influence the efficiency of catalytic oxidation via reacting with the superoxide, reactive radicals, and heterogeneous catalysts. The impacts of the ions and background matters need to be evaluated in this novel oxidative system. It should also be pointed out that the current experiments in this study are performed at a laboratorial scale. The reaction conditions and dosage of the oxidant and carbocatalysts need be adjusted and optimized in the real wastewater applications, meanwhile, the total cost, mineralization effectiveness, recovery and post-treatment of the deactivated catalysts should be taken into considerations.
